
Connecting the Dots

Shedding light on the self-assembly of semiconductor nanocrystals with synchrotron X-ray scattering techniques

PhD thesis, Universiteit Utrecht

Connecting the Dots

Shedding light on the self-assembly of semiconductor nanocrystals with synchrotron
X-ray scattering techniques

Jaco Geuchies, October 2017

Printed by: Uitgeverij BOXPress || Proefschriftmaken.nl

ISBN: 978-94-629-5684-1

Connecting the Dots

Shedding light on the self-assembly of semiconductor nanocrystals with synchrotron X-ray scattering techniques

Het verbinden van de stippen

Licht werpen op de zelf-organisatie van halfgeleider nanokristallen met behulp van synchrotron Röntgen-verstrooiings technieken

(met een samenvatting in het Nederlands)

Proefschrift

ter verkrijging van de graad van doctor aan de Universiteit Utrecht op gezag van de rector magnificus, prof. dr. G.J. van der Zwaan, ingevolge van het besluit van het college voor promoties in het openbaar te verdedigen

op maandag 2 oktober 2017

des middags te 2.30

door

Jacob Jan Geuchies

geboren op 27 januari 1990 te Amersfoort

Promotor: Prof. dr. D.A.M. Vanmaekelbergh
Copromotoren: Dr. A.V. Petukhov
Dr. O. Konovalov

The work presented in this thesis was financed by the Dutch Organization for Scientific Research ('Nederlandse Organisatie voor Wetenschappelijk Onderzoek' - NWO) and by the European Synchrotron Radiation Facility as a joint project for the Debye Graduate Programme

Table of contents

1.	A brief introduction to colloidal nanocrystals and this thesis	2	◆
2.	Nanocrystals, self-assembly and X-ray scattering	10	◆
3.	Long-range orientation and atomic attachment of nanocrystals in two-dimensional honeycomb superlattices	42	◆
4.	In-situ study of the formation mechanism of two-dimensional superlattices from nanocrystals	58	◆
5.	The adsorption geometry of PbSe nanocrystals at liquid-air interfaces	80	◆
6.	Highly emissive divalent-ion-doped colloidal CsPb _{1-x} M _x Br ₃ perovskite nanocrystals through cation exchange	98	◆
7.	Structural and optical properties of supraparticles formed by self-assembly of CsPbBr ₃ perovskite nanocrystals	124	◆
8.	Summary and outlook	146	◆
	Samenvatting in het Nederlands	154	◆
	List of publications and conference contributions	170	◆
	Acknowledgements - dankwoord	174	◆
	About the author	183	◆



Chapter 1

A brief introduction to colloidal nanocrystals and this thesis

• *Abstract* •

Whether everyone is fully aware of it or not, nanotechnology impacts our everyday life. Silicon, and many other materials used in computerchips, smart phones and other devices, are being produced using advanced techniques to create smaller and smaller electronics. Nanoscience is the study of the (opto-electronic) structure of materials on the scale of nanometers. We use colloidal nanocrystals throughout this thesis, that is nanocrystals dispersed in solution, to create larger hierarchical superstructures of these crystals; crystals of nanocrystals. Moreover, the nanocrystals we study are all semiconductors, materials which we can turn on and off electronically. Semiconductors are used in a large number of applications, ranging from computerchips to solar cells. Throughout this thesis we prepare novel 2-D and 3-D semiconductors from coupled nanocrystal building blocks.

This chapter serves as an introduction to people new to the field of nanoscience and nanocrystals. A brief overview of unintended use of nanocrystals throughout history is given, followed by more modern day applications, after which a description of the two types of particles which are investigated throughout this thesis is presented; lead selenide nanocrystals and cesium lead bromide nanocrystals. We conclude with a summary of the chapters.

1.1 - Introduction

The prefix ‘nano’ in nanoscience comes from the Greek word *nánnos*, meaning dwarf. It is used throughout this thesis to indicate a length scale that is one billionth of a meter, or 0.000000001 meter. The actual scale of this number is hard to visualize but hopefully the following example somewhat helps. When one takes the diameter of the earth (12742 km) and compare it to the diameter a football (23 cm), it is a factor 55400000 times smaller. When you now shrink this football by the same ratio, one ends up around 4 nanometers, roughly the size of the nanocrystals used throughout this thesis. Alternatively you could imagine cutting your hair, which has a diameter of roughly 100 micrometers, in 100000 pieces, each being 1 nanometer in diameter. Due to their small size, nanoparticles have an incredibly large surface-to-volume ratio. As most chemical reactions happen at surfaces of materials, this makes them very useful for applications in amongst others, catalysis. On the other hand, to be able to observe the inherent quantized properties of small semiconductor nanocrystals, the atoms at the surface need to be electronically passivated. This is possible by using organic ligand molecules and/or inorganic shells.

Throughout history nanoparticles have been used unintentionally, some examples of which are given in Figure 1.1. Ancient Egyptians produced PbS nanocrystals using hair dyes based on lead oxide and lime, which absorb a large portion of the visible light¹ as PbS is a semiconductor

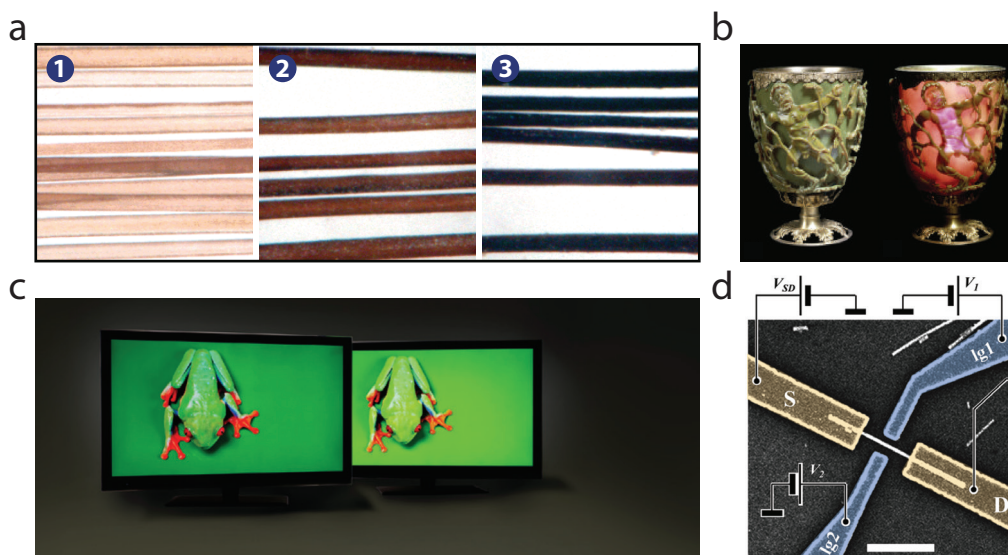


Figure 1.1: Applications of nanoparticles throughout history. (a) In ancient Egypt, people colored their hair with a lead oxide and lime containing dye, forming PbS nanoparticles which absorb a large part of the visible light, creating a black color. Reused with permission from reference [1]. (b) A fourth century Roman glass cup, also known as the Lycurgus cup, illuminated with ambient light from the front (left) and illuminated from the back. The glass contains alloyed nanoparticles of gold and silver which absorb a certain part of the visible spectrum. Reused with permission from reference [2]. (c) Nowadays cadmium selenide nanocrystals are already being used in televisions, called Quantum Dot displays. The broader range of colors that these nanocrystals can emit create more vivid images, as can be seen on the left television screen. Reused with permission from reference [3]. (d) A nanowire implemented in a transistor geometry. This system has been created using a plethora of techniques, such as lithography, vapour-liquid-solid nanowire growth and metal deposition in an electron microscope. Nowadays, transistors which are used in our computer start to reach a size of 15-22 nanometers. The scalebar equals 1 μm . Reused with permission from reference [4].

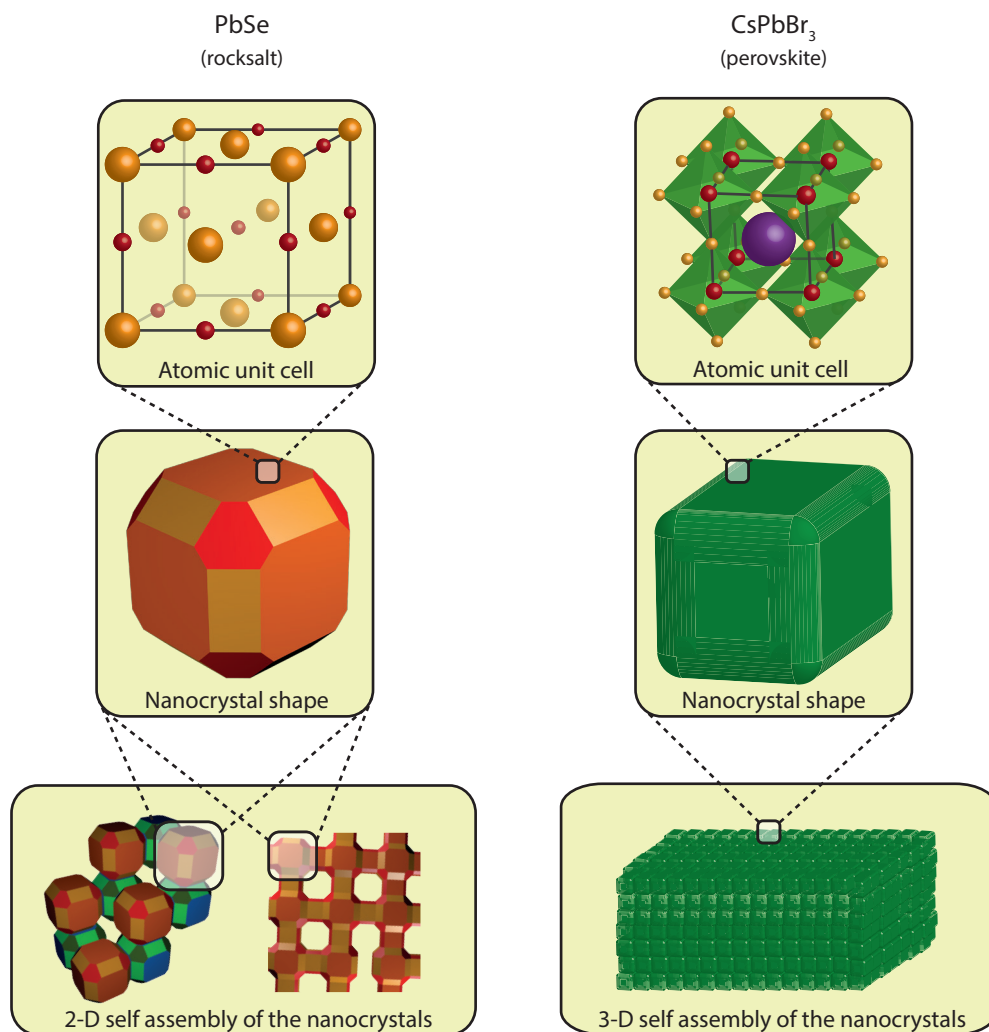


Figure 1.2: Schematic representation of the atomic structure, the nanocrystal shape and the self-assembled superlattices of the particles studied throughout this thesis. The images in the left column show the PbSe rocksalt atomic unit cell (top), the truncated cubic shape of the NCs (middle) and two-dimensional self-assembled superlattices (bottom) that we synthesized throughout this thesis. The images in the right column show the CsPbBr₃ perovskite simple cubic atomic unit cell (also known as a perovskite unit cell, top), the cubic shaped nanocrystals (middle) and the three-dimensional self-assembled superstructure of these nanocrystals (bottom).

with a bandgap in the infrared. Another example is a fourth century Roman cup, with plasmonic Ag-Au nanoparticles embedded in the glass, called the Lycurgus cup, displayed in Figure 1.1(b)². As the plasmon resonance of these nanoparticles absorb large part of the visible light, upon back illumination the glass appears red. Nowadays the small nanocrystals known as quantum dots (QDs, see chapter 2 for a more detailed description) are embedded in television screens. CdSe QDs can be color tuned over the entire visible spectrum and can obtain a larger color gamut than traditional LED-based screens, as shown in Figure 1.1(c)³. A continued effort to decrease the size

of transistors is one of the main driving forces behind nanotechnology. An example of a nanowire transistor is displayed in Figure 1.1(d). Here, an InP/InAs nanowire is synthesized via a vapor-liquid-solid synthesis and placed in a transistor geometry which is created through electron lithography⁴. In 1965, Gordon Moore stated that the number of transistors in an integrated circuit doubles every year⁵, which ever since has pushed research to find new methods to create smaller and smaller devices. Modern transistors inside computers can reach sizes of 15-22 nm, which are created by a complex scheme of lithographic and chemical procedures. However, we are reaching the spatial limit of what is possible to create through lithography and alternative methods need to be investigated.

The nanocrystals we study in this thesis are all semiconductors: materials through which we can control the current by applying an external bias. A well known example, used in computerchips, is silicon, which is the most commonly used semiconductor in the electronics industry. Now instead of using lithographic techniques, or so called top-down techniques, one could envision using nanocrystals instead in a bottom-up approach; we use the nanocrystals as building blocks for larger superstructures, with the eventual goal of creating novel electronic devices out of them. Throughout this thesis we study this process of nanocrystals that self-organize, that is nanocrystals which 'spontaneously' form larger hierarchical structures. The idea behind this is to couple the opto-electronic properties of the individual nanocrystals to those of two- and three dimensional materials. A schematic of the structures is shown in Figure 1.2. We use the infrared-active semiconductor PbSe as a building block to create two-dimensional (flat) superstructures. Furthermore we investigated the inorganic perovskite nanocrystals made of CsPbBr₃ and study their optical properties and their self-assembly behaviour in solution.

1.2 - PbSe quantum dots

The first chapters of this thesis deal with PbSe nanocrystals. The family of lead-chalcogenide IV-VI semiconductors has been researched extensively for their use in infrared detectors and thermal imaging⁶. These materials have a rock-salt atomic crystal lattice, similar to the atomic lattice of NaCl, and a direct band gap, which can be tuned by varying the size of the nanocrystals.

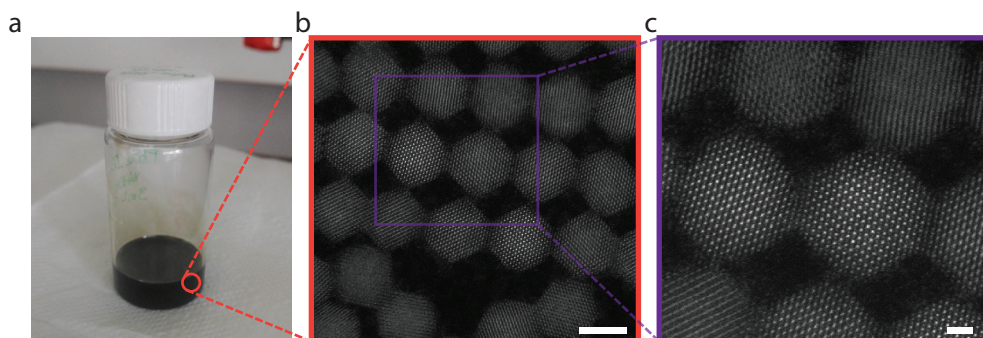


Figure 1.3: PbSe nanocrystals in solution and imaged in an electron microscope. (a) A digital photograph of a dispersion of 5.5 nm PbSe nanocrystals in toluene. **(b)** A dark-field electron micrograph of the PbSe nanocrystals. The nanocrystals appear as white on a dark background. **(c)** Zooming in further in the image shown in **(b)** reveals the atomic lattice with a [110] zone axis. The bright white dots are columns of Pb atoms. Image courtesy of Bart Goris from the EMAT institute in Antwerp. Scalebars equal 5 nm for **(b)** and 1 nm for **(c)**.

Figure 1.3 shows the PbSe nanocrystals in solution and imaged with an electron microscope. The nanocrystals are usually capped with organic molecules, such as oleic acid, to make them soluble in apolar solvents. Figure 1.3(a) shows the nanocrystal dispersion in toluene. The solution has a deep black color since the nanocrystals have a electronic band gap in the infrared. Combined with their large extinction coefficient, this means that they absorb a large portion of the visible light, which is the reason for the deep black color of the NC dispersions. Figure 1.3(b) shows a dark-field electron microscopy image of the nanocrystals. The particles appear as white on a dark background. Their shape is dependent on the amount of ligands present on specific crystal facets⁷, but can generally be well approximated by that of a truncated cube. We use the PbSe nanocrystals to create two-dimensional crystals of these nanocrystals with various geometries. The nanocrystals first self-organize into a crystal, after which they fuse atomically through a process called oriented attachment. Here, the atomic lattices of the nanocrystals align, which is followed by the formation of epitaxial bonds between the nanocrystals. Throughout this thesis we study the geometry and the mechanism of self-assembly of these nanocrystal superlattices.

7

1.3 - CsPbBr₃ perovskite nanocrystals

Perovskite materials have gained a large boost of attention due to their rapidly increasing solar cell efficiency of up to 20%⁸. These materials have a simple cubic perovskite unit cell with a stoichiometry ABX₃, with A a monovalent cation, B a divalent cation and X a monovalent halide. A large amount of research is being done on hybrid perovskite materials, containing both an organic and an inorganic component (for example CH₃NH₃PbI₃). Due to the highly ionic nature of the atomic lattice, these materials are very sensitive to water.

Recently, a method to produce fully inorganic perovskite nanocrystals with extremely bright photoluminescence was reported by the group of Kovalenko⁹. Without any surface passivation, these nanocrystals have photoluminescence quantum yields of up to 90%. Compared to regular quantum dots, where the optical properties are tuned through the size of the nanocrystals, here they are varied by changing the composition of the anionic sublattice, as demonstrated in Figure 1.4(a). The chloride containing nanocrystals emit in the blue, the iodide containing nanocrystals emit in the red and the bromide containing nanocrystals emit in the green. Intermittent color emitting nanocrystals can be realized by combining the different halides into one nanocrystal.

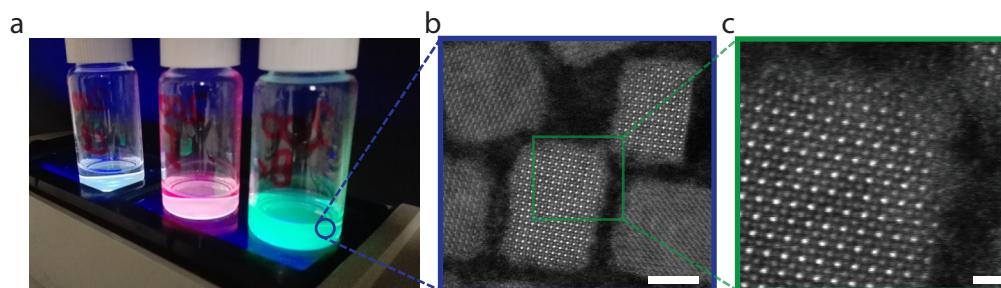


Figure 1.4: CsPb-halide nanocrystals in solution and imaged with an electron microscope. (a) A digital photograph of a dispersions containing CsPbCl₃ (left), CsPbI₃ (middle) and CsPbBr₃ (right) nanocrystals. (b) The nanocrystals have a very distinct cuboidal shape, as shown in the dark-field electron micrograph. (c) Upon zooming in further the atomic perovskite lattice becomes visible. The brightest spots are mixed Pb/halide atomic columns, the less intense spots are the Cs atomic columns and the least intense spots are the Br atomic columns. Image courtesy of Thomas Alantziis from the EMAT institute in Antwerp. Scalebars equal 5 nm for (b) and 1 nm for (c).

In this thesis we show that the opto-electronic properties of these perovskite nanocrystals can be tuned not only by varying the composition of the anionic sublattice, but also by replacing Pb ions inside the atomic lattice with smaller divalent cations. Furthermore we demonstrate that we can induce the self-assembly by decreasing the colloidal stability of the nanocrystals in solution. The nanocrystals inside the formed supraparticles stack in a simple cubic lattice, and align their atomic lattices very well. We also show that we are able to detect NC vacancies on both the surface and in the bulk of the supraparticle with advanced electron microscopy techniques and study the optical properties of the formed structures.

1.4 - Outline of this thesis

Throughout this thesis a variety of experiments on both PbSe and CsPbBr₃ nanocrystals are being outlined. The thesis is structured as follows:

In **Chapter 2** a more thorough explanation on the opto-electronic properties of semiconductor nanocrystals is given. Furthermore, the synthesis of the nanocrystals and the processes involved during the self-assembly of nanoparticles are touched upon. Finally, the main characterization technique, based on synchrotron X-ray scattering, is explained.

Chapter 3 presents the formation of a honeycomb superlattice, made by self-assembling PbSe nanocrystals on an ethylene glycol liquid. The constituent nanocrystals inside the superlattice are atomically coherent, meaning that their atomic lattices are aligned, and they are epitaxially connected. We characterize the geometry of the structure with electron tomography, which shows that the honeycomb lattice is buckled into an octahedral symmetry, where neighboring nanocrystals occupy a different plane of height.

Chapter 4 presents an in-situ study on the formation mechanism of superlattices from PbSe nanocrystals. We use in-situ synchrotron time-resolved grazing-incidence X-ray scattering techniques to simultaneously probe nanocrystal motion, crystallographic alignment, and nanocrystal attachment. The results are complemented with high-resolution electron microscopy and theoretical simulations to create a full picture on the self-assembly process.

In **Chapter 5** we extend the used X-ray scattering techniques with specular X-ray reflectivity measurements to create a three-dimensional picture of how PbSe nanocrystals adsorb at the ethylene glycol - air interface. We show that larger nanocrystals have a preferential orientation at the liquid-air interface, which is mostly likely the caused by a more pronounced faceting of the particles with increasing size.

Chapter 6 shows results obtained on cation-exchange experiments on CsPbBr₃ nanocrystals. We show that the photoluminescence blueshifts when doping the nanocrystals with several divalent cations, as a results of a contraction of the atomic lattice. The good spectral features, such as high photoluminescence quantum yield and narrow emission linewidth are retained in the doped nanocrystals.

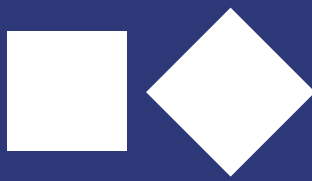
In **Chapter 7** we show that we are able to self-assemble the CsPbBr₃ nanocrystals into large, cuboidal supraparticles. The nanocrystals in such a supraparticle are atomically aligned, but not

connected. We show that there are various types of localized NC vacancies present, both on the surface and in the bulk of the supraparticles, which hints towards attractive interactions between the nanocrystals. Furthermore we study the optical properties of the supraparticles, which indicate that there is increased electronic coupling between the constituent nanocrystals, leading to a redshift of the emission of a supraparticle compared to the nanocrystals in solution.

References

1. Philippe Walterm et al. "Early Use of PbS Nanotechnology for an Ancient Hair Dyeing Formula". *Nano Lett.* **6**, 2215–2219 (2006).
2. Freestone, I., Meeks, N., Sax, M. & Higgitt, C. "The Lycurgus Cup — A Roman nanotechnology". *Gold Bull.* **40**, 270–277 (2007).
3. "Nanocrystals in their prime". *Nat. Nanotechnol.* **9**, 325–325 (2014).
4. Roddaro, S., Pescaglini, A., Ercolani, D., Sorba, L. & Beltram, F. "Manipulation of Electron Orbitals in Hard-Wall InAs/InP Nanowire Quantum Dots". *Nano Lett.* **11**, 1695–1699 (2011).
5. Moore, G. E. "Cramming more components onto integrated circuits", Reprinted from *Electronics*, volume 38, number 8, April 19, 1965, 114. *IEEE Solid-State Circuits Newsl.* **20**, 33–35 (2006).
6. Vergara, G. et al. "Polycrystalline lead selenide: the resurgence of an old infrared detector". *Opto-Electronics Rev.* **15**, 110–117 (2007).
7. Peters, J. L. et al. "Ligand-induced shape transformation of PbSe nanocrystals". *Chem. Mater.* *acs.chemmater.7b01103* (2017).
8. Eperon, G. E. et al. "Perovskite-perovskite tandem photovoltaics with optimized bandgaps". *Science* (80-.). (2016).
9. Protesescu, L. et al. "Nanocrystals of Cesium Lead Halide Perovskites (CsPbX₃, X = Cl, Br, and I): Novel Optoelectronic Materials Showing Bright Emission with Wide Color Gamut". *Nano Lett.* **15**, 3692–3696 (2015).





Chapter 2

Nanocrystals, self-assembly and X-ray scattering

• *Abstract* •

In 1993 Chris Murray, David Norris and Mounji Bawendi developed the first reliable method to synthesize colloidal nanocrystals (NCs) with excellent (low) polydispersity and bright luminescence from the lowest exciton state¹. Whereas epitaxial quantum dots were already well known and broadly studied, the synthesis of colloidal semiconductor nanocrystals opened the gate for a new field of research. This chapter deals with the opto-electronic properties of such colloidal quantum dots and how these can be tuned by varying the size, shape and composition of the nanocrystals. The nanocrystals can be used as building blocks to bottom-up create larger structures through self-assembling them in either two or three dimensions. The thermodynamics driving this self-assembly process are briefly touched upon. Moreover one of the main characterization techniques based on X-ray scattering is dealt with throughout this chapter

With contributions from: Oleic Acid-Induced Atomic Alignment of ZnS Polyhedral Nanocrystals.

Van der Stam, W.; Rabouw, F. T.; Vonk, S. J. W.; Geuchies, J. J.; Ligthart, H.; Petukhov, A. V.; de Mello Donega, C. *Nano Lett.* **16**, 2608–14 (2016).

2.1 - Introduction

Nanocrystals (NCs) are very small crystalline objects with diameters ranging from one to several tens of nanometers. Owing to their very small size, they all share the common feature of having a very large surface-to-volume ratio. In a bulk material the number of missing bonds at the surface consists out of such a minute fraction, that they do not alter the material properties. As the particles become smaller and smaller, the surface eventually starts to dominate the properties of the material. At the nanometer lengthscale the surface can completely alter some properties, such as photoluminescence or solubility. On the other hand, to be able to observe the inherent quantum properties of small nanocrystals, the atoms at the surface need to be electronically passivated. This is possible by using organic ligand molecules and/or inorganic shells.

The NCs used in this thesis are made of semiconductor materials. A semiconductor is a material which has an energy gap between its highest occupied molecular orbital (HOMO) and its lowest unoccupied molecular orbital (LUMO). This energy gap is referred to as the band gap of the material. In bulk-like materials we cannot truly separate the individual energy levels anymore and we refer to them as bands. The valence band consists out of all energy levels below the HOMO and the conduction band consists out of all energy levels above the LUMO. A more coincise picture of semiconductor nanocrystals will be given below.

2.1.1 - From bulk to nano and back

It is instructive to look at the electronic properties of a bulk semiconductor before going to the properties of a semiconductor NC. Due to the periodicity of the atomic lattice, the electronic band structure can be completely projected into the first Brillouin zone. The atomic lattice gives rise to a potential energy landscape, which pushes the electronic bands away from each other and, for a sufficiently strong potential, a bandgap is formed.

Many textbooks used by physicists, that focus on the properties of bulk semiconductors, show wavevector-energy diagrams, also known as dispersion relations, to depict the properties of the materials. Textbooks more oriented towards chemists tend to neglect electron momentum and show a more schematic representation of the valence and conduction band. The latter is generally used to describe the electronic structure of nanocrystals in a bottom up approach.

There are roughly 10^2 - 10^5 atoms in the nanocrystals used in this thesis, compared to roughly 10^{22} atoms in bulk materials. The high amount of atoms, donating a large amount of electron and hole states to the semiconductor bands, make that the electronic density of states (DOS) has to be described as a quasi continuum, as the individual states cannot be resolved anymore². For semiconductor NCs, the DOS near the edges of the valence and conduction band becomes more discrete and several exciton states, i.e. excited states in which the electron and hole are bound together via Coulomb interactions, can be resolved through absorption spectroscopy³⁻⁶. In a simple picture, these electronic states inside NCs can be thought of as a linear combination of atomic orbitals; all the atoms in the nanocrystal donate their atomic orbitals to form molecular orbitals inside the nanocrystal. Since the number of constituent atoms inside the nanocrystal is low, the DOS near the band edges is also low and gives rise to discrete energy levels.

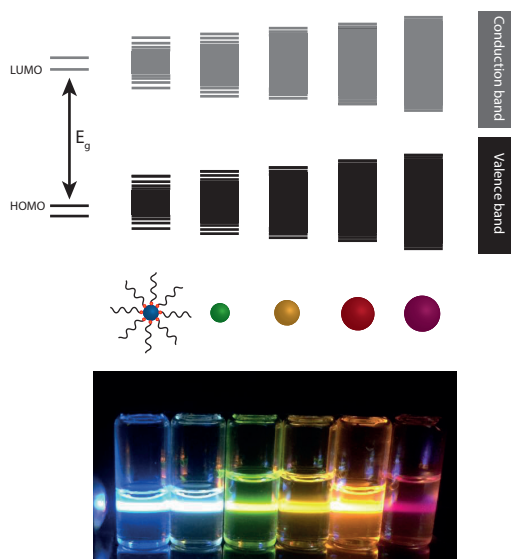


Figure 2.1: Colloidal semiconductor nanocrystals and their opto-electronic properties. The Figure shows a simplified schematic of the band structure of these NCs. In a simple molecule the lowest energy states are all filled with electrons according to the Aufbau principle. The difference between the highest occupied molecular orbital (HOMO) and the lowest unoccupied molecular orbital (LUMO) gives rise to an energy gap. When an electron absorbs a photon it has to overcome this energy gap. This energy gap is also present in semiconductor solids, where it is called the band gap of that material. The large amount of atoms make the spacing between the energy levels much smaller than the thermal energy, i.e. they are described as quasi-continuous bands. Semiconductor nanocrystals have size-dependent opto-electronic properties. The band gap energy is determined by the quantum-confinement effect. Small (2 nm) CdSe nanocrystals emit in the blue spectral region, since the charge carriers are more confined compared to larger particles. These larger CdSe nanocrystals (6 nm) emit in the red spectral region. Photograph courtesy of Federico Montanarella.

Colloidal quantum dots (QDs) are a special type of nanocrystals. A semiconductor nanocrystal is called a quantum dot when its diameter is smaller than a certain critical radius, the exciton Bohr radius. It defines how large the spatial extension of the exciton wavefunction is in bulk materials, which is governed by a balance between Coulomb attraction of the electron-hole pair and confinement energy. When one decreases the size of the particle below this critical radius, the kinetic energy of the envelope wavefunction increases, which pushes the band potentials to higher and lower energies for the conduction band and valence band respectively. The charge carriers inside the nanocrystals now experience a confinement energy which scales with their size; the same type of material is able to emit and/or absorb in different parts of the spectrum. Although NCs are likely very prone to strain, structural studies indicate that they roughly retain the bulk crystal structure and lattice parameter, leaving surface effects out of the picture. Well known examples are CdSe, with a Bohr exciton radius of 5 nm⁷ and PbSe with a Bohr exciton radius of 46 nm⁸.

Early work on semiconductor nanocrystalline materials has been done by Ekimov, who studied these NCs in glassy matrices^{9,10}, and Henglein¹¹ and Brus¹², who studied the NCs in colloidal solutions. At the same time, a solid theory around the opto-electronic properties of QDs was developed by Efros¹³. A vast synthetic library has been developed since the first organo-metallic synthesis of colloidal Cd chalcogenide QDs in 1993 by Bawendi et al.¹, containing procedures to synthesize nanomaterials with different sizes and different shapes¹⁴⁻¹⁸. The dimensionality of the confinement in nanocrystal systems has a large impact on the electronic properties through the DOS. QDs are experiencing quantum confinement in all three dimensions and the electronic DOS is a series of very sharp lines. For QDs the size dispersion can be relatively well controlled, however in colloidal dispersions there are always some size and shape variations between individual NCs in solution. This broadening of the size distribution, called inhomogeneous broadening, comes from the competition between nucleation and growth during the colloidal synthesis of these particles. This is clearly observed as a broadening of the excitonic absorption and photoluminescence peaks in well known QD systems, such as CdSe and PbSe¹⁹.

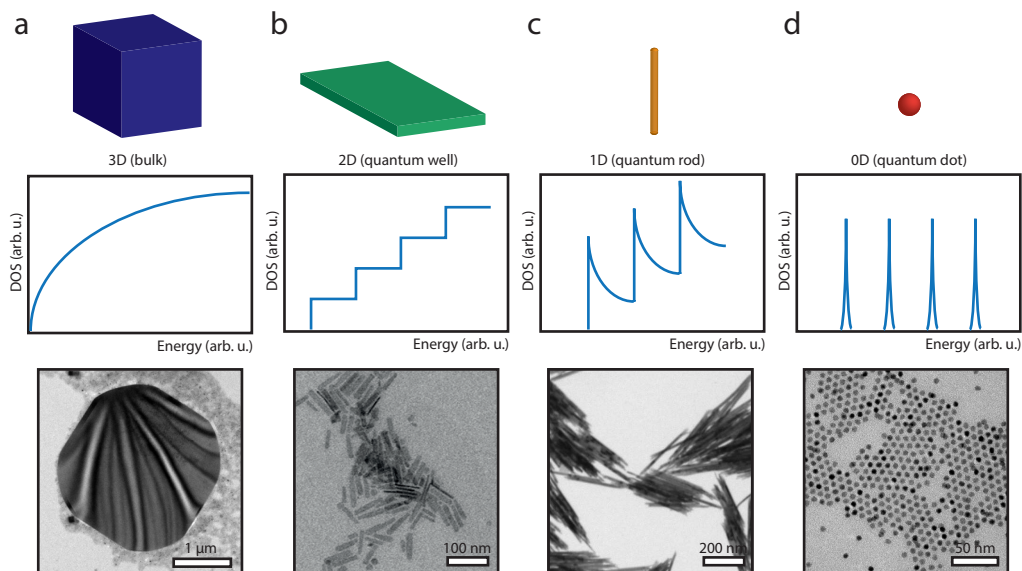


Figure 2.2: Nanocrystal dimensionality versus confinement effects on the density of electronic states. From left to right increasing number of confined dimensions. The top row show schematics of the structures, the second row shows the density of (electronic) states for that dimensionality and the bottom row show electron microscopy images of some example structures. **(a)** Charge carriers in bulk materials experience no quantum confinement. The DOS is approximated by a free electron gas. The TEM image shows a microcrystal of CsPbBr₃. **(b)** Charge carriers inside a nanoplatelet experience quantum confinement in only one direction. The DOS is a sequence of step functions. The TEM image shows colloidal CdSe nanoplatelets (image courtesy of Annelies van der Bok). **(c)** In a nanorod the charge carriers are confined in two directions and the DOS shows Van Hove singularities. The TEM image shows bundled CsPbBr₃ nanowires. **(d)** Inside quantum dots the charge carriers are confined in all three directions. The DOS is a series of narrow lines. The TEM image shows PbSe nanocrystals.

One-dimensional nanorods and nanowires, which experience confinement of the charge carriers in two dimensions, are also synthetically available through direct synthesis methods exploring facet-specific ligand binding and the resulting anisotropic growth of the NC nuclei¹⁵. Moreover several methods using cation exchange have been used to synthesize chemically diverse nanowires²⁰⁻²³. The DOS shows $E^{-1/2}$ dependence. Moreover the rods can be self-assembled into membrane-like sheets^{24,25}, with interesting applications in photovoltaics and photocatalysis.

More recently, 2-D colloidal semiconductors have been synthesized by Dubertret et al., of which the thickness can be controlled with atomic precision^{16,26}. Since the excitons are confined in only one direction, on which there is no inhomogenous broadening of the optical transitions the nanoplatelets show extremely narrow lorentzian emission profiles. Several types of heterostructures have been synthesized by now, including core-shell^{27,28}, core-crown^{29,30} and core-crown-shell nanoplatelets³¹, each exhibiting unique opto-electronic properties. Moreover, when compared to for example QDs, the nanoplatelets have a significantly decreased fluorescence lifetime, due to their giant oscillator strength. Their exact formation mechanism, explaining how atomic thickness control is achieved is still being discussed extensively^{32,33}. The two mechanisms, growth via attachment of small nuclei vs. intrinsic anisotropic growth of each nucleus, still have to be verified experimentally.

Individual nanocrystals can be used to build larger hierarchical structures, i.e. crystals of nanocrystals, through a process called self-assembly or self-organization. This process is common in nature, for example in proteins³⁴, DNA³⁵ and bacteriophages³⁶. Even in the early 1960's, Sanders et al. showed that the beautiful reflections coming from opal gemstones originates from well ordered silica (glass) microparticles³⁷. The crystallinity of the silica superlattice causes white light that hits the opal to break up into well defined Bragg reflections in the visible range of the spectrum.

These so called superstructures, supraparticles or superlattices can crystallize in a wide variety of crystal structures^{38,39}. Moreover, recent work developed synthetic protocols to create epitaxial connections between NCs using only a specific subset of NC facets⁴⁰. By making atomically coherent 2-D superlattices, structures resembling a graphene-like lattice have been formed, where the lattice positions occupied by carbon atoms in graphene are now replaced with nanocrystals⁴¹. We now get a material which should theoretically act like a 2-D semiconductor, but with the tunability of the QDs; a quantum well with a hexagonal periodicity of holes. Atomistic tight-binding calculations have shown the occurrence of Dirac-type bands, i.e. linear E, \mathbf{k} bands, around the K point, in both the valence and conduction band of zinc-blende CdSe superlattices with graphene-like and silicene-like geometries^{42,43}. The high degree of tunability makes these materials very interesting for applications in opto-electronics, e.g. high-speed transistors.

2.1.2 - Nanocrystal synthesis and post-synthetic treatment

The nanocrystal syntheses are often done in high-boiling, apolar media, e.g. octadecene. In order to keep the nanocrystals stable inside these solutions they are capped with surfactants, also called ligands, during their synthesis. These ligands have a binding group, which can bind to undercoordinated surface atoms and a long alkyl chain to keep the nanocrystals stabilized in solution. Common examples of used ligands are oleic acid, oleylamine and trioctyl phosphine.

Synthetic methods aim to produce particles with an as low as possible distribution of NC sizes. The method developed in the group of Bawendi¹ was based upon classic work of La Mer and Dinegar in 1950⁴⁴ on colloid formation and tries to separate the nucleation and growth stages of the NC formation⁴⁵. The growth over time of the nanoparticles can be schematically represented in a La Mer diagram, depicted in Figure 2.3(a) which contains three distinct regions⁴⁶. Region I, the induction of the reaction, starts with the addition of the precursors of the reaction and ends when small nuclei are formed. Region II marks the start and end of the nucleation period, which generally needs to be as narrow in time as possible to separate it from region III, the growth region, to not defocus the size distribution of the nanoparticles. In the nucleation region the formed nuclei need to be sufficiently large in size in order to grow and not redissolve. The size for which the probabilities for redissolving and growing the nanoparticle are equal is referred to as the critical radius r_c (see also Figure 2.3(b)). Nuclei with a radius equal to or larger than r_c are only formed at a critical concentration of monomers, c_c , where the solution is supersaturated. During a typical hot-injection synthesis, the supersaturation of the reaction mixture can be achieved by a inducing a rapid increase of monomer concentration in solution through the quick injection of precursors. The growth of the nanocrystals, depicted in region III, is often quenched before an equilibrium state is reached to prevent Ostwald ripening. Ostwald ripening arises from an increased Laplace pressure in smaller particles, resulting in faster dissolution and ripening into the larger particles.

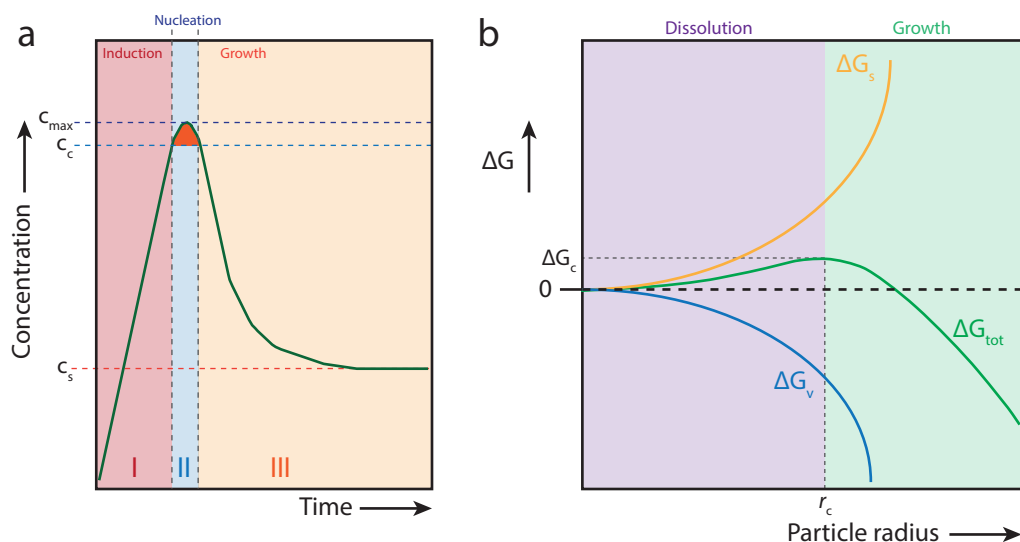


Figure 2.3: Nucleation and growth of nanocrystals during their synthesis. (a) A La Mer diagram, which schematically shows the stages of nanocrystal nucleation and growth: the induction regime (stage I), the nucleation regime (stage II) and the growth regime (stage III). The orange area in the curve depicts the range where the supersaturated solution has a concentration higher than a certain critical concentration (c_c) where nanocrystal growth is favored over dissolution. To create NCs with as narrow a size distribution as possible, the critical stage during nucleation should be as narrow as possible. (b) Change in Gibbs free energy during the formation of a spherical nucleus. The balance between surface and volume energies makes that below a critical radius r_c , the nuclei redissolve, whereas above r_c they grow in solution.

The competition between nucleation and growth of the nanocrystals is dictated by the total free energy of formation for the NCs, through two opposing components; the volume free energy (ΔG_v) and the surface free energy (ΔG_s), and is given by^{47,48}

$$\Delta G_{tot} = \Delta G_v + \Delta G_s = -\frac{4}{3}\pi r^3 \rho \Delta \mu + 4\pi r^2 \gamma \quad 2.1$$

Here ΔG_{tot} is the total change in free energy for the formation of a spherical nucleus of radius r , with density ρ . The interfacial tension between the solution in which the nucleus grows and the surface of the nucleus is γ . Creating volume is energetically favorable, i.e. it decreases the system's total free energy, whereas creating surface is energetically unfavorable, i.e. it increases the system's total free energy. Due to the opposing signs of these two terms, the total free energy will have a maximum, as depicted in Figure 2.3(b), for nuclei with a certain critical radius r_c (and is given by setting the derivative of equation 2.1 to zero).

Several post-synthetic strategies have been developed to create hetero-nanostructures². By combining the appropriate materials, the overlap between the electron and hole wavefunctions can be tailored. There are three distinct types of overlap: in Type-I materials, the exciton is confined completely to one material, resulting in a large electron-hole wavefunction overlap. In Type-II materials, the exciton is spatially separated, with the hole in one material and the electron in the other, resulting in a small electron-hole wavefunction overlap. The intermediate regime for Type-I^{1/2} is when one of the charge carriers is delocalized over both materials, whereas the

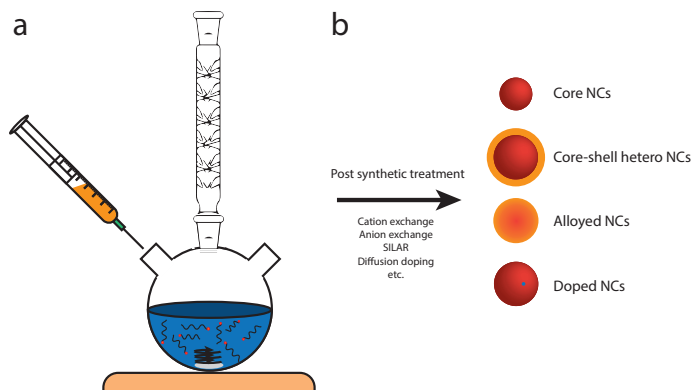


Figure 2.4: Nanocrystal synthesis and post-synthetic treatments leading to heterostructures. (a) The synthesis of nanocrystals as performed throughout this thesis, is based on separating the nucleation and growth stages of the NC formation through a hot-injection method. A syringe with precursor 'A' is rapidly injected in a boiling solvent with precursor 'B'. Rapid nucleation occurs, and the temperature drops to a regime where only growth is preferred. (b) After the synthesis, several post-synthetic methods can be used to create heterostructures. Examples of such methods are cation exchange, anion exchange, SILAR and diffusion doping. The resulting heterostructure can not only improve the overall chemical stability of the particles, but also significantly alter their opto-electronic properties.

other is confined in one. Tailoring the spatial separation of the electron and hole wavefunctions can be used to engineer the desired structures; Excitons localized in the core of Type-I core-shell nanocrystals will experience less effects of surface defects, which can lead to luminescence quenching. In Type-II nanocrystals, the exciton is easier spatially separated due to the reduction in electron and hole wavefunction overlap, which is beneficial for photo-voltaic applications.

One of these post-synthetic methods is the successive ion-layer adsorption reaction (SILAR) method⁴⁹. This allows one to deposit one layer after another on top of your nanocrystals, coating them in a shell of a different material. A benefit of this technique is that you do not sacrifice material of your parent NC to change its properties. The lattice mismatch between the to-be deposited material and that of the parent NCs has to be small (<5%) in order to avoid the build-up of lattice strain, leading to defects and quenching sites and changes in the photoluminescence⁵⁰.

Other methods involve anion and cation exchange reactions, where the ions of the parent NC are directly exchange for different ions. Topotactic cation exchange reactions, i.e. the atomic crystal lattices of the NCs are unaltered after the reaction, are commonplace in colloidal semiconductor II-VI, IV-VI and III-V NCs, allowing access to a variety of compositions and shapes that are not attainable through direct synthesis protocols^{20,51-53}. By tuning the reaction, e.g. by the reactivity of the used precursors, their concentration or the temperature of the reaction, several types of morphologies can be obtained. For example, by tuning the reaction temperature, Zn ions can be exchanged with Cd ions to form either core-shell or alloyed nanocrystals, each having its own unique optical properties⁵⁴.

Furthermore, the composition of colloidal halide perovskite NCs can be post-synthetically tailored through topotactic anion-exchange reactions with preservation of the size and shape of the parent NCs^{55,56}, by exchanging the constituent halide ions of the lattice (despite a small

lattice expansion or contraction). This is in striking contrast to what has been commonly observed for anion exchange reactions in colloidal II-VI semiconductor NCs, which typically result in severe size and shape transformations, often leading to hollow NCs^{57,58}.

The introduction of impurity ions in colloidal II-VI and III-V semiconductor NCs provides another synthetic tool to control the optoelectronic properties and to enrich the parent NCs with novel functionalities, such as magnetism due to dopants with unpaired electrons in the dopant⁵⁹, or increased effective Stokes shift due to exciton recombination via the impurity ions^{60,61}. Furthermore, impurity doping of perovskite thin films has been shown to improve their performance in solar cells⁶²⁻⁶⁴. Recently, Mn²⁺ doping in colloidal CsPbCl₃ perovskite NCs has been achieved by a direct synthesis method, in which PbCl₂ and MnCl₂ precursors were mixed in the desired ratio, leading to NCs with the characteristic Mn²⁺ emission^{65,66}. In Chapter 6 it will be shown that post-synthetic doping of CsPbBr₃ nanocrystals can significantly shift their emission to the blue part of the spectral region without losing the outstanding photoluminescence quantum yield and narrow linewidth of the parent NCs.

The particles are usually washed after their synthesis, to remove additional unreacted precursors for example, by addition of a polar solvent, which destabilizes the particles from the colloidal suspension so that they can be precipitated through centrifugation and redispersed in clean solvents. We will show in Chapter 7 that this can also be utilized to induce the self-organization of the nanocrystals into larger superlattices. The NCs can be dispersed in a wide variety of solvents, which makes them easily processable on larger scales. Combined with the tunable electronic properties, these nanoparticles are envisioned to be very useful for various applications, ranging from catalysis to high-tech opto-electronics. Nowadays the first quantum-dot televisions are already commercially available⁶⁷.

2.1.3 - Self-assembly and oriented attachment

Self-assembly and oriented attachment are driven through certain interactions between nanocrystals. These interactions differ in magnitude and have different distances dependencies. In general a system undergoes spontaneous self-assembly if there is a lowering of the Gibbs free energy of that system.

$$\Delta G = \Delta H - T\Delta S \quad 2.2$$

Here ΔG is the change in Gibbs free energy, ΔH is the change in enthalpy and ΔS is the change in entropy going from the initial to the final state of the system. Note that the above equation is valid for constant temperature, pressure and number of particles during the phase transition, which is the case in the experiments presented in this thesis. From the second law of thermodynamics we know that the free energy of an isolated system decreases in any spontaneous process. Analogous to the description above, the self-organization of non-interacting nanocrystals into superlattices can be described by the chemical potential of the nanocrystals in a colloidal suspension μ .

$$\mu = \mu^* + k_B T \ln\left(\frac{c}{c^*}\right) \quad 2.3$$

One could regard μ as the average free energy per nanocrystal. In order to achieve crystallization of colloidal particles, one has to create conditions in which the colloids get a high chemical potential in solution⁶⁸. From the above equation it becomes clear that either the standard

chemical potential of the nanocrystals in solution, μ^* , should be increased, or alternatively the concentration of the dispersion c should be increased. For example, addition of an anti-solvent, which destabilizes the colloidal particles in solution, increases the potential energy per particle and hence increases μ^* , whereas evaporating the solvent of the dispersion also increases the chemical potential through an increasing particle concentration. We use the former in Chapter 7 to induce the growth of 3-D superlattices of CsPbBr₃ in solution.

Let us go back to interactions in between colloidal particles in solution and start by considering the most ideal case of inter-nanocrystal interactions, namely hard-sphere interactions. The interaction potential between two particles goes to infinity when they start to overlap and is equal to zero when particles do not overlap. An easy extension into this model is so called steric interaction, where the ligand coronas of the particles are allowed to overlap, which generates a repulsion between the particles due to an increase of the osmotic pressure in the overlap region. The hard-sphere like interparticle interaction is already sufficient to explain several types of self-assembly and phase behaviour⁶⁹.

Intuitively, a decrease of the entropy of the total system is expected to decrease when particles go from a fluid or gas-like state to a crystalline state. An ordinary procedure to induce colloidal crystallization is slow evaporation of the NC solvent. As the solvent evaporates, the concentration of NCs increases and the free volume per particle decreases. When the available volume approaches twice the volume of one NC, the system might undergo a phase transition from a disordered to an ordered state. Upon ordering, the configurational entropy per particle is decreased, however the free volume entropy per particle is increased due to the availability of more free space for translational and rotational movements⁷⁰. Put differently, the nanoparticles have more room to ‘wiggle’ inside the crystalline state, than they have when they are in a jammed random state. It has been shown that the gain in free volume entropy can be larger than the decrease in configurational entropy, hence stabilizing the crystallized state⁷¹.

Electrostatic interactions can be both repulsive, when opposing charged particles have the same charge, or attractive, when the opposing charged particles have opposite charge. When nanocrystals form epitaxial bonds between the atomic lattice, e.g. in the PbSe superlattices studied in this thesis, there is the occurrence of atomic bond formation. In order for attachment to occur, first the capping ligands have to leave the reactive surfaces. After detachment of the ligands, the now undercoordinated Pb atoms of one nanocrystal can form bonds with the Se atoms in the other. The charge present on these atoms is opposite and forms an attractive interaction between the opposing NC facets.

A third interaction which is always present between nanocrystals is Van der Waals interaction, which finds its origin in the atoms making up the nanocrystals. Van der Waals interactions consist out of three parts; Keesom, Debye and London interactions⁷². Keesom interactions are those between permanent dipoles of atoms and molecules. Debye interactions is that of permanent dipole in one molecule with induced dipoles in another atom or molecule. London interactions are interactions between two induced dipoles and result from spontaneous fluctuations of charges inside atoms. The combinations of these three interactions are dubbed Van der Waals interactions, and they show a $1/r^6$ distance dependency. Especially for heavy metallic nanoparticles, the Van der Waals interactions can become so strong that even the organic ligands cannot prevent

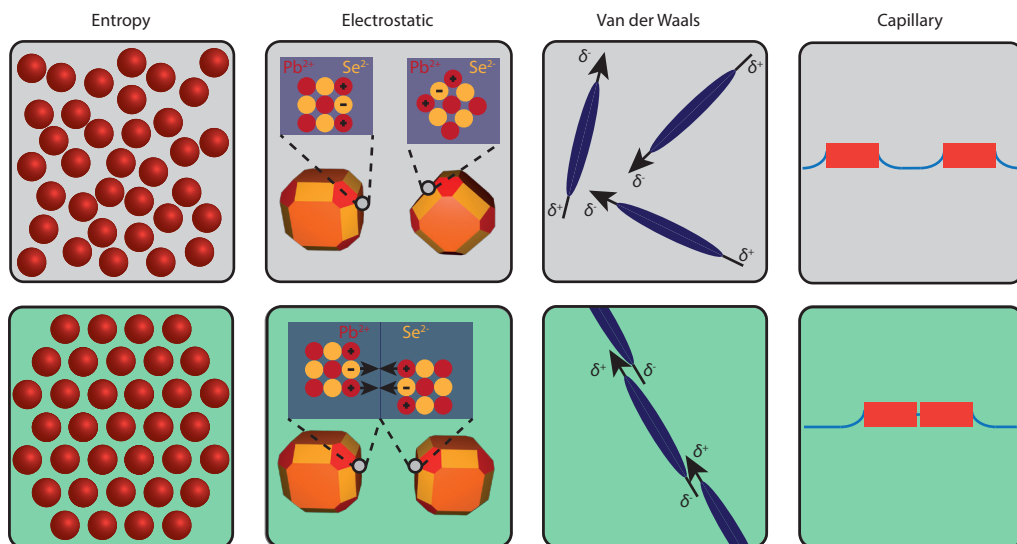


Figure 2.5: Schematic representation of different interparticle interactions between nanocrystals. (a) Entropic or hard-sphere interactions. In the crystalline state the particles have more room to ‘wobble’ compared to the jammed liquid state. **(b)** Electrostatic or coulombic interactions, present for example when nanocrystals have to align and fuse their atomic lattices during oriented attachment. **(c)** An example of Van Der Waals forces, i.e. dipole-dipole interaction, which arise due to delocalized and fluctuating charges over a colloid. Van Der Waals interactions are present between all materials. **(d)** Capillary interactions between NCs, which originate due to distortions of a liquid interface. Note that here they are displayed attractive in nature, but they can also be repulsive.

the nanoparticles from aggregating in solution⁷³.

The presence of an electric dipole moment has already been reported for CdSe, ZnSe and PbSe nanocrystals, but these results are contested by several experiments. The presence of electric dipole moment inside PbSe nanocrystals is still under heavy debate⁷⁴⁻⁷⁶. A recent study using very high resolution diffraction measurements has shown that the rock-salt atomic lattice of PbSe is distorted along the [111] direction, which should lead to a significant permanent dipole in the nanocrystals, since the [111] direction is polar⁷⁷. The presence of a permanent electric dipole moment could for example explain the formation of linear aggregates.

A fourth interaction is present when nanoparticles adsorb at an interface, e.g. a liquid-air interface. The adsorption of a particle can induce a distortion of the interface, as the particle will try to reach a certain contact angle or adsorption geometry. This distortion of the interface can induce an anisotropic force, due to the distortions of the interface, when the adsorbing particle is non-spherical, i.e. capillary forces. Soligno, Dijkstra and Van Roij studied the adsorption of cubic particles at a fluid-air interface and show that these particles induce different types of distortions upon different adsorption geometries⁷⁸. One adsorption geometry specifically, i.e. when a corner of the cube is pointing perpendicular to the liquid-plane, shows a hexapolar distortion. The similarities between the simulated NCs in this article and the honeycomb superlattices in Chapter three is striking. The authors furthermore show that the interaction strength and the distortions scale with the particle size. For small NCs, the distortion of the interface is in the order of magnitude of the particle size and the capillary energies are several $k_B T$.

The type of interactions which occur between the NCs in this thesis are touched upon in each consecutive Chapter when possible. Some types of interaction, e.g. capillary interactions might play an important role indeed during the self-assembly of the PbSe NCs at a liquid-air interface, but are difficult to access experimentally, especially for the particle sizes and magnitudes of interfacial distortions encountered during the experiments presented in this thesis.

2.1.4 - Geometric control over the superlattice dimensionality

Self-assembly of nanoparticles in solutions has been frequently applied over the last decade to create long-range ordered NC solids⁷⁹⁻⁸¹. However, the full geometry of these solids is difficult to control, as the addition of nanocrystals to the solid from solution can be done from all directions. Even if there are energetically favored positions to add the NCs to the existing agglomerate, there is no imposed control over the shape other than what nature dictates in this case. Several methods which confine the self-assembly process have been utilized so far to create well defined superlattice geometries, which are schematically depicted in Figure 2.6.

An example of a novel synthesis strategy to create 3-D assemblies with a well defined geometry uses a microemulsion method (see Figure 2.6(b)). The nanocrystals are dispersed in an apolar phase, which is emulsified in a water phase in a sheer cell, creating an oil-in-water emulsion. The apolar emulsion droplets, containing the NCs in a low-boiling solvent, evaporate over time, which forces the particles together into spherical supraparticles, which adapt several crystal structures when NCs with low enough polydispersity are used⁸². Supraballs with luminescent nanocrystals show amongst others whispering gallery modes, due to the high refractive index contrast between the inside and outside of the sphere⁸³.

In this thesis we mostly study 2-D self-assembled materials, inspired by materials such as graphene. In order to create materials with a reduced dimensionality, we have to confine the self-assembly process of the NCs to two dimensions. The method pioneered by Murray et al., uses a liquid substrate (as shown in Figure 2.6(c)). In this liquid the colloids do not dissolve, but adsorb at the liquid-air interface due to surface energy considerations after solvent evaporation⁸⁴. Nanoparticle monolayers can be obtained in which the NCs are epitaxially connected resulting in excellent long-range nanocrystalline order. The first superlattices made by this method were still several NC monolayers thick and consisted out of different types of NCs.

When using more reactive NCs, such as PbSe, one can obtain not only good long-range nanocrystalline order (with several different 2-D nanocrystal geometries), but also the individual NCs align crystallographically and fuse atomically⁴⁰. The resulting superlattices can have a thickness down to a NC monolayer and can be scooped off the interface by simple fishing or Langmuir-Schaeffer like stamping of the NC film. The relative easyness to handle and versatility makes this process to create 2-D semiconductors attractive for industrial applications.

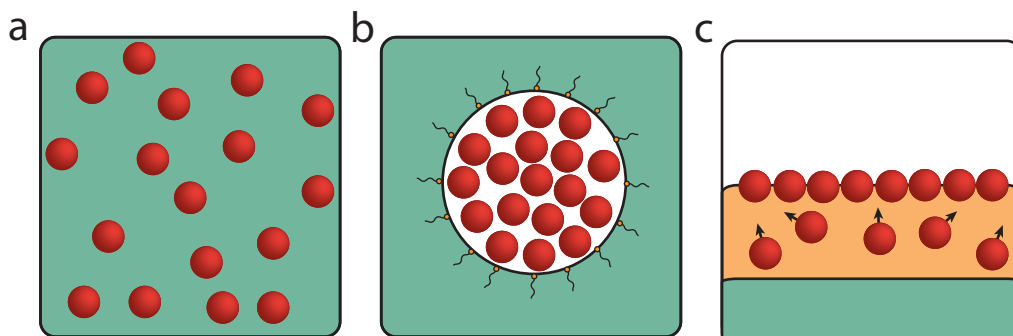


Figure 2.6: Control over superlattice geometries through confinement of the self-assembly process. (a) NCs in solution self-assembly in three-directions, but the final shape of the superlattice cannot be control externally. (b) Confinement of the self-assembly process in three dimensions through a microemulsion method. The resulting shape of the supraparticles comes from the spherical droplet. (c) Two dimensional confinement of the self-assembly process, as is studied mostly throughout this thesis. The NCs are confined at a liquid-liquid or liquid-air interface, which can result into superlattices which have a thickness of a NC monolayer.

2.1.5 - How to measure the structure and properties of NCs and their superlattices?

The sizes of the nanocrystals in this thesis are too small to be studied through conventional optical microscopy. Electron microscopy provides much higher spatial resolution and is used throughout this thesis in various forms. Conventional bright-field transmission electron microscopy (TEM) is generally used to obtain a first characterization of the particles. Here the sample is illuminated by a collimated parallel beam of electrons and the contrast is caused by absorption and scattering (particles appear black on a white background). When necessary, scanning-transmission electron microscopy (STEM), in particular when used in high-angle annular dark-field (HAADF) mode, is used to obtain high-resolution experiments on the NCs which can be atomically resolved^{85,86}. In this case, the electron beam is focussed and the sample is raster scanned to obtain an image. The electrons of the incoming beam will scatter on the electron density of the nanocrystals (or atoms) and are collected on an annular detector (particles appear white on a dark background). Three-dimensional information can be obtained through electron-tomography⁸⁷, where a series of 2-D tilt projections are combined to form a 3-D tilt-series of the object of interest. Complex algorithms are then used to retrieve the 3-D structure of the object of interest.

In some occasions, also scanning-probe microscopy, in particular scanning tunneling microscopy (STM) is applied to characterize the NC superlattices as well⁸⁸. The optical properties of the NCs are characterized with absorption spectroscopy (how much photons are absorbed by the NCs at each photon energy) and (time resolved) photoluminescence spectroscopy (which energy do the photons have when they are reemitted by the NCs after excitation).

For all the in-situ measurements that we performed to study the self-assembly of NCs, we used specialized X-ray scattering techniques. These techniques allow us to study the self-assembly processes in more detail under reaction conditions on both nanocrystal and atomic lengthscales. The next section will discuss the applied techniques in more detail.

2.2 - X-rays, synchrotrons and diffraction

To study the self-assembly of nanocrystals on a liquid surface puts restrictions on the techniques that can be used. First of all we need to be able to measure the process under in-situ conditions, i.e. ambient pressure and nitrogen atmosphere. This limits the use of electron microscopy, even though a lot of progress using liquid-cells has been made over recent years⁸⁹⁻⁹¹. We cannot use simple optical microscopy, since the nanoparticles used in this thesis are much smaller than the wavelength of visible light. One way to overcome this is to use photons with a shorter wavelength, such as X-rays. We do however need a large flux of photons, to get a decent signal from a nanoparticle monolayer.

X-rays were discovered by the German physicist Wilhelm Röntgen in 1895, using a discharge tube and a fluorescent plate. For our experiments, however, we need a brighter source, e.g. a synchrotron. Synchrotron generated X-rays were discovered in 1947 and were seen as an undesired effect until 1967, when their usefulness as a source of X-ray photons was recognized⁹². A general introduction to synchrotrons and X-ray diffraction and scattering will be given in the next sections.

2.2.1 - The European Synchrotron Radiation Facility and ID10

The first plea to start a European synchrotron was done in 1975 by professor William Gordon of the Imperial College in London. It took until 1992 for the first electron beam to orbit through the storage ring of the The European Synchrotron Radiation Facility (ESRF) in Grenoble, France. Nowadays it is one of the world's most brilliant X-ray source, specialized in a variety of techniques ranging from X-ray scattering experiments to advanced X-ray spectroscopic methods.

The layout of most synchrotrons in the world is rather similar, the difference mostly comes from the energy at which the electrons are orbiting inside the storage ring. The ESRF storage ring layout is presented in Figure 2.7(a). The electrons are generated in a linear accelerator, in which small bunches of electrons are accelerated into a booster synchrotron. This booster serves to accelerate the electrons up to 6 GeV (in the case of the ESRF), after which they are inserted into the storage ring. Inside the storage ring, the electron bunches are constantly expanding in size as the electrons inside one bunch repel each other. This requires for them being focussed, i.e. compressed together, in the straight sections of the synchrotron by quadrupolar and hexapolar magnets.

According to the equations of Maxwell, a charged particle emits electromagnetic radiation when it is accelerated or forced to change the direction of its motion^{93,94}. Like this, the synchrotron works similar to a radio antenna, but instead of generating radiowaves, X-rays are produced. The X-ray photons are generated inside two components, in which the electrons are forced to deviate from their linear trajectory. The first component is a bending magnet, in which the Lorentz force of the magnetic field forces the electrons to deviate from their trajectory and go from one straight section inside the synchrotron to another.

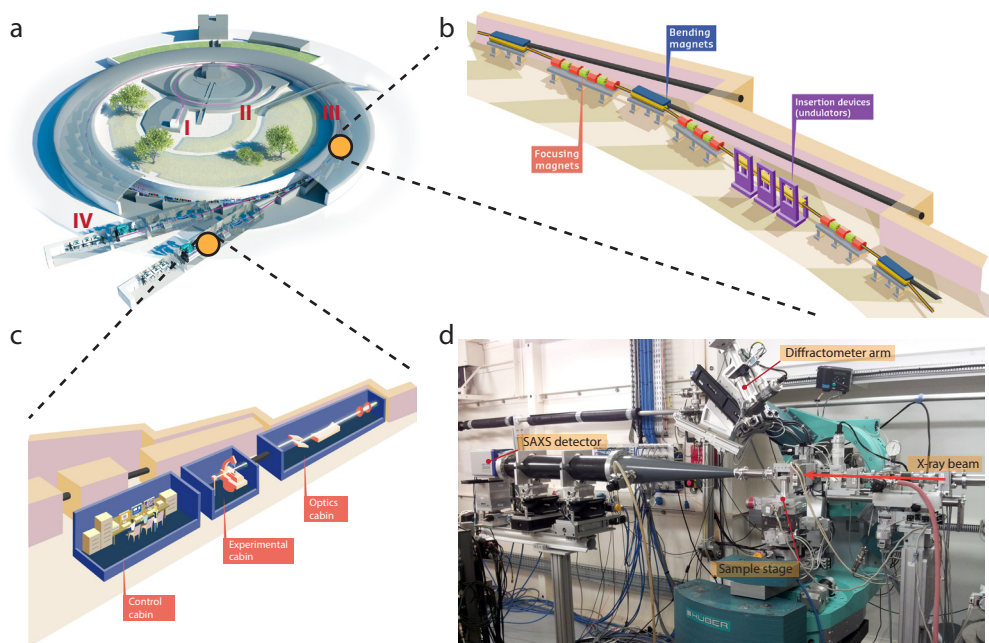


Figure 2.7: The ESRF and ID10, where most X-ray scattering experiments described in this thesis were performed. (a) Schematic of the ESRF synchrotron. (I) The electron bunches are generated in a linear accelerator and accelerated to roughly 200 MeV. (II) The booster synchrotron, which acts as a preaccelerator for the storage ring. The electrons are accelerated to an energy of 6 GeV before they are inserted into the storage ring (III), where they are deflected from their path by bending magnets and undulators, and hence produce X-ray photons. The complete circumference of the ESRF storage ring is 844 m. Experiments are performed at dedicated beamlines (IV), which contain an optics hut, experimental hut and control cabin. (b) Schematic of the storage ring layout with its several lattice components. The electron bunches are focussed by hexapole and quadrupole magnets. The X-ray photons are generated at bending magnets and undulators, which are coupled to dedicated end stations. (c) Typical layout of a beamline at the ESRF. The X-ray photons are passed through an optics hut, with mirrors and monochromators to finetune the X-ray beam, followed by an experimental hut, where the experiments take place, and a control hut where the experiments are monitored. (d) Photograph of the ID10 beamline, experimental hut one, which is dedicated to high resolution X-ray scattering and surface diffraction on liquid and solid interfaces. A typical experimental setup and its critical components are shown, which can be adapted to perform different types of experiments. Image courtesy for (a-c) of G. Admans, ESRF.

Due to their relativistic speed, electrons emit X-ray photons tangentially to the bending electron beam and end stations are built in this direction to exploit these photons to do experiments with. Another component which generates X-rays is called an undulator, also known as an insertion device. These are devices with rows of magnets of which the direction of the magnetic field is altered between consecutive magnets. This causes the electrons to first move to the left in the first magnetic field, after which they are forced to move to the right by magnetic field from the next set of magnets, which is repeated many times. This ‘wiggling’ motion of the electrons causes them to produce a large flux of monochromatic photons, up to 10^{12} photons/s/100 mA storage ring current, which is currently one of the the brightest sources of X-rays besides a free-electron laser facility. The very intense X-ray beam opens of a wealth of possible experiments, not achievable with common lab X-ray sources.

The ID10 beamline, at which most of the experiments presented in this thesis were performed, is split up into two endstations. One endstation is specialized in coherent scattering experiments, such as coherent diffraction imaging and X-ray photon-correlation spectroscopy. The other endstation is specialized in high resolution X-ray diffraction and scattering on liquid and solid surfaces and interfaces. This makes the beamline ideally suited to study the self-assembly of nanoparticles at liquid-air interfaces, as described in Chapters 3, 4 and 5. The relatively high X-ray energy (up to 30 keV) also allows for the study of buried surfaces e.g. liquid-liquid interfaces. The main techniques used at this beamline are grazing-incidence scattering and specular X-ray Reflectivity (XRR) measurements. We used the expertise and advantages of the ID10 endstation to study nanoparticle assembly processes at liquid-air interfaces, by combining small-angle X-ray scattering with wide-angle X-ray scattering, characterizing the system on both atomic and nanoparticle lengthscales simultaneously. The following section will give a brief introduction on the scattering processes and try to show how to interpret and read the scattering patterns.

2.2.2 - Reciprocal space and X-ray diffraction

The words scattering and diffraction are being used analogously throughout literature with the only difference that scattering often refers to disordered structures, while diffraction is usually associated with periodically-ordered structures yielding sharp peaks.

Diffraction on crystals was analytically described first in 1913 by William Lawrence Bragg and his son William Henry Bragg shortly after the discovery of X-rays⁹⁵. Upon illumination of a crystalline solid with monochromatic X-rays they observed that under very specific angles intense reflections were visible. They described this diffraction by modelling the crystal as a set of discrete planes of electron density upon which the X-ray photons scatter. The famous Bragg law for diffraction was already earlier formulated in reciprocal space by Max von Laue, who gave the Laue conditions for constructive interference.

The field of X-ray crystallography took off and the first X-ray diffraction experiments were mainly focussed on unravelling the structure of several minerals. The first atomic structure to be solved was that of rock-salt NaCl crystals⁹⁶, followed by the structure of diamond⁹⁷. It took researchers roughly five to ten more years to resolve more complicated structures such as graphite⁹⁸. These experiments were done on structures with simple and symmetric unit cells containing a relatively low number of atoms. In the 1950s the infamous ‘photo 51’ was taken by Raymond Gosling and Rosalind Franklin, which is the diffraction image taken on a crystallized sample of DNA. This resulted in the discovery of the double-helix structure of DNA⁹⁹ and the Nobel prize for Watson and Crick, who had not done the actual diffraction experiment, but did interpret the data¹⁰⁰. The discovery of the double-helix structure is seen by many as the start of modern structural biology and protein crystallography. The diffraction patterns of these systems look incredibly complicated, as the unit cells of these crystals contain often thousands of atoms and have a low symmetry compared to, for example, NaCl.

The methods to describe crystals and diffraction, both on the atomic and nanocrystal length scales will be described in this section. Moreover typical setups used to perform these experiments and some prototypical experimental data will be described and clarified.

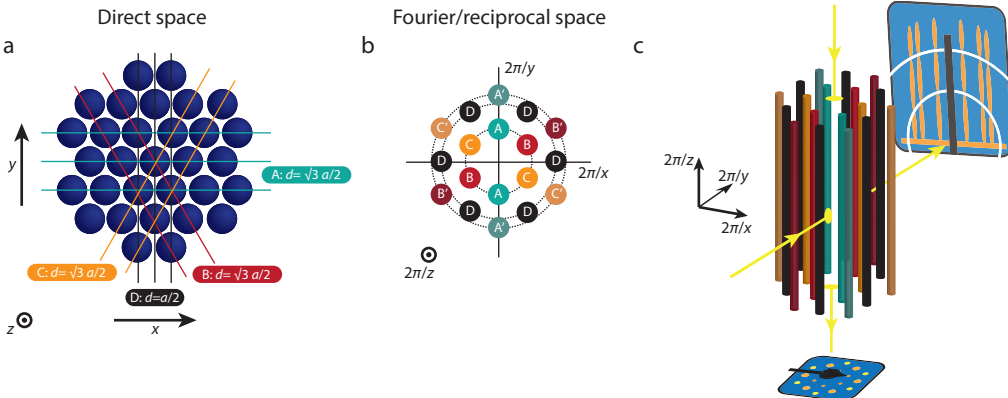


Figure 2.8: A hexagonal lattice in direct and reciprocal space. (a) Direct space, or real space, 2-D hexagonal lattice of spheres, with interparticle spacing a . The $\{10\}$ and $\{11\}$ lattice planes are indicated in blue/red/yellow and black respectively. (b) The hexagonal lattice in reciprocal space. The reciprocal space lattice points correspond to a series of planes in direct space. Since the reciprocal lattice is the Fourier transform of the direct space lattice, reciprocal space is also referred to as Fourier space. (c) Since the 2-D hexagonal lattice is small in the z -direction in real space, it becomes large along this direction in reciprocal space. When doing diffraction, one makes a slice-through of the reciprocal space lattice. The observed diffraction pattern depends in which direction this cut through is made (i.e. how the Ewald sphere cuts through reciprocal space, see below).

Instead of describing all atoms inside a large crystal, one can describe the crystal in frequency space. This means that we account for all periodicities inside the crystal occurring in crystallographic directions. Mathematically the process, of going from the direct space (or real space) crystal to the reciprocal lattice, is called a Fourier transformation. We go from a real space lattice described by $\mathbf{R}_n = n_1 \mathbf{a}_1 + n_2 \mathbf{a}_2 + n_3 \mathbf{a}_3$ to a reciprocal lattice $\mathbf{G} = h \mathbf{b}_1 + k \mathbf{b}_2 + l \mathbf{b}_3$. The real space crystal is described by a unit cell with lattice vectors \mathbf{a}_1 , \mathbf{a}_2 , \mathbf{a}_3 and volume V , which repeats through space through multiplication with constants n_1 , n_2 and n_3 ^{101,102}. The reciprocal lattice basis vectors are then described as

$$\mathbf{b}_1 = 2\pi \frac{\mathbf{a}_2 \times \mathbf{a}_3}{V}, \mathbf{b}_2 = 2\pi \frac{\mathbf{a}_3 \times \mathbf{a}_1}{V}, \mathbf{b}_3 = 2\pi \frac{\mathbf{a}_1 \times \mathbf{a}_2}{V} \quad 2.4$$

$$V = \mathbf{a}_1 \cdot (\mathbf{a}_2 \times \mathbf{a}_3) = \mathbf{a}_2 \cdot (\mathbf{a}_3 \times \mathbf{a}_1) = \mathbf{a}_3 \cdot (\mathbf{a}_1 \times \mathbf{a}_2)$$

In Figure 2.8(a) part of a 2-D hexagonal lattice of spheres is drawn. This can be a monolayer of nanocrystals at a liquid-air interface for example. The periodicities inside the crystal are identified as lattice planes, which are indicated with their Miller indices h, k and l . These planes have a set periodicity in a given direction, which indicates that they become a point in reciprocal space; their position in reciprocal space is given by the frequency at which it occurs in real space, their direction in reciprocal space depends on the direction in which this periodicity occurs in real space. Since we measure a direct slice-through of the reciprocal lattice in a scattering experiment, we can calculate back what the structure looks like in real space.

When one now looks at the reciprocal lattice of this 2-D hexagonal lattice, displayed in Figure 2.8(b), the sets of lattice planes are given as reciprocal lattice points. Each reciprocal lattice point is perpendicular to a lattice plane in real space. As a physical explanation this can be seen as an X-ray photon being reflected in the directions perpendicular to the lattice plane or similarly that the periodicity of these lattice planes travels in a direction perpendicular to these planes.

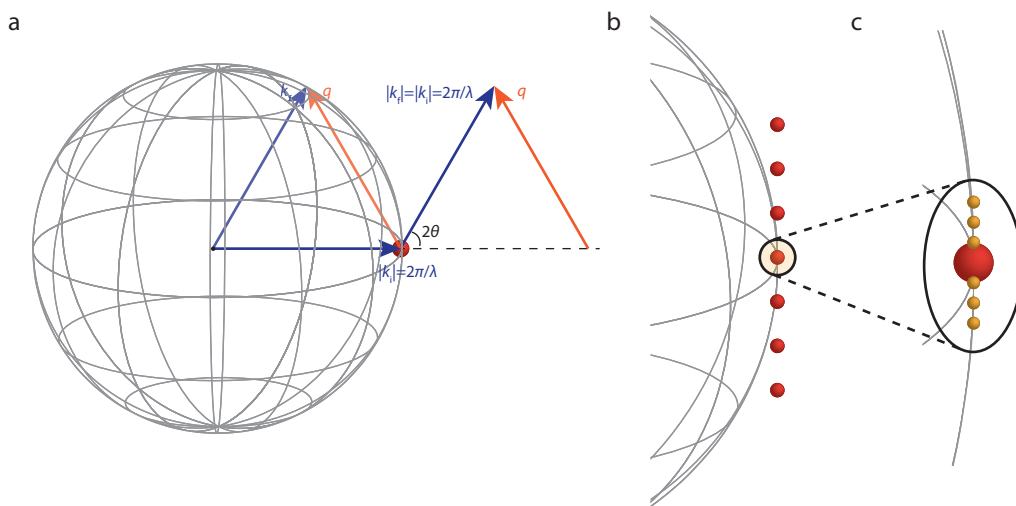


Figure 2.9: Ewald sphere construction of an elastic scattering event. (a) An incident X-ray photon with wavevector \mathbf{k}_i hits a scatterer, e.g. an atom, causing the X-ray photon to change direction. Detected photons will be scattered constructively in directions governed by Bragg's law. Note that the scattered photon, with wavevector \mathbf{k}_f , is scattered elastically. This means that the magnitude of the wavevector has not changed, only the direction. Instead looking at intensity vs. diffraction angle, which is energy dependent, one can also use intensity vs. momentum transfer vector \mathbf{q} , which is energy independent. (b) Ewald sphere combined with an atomic lattice (red spheres). The Laue condition for diffraction states that the scattering vector \mathbf{q} should equal a reciprocal lattice vector \mathbf{G} to interfere constructively. (c) The reciprocal lattice of an atomically coherent superlattice has a superimposed reciprocal lattice of the nanocrystal lattice (yellow spheres). These occur at smaller distances in reciprocal space, since the lengthscales of the nanocrystal lattice are much larger than those of the atomic lattice. This gives the basis for SAXS, since the relatively large curvature of the Ewald sphere w.r.t. the atomic lattice, lets the sphere intersect a large number of reciprocal lattice points of the nanogeometry.

When obtaining a diffraction pattern from a crystalline object, the X-rays are scattered constructively in directions governed by Bragg's law, $2d_{hkl}\sin(\theta)=n\lambda$. This relatively simple law is used to characterize crystalline and amorphous phases of all different sorts of materials. Obtaining a 2-D diffraction pattern is in principle the same as making a slice through of the reciprocal lattice of a material. Depending on the orientation of the material, hence the orientation of the reciprocal lattice, one obtains a different projection, which is depicted in Figure 2.8(c).

It is only around absorption edges, where core electrons are excited, that there is a significant contribution of absorption. Changing the effective number of scattering electrons, we can solve the phase problem and figure out where elements sit in the structure. This can be used to do element specific scattering experiments, so called anomalous X-ray diffraction, where one looks at the changes in diffraction patterns below or above an absorption edge of an element present inside the material. It has for example been used to determine the structure of the blue copper protein inside in cucumbers, more specifically the position of the Cu ion inside the protein, by using the scattering contrast above and below a Cu absorption edge¹⁰³. Another example of anomalous diffraction is the measurement strain maps in SiGe nanostructures for both the Si and Ge components separately^{104,105}, again by changing the diffraction contrast by measuring above and below the different absorption edges of the two components.

Throughout this thesis we only consider elastic X-ray scattering, i.e. there is no net energy loss between the incoming photons and the scattered photons. A different way of saying this is that the magnitude of the wavevector is not changed upon scattering on an atom: $|\mathbf{k}_i| = |\mathbf{k}_f| = 2\pi/\lambda$, with \mathbf{k}_i and \mathbf{k}_f the wavevector of the incoming photon and the wavevector of the scattered photon respectively. Now instead of using the angle between the incoming and scattered photons (2θ) as a variable, we can also use the so called momentum transfer vector \mathbf{q} (or scattering vector), which can be seen as the “push” that the photons receive upon scattering, changing their direction, i.e. $\mathbf{q} = \mathbf{k}_f - \mathbf{k}_i$. Straightforward geometry can show that the Bragg angle and the momentum transfer vector are interchangeable $|\mathbf{q}| = 4\pi \sin(\theta)/\lambda$. The use of \mathbf{q} instead of 2θ has another benefit, in the sense that we have an energy independent variable to plot versus the intensity. This is extremely useful in unifying all data, as many diffractometers and synchrotron experiments use X-rays with different photon energies.

Elastic scattering has another consequence for our experiment. The Laue condition for constructive interference, which is a reformulation of Bragg’s law in reciprocal space, states that for constructive interference to occur, the scattering vector should equal a reciprocal lattice vector, $\mathbf{q} = \mathbf{G}$. Figure 2.9(a) describes this effect in reciprocal space. If we project the wavevectors of the incoming and scattered photon into the same basis, we see that they describe a perfect sphere. This is the so called Ewald sphere, which has a radius equal to the length of the wavevector of the incoming and scattered photon. Projecting the scattering vector here as well, we see in Figure 2.9(a) that it always follows the surface of the Ewald sphere, meaning that only when the Ewald sphere intersects reciprocal lattice points of the material of interest there will be constructive interference (as is depicted in Figure 2.9(b))¹⁰².

The Ewald sphere construction for scattering is also particularly useful when demonstrating the principle behind SAXS. The larger periodicity for nanocrystal superlattices make that the reciprocal lattice is actually small, as depicted in Figure 2.9(c). Since these points are close to each other in reciprocal space, the curvature of the Ewald sphere is negligible, leading to efficient scattering from a lot of reciprocal lattice points if the superlattice long-range order is good.

From Bragg’s law it becomes immediately clear that smaller d -spacings scatter at larger angles and larger d -spacings scatter at small angles. The latter technique, small-angle X-ray scattering (SAXS), is used to characterize particles with sizes and interparticle distances ranging from nanometers to microns. The first technique, wide-angle X-ray scattering (WAXS), looks at scattering or diffraction on interatomic lengthscales. Combining the two techniques gives an incredibly powerful tool to characterize the superlattices studied in this thesis on all lengthscales present in the system.

Now we have a tool to describe the direction in which the X-ray photons are scattered, but we also need to describe the intensity of the scattered signal as function of outgoing angle. In principle the scattered amplitude contains two terms which arise due to the size and shape of the scattering object and from the spatial arrangement of these objects:

$$S(\mathbf{q}) = \sum_j P_j(\mathbf{q}) e^{-i\mathbf{R}_j \cdot \mathbf{q}} = \sum_j P_j(\mathbf{q}) e^{-i2\pi(x_j h + y_j k + z_j l)} \quad 2.5$$

$S(\mathbf{q})$ is the structure factor, which depends on the spatial arrangement of the particles inside the repeating unit cell, where the sum runs over all atoms present in the unit cell, j , which coordinates are given by x_j, y_j and z_j . The structure factor explains for example why in FCC lattices only certain reflections, i.e. those with their Miller indices all even or all odd, are allowed. This can be seen for example in the case of PbSe, which has an FCC rocksalt atomic crystal structure and an example is given below. The factor $P(\mathbf{q})$ is the atomic form factor, which depends on amongst others the electron density on an element. For example, KCl and KBr both have an FCC rocksalt crystal structure, but since K^+ and Cl^- have a similar size and similar number of electrons, the diffraction looks like it originates from a simple cubic lattice¹⁰¹. Often the scattering amplitude, $A(\mathbf{q})$, is generalized as a product of the phase term (often called structure factor) and an amplitude term:

$$A(\mathbf{q}) \propto S(\mathbf{q})P(\mathbf{q}) \quad 2.6$$

In the nanocrystal scattering regime, $P(\mathbf{q})$ is the squared modulus of the Fourier transformation of the scattering particle and so it describes the influence of the particle size and shape on the scattered intensity. An example for spherical particles is given further on in this section. Note that one single unit cell does not give rise to Bragg reflections, so eq. 2.5 technically has to be summed over the number of unit cells in all directions to obtain the so called Laue functions¹⁰⁶.

It is important to note that in this thesis we work with hierarchical structures; systems which are crystalline on both the nanocrystal and atomic length scales. When recording the diffraction we also have to interpret the scattering signal on these two length scales. On the atomic lengthscale, eq. 2.5 has an amplitude part of the scattered photons, the atomic form factor, which describes how strong certain *atoms* scatter. It secondly contains a phase part of the scattered signal (the structure factor), originating from the positions of the *atoms* inside the unit cells and the constructive and destructive interference that occurs when photons scatter on them. On the nanocrystal length scales, the structure factor originates from the positions of the scattering *nanocrystals*, whereas the formfactor originates from scattering of the *nanocrystal* size and shape. Experimentally, only the intensity of the diffracted signals and not their phase can be measured. Intensity alone is directly related to the autocorrelation function of the electronic density profile in the sample, which does not guarantee a unique reconstruction of the sample structure in the direct space. An example where this phase problem is solved is in coherent diffraction imaging, where the use of a coherent beam of X-ray photons allows one calculate the phase via iterative algorithms¹⁰⁷⁻¹¹⁰. Once the phase is known, the structure of the scattering object can be obtained by a back Fourier transform of the complex scattering amplitudes.

Figure 2.10 shows an experimental scattering curve for PbSe nanocrystals in solution. By using variable sample-to-detector distances a large \mathbf{q} -range can be sampled covering both nanocrystal reflections at small angles and atomic reflections at larger angles. The obtained scattering curve can generally be separated into two regions; the region at higher angles (indicated yellow), or high scattering vector \mathbf{q} , originates from atomic reflections of the rock-salt PbSe lattice. The second region at smaller angles (indicated red), or small scattering vector \mathbf{q} , originates from nanocrystal form-factor scattering. Let us first focus on the WAXS region where the atomic reflections are visible. Since the PbSe atomic lattice has an FCC basis, only lattice planes with Miller indices that are all even, or all odd will interfere constructively, due to structure factor

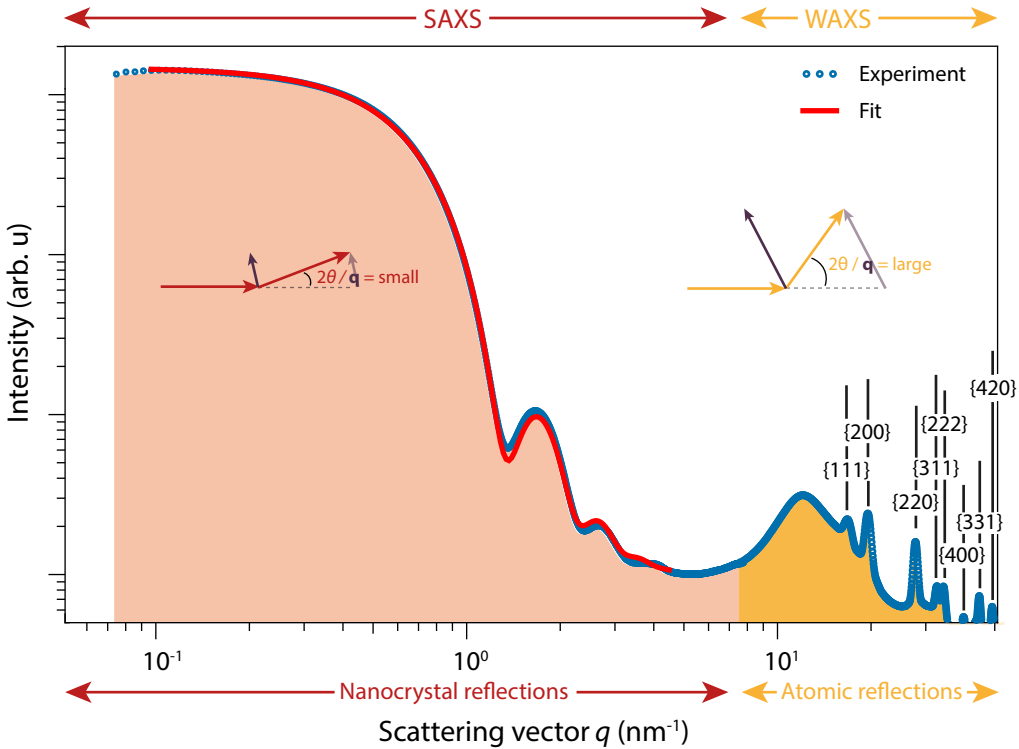


Figure 2.10: X-ray scattering pattern covering a large q -range of 5.5 nm PbSe nanocrystals in solution. The above Figure shows the experimental small-angle X-ray scattering pattern, showing form-factor scattering from the individual nanocrystals, and connected wide-angle X-ray scattering pattern, showing scattering from the atomic lattice, of PbSe nanocrystals (blue data points). At small angles, or rather small q , the oscillations are fitted with form-factor for polydisperse spheres (red solid line). The PbSe atomic reflections at wide angles are labeled with their corresponding Miller indices. The broad feature at 12 nm^{-1} is a toluene reflection. Data was taken at beamline ID02 of the European Synchrotron Radiation Facility, Grenoble, France, at an X-ray energy of 12.4 keV.

considerations. As can be seen from the labels, only reflections from the {111}, {200}, {220}, {311}, {222}, {400}, {331} and {420} planes are visible.

The region for small-angle scattering is dominated by form-factor scattering, which can be seen as the undulating signal in the red region of Figure 2.10. No structure factor peaks are observed in the region where the nanocrystals reflections are visible, since the nanocrystals hardly interact with each other. The periodicity of the observed fringes can be fitted with the form-factor for polydisperse spheres to give details not only about the size and polydispersity of the sample, but also about interparticle interactions which may or may not be present¹¹¹.

The form factor of a sphere, averaged over a Gaussian size distribution, is given by

$$\langle P(q) \rangle_R = \frac{1}{\sqrt{2\pi} \sigma_R} \int_0^\infty e^{-\frac{1}{2} \left(\frac{R-R_0}{\sigma_R} \right)^2} 3V \left[\frac{\sin(qR) - qR \cos(qR)}{(qR)^3} \right]^2 dR \quad 2.7$$

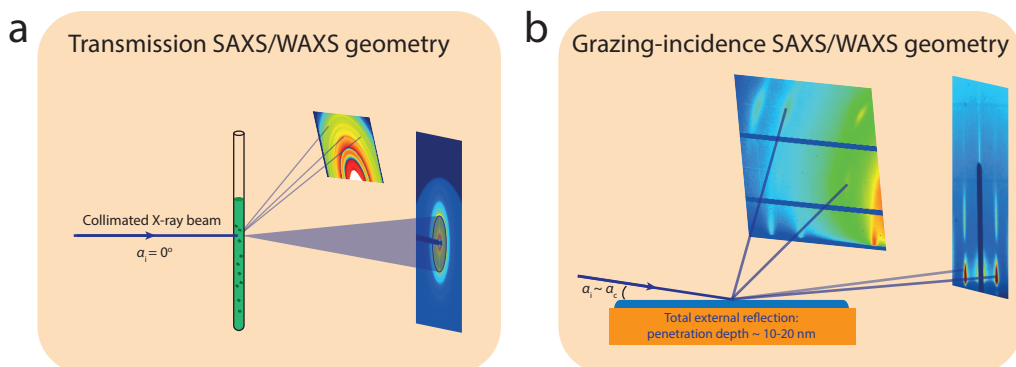


Figure 2.11: Experimental setup for transmission SAXS/WAXS and GISAXS/GIWAXS. (a) Transmission SAXS/WAXS can be performed on a capillary with nanocrystals in solution. The scattering patterns are often azimuthally integrated for analysis. (b) To study nanocrystals on interfaces, the X-ray beam is tilted down towards the surface. Due to total external reflection of the X-ray photons, the top 10-20 nm of the surface is probed when working around the critical angle of the material of interest.

where R_0 and σ_R are the mean particle radius and standard deviation of the particle radius respectively and V the particle volume. Fitting the data in Figure 2.10 for the PbSe nanocrystals (red solid line) gives a particle size of 6.1 ± 0.7 nm. This is, however, a fit of a particle without surfactants and hence gives information about the inorganic core of the nanocrystal only. The ligand corona around the particles can also be taken into account to give information on the hydrodynamic radius^{112,113}. In the presented example, the electron density contrast between the oleate ligand corona and toluene is very small and thus the SAXS pattern can be quite accurately fitted with only the form-factor of a polydisperse inorganic core.

2.2.3 - Grazing incidence X-ray scattering

All materials have a refractive index in the X-ray region which is smaller than one. This leads to total external reflection; when the incoming X-ray beam impinges on the surface of interest at an angle lower than the materials' critical angle, α_c (milliradians), the X-ray photons will be reflected from the interface and only have an evanescent component inside the material. This evanescent wave is exponentially damped over several nanometers, even if there is no absorption. Above the critical angle (if there is no total external reflection) there is no evanescent wave. The wave can be damped exponentially, but this is then due to absorption. In a non-absorbing material the penetration depth is in principle infinite (since $\text{Im}(k_z)=0$). When there is total external reflection the wavevector component k_z is almost purely imaginary; if there is transmission into an absorbing material it has a real component; a damped wave. This gives us a depth sensitive probe; by changing the grazing angle and hence the penetration depth of the X-ray photons, we can obtain information from both the bulk and the surface of a material of interest.

The study of nanocrystals on a liquid-surface are performed under this so-called grazing incidence geometry, depicted in Figure 2.11(b). Compared to the normal transmission SAXS/WAXS geometry, depicted in Figure 2.11(a), the collimated X-ray beam has to be bend down towards the liquid surface. This is either achieved using X-ray mirrors, or by using a crystal

deflection scheme. Here one or two crystals are placed in a Bragg condition of one of their reflections, and they are rotated such that the photons follow the 2θ cone. The diffractometer arm, carrying the detectors, has to be rotated accordingly to follow the path of the X-ray beam.

One way to model the interfacial part of the scattering signal is through a so-called Vineyard factor¹¹⁴, $V(q_z)$, which describes the scattering amplitude in the direction perpendicular to the surface or interface. This factor takes into account the reflection from the surface according to:

$$V(q_z) = \begin{cases} 0 & , \quad q_z < \frac{2\pi}{\lambda} \sin(\alpha_c) \\ \left| \frac{2k_{tz}}{k_{tz} + \sqrt{k_{tz}^2 - \left(\frac{2\pi}{\lambda} \sin(\alpha_c)\right)^2} + iv} \right|^2 & , \quad q_z \geq \frac{2\pi}{\lambda} \sin(\alpha_c) \end{cases} \quad 2.8$$

Where $k_{tz} = q_z - (2\pi/\lambda) \sin(\alpha_i)$. The term v is given by β/δ , the imaginary (β) and real (δ) part of the refractive index, and accounts for absorption of X-rays by the nanocrystals. In general v is very low (< 0.01), especially since we avoid working around absorption edges for the materials of interest, and this term is omitted.

It is possible to analytically calculate the full scattering signal of any material through the distorted wave Born approximation (DWBA)¹¹⁵. This takes multiple scattering effects into account, such as interference between scattering from the direct and reflected beam, into account by calculating the Fresnel coefficients of each scattering term. An extra feature that arise from DWBA theory compared to the simplified Vineyard approach, is for example the appearance of the Yoneda peak, which appears as an increased scattering intensity at the critical angle of the sample, i.e. where the scattering of the material has its maximum.

Through the above described Vineyard approach the total scattering pattern in an X-ray scattering experiment in grazing incidence geometry can be approximated as the product of the structure factor of the lattice, the form factor of the constituent particles and the Vineyard factor, i.e. $S(\mathbf{q}) \cdot P(\mathbf{q}) \cdot V(q_z)$.

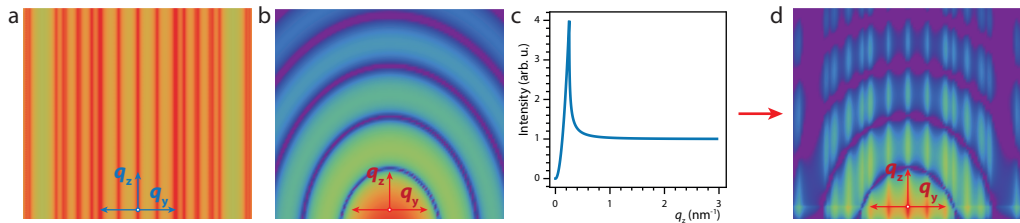


Figure 2.12: Modelling grazing-incidence small-angle X-ray scattering patterns. (a) Structure factor of a 2-D hexagonal crystal of 5 nm diameter nanocrystals. (b) Form-factor factor scattering for 5 nm monodisperse spheres. (c) Vineyard factor, modelling the effect of the reflecting X-ray beam on the surface. The incoming X-ray photons have an energy of 22 keV and hit the surface at a glancing angle of 0.1° . (d) Total scattering pattern, which is the product of the structure factor, form-factor and Vineyard factor. Note that the direct beam, i.e. the reflection at $q_y=0$ and $q_z=0$, is usually blocked with a beamstop to prevent damage to the detector, since it is very intense.

An example of the modelling of the GISAXS pattern through this Vineyard approach is displayed in Figure 2.12 above. The structure factor of a two-dimensional hexagonal lattice of spheres

is shown in Figure 2.12(a), where the consecutive order of $1:\sqrt{3}:2:\sqrt{7}$ of peak positions in the horizontal scattering direction shows the signature of this lattice. Since the lattice is 2-D in the horizontal plane in real space, the structure factor appears as elongated rods in reciprocal space. The form factor of spherical particles with a diameter of 5 nm is displayed in Figure 2.12(b), where the periodicity of the fringes is governed by the particle size. The Vineyard factor for this 2-D hexagonal lattice is shown in Figure 2.12(c). The relative high intensity at $q_z = 0.3 \text{ nm}^{-1}$ is the increased intensity around critical angle for total external reflection, where the incident and reflected waves are in phase at the substrate surface. This is displayed as the so called horizon of the total scattering pattern, presented in Figure 2.12(d), which is the product of Figures 2.12(a), (b) and (c), i.e. the structure factor times the form factor times the Vineyard factor.

The full series of diffraction experiments performed throughout this thesis, including electron diffraction, and the alignment of the X-ray beam and the detectors during a typical experiment in grazing-incidence geometry, is shown in Figure 2.13. The X-ray photons are scattered in the forward direction to a detector collecting the GISAXS signal, where inter-nanoparticle distances and nanocrystalline structures can be followed in-situ over time. The GISAXS detector is usually at a relatively large distance, depending on the X-ray photon energy, since Bragg reflections need to be sufficiently diverged in order to be separated from the direct beam. At larger scattering angles and closer distances a GIWAXS detector is placed, where the atomic planes scatter and hence the crystallographic orientation and atomic coherency of the NCs and superlattices can be studied. Inside an electron microscope there is often the option to perform (selected area) electron diffraction. Combined with the normal imaging modes, this allows us to characterize the same material ex-situ, which can be compared to the information acquired during the X-ray scattering experiments.

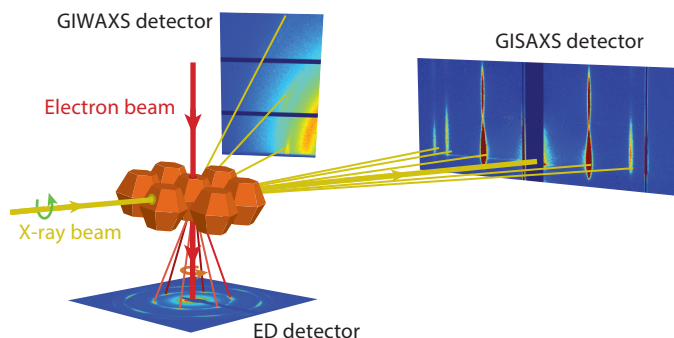


Figure 2.13: Typical experimental geometries used throughout this thesis during grazing-incidence X-ray scattering experiments and electron diffraction. The incoming X-ray beam hits the sample at a shallow angle, often around the critical angle for total external reflection, and is scattered in the forward direction to a detector at large distances to record the small-angle scattered X-ray photons. Another detector is placed at a wider angle to collect the atomic diffraction from the nanocrystals. During electron diffraction experiments inside an electron microscope, the sample is hit by the electron beam from above, normal to the plane of the 2-D lattice. The scattered electrons are collected on a CCD camera below the sample. Image courtesy of Ward van der Stam.

2.2.4 - Specular X-ray reflectivity

From the grazing-incidence scattering we mostly obtain in-plane information about the structures of interest, even though also out-of-plane information can be obtained through very extensive modelling of the 2-D scattering patterns. To add a third dimension to the acquired information, also specular X-ray reflectivity (XRR) can be used. Here, the angle of incidence is varied and kept equal to the exit angle. This means that the scattering vector lies perfectly perpendicular to the interface, and will only have a z -component. By monitoring the intensity as a function of angle, one can obtain a reflectivity curve, which after fitting can give the electron density profile along the z -direction.

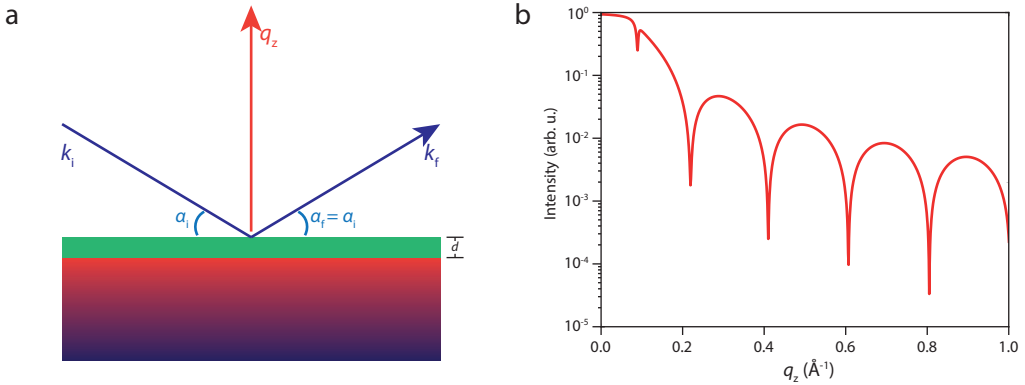


Figure 2.13: Geometry of experiment and calculated X-ray reflectivity curve of a thing slab of W on a Si substrate. (a) Geometry of the specular XRR experiment. The incoming beam impinges the surface at an angle of incidence α_i , which is kept equal to the exit angle α_f . The scattering vector \mathbf{q} now only has a component in the z -direction (q_z), i.e. perpendicular to the sample substrate, and detailed depth information can be acquired. (b) Calculated reflectivity curve for a 40 nm thick film of W on a Si substrate. The apparent fringes in the reflectivity curve originate from constructive and destructive interference between reflections from the top and bottom layer respectively.

X-ray photons are scattered on electron density gradients during all types of scattering experiments described above. The reflectivity is only sensitive to the out-of-plane structure, as the scattering vector in this geometry is always perpendicular to the surface. The reflectivity profile can be computed through the equation below, where we consider the contribution from a thin slab at a depth z , and then summing up all the contributions from a graded interface, each with a change in phase $e^{iq_z z}$. The electron density profile of this interface is given by $f(z)$ and the reflectivity curve is described by¹⁰²;

$$\frac{R(q_z)}{R_F(q_z)} = \left| \int_{-\infty}^{\infty} \frac{df}{dz} e^{iq_z z} dz \right|^2 \quad 2.9$$

Expressed in words, the above equation says that the ratio between the measured reflectivity and the Fresnel reflectivity of an ideally sharp interface is absolute square of the Fourier transform of the electron density gradient across an interface.

A schematic of the specular XRR experiment can be found in Figure 2.13(a). The angle of incidence α_i and exit angle α_f are kept equal and are scanned simultaneously, while the intensity

of the specular reflection is recorded. From a thin slab, presented in the same Figure, there will be constructive and destructive interference from photons reflected from the top and bottom layer, resulting in so called Kiessig fringes, where the periodicity of these fringes in q_z will be $2\pi/d$.

Specular XRR has been used in quite some experiments already. For example to study the formation of phospholipid monolayers and bilayers¹¹⁶, bacterial protein coupling to lipid layers¹¹⁷, the assembly of silica nanoparticle monolayers at the air-water interface¹¹⁸ and its combination with amphiphilic block copolymers¹¹⁹. We will show in Chapter 5 that the combination of GISAXS, GIWAXS and XRR can give the full three-dimensional information on the adsorption geometry of PbSe nanocrystals at the ethylene glycol-air interface.

References

1. Murray, C. B., Norris, D. J. & Bawendi, M. G. "Synthesis and characterization of nearly monodisperse CdE (E = sulfur, selenium, tellurium) semiconductor nanocrystallites". *J. Am. Chem. Soc.* **115**, 8706–8715 (1993).
2. De Mello Donegá, C. et al. "Synthesis and properties of colloidal heteronanocrystals". *Chem. Soc. Rev.* **40**, 1512–1546 (2011).
3. Moreels, I. et al. "Size-Dependent Optical Properties of Colloidal PbS Quantum Dots". *ACS Nano* **3**, 3023–3030 (2009).
4. Kamal, J. S. et al. "Size-Dependent Optical Properties of Zinc Blende Cadmium Telluride Quantum Dots". *J. Phys. Chem. C* **116**, 5049–5054 (2012).
5. de Mello Donegá, C. & Koole, R. "Size Dependence of the Spontaneous Emission Rate and Absorption Cross Section of CdSe and CdTe Quantum Dots". *J. Phys. Chem. C* **113**, 6511–6520 (2009).
6. Kagan, C. R., Murray, C. B., Nirmal, M. & Bawendi, M. G. "Electronic Energy Transfer in CdSe Quantum Dot Solids". *Phys. Rev. Lett.* **76**, 1517–1520 (1996).
7. Norris, D. J., Sacra, A., Murray, C. B. & Bawendi, M. G. "Measurement of the size dependent hole spectrum in CdSe quantum dots". *Phys. Rev. Lett.* **72**, 2612–2615 (1994).
8. Lipovskii, A. et al. "Synthesis and characterization of PbSe quantum dots in phosphate glass". *App. Phys. Lett.* **71**, (1998).
9. Ekimov A. I. & Onushchenko A. A. "Quantum size effect in three-dimensional microscopic semiconductor crystals". *Jetp Lett.* **34**, 345–349 (1981).
10. Ekimov A. I. & Onushchenko A. A. "Size quantization of the electron energy spectrum in a microscopic semiconductor crystal". *Jetp Lett.* **40**, 1136–1139 (1984).
11. Aifassl, Z., Bahnemann, D. & Henglein, A. "Photochemistry of Colloidal Metal Sulfides. 3. Photoelectron Emission from CdS and CdS-ZnS Co-Colloids". *J. Phys. Chem.* **86**, 4656–4657 (1982).
12. Brus, L. E. "Electron-electron and electron-hole interactions in small semiconductor crystallites: The size dependence of the lowest excited electronic state". *J. Chem. Phys.* **80**, 4403–4409 (1984).
13. Efros, A. & Efros, A. "Interband absorption of light in a semiconductor sphere". *Sov. Phys.* (1982).
14. Alivisatos, A. P. et al. "Shape control of CdSe nanocrystals". *Nature* **404**, 59–61 (2000).
15. Manna, L., Milliron, D. J., Meisel, A., Scher, E. C. & Alivisatos, A. P. "Controlled growth of tetrapod-branched inorganic nanocrystals". *Nat. Mater.* **2**, 382–385 (2003).
16. Ithurria, S. et al. "Colloidal nanoplatelets with two-dimensional electronic structure". *Nat. Mater.* **10**, 936–941 (2011).
17. Van der Stam, W. et al. "Solution-Processable Ultrathin Size- and Shape-Controlled Colloidal Cu_{2-x}S Nanosheets". *Chem. Mater.* **27**, 283–291 (2015).
18. Van der Stam, W. et al. "Shape Control of Colloidal Cu_{2-x}S Polyhedral Nanocrystals by Tuning the Nucleation Rates". *Chem. Mater.* **28**, 6705–6715 (2016).

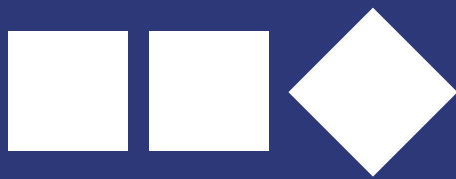
19. Gilmore, R. H., Lee, E. M. Y., Weidman, M. C., Willard, A. P. & Tisdale, W. A. "Charge Carrier Hopping Dynamics in Homogeneously Broadened PbS Quantum Dot Solids". *Nano Lett.* **17**, 893–901 (2017).
20. Van der Stam, W., Bladt, E., Rabouw, F. T., Bals, S. & de Mello Donega, C. "Near-Infrared Emitting CuInSe₂/CuInS₂ Dot Core/Rod Shell Heteronanorods by Sequential Cation Exchange". *ACS Nano* **9**, 11430–11438 (2015).
21. Lee, D. et al. "Direct Cd-to-Pb Exchange of CdSe Nanorods into PbSe/CdSe Axial Heterojunction Nanorods". *Chem. Mater.* **27**, 5295–5304 (2015).
22. Bals, S. et al. "Three-Dimensional Atomic Imaging of Colloidal Core–Shell Nanocrystals". *Nano Lett.* **11**, 3420–3424 (2011).
23. Casavola, M. et al. "Anisotropic Cation Exchange in PbSe/CdSe Core/Shell Nanocrystals of Different Geometry". *Chem. Mater.* **24**, 294–302 (2012).
24. Pietra, F. et al. "Semiconductor Nanorod Self-Assembly at the Liquid/Air Interface Studied by in Situ GISAXS and ex Situ TEM". *Nano Lett.* **12**, 5515–5523 (2012).
25. Lin, X. et al. "Fabrication of transparent SERS platform via interface self-assembly of gold nanorods and gel trapping technique for on-site real time detection". *Phys. Chem. Chem. Phys.* **17**, 31324–31 (2015).
26. Ithurria, S. & Dubertret, B. "Quasi 2D Colloidal CdSe Platelets with Thicknesses Controlled at the Atomic Level". *J. Am. Chem. Soc.* **130**, 16504–16505 (2008).
27. Mahler, B., Nadal, B., Bouet, C., Patriarche, G. & Dubertret, B. "Core/Shell Colloidal Semiconductor Nanoplatelets". *J. Am. Chem. Soc.* **134**, 18591–18598 (2012).
28. Tessier, M. D. et al. "Spectroscopy of Colloidal Semiconductor Core/Shell Nanoplatelets with High Quantum Yield". *Nano Lett.* **13**, 3321–3328 (2013).
29. Tessier, M. D. et al. "Efficient Exciton Concentrators Built from Colloidal Core/Crown CdSe/CdS Semiconductor Nanoplatelets". *Nano Lett.* **14**, 207–213 (2014).
30. Pedetti, S., Ithurria, S., Heuclin, H., Patriarche, G. & Dubertret, B. "Type-II CdSe/CdTe Core/Crown Semiconductor Nanoplatelets". *J. Am. Chem. Soc.* **136**, 16430–16438 (2014).
31. Kelestemur, Y. et al. "Platelet-in-Box Colloidal Quantum Wells: CdSe/CdS@CdS Core/Crown@Shell Heteronanoplatelets". *Adv. Funct. Mater.* **26**, 3570–3579 (2016).
32. Bouet, C. et al. "Flat Colloidal Semiconductor Nanoplatelets". *Chem. Mater.* **25**, 1262–1271 (2013).
33. Riedinger, A. et al. "An intrinsic growth instability in isotropic materials leads to quasi-two-dimensional nanoplatelets". *Nat. Mater.* (2017). doi:10.1038/nmat4889
34. McManus, J. J., Charbonneau, P., Zaccarelli, E. & Asherie, N. "The physics of protein self-assembly". *Curr. Opin. Colloid Interface Sci.* **22**, 73–79 (2016).
35. Andersen, E. S. "Biomolecular self-assembly: DNA origami rewired". *Nat. Nanotechnol.* **10**, 733–734 (2015).
36. Poranen, M. M. & Tuma, R. "Self-assembly of double-stranded RNA bacteriophages". *Virus Res.* **101**, 93–100 (2004).
37. Sanders, J. V. "Colour of Precious Opal". *Nature* **204**, 1151–1153 (1964).
38. Bartlett, P., Ottewill, R. H. & Pusey, P. N. "Superlattice formation in binary mixtures of hard-sphere colloids". *Phys. Rev. Lett.* **68**, 3801–3804 (1992).
39. Hynninen, A.-P., Christova, C. G., van Roij, R., van Blaaderen, A. & Dijkstra, M. "Prediction and Observation of Crystal Structures of Oppositely Charged Colloids". *Phys. Rev. Lett.* **96**, 138308 (2006).
40. Evers, W. H. et al. "Low-Dimensional Semiconductor Superlattices Formed by Geometric Control over Nanocrystal Attachment". *Nano Lett.* **13**, 2317–2323 (2013).
41. Boneschanscher, M. P. et al. "Long-range orientation and atomic attachment of nanocrystals in 2D honeycomb superlattices". *Science* (80-.). **344**, (2014).
42. Kalesaki, E. et al. Dirac Cones, "Topological Edge States, and Nontrivial Flat Bands in Two-Dimensional Semiconductors with a Honeycomb Nanogeometry". *Phys. Rev. X* **4**, 11010 (2014).

43. Beugeling, W. et al. "Topological states in multi-orbital HgTe honeycomb lattices". *Nat. Commun.* **6**, 6316 (2015).
44. LaMer, V. K. & Dinegar, R. H. "Theory, Production and Mechanism of Formation of Monodispersed Hydrosols". *J. Am. Chem. Soc.* **72**, 4847–4854 (1950).
45. Alivisatos, A. P. "Perspectives on the Physical Chemistry of Semiconductor Nanocrystals". (1996). doi:10.1021/JP9535506
46. Park, J., Joo, J., Kwon, S. G., Jang, Y. & Hyeon, T. "Synthesis of Monodisperse Spherical Nanocrystals". *Angew. Chemie Int. Ed.* **46**, 4630–4660 (2007).
47. Kumar, S. & Nann, T. "Shape Control of II–VI Semiconductor Nanomaterials". *Small* **2**, 316–329 (2006).
48. de Mello Donegá, C., Liljeroth, P. & Vanmaekelbergh, D. "Physicochemical Evaluation of the Hot-Injection Method, a Synthesis Route for Monodisperse Nanocrystals". *Small* **1**, 1152–1162 (2005).
49. J. Jack Li, † et al. "Large-Scale Synthesis of Nearly Monodisperse CdSe/CdS Core/Shell Nanocrystals Using Air-Stable Reagents via Successive Ion Layer Adsorption and Reaction". (2003).
50. Smith, A. M., Mohs, A. M. & Nie, S. "Tuning the optical and electronic properties of colloidal nanocrystals by lattice strain". *Nat. Nanotechnol.* **4**, 56–63 (2009).
51. Beberwyck, B. J., Surendranath, Y. & Alivisatos, A. P. "Cation Exchange: A Versatile Tool for Nanomaterials Synthesis". *J. Phys. Chem. C* **117**, 19759–19770 (2013).
52. Gupta, S., Kershaw, S. V. & Rogach, A. L. "25th Anniversary Article: Ion Exchange in Colloidal Nanocrystals". *Adv. Mater.* **25**, 6923–6944 (2013).
53. De Trizio, L. & Manna, L. "Forging Colloidal Nanostructures via Cation Exchange Reactions". *Chem. Rev.* **116**, 10852–10887 (2016).
54. Groeneveld, E. et al. "Tailoring ZnSe–CdSe Colloidal Quantum Dots via Cation Exchange: From Core/Shell to Alloy Nanocrystals". *ACS Nano* **7**, 7913–7930 (2013).
55. Akkerman, Q. A. et al. "Tuning the Optical Properties of Cesium Lead Halide Perovskite Nanocrystals by Anion Exchange Reactions". *J. Am. Chem. Soc.* **137**, 10276–10281 (2015).
56. Nedelcu, G. et al. "Fast Anion-Exchange in Highly Luminescent Nanocrystals of Cesium Lead Halide Perovskites (CsPbX₃, X = Cl, Br, I)". *Nano Lett.* **15**, 5635–5640 (2015).
57. Hodges, J. M., Kletetschka, K., Fenton, J. L., Read, C. G. & Schaak, R. E. "Sequential Anion and Cation Exchange Reactions for Complete Material Transformations of Nanoparticles with Morphological Retention". *Angew. Chemie* **127**, 8793–8796 (2015).
58. Wu, H.-L. et al. "Formation of pseudomorphic nanocages from Cu₂O nanocrystals through anion exchange reactions". *Science* (80-.). 351, (2016).
59. Dana A. Schwartz, Nick S. Norberg, Quyen P. Nguyen, Jason M. Parker, and Gamelin*, D. R. "Magnetic Quantum Dots: Synthesis, Spectroscopy, and Magnetism of Co²⁺- and Ni²⁺-Doped ZnO Nanocrystals". (2003). doi:10.1021/JA036811V
60. Knowles, K. E., Nelson, H. D., Kilburn, T. B. & Gamelin, D. R. "Singlet–Triplet Splittings in the Luminescent Excited States of Colloidal Cu⁺:CdSe, Cu⁺:InP, and CuInS₂ Nanocrystals: Charge-Transfer Configurations and Self-Trapped Excitons". *J. Am. Chem. Soc.* **137**, 13138–13147 (2015).
61. Meinardi, F. et al. "Large-area luminescent solar concentrators based on 'Stokes-shift-engineered' nanocrystals in a mass-polymerized PMMA matrix". *Nat. Photonics* **8**, 392–399 (2014).
62. Pérez-del-Rey, D. et al. "Strontium Insertion in Methylammonium Lead Iodide: Long Charge Carrier Lifetime and High Fill-Factor Solar Cells". *Adv. Mater.* **28**, 9839–9845 (2016).
63. Frolova, L. A., Anokhin, D. V., Gerasimov, K. L., Dremova, N. N. & Troshin, P. A. "Exploring the Effects of the Pb²⁺ Substitution in MAPbI₃ on the Photovoltaic Performance of the Hybrid Perovskite Solar Cells". *J. Phys. Chem. Lett.* **7**, 4353–4357 (2016).
64. Abdelhady, A. L. et al. "Heterovalent Dopant Incorporation for Bandgap and Type Engineering of Perovskite Crystals". *J. Phys. Chem. Lett.* **7**, 295–301 (2016).
65. Liu, W. et al. "Mn²⁺-Doped Lead Halide Perovskite Nanocrystals with Dual-Color Emission Controlled by Halide Content". *J. Am. Chem. Soc.* **138**, 14954–14961 (2016).

66. Parobek, D. et al. “Exciton-to-Dopant Energy Transfer in Mn-Doped Cesium Lead Halide Perovskite Nanocrystals”. *Nano Lett.* acs.nanolett.6b02772 (2016). doi:10.1021/acs.nanolett.6b02772
67. Bourzac, K. “Quantum dots go on display”. *Nature* **493**, 283–283 (2013).
68. Vanmaekelbergh, D. “Self-assembly of colloidal nanocrystals as route to novel classes of nanostructured materials”. *Nano Today* **6**, 419–437 (2011).
69. Bolhuis, P. G., Frenkel, D., Mau, S.-C. & Huse, D. A. “Entropy difference between crystal phases”. *Nature* **388**, 235–236 (1997).
70. Bodnarchuk, M. I., Kovalenko, M. V., Heiss, W. & Talapin, D. V. “Energetic and Entropic Contributions to Self-Assembly of Binary Nanocrystal Superlattices: Temperature as the Structure-Directing Factor”. *J. Am. Chem. Soc.* **132**, 11967–11977 (2010).
71. Eldridge, M. D., Madden, P. A. & Frenkel, D. “Entropy-driven formation of a superlattice in a hard-sphere binary mixture”. *Nature* **365**, 35–37 (1993).
72. Israelachvili, J. N. “Intermolecular and Surface Forces”. 107–132 (2011). doi:10.1016/B978-0-12-375182-9.10006-5
73. Evers, W. H. et al. “Entropy-Driven Formation of Binary Semiconductor-Nanocrystal Superlattices”. *Nano Lett.* **10**, 4235–4241 (2010).
74. Kortschot, R. J., van Rijssel, J., van Dijk-Moes, R. J. A. & Ern , B. H. “Equilibrium Structures of PbSe and CdSe Colloidal Quantum Dots Detected by Dielectric Spectroscopy”. *J. Phys. Chem. C* **118**, 7185–7194 (2014).
75. D. V. T., Shevchenko, E. V., Murray, C. B., and, A. V. T. & Kr l*, P. “Dipole–Dipole Interactions in Nanoparticle Superlattices”. (2007). doi:10.1021/NL070058C
76. Mark Klokkenburg, †,‡ et al. “Dipolar Structures in Colloidal Dispersions of PbSe and CdSe Quantum Dots”. (2007). doi:10.1021/NL0714684
77. Bertolotti, F. et al. “Crystal symmetry breaking and vacancies in colloidal lead chalcogenide quantum dots”. *Nat. Mater.* **15**, 987–994 (2016).
78. Soligno, G., Dijkstra, M. & van Roij, R. “Self-Assembly of Cubes into 2D Hexagonal and Honeycomb Lattices by Hexapolar Capillary Interactions”. *Phys. Rev. Lett.* **116**, 258001 (2016).
79. Kagan, C. R. & Murray, C. B. “Charge transport in strongly coupled quantum dot solids”. *Nat. Nanotechnol.* **10**, 1013–1026 (2015).
80. Elena V. Shevchenko, † et al. “Self-Assembled Binary Superlattices of CdSe and Au Nanocrystals and Their Fluorescence Properties”. (2008). doi:10.1021/JA710619S
81. Talapin, D. V. et al. “A New Approach to Crystallization of CdSe Nanoparticles into Ordered Three-Dimensional Superlattices”. *Adv. Mater.* **13**, 1868 (2001).
82. De Nijs, B. et al. “Entropy-driven formation of large icosahedral colloidal clusters by spherical confinement”. *Nat. Mater.* **14**, 56–60 (2014).
83. Vanmaekelbergh, D. et al. “Shape-Dependent Multiexciton Emission and Whispering Gallery Modes in Supraparticles of CdSe/Multishell Quantum Dots”. *ACS Nano* **9**, 3942–3950 (2015).
84. Dong, A., Chen, J., Vora, P. M., Kikkawa, J. M. & Murray, C. B. “Binary nanocrystal superlattice membranes self-assembled at the liquid–air interface”. *Nature* **466**, 474–477 (2010).
85. Sohlberg, K. et al. “Insights into the physical chemistry of materials from advances in HAADF-STEM”. *Phys. Chem. Chem. Phys.* **17**, 3982–4006 (2015).
86. Van Aert, S. et al. “Quantitative atomic resolution mapping using high-angle annular dark field scanning transmission electron microscopy”. *Ultramicroscopy* **109**, 1236–1244 (2009).
87. Van Tendeloo, G., Bals, S., Van Aert, S., Verbeeck, J. & Van Dyck, D. “Advanced Electron Microscopy for Advanced Materials”. *Adv. Mater.* **24**, 5655–5675 (2012).
88. Swart, I., Liljeroth, P. & Vanmaekelbergh, D. “Scanning probe microscopy and spectroscopy of colloidal semiconductor nanocrystals and assembled structures”. *Chem. Rev.* **116**, 11181–11219 (2016).
89. Ross, F. M. “Opportunities and challenges in liquid cell electron microscopy”. *Science* (80-.). **350**, (2015).

90. Zheng, H., Claridge, S. A., Minor, A. M., Alivisatos, A. P. & Dahmen, U. "Nanocrystal Diffusion in a Liquid Thin Film Observed by in Situ Transmission Electron Microscopy". *Nano Lett.* **9**, 2460–2465 (2009).
91. Powers, A. S. et al. "Tracking Nanoparticle Diffusion and Interaction during Self-Assembly in a Liquid Cell". *Nano Lett.* [acs.nanolett.6b02972](https://doi.org/10.1021/acs.nanolett.6b02972) (2016). doi:10.1021/acs.nanolett.6b02972
92. History of synchrotron X-rays. Available at: <http://www.esrf.eu/about/synchrotron-science/history-synchrotron>. (Accessed: 21st December 2016)
93. Heaviside, O. "Electrical papers" **2**, (1894).
94. Griffiths, D. J. (David J.) "Introduction to electrodynamics". (Prentice Hall, 1999).
95. Bragg, W. H. & Bragg, W. L. "The Reflection of X-rays by Crystals". *Proc. R. Soc. London A Math. Phys. Eng. Sci.* **88**, (1913).
96. Bragg, W. L. "The Structure of Some Crystals as Indicated by Their Diffraction of X-rays". *Proc. R. Soc. London A Math. Phys. Eng. Sci.* **89**, (1913).
97. Bragg, W. H. & Bragg, W. L. "The Structure of the Diamond". *Nature* **91**, 557–557 (1913).
98. Debye, P. & Scherrer, P. "Interferenzen an regellos orientierten Teilchen im Röntgenlicht". *I. Nachrichten von der Gesellschaft der Wissenschaften zu Göttingen, Math. Klasse* 1916, 1–15.
99. Watson, J. D. & Crick, F. H. C. "Molecular Structure of Nucleic Acids: A Structure for Deoxyribose Nucleic Acid". *Nature* **171**, 737–738 (1953).
100. "Due credit". *Nature* **496**, 270–270 (2013).
101. Kittel, C. "Introduction to solid state physics". (Wiley, 2005).
102. Als-Nielsen, J. & McMorrow, D. "Elements of Modern X-ray Physics". (John Wiley & Sons, Inc., 2011). doi:10.1002/9781119998365
103. Guss, J. et al. "Phase determination by multiple-wavelength x-ray diffraction: crystal structure of a basic "blue" copper protein from cucumbers". *Science* (80-.). **241**, (1988).
104. Schüllli, T. U. et al. "Direct Determination of Strain and Composition Profiles in SiGe Islands by Anomalous X-Ray Diffraction at High Momentum Transfer". *Phys. Rev. Lett.* **90**, 66105 (2003).
105. Malachias, A. et al. "3D Composition of Epitaxial Nanocrystals by Anomalous X-Ray Diffraction: Observation of a Si-Rich Core in Ge Domes on Si(100)". *Phys. Rev. Lett.* **91**, 176101 (2003).
106. Kakudo, M. (Masao) & Kasai, N. (Nobutami). X-ray diffraction by macromolecules. Springer, (Kodansha, 2005).
107. Miao, J., Charalambous, P., Kirz, J. & Sayre, D. "Extending the methodology of X-ray crystallography to allow imaging of micrometre-sized non-crystalline specimens". *Nature* **400**, 342–344 (1999).
108. Robinson, I. K., Vartanyants, I. A., Williams, G. J., Pfeifer, M. A. & Pitney, J. A. "Reconstruction of the Shapes of Gold Nanocrystals Using Coherent X-Ray Diffraction". *Phys. Rev. Lett.* **87**, 195505 (2001).
109. Gulden, J. et al. "Coherent x-ray imaging of defects in colloidal crystals". *Phys. Rev. B* **81**, 224105 (2010).
110. Shabalin, A. G. et al. "Revealing Three-Dimensional Structure of an Individual Colloidal Crystal Grain by Coherent X-Ray Diffractive Imaging". *Phys. Rev. Lett.* **117**, 138002 (2016).
111. Pabisch, S., Feichtenschlager, B., Kickelbick, G. & Peterlik, H. "Effect of interparticle interactions on size determination of zirconia and silica based systems – A comparison of SAXS, DLS, BET, XRD and TEM". *Chem. Phys. Lett.* **521**, 91–97 (2012).
112. Holger Borchert, *,†,‡ et al. "Determination of Nanocrystal Sizes: A Comparison of TEM, SAXS, and XRD Studies of Highly Monodisperse CoPt₃ Particles". *Langmuir* **21** (5), 1931–1936 (2005).
113. Diroll, B. T. et al. "Quantifying 'Softness' of Organic Coatings on Gold Nanoparticles Using Correlated Small-Angle X-ray and Neutron Scattering". *Nano Lett.* **15**, 8008–8012 (2015).
114. Heitsch, A. T., Patel, R. N., Goodfellow, B. W., Smilgies, D.-M. & Korgel, B. A. "GISAXS Characterization of Order in Hexagonal Monolayers of FePt Nanocrystals". *J. Phys. Chem. C* **114**, 14427–14432 (2010).
115. Lazzari, R. A. "IsGISAXS: a program for grazing-incidence small- angle X-ray scattering analysis of supported islands". *J. Appl. Cryst* **35**, 406–421 (2002).

116. Wang, S. T., Fukuto, M. & Yang, L. "In situ x-ray reflectivity studies on the formation of substrate-supported phospholipid bilayers and monolayers". *Phys. Rev. E* **77**, 31909 (2008).
117. Weygand, M. et al. "Bacterial S-Layer Protein Coupling to Lipids: X-Ray Reflectivity and Grazing Incidence Diffraction Studies". *Biophys. J.* **76**, 458–468 (1999).
118. Mouri, E. et al. "X-Ray Reflectometry Confirms Polymer-Grafted Silica Particle Monolayer Formation at the Air–Water Interface". *J. Nanosci. Nanotechnol.* **9**, 327–333 (2009).
119. Li Destri et al. "The Link Between Self-Assembly and Molecular Conformation of Amphiphilic Block Copolymers Monolayers at the Air/Water Interface: The Spreading Parameter". *Langmuir* **31**, 8856–8864 (2015).



Chapter 3

“Like bees building a honeycomb”

• *Abstract* •

Oriented attachment of synthetic semiconductor nanocrystals is emerging as a route for obtaining new semiconductors that can have Dirac-type electronic bands such as graphene, but also strong spin-orbit coupling. The two-dimensional (2-D) assembly geometry will require both atomic coherence and long-range periodicity of the superlattices. We show how the interfacial self-assembly and oriented attachment of nanocrystals results in 2-D metal chalcogenide semiconductors with a honeycomb superlattice. We present an extensive atomic and nanoscale characterization of these systems using direct imaging and X-ray scattering methods. The honeycomb superlattices are atomically coherent over several nanocrystals and have an octahedral symmetry that is buckled; the nanocrystals occupy two parallel planes. Considerable necking and large-scale atomic motion occurred during the attachment process.

Based on: Long-Range Orientation and Atomic Attachment of Nanocrystals in 2D Honeycomb Superlattices.

Mark P. Boneschanscher, Wiel H. Evers, [Jaco J. Geuchies](#), Thomas Altantzis, Bart Goris, Freddy T. Rabouw, Susan A.P. van Rossum, Herre S. J. van der Zant, Laurens D. A. Siebbeles, Gustaaf van Tendeloo, Ingmar Swart, Jan Hilhorst, Andrei V. Petukhov, Sara Bals, Daniel Vanmaekelbergh

Science **344**, 6190, 1377-1380 (2014)

3.1 - Introduction

Oriented attachment is a process in which two adjacent nanocrystals form a single one, due to an atomically matched bond formation between two specific facets. The oriented attachment of nanocrystals of transition metal (hydro)oxides¹⁻³ and of calcium salts^{4, 5} in aqueous media has been studied in detail, as it is a widespread process in biomineralization. In colloid nanoscience, pre-synthesized nanocrystals with well-defined facets dispersed in organic solvents have been used^{6, 7}. Controlled oriented attachment is currently emerging as a route to form extended one and two-dimensional single-crystalline semiconductors of II-VI and IV-VI compounds⁸⁻¹², which are of interest in opto-electronics.

With truncated nanocubes of the Pb-chalcogenide family, 2-D atomically coherent ultra-thin quantum wells¹¹ as well as superlattices with long-range square or honeycomb nanogeometry¹² were recently reported. The formation of such systems is highly remarkable, as several demanding conditions have to be fulfilled: the nanocrystal building blocks must be nearly monodisperse in size and shape, and attachment should only occur with a geometrically defined subset of nanocrystal facets of one sort. The high degree of atomic and nanoscale order in such systems is far from understood. This is most obvious for extended, atomically coherent PbSe superlattices with honeycomb nanogeometry. In this case, several questions emerge on the large-scale crystallographic orientation of the nanocrystals, the role of surface passivation of specific facets, and the atomic mechanism of attachment.

In this chapter, we present an atomic and nanoscale analysis of atomically coherent PbSe and CdSe honeycomb superlattices. Using High-Angle Annular Dark-Field Scanning Transmission Electron Microscopy (HAADF-STEM) and tomography, we show that the honeycomb structures are buckled, i.e., have nanocrystals occupying two parallel planes, and hence show nanoscale analogy with the atomic silicene honeycomb structure. The specific orientation of the nanocrystals in the 2-D superlattice extends over hundreds of unit cells, suggesting that such types of single crystals must be formed from a pre-ordered state, e.g., at the liquid-air interface. We show that the nanocrystals in the honeycomb structure are considerably elongated in the direction of the nanocrystal-nanocrystal bond, compared to the native building blocks. This points to a bond formation via necking accompanied with a gradual release of the capping molecules and vast atomic motion. Moreover, the 2-D honeycomb structures of PbSe with a rock-salt atomic lattice are robust enough to be transformed into 2-D CdSe lattices with a zinc blende atomic lattice by cation-exchange, keeping the anionic sublattice and the honeycomb nanogeometry intact.

This opens a route to a new class of 2-D semiconductors with tunable composition and bond lengths. In these structures the nanoscale honeycomb geometry has been predicted to result in conduction bands that can be filled with Dirac-type charge carriers as in graphene, with — in contrast to graphene — strong spin-orbit coupling¹³. Such honeycomb semiconductors, with periodicities of <10 nm, cannot be created by conventional top-down methods such as lithography and hold promise for applications in transistor technology.

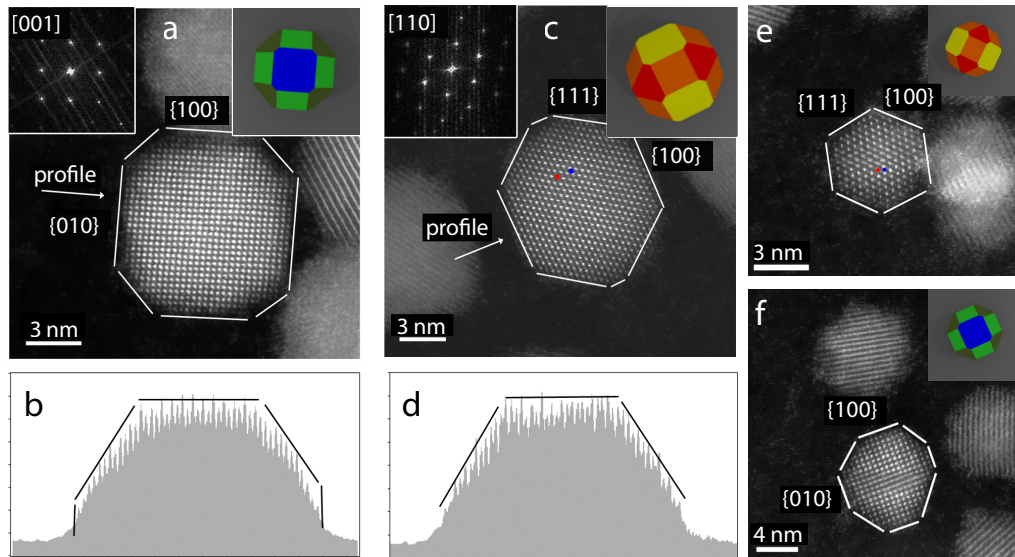


Figure 3.1: High resolution HAADF-STEM images of the individual PbSe nanocrystals. (a) PbSe nanocrystal of roughly 9 nm recorded with a [001] zone axis. (b) Intensity profile along the [010] direction indicated in (a). (c) Similar nanocrystal as displayed in (a), but recorded along the [110] zone-axis direction. (d) Intensity profile along the [100] direction indicated in (c). (e) PbSe nanocrystal with a diameter of 5 nm. (f) Similar nanocrystal as displayed in panel (e). The insets at the left and right top of the images show the Fourier transform of the atomic lattice and a schematic nanocrystal respectively.

3.2 - Results and discussion

We start off by characterizing the building blocks of our to-be superlattices; the PbSe nanocrystals. After their synthesis, they were dropcasted on Cu TEM grids and characterized by aberration corrected HAADF-STEM. Atomically resolved images of single nanocrystals are presented in Fig. 3.1 show a clear presence of {100} and {111} facets (possibly also {110} facets). The micrograph in Fig. 3.1(a) shows a nanocrystal with a [001] zone axis (see also Fig. 3.1(f)), which shape matches very well with the displayed inset on the top-right of a cantellated nanocube. A similar nanocrystal on the same grid is imaged along the [110] zone axis and is shown in Fig. 3.1(b) and 3.1(e). From the intensity profiles in Figs. 3.1(b) and 3.1(d), the facetting of the nanocrystals also becomes apparent. For the continuation of the chapter, we will assume that the nanocrystals indeed have the shape of cantellated cubes.

To synthesize the honeycomb superlattices, a dispersion of nanocrystals in toluene is gently dropcast on an ethylene glycol subphase (see Fig. 3.2(a)), which acts as an immiscible liquid substrate (see Fig. 3.2(b)). The toluene is allowed to evaporate in a nitrogen purged glovebox under ambient pressure, concentrating the nanocrystal solution over time. An hour after the start of the solvent evaporation, a thin nanocrystal film is left behind at the liquid-air interface. This film can be scooped with any desired substrate for further analysis, e.g. highly oriented pyrolytic graphite (HOPG) for STM, a Si(001) wafer for diffraction experiments or a Cu TEM grid for electron microscopy.

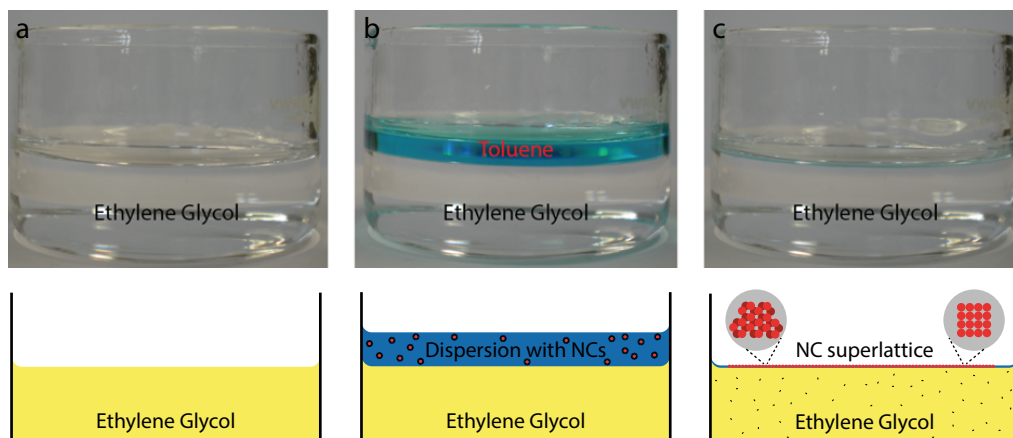


Figure 3.2: Schematic representation of the oriented attachment experiments. (a) The ethylene glycol is placed inside a petri dish, and serves as an immiscible liquid substrate for the nanocrystal containing dispersion. (b) The solution containing the PbSe nanocrystals (often toluene or hexane) is placed on top of the ethylene glycol. The volatile solvent is allowed to gently evaporate over the course of roughly an hour. (c) After the solvent of the nanocrystals has evaporated, the nanocrystal superlattice floats as a thin film on top of the ethylene glycol at the liquid-gas interface. The resulting superlattice can be scooped off the liquid with any desired substrate, e.g. a TEM grid or a graphite substrate for scanning-probe microscopy experiments.

Figure 3.3 presents the honeycomb structure obtained by oriented attachment of PbSe nanocrystal building blocks [12]. The initial building blocks have the shape of a cantellated cube, approaching that of a rhombicuboctahedron. As discussed above, this implies that the nanoparticle is terminated with $\{100\}$, $\{110\}$, and $\{111\}$ facets. To estimate the nanoparticle size we determined the radially averaged diameter of the TEM projections, and found this to be 5.4 ± 0.4 nm. The oriented attachment of these nanoparticles results in structures with long range periodicity, as visualized by means of an equilateral triangle spanning the same number of unit cells at each vertex in the HAADF-STEM image, shown in Fig. 3.3(a). This is also confirmed by taking the Fourier transform of the micrograph, which is displayed as an inset to the figure. Zooming in on the honeycomb structure in Fig. 3.3(b) reveals that the $\langle 111 \rangle$ axes of the nanocrystals are perpendicular to the substrate, and that the $\langle 110 \rangle$ axes are perpendicular to the nanocrystal-nanocrystal bonds. This is also corroborated by the recorded electron diffraction (ED) patterns, displayed in Fig. 3.3(c). Furthermore the structures have a high degree of crystallinity, as observed by the occurrence of sharp spots in ED patterns recorded on selected areas with a diameter of 200 nm.

In the trigonal model the attachment takes place via the $\{110\}$ facets, meaning that it has the $\langle 110 \rangle$ axes parallel to the nanocrystal bonds. However, both the high resolution HAADF-STEM images and the electron diffraction patterns show that in our experiment the $\langle 110 \rangle$ axes are perpendicular to the nanocrystal bonds. This allows us to discard the trigonal model. Another indication is found in the buckling of the honeycomb: in the HAADF-STEM images we sometimes observe additional scattering strength on the nanocrystal bonds, indicating a larger than average thickness of the sample at that position. However, both the tetrahedral and octahedral model are buckled and have the $\langle 110 \rangle$ nanocrystal axes perpendicular to the nanocrystal bonds, making it impossible to discriminate between the two by electron diffraction or the 2-D projections from

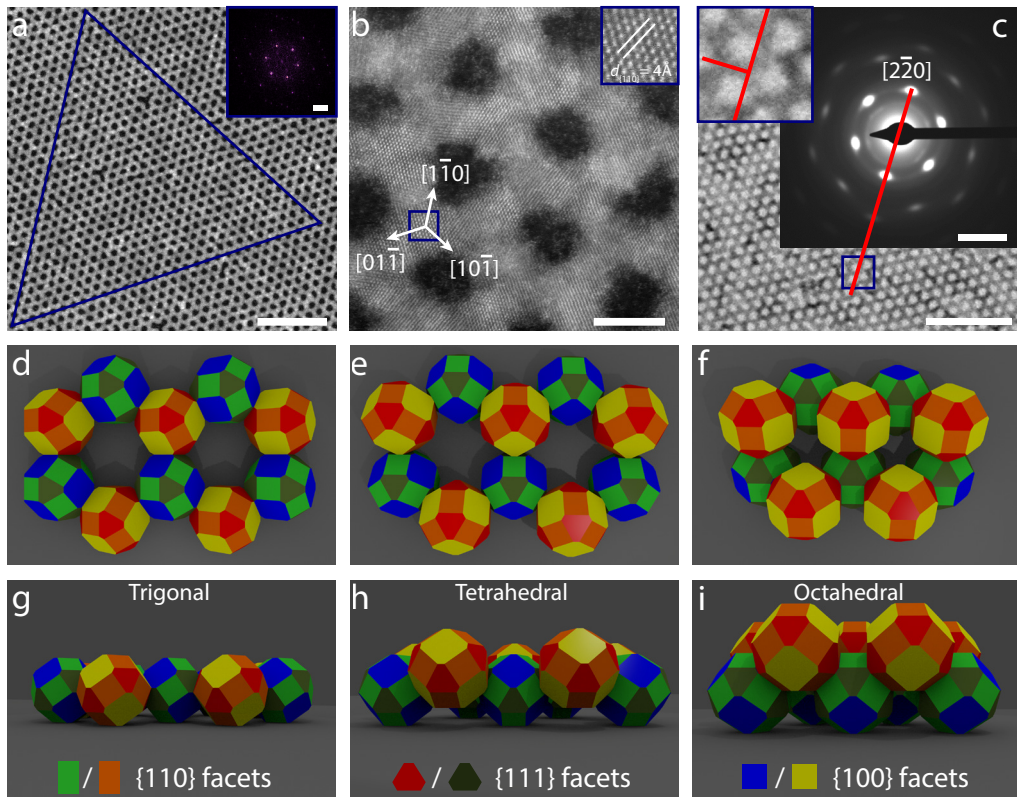


Figure 3.3: Honeycomb superlattices made from PbSe nanocrystals. (a) HAADF-STEM image of the honeycomb superlattice. The equilateral triangle and the Fourier transform of the image show the long-range order of the structure. (b) High resolution HAADF-STEM image, showing that the nanocrystals inside the superlattice have the $[111]$ axis perpendicular to the plane of the superlattice and have their $\langle 1\bar{1}0 \rangle$ axes perpendicular to the nanocrystal bonds. (c) Bright-field TEM image and corresponding electron diffraction pattern. The electron diffraction pattern shows not only the orientation of the individual nanocrystals within the superlattice, but also their orientation with respect to the honeycomb periodicity of the lattice (red line and inset), which confirms that the $\langle 1\bar{1}0 \rangle$ axes are perpendicular to the nanocrystal bonds. (d,g) Top and sideview of the trigonal honeycomb model, in which the nanocrystals attach with their $\{110\}$ facets, their bond angles are 120° and all nanocrystals are in the same plane of height. (e,h) Top and sideview of the tetrahedral honeycomb model, in which the nanocrystals attach with their $\{111\}$ facets, their bond angles are 109.5° and the superlattice is buckled. (f,i) Top and sideview of the octahedral honeycomb model, in which the nanocrystals attach with their $\{100\}$ facets, their bond angles are 90° and the superlattice is buckled.

high resolution HAADF-STEM. Distinguishing which of the two models is correct is key to understanding the oriented attachment process, since it will shed light on which facet is reactive and eventually attaches during the synthesis. Based on the analyses presented so far, we are not able to resolve which of the two structures is correct.

Defects are also present on both the atomic and nanocrystal length scales. Several point defects are observed in Fig. 3.3(a), not uncommon to the atomic graphene. A larger ‘footprint’ like defect is presented in the methods section (Fig. 3.9). The defects seem to not hamper the long-range periodicity of the superlattice however. Also in the atomically resolved image in Fig. 3.3(b) we see that not all nanocrystals have their $[111]$ axis perfectly perpendicular to the electron beam,

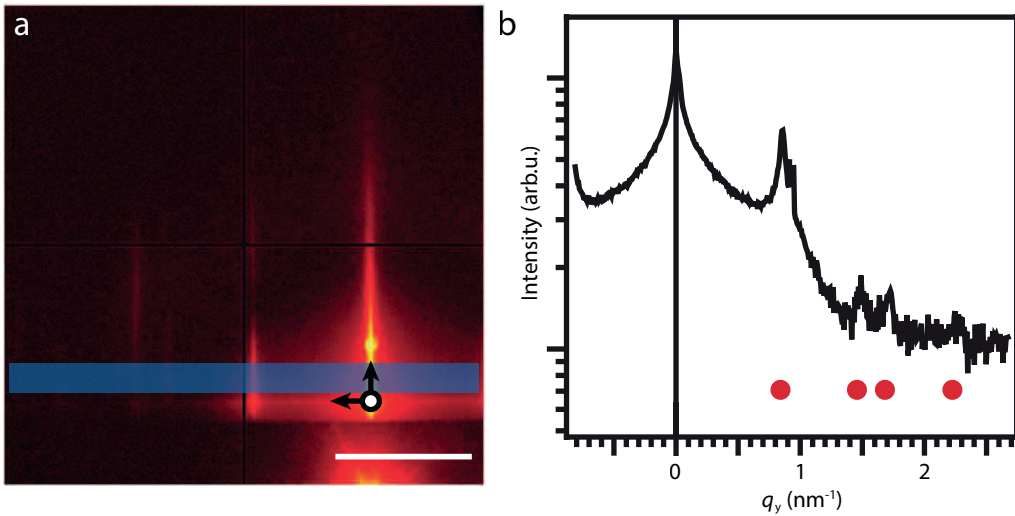


Figure 3.4: Grazing-incidence small-angle X-ray scattering pattern on the honeycomb superlattice (a) GISAXS pattern of a honeycomb superlattice on a Si(100) substrate. (b) Intensity trace along the horizontal scattering direction indicated by the blue shaded region in . The positions of the scattering rods in the horizontal scattering direction q_y , with relative positions of $1:\sqrt{3}:2:\sqrt{7}$ (indicated with red dots), are characteristic of hexagonal symmetry in the lattice, but do not confirm or exclude the presence of buckling within the superlattice. The scalebar in (a) denotes 1 nm^{-1} .

indicating that the nanocrystals show some form of rotational disorder. These defects could hamper the transport of charge carriers in these materials.

The grazing-incidence small-angle X-ray scattering (GISAXS) pattern of a PbSe honeycomb superlattice on a Si(100) substrate is presented in figure 3.4(a). As the X-ray beam is spread out over a large surface on the substrate, we probe a large area of the superlattice and can obtain statistically valid information. The scattering rods are indicative for a 2-D structure. The scattering pattern is integrated in the q_z direction and the intensity trace is presented in figure 3.4(b). The position of these scattering rods in the horizontal scattering direction, q_y , are 0.85 nm^{-1} , 1.48 nm^{-1} , 1.71 nm^{-1} and 2.26 nm^{-1} follow the characteristic $1:\sqrt{3}:2:\sqrt{7}$ trend, indicative of hexagonal symmetry within the superlattice (consistent with scattering on the hexagonal array of holes in the honeycomb superlattice). The peak position of the first scattering rod is used to determine the hole-to-hole distance inside the honeycomb lattice, and is equal to 8.5 nm . Out-of-plane information on the honeycomb superlattice can be in principle obtained from the scattering pattern, by looking at the intensity of the scattering rods in the q_z direction, however this analysis is not conclusive on the exact structure of the honeycomb superlattice.

Scanning tunneling microscopy measurements were performed using an Omicron LT-STM at temperatures $< 4.5 \text{ K}$ and a base pressure $< 10^{-10} \text{ mbar}$. The as-prepared honeycomb samples were placed on a HOPG substrate. To further facilitate the imaging, the samples were annealed in the UHV chamber at temperatures of $100 \text{ }^\circ\text{C}$ for > 24 hours. Topographic measurements were performed in current-feedback mode using cut PtIr tips at typical feedback settings of 3.5 V and 20 pA . Depending on the sharpness of the tip we were able to resolve all nanocrystals in the honeycomb structure, e.g. like in figure 3.5(a).

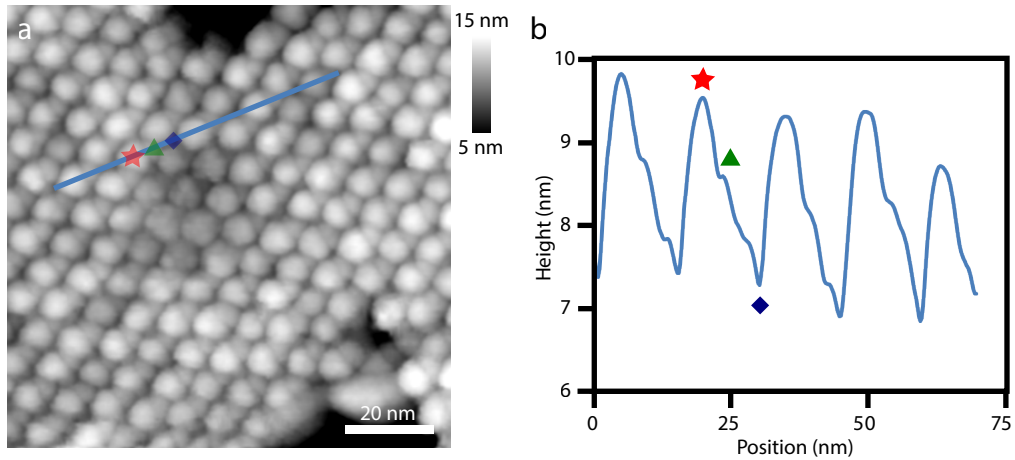


Figure 3.5: Scanning tunneling microscopy on the honeycomb superlattice (a) STM topography showing the higher (red star) and lower (green triangle) nanocrystals inside the buckled honeycomb superlattice. (b) Height profile along the blue line in (a).

The high degree of buckling is immediately apparent in the STM topographic images, which is displayed in a linetrace in figure 3.5(b). However, it is not possible to give a quantitative measure for the difference in nanocrystal height, since the tip sharpness largely determines the height at which we see the different nanocrystals. When the tip radius is comparable to, or lower than, the nanocrystal radius, the tip is able to resolve the nanoparticles in the lower lying sublattice. When the tip radius is larger than the nanocrystal radius, only nanocrystals from the top sublattice will be visible. Nonetheless, we can extract bond lengths and next-nearest neighbor bond lengths from the STM images. Here, we find bond lengths of 6.1 ± 0.3 nm and next-nearest neighbor bond lengths of 8.5 ± 0.8 nm, which compares well to the value obtained from GISAXS. Both methods do not directly prove whether the honeycomb superlattice has the octahedral or tetrahedral structure.

The full three-dimensional structure of the honeycomb superlattice is resolved through electron tomography. In figure 3.6 the data for the PbSe honeycomb superlattice is presented. Fig. 3.6(a) shows the tomogram, which is integrated in the direction perpendicular to the substrate. Two orthoslices, which are taken in different directions in the superlattice, are shown in Fig. 3.6(b) and 3.6(c). They clearly show the buckling of the honeycomb lattice, where each neighbouring nanocrystal occupies positions at a different height. An isovolume rendering is made (see Fig. 3.6(d)) and automated particle detection is applied to determine the coordinates of the constituent nanocrystals (Fig. 3.6(e)). From the particle coordinates, parameters such as bond angle (Fig. 3.6(f)), bond length (Fig. 3.6(g)) and NNN bond length (Fig. 3.6(h)) could be extracted.

The obtained bond angle of $95 \pm 5^\circ$ proves that the honeycomb superlattice has an octahedral structure and the facets that are epitaxially connected are the $\{100\}$ facets. The obtained bond length of 6.0 ± 0.5 nm and NNN bond length of 8.9 ± 0.6 match again well with the GISAXS and STM measurements. Furthermore the ratio between the bond length and the NNN bond length is 1:1.48, slightly higher than the expected value for an octahedral lattice ($1:\sqrt{2}$, compared to $1:\sqrt{8/3}$ for the tetrahedral lattice and $1:\sqrt{3}$ for the trigonal lattice), which is in agreement with the

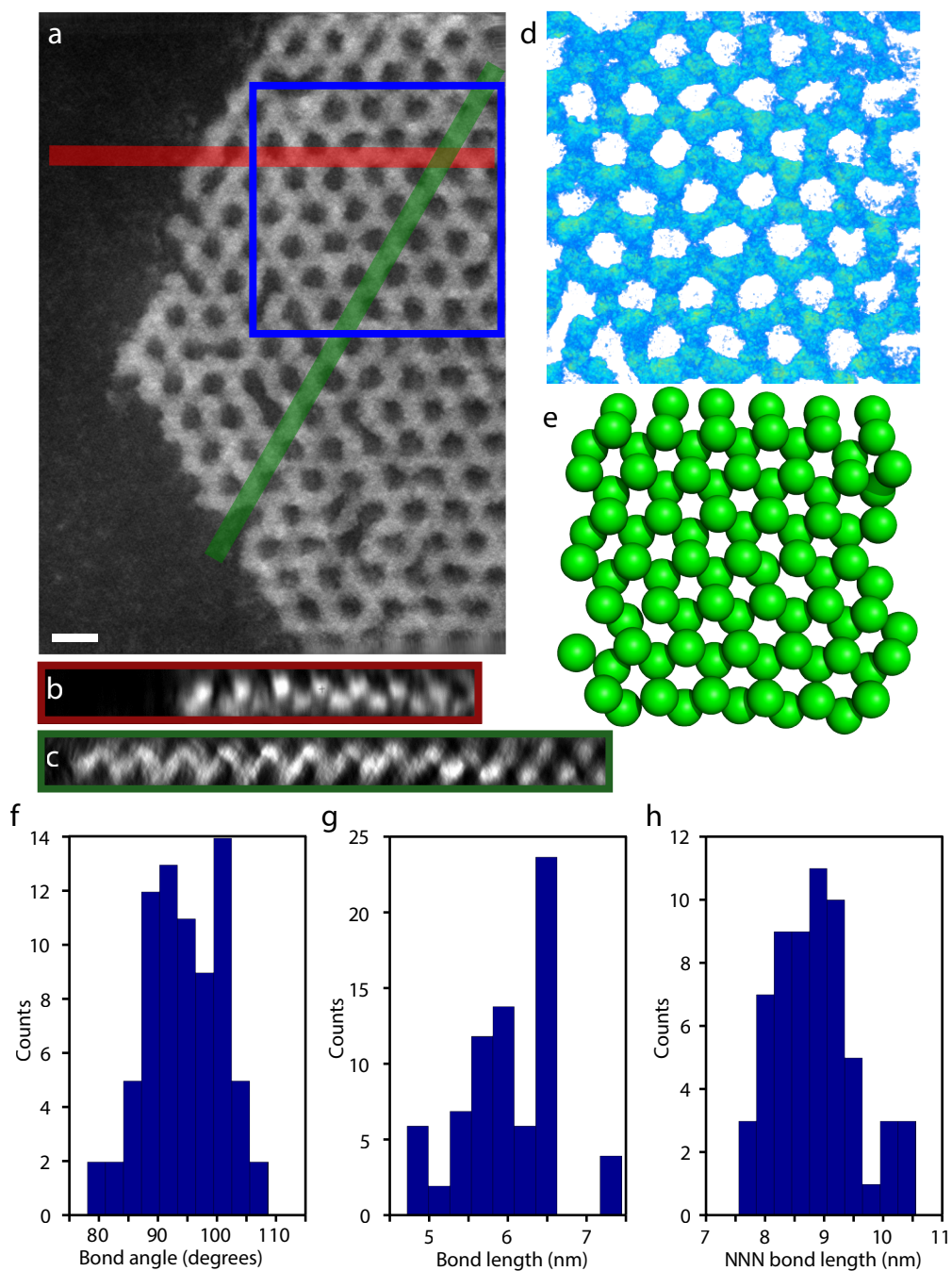


Figure 3.6: HAADF-STEM tomography on a PbSe honeycomb superlattice (a) Integrated tomogram along the direction perpendicular to the superlattice plane. (b,c) Orthoslices through the tomogram along the lines indicated in (a). (d) Isovolume rendering of the blue region in (a). (e) Results of the automated particle detection performed on the same region as in (d). From the detected particle coordinates, the NC-NC bond angle (f), bond length (g) and next-nearest neighbour bond length (h) were determined. The scalebar denotes 5 nm.

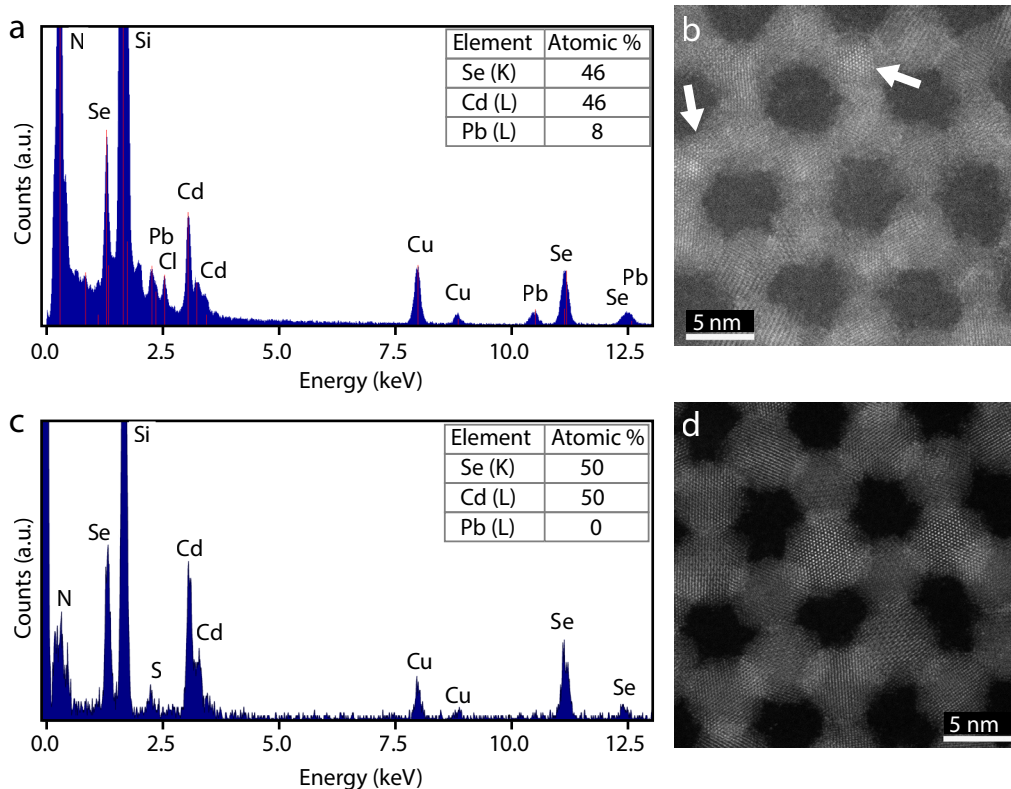


Figure 3.7: Cation exchange from PbSe to CdSe honeycomb superlattices. (a) EDS spectrum of a partially exchanged Pb/Cd-Se superlattice. (b) The HAADF-STEM image corresponding to the sample in (a). Note the core-shell PbSe/CdSe structure. (c) EDS spectrum of a fully exchanged CdSe honeycomb superlattice, showing a 1:1 ratio of Cd:Se and an absent, or non-detectable, amount of Pb. (d) HAADF-STEM image of the sample shown in (c), showing a lack of PbSe cores.

bond-angle being slightly higher than 90° . Furthermore the ratio between the bond length and the NNN bond length is 1:1.48, slightly higher than the expected value for an octahedral lattice ($1:\sqrt{2}$, compared to $1:\sqrt{8/3}$ for the tetrahedral lattice and $1:\sqrt{3}$ for the trigonal lattice), which is in agreement with the bond-angle being slightly higher than 90° .

The measured bond length of 6.0 ± 0.5 nm is 11% larger than the initial nanocrystal size of 5.4 ± 0.4 nm. Li et al.³ showed that their iron oxyhydroxide nanocrystals are under continuous rotation and translation through Brownian motion in solution, until they are perfectly aligned with their neighbour's atomic lattice. It is only then that there is a sudden snap to contact over less than 1 nm, where there is a large scale movement of surface atoms towards the contact point to form a rigid bond in between the nanocrystals. We propose that, during oriented attachment process described here, after the nanocrystals aligned their atomic lattices, there is atomic scale necking as a first step in the attachment. The capping molecules, still present on the $\{100\}$ facets, are gradually released, and the surface atoms of the nanocrystal move to extend the neck in the direction perpendicular to the bond axis. This results also in the more open honeycomb superlattice we observe, different from the more closed models based on a direct 'click' between

opposing {100} facets.

In the mechanism we propose, not all capping molecules have to be released simultaneously from one facet, allowing for attachment pathways with lower activation energies. The proposed neck formation during the attachment process has been proposed before for the growth of several metallic nanoparticles^{20,21}.

Since the emergence of graphene²⁴, there has been a lot of interest in the electronic properties of charge carriers confined into a honeycomb lattice²⁵⁻²⁹. As an example, through recent developments in molecule manipulation an STM, a molecular graphene lattice has been created by confining the electrons of the Cu(111) surface state into a honeycomb lattice by creating an hexagonal lattice of well positioned CO molecules²⁵. For the structures we have synthesized in this work, Dirac-type conduction bands and valence bands are predicted for honeycomb lattices of CdSe¹³, while the bandgap remains close to that of a CdSe quantum well. We show that we are able to transform the rock-salt PbSe honeycombs superlattice into zinc blende CdSe through a cation-exchange reaction, preserving the orientation of the Se anion sublattice. This is in line with earlier work on similar types of cation exchange, where the anionic sublattice was preserved during the reaction^{32,33}. The results for the cation exchange are presented in Fig. 3.7.

We first attempt to visualize the cation exchange reaction, by performing partial cation exchange. Here the sample was only heated to 110°C for 45 minutes. Fig. 3.7(a) shows the spectrum obtained with energy-dispersive X-ray spectroscopy (EDS). The Pb-to-Cd exchange starts on the surface, as can be seen by the observed boundary between the PbSe cores and the CdSe shells in Fig 3.7(b). Upon full cation exchange we obtain a Cd:Se ratio of 1:1, as shown in the EDS spectrum in Fig. 3.7(c), where the amount of Pb is below the detection level (<1%). The observed Cu signal in both EDS spectra originates from the TEM grid holder. The HAADF-STEM image of the fully exchanged sample in Fig. 3.7(d) shows that the orientation of the Se sublattice with respect to the honeycomb nanogeometry is conserved, demonstrating the success of the cation exchange reaction and the preservation of the atomic coherency of the nanocrystals. The rigidity of the lattice is also shown in tomography experiments on the CdSe honeycomb superlattice, presented in Fig. 3.8, where the bond angles and bond lengths are similar to the PbSe superlattice.

3.3 - Conclusions and outlook

In this chapter we have provided a general route to the formation of atomically coherent honeycomb structures of different chemical constituents with a periodicity in the range of 5–10 nm. We have studied the honeycomb structure obtained by oriented attachment of PbSe in detail, using various atomic and nanoscale characterization techniques. We have shown that these PbSe honeycomb structures have an octahedral symmetry, resulting in a buckled structure similar to silicene. Furthermore, we have proven that neck-formation plays an important role in the oriented attachment of these structures. Finally, we have shown the general applicability of our approach, by combining the oriented attachment with cation exchange to prepare CdSe honeycomb structures with a zinc blende atomic structure. This opens up a route to new nanomaterial structures with tailored opto-electronic properties, currently not available through top-down techniques such as lithography.

3.4 - Methods

Nanocrystal synthesis. As a starting material for the oriented attachment, PbSe nanocrystals were prepared using the method described by Steckel et al. (28). The synthesis was performed in a water and oxygen free environment. (a) 1.54 g of lead acetate trihydrate (99.999% Aldrich), 3.34 g of oleic acid (OA, 90% Aldrich) and 12.86 g octadecene (ODE, 90% Aldrich) were heated to 130 °C under low pressure (10-3 bar) for ~3 hours. (b) A second mixture containing 1.12 g Se (99.999% Alfa Aesar), 14.87 mL trioctylphosphine (TOP, 90% Fluka) and 0.13 mL diphenylphosphine (DPP, 98% Aldrich) was prepared by dissolving the Se. Subsequently solution (a) was heated in a three-necked round-bottom flask to 180 °C and solution (b) was injected into solution (a). The reaction mixture was kept at a constant temperature of 150 °C. After 40 seconds the reaction mixture was quenched with 20 mL butanol. The crude synthesis mixtures were washed twice by precipitation with methanol, centrifugation and redispersion of the sediment in toluene.

Oriented attachment of the PbSe nanocrystals. Single crystal thin films of PbSe with a nanoscale honeycomb geometry were prepared by oriented attachment, in a method adapted from the one reported previously (5). A glass petri-dish (Ø 27 mm) was filled with 6.5 mL of ethylene glycol. Then a volume of 350 µL of the nanocrystal suspension with an initial concentration of 1.76×10^{-7} mol/L was placed on top of the ethylene glycol solution. The ethylene glycol serves as an immiscible liquid substrate for the nanocrystal solution. Then the solvent was allowed to evaporate, as depicted in Fig. 3.2. Subsequently the liquid was heated to 30-80 °C for 15 minutes to anneal the sample and improve attachment. After annealing a sample was taken from the ethylene glycol layer at the center of the petri-dish and placed under vacuum to evaporate the residual ethylene glycol. All experiments were performed in a nitrogen purged glove box (oxygen and water concentration <1 ppm).

In order to obtain honeycomb lattices with about 70% yield, the external parameters have to be fine-tuned: the temperature has to be roughly 20°C; the nanocrystal concentration once the suspension is drop casted on the glycol substrate present in the petri-dish is 1×10^{-11} mol \times cm $^{-2}$ (± 5 %). In the monolayer films the honeycomb structures are predominant and can extend over several micrometers. In some cases, however, ordered linear and/or square structures are also observed. The structures typically have some defects, such as the missing nanocrystals and bonds, as can be seen in Fig. 3.3, similar to the vacancies or missing bonds that are often observed in freestanding graphene.

Electron microscopy and tomography. Nanocrystals and honeycombs were imaged using both bright field TEM and HAADF-STEM. The conventional TEM images were obtained using a FEI Tecnai 12, FEI Tecnai 20, and a Philips CM30T microscope. The HAADF-STEM and measurements were performed using a double aberration corrected FEI TITAN operated at 300 kV. The semi convergence angle of the electron probe used during acquisition was 21.4 mrad. Both electron tomography series were acquired in HAADF-STEM mode using a double aberration corrected cubed FEI Titan 50-80 electron microscope operated at 300 kV. For the acquisition of the PbSe series we used a tilt range from -50 to +56 and an increment of 2 degrees, and for the CdSe sample a tilt range from -64 to +60 and increment of 2 degrees. A Fischione model 2040 tilt rotation holder was used for the acquisition of both tilt series. The reconstruction of the tilt series was performed using the Simultaneous Iterative Reconstruction Technique (SIRT) as implemented in Inspect 3D software.

Scanning tunneling microscopy. Scanning tunneling microscopy measurements were performed using an Omicron LT-STM at temperatures < 4.5 K and a base pressure < 10^{-10} mbar. The as-prepared honeycomb samples were placed on a highly-oriented pyrolytic graphite (HOPG) substrate. To facilitate the imaging the samples were annealed in the UHV chamber at temperatures of ~100 °C for 24 hours. Topographic measurements were performed in current-feedback mode using cut PtIr tips at typical feedback settings of 3.5 V and 20 pA.

GISAXS measurements. GISAXS patterns were recorded at beamline ID01 at the European Synchrotron Radiation Facility in Grenoble. We used an x-ray beam with an energy of 9 keV incident at a grazing angle of 0.7 degrees. The scattered intensity was recorded by a Maxipix single photon counting detector, consisting of four chips of 256 \times 256 pixels each with a pixel size of 55 \times 55 µm 2 . The superlattices were scooped on a Si(001) wafer.

Cation exchange of the honeycomb superlattice. The conversion of the rock-salt PbSe honeycomb structures into zinc blende CdSe honeycomb structures was done by placing the PbSe sheet on a substrate (SiN TEM-grid), which was then immersed in a 0.1 mol/L Cd-oleate solution in 1-octadecene and heated to 150 °C for 1 hour. Subsequently the solution was heated to 170 °C for 15 minutes. Finally, the substrate was cleaned several times by immersion in toluene, methanol/butanol (1:2) and methanol.

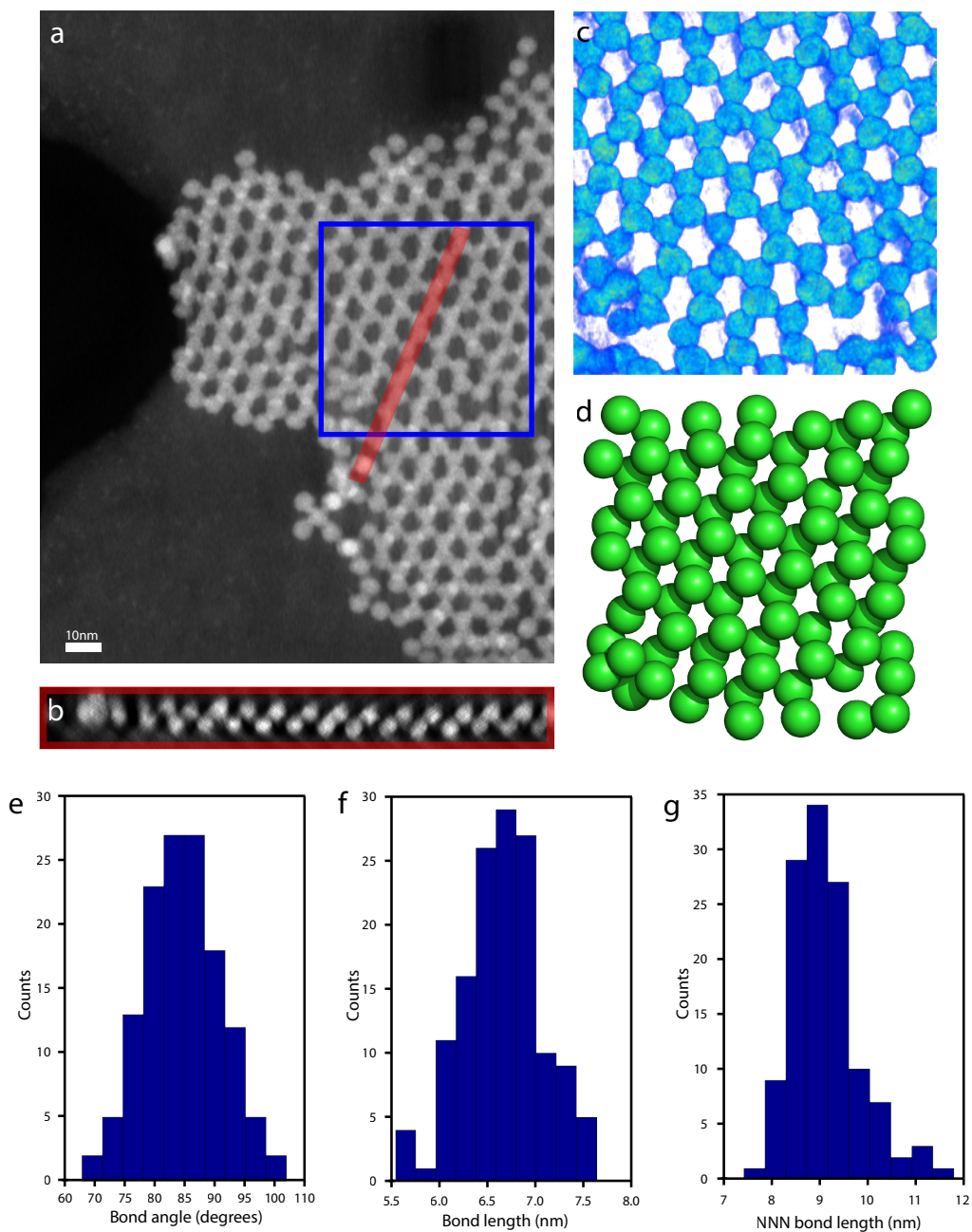


Figure 3.8: HAADF-STEM tomography on a CdSe honeycomb superlattice (a) Integrated tomogram along the direction perpendicular to the superlattice plane. (b) Orthoslice through the tomogram along the lines indicated in (a). (c) Isovolume rendering of the blue region in (a). (d) Results of the automated particle detection performed on the same region as in (d). From the detected particle coordinates, the NC-NC bond angle (e), bond length (f) and next-nearest neighbor bond length (g) were determined.

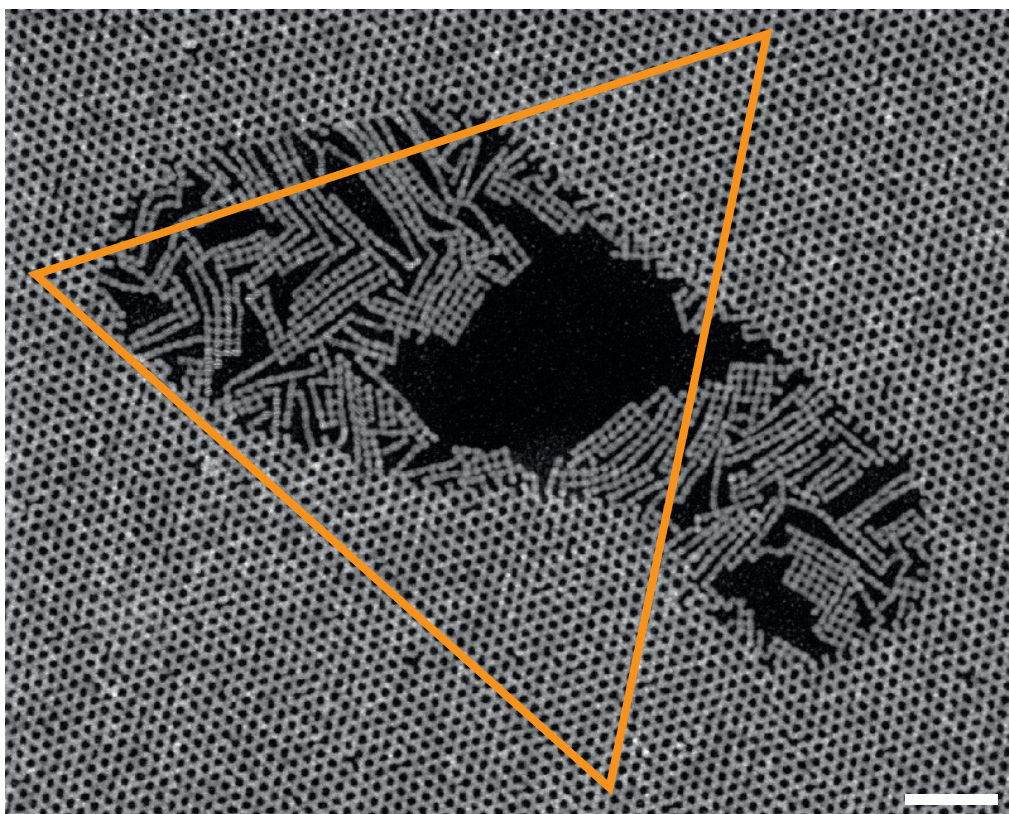


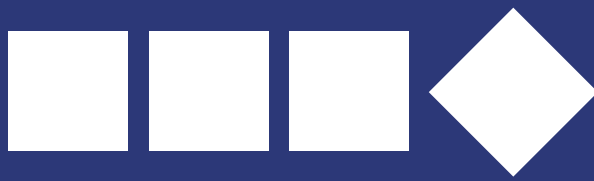
Figure 3.9: HAADF-STEM image of a large ‘footprint’ defect inside a PbSe honeycomb superlattice. The displayed equilateral triangle shows that the periodicity of the superlattice is conserved over the defect. Several smaller point defects, i.e. missing nanocrystals inside the superlattice, can also be observed. The scalebar equals 50 nm.

3

References

1. Penn, R. L. & Banfield, J. F. “Imperfect Oriented Attachment: Dislocation Generation in Defect-Free Nanocrystals”. *Science* (80-.). **281**, (1998).
2. Banfield, J. F. “Aggregation-Based Crystal Growth and Microstructure Development in Natural Iron Oxyhydroxide Biomineralization Products”. *Science* (80-.). **289**, 751–754 (2000).
3. Li, D. et al. “Direction-specific interactions control crystal growth by oriented attachment”. *Science* **336**, 1014–8 (2012).
4. Pouget, E. M. et al. “The Initial Stages of Template-Controlled CaCO₃ Formation Revealed by Cryo-TEM”. *Science* (80-.). **323**, (2009).
5. Dey, A. et al. “The role of prenucleation clusters in surface-induced calcium phosphate crystallization”. *Nat. Mater.* **9**, 1010–1014 (2010).
6. Zhang, J. et al. “Progress of nanocrystalline growth kinetics based on oriented attachment”. *Nanoscale* **2**, 18–34 (2010).
7. Niederberger, M. et al. “Oriented attachment and mesocrystals: Non-classical crystallization mechanisms based on nanoparticle assembly”. *Phys. Chem. Chem. Phys.* **8**, 3271–3287 (2006).
8. Pacholski, C., Kornowski, A. & Weller, H. “Self-assembly of ZnO: from nanodots to nanorods”. *Angew. Chem. Int. Ed. Engl.* **41**, 1188–91 (2002).

9. Cho, K.-S., Talapin, D. V, Gaschler, W. & Murray, C. B. "Designing PbSe nanowires and nanorings through oriented attachment of nanoparticles". *J. Am. Chem. Soc.* **127**, 7140–7 (2005).
10. Koh, W., Bartnik, A. C., Wise, F. W. & Murray, C. B. "Synthesis of Monodisperse PbSe Nanorods: A Case for Oriented Attachment". *J. Am. Chem. Soc.* **132**, 3909–3913 (2010).
11. Schliehe, C. et al. "Ultrathin PbS sheets by two-dimensional oriented attachment". *Science* **329**, 550–3 (2010).
12. Evers, W. H. et al. "Low-dimensional semiconductor superlattices formed by geometric control over nanocrystal attachment". *Nano Lett.* **13**, 2317–23 (2013).
13. Kalesaki, E. et al. "Dirac Cones, Topological Edge States, and Nontrivial Flat Bands in Two-Dimensional Semiconductors with a Honeycomb Nanogeometry". *Phys. Rev. X* **4**, 11010 (2014).
14. Steckel, J. S., Yen, B. K. H., Oertel, D. C. & Bawendi, M. G. "On the mechanism of lead chalcogenide nanocrystal formation". *J. Am. Chem. Soc.* **128**, 13032–3 (2006).
15. Friedrich, H. et al. "Quantitative Structural Analysis of Binary Nanocrystal Superlattices by Electron Tomography". *Nano Lett.* **9**, 2719–2724 (2009).
16. Boneschanscher, M. P. et al. "Electron tomography resolves a novel crystal structure in a binary nanocrystal superlattice". *Nano Lett.* **13**, 1312–6 (2013).
17. Midgley, P. A. & Weyland, M. "3D electron microscopy in the physical sciences: the development of Z-contrast and EFTEM tomography". *Ultramicroscopy* **96**, 413–431 (2003).
18. van Huis, M. A. et al. "Low-Temperature Nanocrystal Unification through Rotations and Relaxations Probed by in Situ Transmission Electron Microscopy". *Nano Lett.* **8**, 3959–3963 (2008).
19. van Huis, M. A. et al. "Atomic Imaging of Phase Transitions and Morphology Transformations in Nanocrystals". *Adv. Mater.* **21**, 4992–4995 (2009).
20. Yuk, J. M. et al. "High-Resolution EM of Colloidal Nanocrystal Growth Using Graphene Liquid Cells". *Science* (80-.). **336**, 61–64 (2012).
21. Yuk, J. M. et al. "In situ atomic imaging of coalescence of Au nanoparticles on graphene: rotation and grain boundary migration". *Chem. Commun.* **49**, 11479 (2013).
22. Luther, J. M., Zheng, H., Sadtler, B. & Alivisatos, A. P. "Synthesis of PbS Nanorods and Other Ionic Nanocrystals of Complex Morphology by Sequential Cation Exchange Reactions". *J. Am. Chem. Soc.* **131**, 16851–16857 (2009).
23. Beberwyck, B. J., Surendranath, Y. & Alivisatos, a. P. "Cation Exchange: A Versatile Tool for Nanomaterials Synthesis". *J. Phys. Chem. C* **117**, 19759–19770 (2013).
24. Castro Neto, A. H., Guinea, F., Peres, N. M. R., Novoselov, K. S. & Geim, A. K. "The electronic properties of graphene". *Rev. Mod. Phys.* **81**, 109–162 (2009).
25. Gomes, K. K., Mar, W., Ko, W., Guinea, F. & Manoharan, H. C. "Designer Dirac fermions and topological phases in molecular graphene". *Nature* **483**, 306–310 (2012).
26. De Simoni, G. et al. "Delocalized-localized transition in a semiconductor two-dimensional honeycomb lattice". *Appl. Phys. Lett.* **97**, 132113 (2010).
27. Gibertini, M. et al. "Engineering artificial graphene in a two-dimensional electron gas". *Phys. Rev. B* **79**, 241406 (2009).
28. Park, C.-H., Yang, L., Son, Y.-W., Cohen, M. L. & Louie, S. G. "New Generation of Massless Dirac Fermions in Graphene under External Periodic Potentials". *Phys. Rev. Lett.* **101**, 126804 (2008).
29. Park, C.-H. & Louie, S. G. "Making Massless Dirac Fermions from a Patterned Two-Dimensional Electron Gas". *Nano Lett.* **9**, 1793–1797 (2009).
30. Nádvořník, L. et al. "From laterally modulated two-dimensional electron gas towards artificial graphene". *New J. Phys.* **14**, 53002 (2012).
31. Sushkov, O. P. & Castro Neto, A. H. "Topological Insulating States in Laterally Patterned Ordinary Semiconductors". *Phys. Rev. Lett.* **110**, 186601 (2013).
32. Bals, S. et al. "Three-Dimensional Atomic Imaging of Colloidal Core-Shell Nanocrystals". *Nano Lett.* **11**, 3420–3424 (2011).
33. Casavola, M. et al. "Anisotropic Cation Exchange in PbSe/CdSe Core/Shell Nanocrystals of Different Geometry". *Chem. Mater.* **24**, 294–302 (2012).



Chapter 4

“Nanocrystals in motion”

• *Abstract* •

Oriented attachment of PbSe nanocubes can result in the formation of two-dimensional (2-D) superstructures with long-range nanoscale and atomic order^{1,2}. This questions the applicability of classic models in which the superlattice grows by first forming a nucleus, followed by sequential irreversible attachment of nanocrystals^{3,4}, as one misaligned attachment would disrupt the 2D order beyond repair. Here, we demonstrate the formation mechanism of 2-D PbSe superstructures with square geometry by using in-situ grazing-incidence X-ray scattering (small-angle and wide-angle), ex-situ electron microscopy, and Monte Carlo simulations. We observed nanocrystal adsorption at the liquid/gas interface, followed by the formation of a hexagonal nanocrystal monolayer. The hexagonal geometry transforms gradually through a pseudo-hexagonal phase into a phase with square order, driven by attractive interactions between the {100} planes perpendicular to the liquid substrate, which maximize facet-to-facet overlap. The nanocrystals then attach atomically via a necking process, resulting in 2-D square superlattices.

Based on: In-situ Study of the Formation Mechanism of Two-Dimensional Superlattices from Nanocrystals.

Jaco J. Geuchies, Carlo van Overbeek, Wiel H. Evers, Anjan. P. Gantapara, Freddy T. Rabouw, Jan Hilhorst, Joep L. Peters, Oleg Kononov, Andrei V. Petukhov, Marjolein Dijkstra, Laurens D.A. Siebbeles, D. Vanmaekelbergh.

Nature Materials 15 (12), 1248-1254 (2016)

4.1 - Introduction

Oriented atomic attachment of colloidal nanocrystals (NCs), i.e. the formation of a single crystal by atomic connection of smaller crystals, is an important process in geology⁵⁻⁸, and recently gained much attention as a preparation tool in semiconductor nanoscience^{9,10}. We reported a method to prepare 2-dimensional atomically coherent PbSe superlattices, starting from a suspension of PbSe NCs^{1,2}. The NCs have the shape of a truncated cube, consistent with the rock salt crystal structure of PbSe (see Fig. 4.1(a)). A suspension of these NCs is cast onto a surface of an immiscible liquid, ethylene glycol, and the solvent is evaporated at room temperature. During the evaporation, extended sheets are formed with a thickness of one NC monolayer¹.

The 2-D structure shows a nanoscale geometry with square periodicity with, to some extent, also atomic coherency. In this so-called square geometry, all NCs are directed with a $\langle 100 \rangle$ axis perpendicular to the 2-D plane, and are laterally connected via the in-plane $\{100\}$ facets. This means that two out of six $\{100\}$ facets, namely those at the top and the bottom of the 2-D sheet, are not used for attachment.

Nanocrystal self-assembly and atomic attachment forms a unique route to prepare 2-D semiconductors with a superimposed geometry on the nanometer scale that influences the band structure and can result in semiconductors with Dirac-type valence and conduction bands and high charge carrier mobility¹⁰⁻¹⁴. Although superlattices with a square geometry are slightly disordered on the atomic scale, they show amazing long-range ordering on the nano-scale. A better understanding of the formation process is required for further progress in the synthesis of these systems. The 2-D long-range ordering cannot be explained in terms of the classic nucleation and growth model^{3,4}. In this model the interactions between a crystal (nucleus) and building blocks are supposed to be relatively weak, in the order of a few $k_B T$. As a result, the building blocks can bind and unbind to an existing crystal, until the optimal binding geometry is found, resulting in ordering over long distances. In the case of superlattice formation by oriented attachment of NCs this mechanism cannot be operative, because per NC-NC connection, chemical bonds are formed between tens of atoms on opposing crystal facets. The corresponding energy change is orders of magnitude larger than the thermal energy, and oriented attachment should therefore be irreversible. Thus “incorrect” irreversible attachments should lead to disruption of the long-range nanoscale order in the superlattice.

Here, we present a real-time study of the growth of 2-D superlattices with a square periodicity. We monitor the reactive self-assembly in real time and in-situ by simultaneous grazing-incidence small-angle and wide-angle X-ray scattering (GISAXS and GIWAXS), see Fig. 4.1(b). Moreover, we scoop the structures formed at different stages of the process for analysis with ex-situ Transmission Electron Microscopy (TEM). Previous work on self-assembly of NCs has either focused on only monitoring the long-range order on the NC scale using GISAXS¹⁵, ex-situ measurements using GISAXS and GIWAXS¹⁶⁻¹⁹ and time resolved GISAXS and GIWAXS on the 3-D self-assembly of PbS nanocrystals, showing an FCC-to-BCC phase transition²⁰. We find that oriented attachment of the nanocrystals by neck formation is preceded by a remarkable sequence of processes: nanocrystal adsorption at the liquid/air interface with the preservation of the rotational degrees of freedom, formation of a dense hexagonal NC phase, finally followed by

a phase transition from hexagonal into square order in the NC monolayer in which the rotations become entirely frozen.

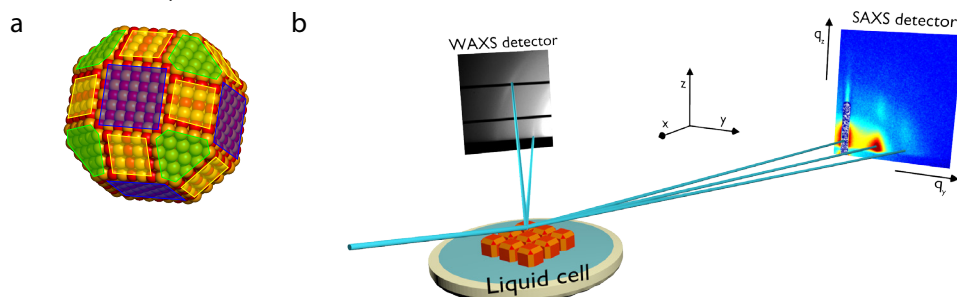


Figure 4.1: Truncated PbSe NCs assembling into an attached superlattice. (a) An atomic model of the PbSe truncated nanocubes used, showing the different facets of the NC. Blue indicates the {100} facets, yellow the {110} facets and green the {111} facets. (b) Schematic of the setup used for in-situ GISAXS/GIWAXS experiments. A dispersion of NCs in toluene evaporates in a liquid sample cell. We examine the process of assembly and attachment using grazing-incidence X-ray scattering (blue), by simultaneously monitoring the atomic order on the wide-angle detector and nanoscale order on the small-angle detector.

4.2 - Results and discussion

Figure 4.1 shows two schematics; (a) shows a model of the PbSe nanocrystals used in these experiments. The nanocrystals have three characteristic facets; {100} facets (blue), containing a stoichiometric amount of Pb and Se atoms, {110} facets (yellow) containing again a mixture of Pb and Se atoms and {111} facets (green), which are Pb only facets. A combination of the rock-salt crystal structure and the facet surface energies force the nanocrystals into a truncated cube like shape.

The experimental setup used in the experiments is displayed in Figure 4.1(b). A drop of NC suspension is placed on top of an ethylene glycol liquid phase and the solvent is allowed to evaporate over the course of one hour. In the forward scattering direction, at a relatively large distance, we position a 2-D detector to collect the GISAXS signal, which allows us to monitor the NC movement and NC self-assembly process over time. At a relatively small distance and under a wide angle, we place a 2-D detector to collect the GIWAXS signal, enabling us to monitor the crystallographic alignment and fusing of the NCs into the superlattice. Combining GISAXS and GIWAXS allows us to obtain a full description of the self-assembly process on both nanocrystal and atomic lengthscales. A photograph and a more detailed description can be found in the Methods section.

In Figure 4.2 we follow the formation of the square superlattice starting from individual NCs, combining ex-situ TEM and electron diffraction (ED) with in-situ GISAXS and GIWAXS. The TEM and X-ray scattering measurements show the same stage in the NC assembly process. However, TEM data should be interpreted with care as a structure extracted at a given time during the self-assembly process may undergo changes during drying. In the initial stages of the self-assembly process (16 minutes after the start of solvent evaporation), it is not clear whether the NCs are still dispersed or already adsorbed at the toluene/air interface (Fig. 4.2(b,c)); but any long-range positional order (Fig. 4.2(a,b)) or atomic orientation (Fig. 4.2(c)) is lacking.



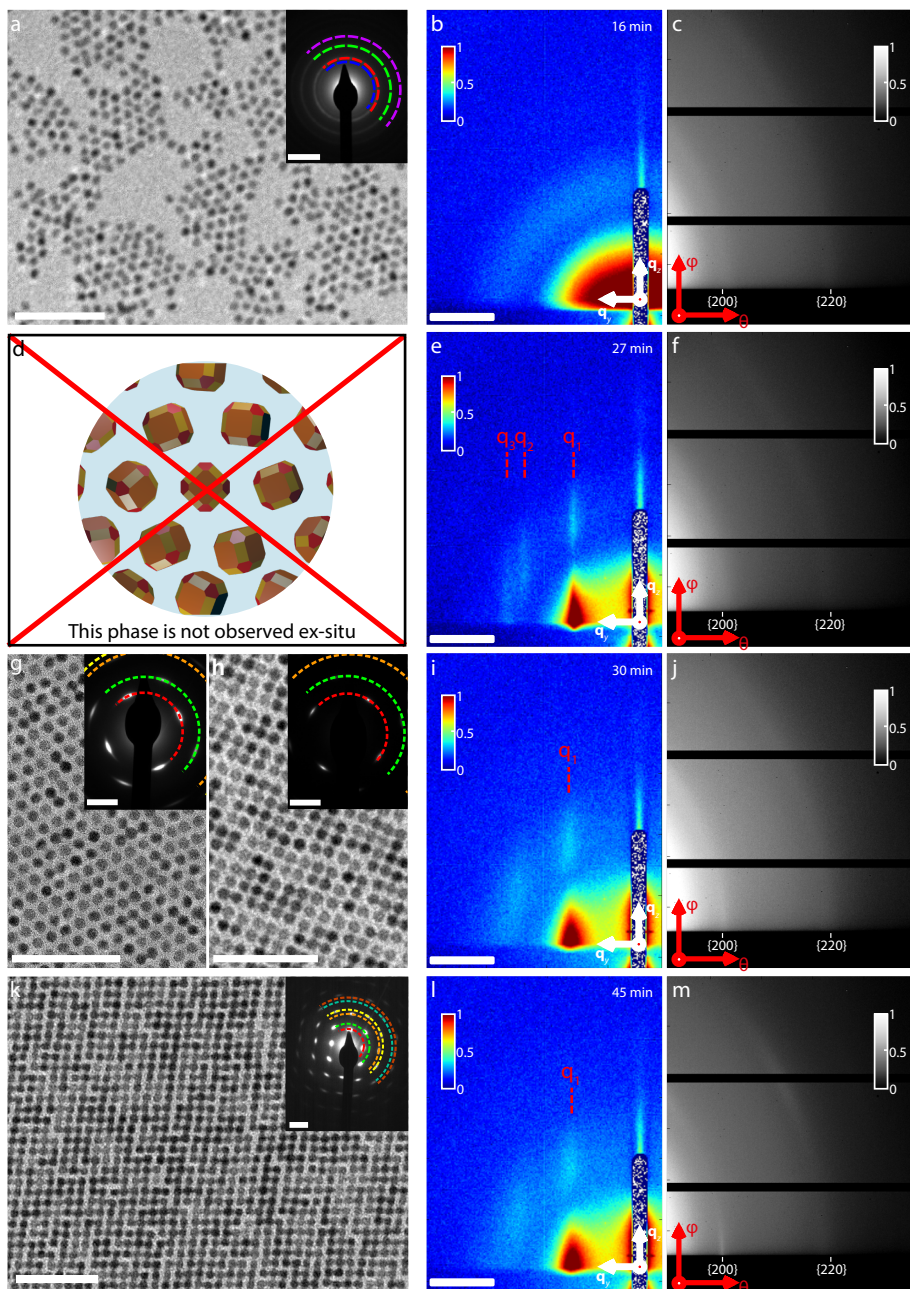


Figure 4.2: The different stages of the self-assembly process towards an oriented attached PbSe NC superlattice. Ex-situ TEM images and in-situ X-ray scattering data are taken at different stages in the hexagonal-to-square phase transition. Top to bottom rows show the different phases over time. **(a)** TEM image of the disordered NCs, obtained by scooping immediately after drop casting on ethylene glycol. Inset shows the corresponding ED pattern, where diffraction rings indicate random orientations of the NCs, i.e. they have rotational freedom. **(b)** At the initial stage, we observe form factor scattering in GISAXS, indicating the presence of NCs without long-range

positional order. **(c)** The GIWAXS pattern shows the full {200} and {220} diffraction rings of PbSe, indicating rotational freedom. **(d)** No hexagonal phase could be isolated ex-situ. **(e)** GISAXS pattern showing the presence of a hexagonal nanocrystal monolayer at the interface, with **(f)** the corresponding GIWAXS pattern. **(g)** TEM image of the pseudo-hexagonal phase, obtained when scooping the NCs just before toluene has completely evaporated. Inset: in ED the rings transformed into arcs. **(h)** TEM image of the initial square phase, before complete attachment of all NCs. Inset: the arcs in the ED have narrowed. **(i)** GISAXS pattern of the corresponding phase. Note that all peaks have broadened. **(j)** GIWAXS pattern corresponding to **(i)**. **(k)** TEM image of the final square phase. Inset: the ED pattern now consists of distinct spots, visible at least up to the {600} reflection. **(l)** GISAXS pattern of the final square phase, with **(m)** the corresponding GIWAXS pattern. Note how the diffraction rings have spots superimposed. The {200} diffraction has a narrower width in the 2θ -direction than before (compare **j**), indicating that the NCs have attached in this direction. All TEM scale bars correspond to 50 nm. The ED scale bars denote 20 nm^{-1} . The colored rings in the ED patterns display the position of the diffraction rings: blue = {111}, red = {200}, green = {220}, purple = {222}, orange = {400}, yellow = {420}, turquoise = {440}, brown = {600}. All GISAXS scale bars denote 1 nm^{-1} .

After 27 minutes, diffraction rods appear in the GISAXS pattern (Fig. 4.2(e)), at scattering vectors of 0.80 nm^{-1} , 1.39 nm^{-1} and 1.61 nm^{-1} , consistent with a 2-D hexagonal structure at the liquid-gas interface. We were not able to isolate this structure ex-situ (Fig. 4.2(d)), demonstrating the importance of the in-situ scattering measurements. The corresponding GIWAXS pattern in Fig. 4.2(f) still shows the PbSe {200} and {220} diffraction rings, with no sign of a preferential crystallographic orientation or attachment of the NCs. We conclude that at this stage the NCs behave as hard spheres. Indeed, hard sphere interactions between NCs confined on a 2-D interface leads to entropically driven packing into a hexagonal structure^{21,22}. Our difficulty in isolating this phase ex-situ indicates that short-range repulsive contributions from the solvent may be important to the hard sphere-like interaction potential.

At longer times, a complete monolayer of NCs is adsorbed at the interface. The NCs form a 2-D pseudo-hexagonal close-packed layer (Fig. 4.2(g)), with bond-angles deviating from the 60° of a perfect hexagonal structure. In the corresponding ED pattern the {111} and {222} rings disappear, meaning that all NCs have a {100} facet pointing upwards. Moreover, the ED pattern shows diffraction arcs rather than full rings, indicating that the NCs have a preferred crystallographic orientation in the 2-D plane. The width of the arcs reflects the remaining in-plane rotational freedom of the NCs. In the GISAXS pattern obtained 30 minutes after the start of the experiment (Fig. 4.2(i)) the first diffraction rod has moved further from the origin, indicating that the average NC-NC distance has decreased compared to Fig. 4.2(e). The diffraction peaks are broader than before, consistent with a peak splitting due to deviations of the superlattice symmetry from perfectly hexagonal. An alternative explanation for the broadening of the GISAXS reflections could be the increase of superlattice disorder due to evaporation of residual solvent^{23,24}. However, we point out that we scooped a sample of this exact sample and confirmed the formation of the square superlattice (see Figure 4.14), supporting the former interpretation of the scattering data. In the corresponding GIWAXS pattern (Fig. 4.2(j)) we observe the first indications of spots of increased intensity on the atomic diffraction rings, indicative for NC orientation with a $\langle 100 \rangle$ axis perpendicular to the liquid-gas interface. In Fig. 4.2(h) many NC-NC atomic connections have formed, but not yet all NCs make the maximum number of four NC-NC bonds with their in-plane {100} facets. The diffraction arcs in the ED pattern have further narrowed, since the rotational freedom has decreased with respect to the pseudo-hexagonal phase of Fig. 4.2(g).



Finally, the NCs attain a square ordered structure (Fig. 4.2(k,l)) with the $\langle 100 \rangle$ direction pointing upward and orientational order in the 2-D plane (inset Fig. 4.2(k)). Furthermore, the NCs attach, as evidenced not only in the TEM image (Fig. 4.2(k)), but also from the narrowing of the $\{200\}$ diffraction spot in the horizontal direction in the GIWAXS pattern (Fig. 4.2(m)). This is confirmed by later TEM measurements on the structure formed during the in-situ measurement.

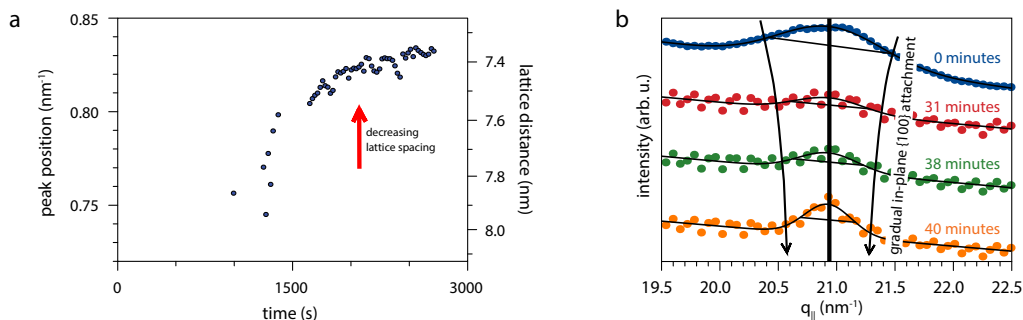


Figure 4.3: Quantitative analysis of the GISAXS and GIWAXS data. (a) Fitted peak positions of the first diffraction rod q_1 in the horizontal scattering direction from the in-situ GISAXS measurements depicted in Figure 4.2. From the position of the diffraction rod the lattice spacing is calculated. (b) Evolution of the peak width of the in-plane $\{200\}$ atomic reflection in the horizontal scattering direction $q_{||}$ over time as measured with GIWAXS. The black line is the calculated position of the $\{200\}$ reflection for a rock salt PbSe crystal structure with a lattice vector of 6 Å.

We now investigate in more detail the structural changes observed in the in-situ experiments. We calculate the time-evolution of the nanoscale lattice spacing from the position of the first diffraction rod in GISAXS (see Fig. 4.3(a)). The fitted peak position in reciprocal space (left axis) increases from 0.74 nm^{-1} to 0.83 nm^{-1} . Realizing that the initial structure has hexagonal symmetry while the final structure is square, this corresponds to a contraction of the NC-NC distance by 17%, from 9.1 nm after 1200 s after injection, to 7.6 nm at 2700 s.

The initial NC-NC distance of 9.1 nm is as expected in a hexagonal monolayer of NCs of 5.7 ± 0.6 nm core diameter separated by oleic acid ligands (roughly 2 nm in length). In the final oriented attached square structure, however, the NC-NC distance of 7.6 nm is 34% larger than the original PbSe NC core diameter. This shows that necking takes place during the atomic attachment, i.e. the formation of a crystal bridge between opposed $\{100\}$ facets^{2,5,25}.

The increase of the average atomic coherence length during the formation can be extracted from the width of the horizontal atomic $\{200\}$ reflections in GIWAXS (see Fig. 4.3(b)). The FWHM of the $\{200\}$ peak of individual NCs in dispersion equals 1.1 nm^{-1} , corresponding to an average crystalline domain size of 5.9 nm, consistent with the NC sizes measured with TEM. During the in-situ experiments, the FWHM decreased to a value of 0.7 nm^{-1} after 31 minutes and 0.5 nm^{-1} after 40 minutes. These values correspond to crystalline domain sizes of 9.1 nm and 13.2 nm in the horizontal $\langle 100 \rangle$ direction. We conclude that when NCs attach atomically, the size of single-crystalline domains grows to on average to a lower limit of two to three NC diameters, which agrees with our observations on the TEM sample obtained from the same experiment (see Fig. 4.14 in the Methods section).

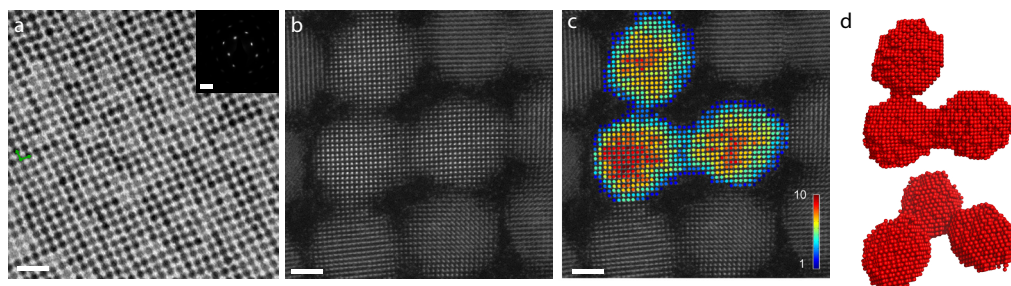


Figure 4.4: HAADF-STEM and atom counting reconstruction on the attached NCs. (a) Typical overview bright-field TEM image on a square superlattice. Inset shows the corresponding ED pattern. (b) More detailed HAADF-STEM image on NCs attached in a square superlattice, showing truly epitaxial connections and connections with crystal defects. (c) Results from the atom counting procedure, using (b) as an input image. The colorbar represents the number of detected atoms in the column. (d) Topview and sideview of the reconstructed atomic model. Scale bars equal 20 nm in **a** (20 nm^{-1} in the ED inset) and 2 nm in **b** and **c**.

In order to study the degree of atomic coherency inside the superlattice, we performed aberration corrected high-angle annular dark-field (HAADF) scanning transmission electron microscopy (STEM) measurements to investigate the atomic lattice. First, Fig. 4.4(a) shows an overview of part of a square sheet, showing that the square nanogeometry is present over many unit cells. In the atomically resolved image of Fig. 4.4(b), we observe atomic connections between the nanocrystals that are fully coherent, and some defective connections as well. These defective connections and the natural dispersion in the nanocrystal size must affect the perfectness of the square geometry, i.e. lead to some variation in the translation vectors. In Figure 4.17 we show that the overall square periodicity (although with its intrinsic variation) is essentially preserved when it is considered over different length scales. From the HAADF-STEM image we extract the number of atoms in each projected atomic column using atom counting (Fig. 4.4(c))^{26,27}. These numbers can then be used as an input for an iterative energy minimization scheme in order to obtain a 3D model for the investigated superlattice as illustrated in Figures 4.4(d)^{28,29}. More experimental details are provided in the Methods section and an additional example of two connected nanocrystals is presented in Fig. 4.12.

Combining all information from the in-situ and ex-situ experiments, we postulate a model for the reactive self-assembly of PbSe nanocubes into the square oriented attached superlattice. Fig. 4.5 shows cartoons of the different phases occurring in the reactive self-assembly. For clarity we omitted the oleic acid ligands from the image. During the toluene evaporation the NCs adsorb at the liquid-gas interface without long-range order (a). As the NC concentration at the interface increases, they start to form a hexagonally packed monolayer at the interface (b). The NCs still behave similar to hard spheres, as any anisotropic interaction is screened by the oleate ligands. Possibly, oleate ligands weakly attached to the $\{100\}$ facets^{30,31}, detach and are absorbed in the ethylene glycol phase. The particles align one of their $\langle 100 \rangle$ directions perpendicular to the liquid-gas surface. The rotational freedom in plane is gradually reduced, in favor of electrostatic and van der Waals interactions between opposed $\{100\}$ facets. This also results in a reduced NC-NC distance (c). Due to the directionality of these in-plane $\{100\}$ attractions, the superlattice has to change its symmetry from hexagonal to square. A similar transition between hexagonal and square symmetry has been predicted from Monte Carlo simulations for a monolayer of hard truncated nanocubes confined at an interface³². Once the NCs are in close proximity, crystalline



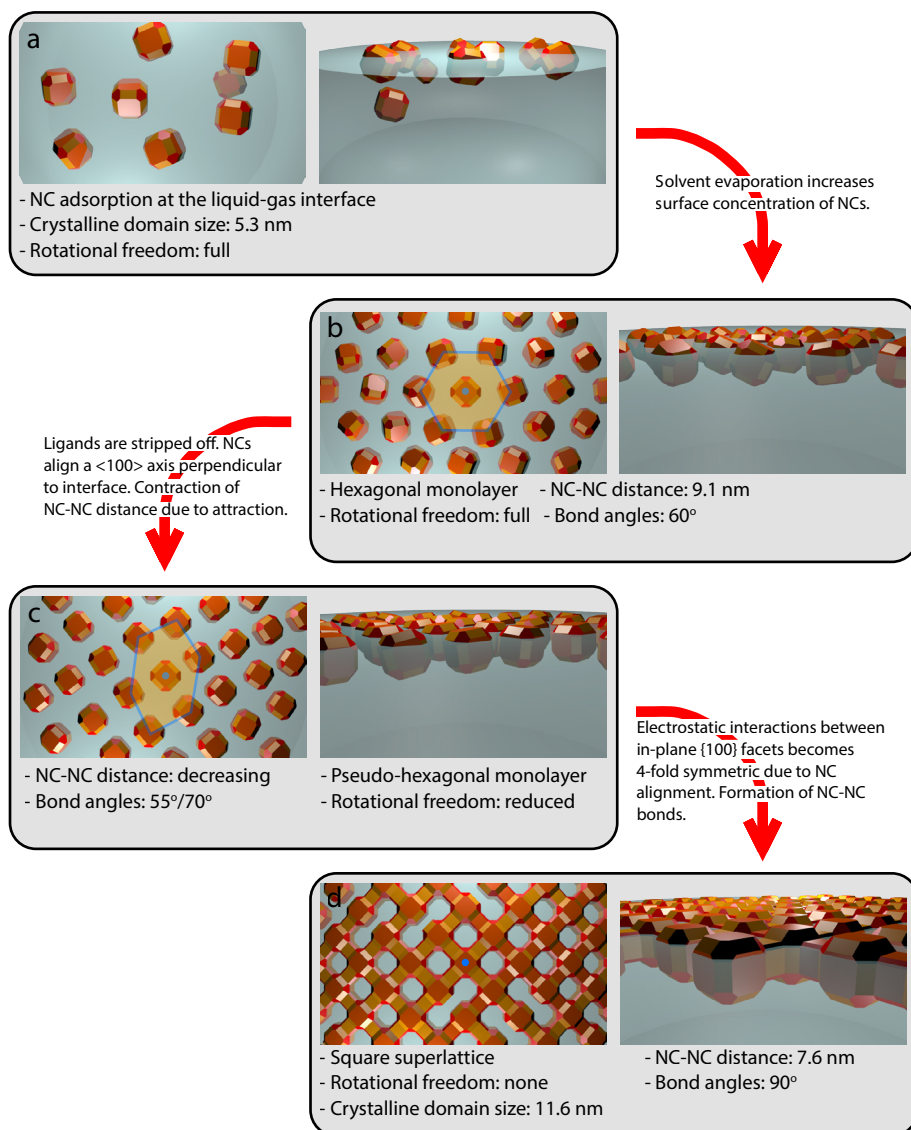


Figure 4.5: Schematic mechanism of the consecutive phase transitions during the reactive self-assembly of the PbSe NCs. Left image shows top views, right image side views. **(a)** As the solvent evaporates, the concentration of the NCs increases, and the particles adsorb at the liquid-gas interface. **(b)** The central NC is indicated with a blue dot. The increase in NC concentration forces the particles to form a hexagonally packed monolayer. **(c)** The ligands on the $\{100\}$ facets stabilizing the particles in the toluene slowly dissolve in the ethylene glycol substrate, thus increasing the $\{100\}$ facet-to-facet attractive interaction and decreasing the NC-NC distance. Due to the directionality of the in-plane $\{100\}$ attractions, the superlattice transforms into a pseudo-hexagonal structure. **(d)** Once the particles are sufficiently close, they connect atomically via necks; the superlattice obtains a square geometry.

bridges grow between neighboring NCs (d). This necking has also been observed in a chemically distinct case of NC attachment^{8,33,34}.

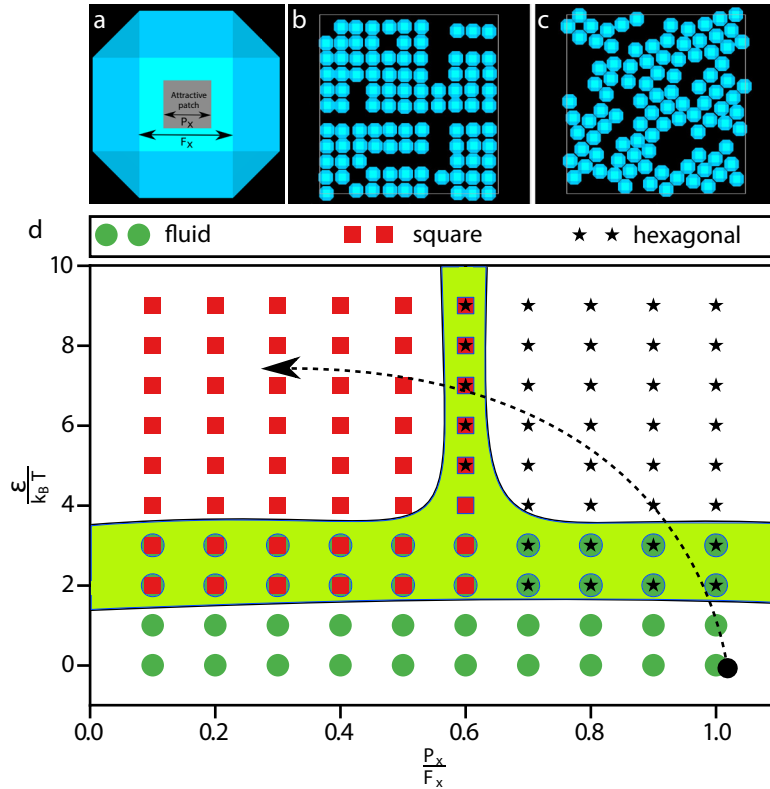


Figure 4.6: Monte Carlo simulations on the truncated nanocubes confined to a 2D plane. (a) Model of the cantellated nanocube used in our NVT simulations. Different facets are indicated along with the attractive patch on the $\{100\}$ facets. Dimension of the patch P_x and the $\{100\}$ facet F_x are also indicated. (b) Square phase ($P_x/F_x = 0.1$, $\epsilon/k_B T = 6$) and (c) hexagonal/pseudo-hexagonal phase ($P_x/F_x = 0.8$, $\epsilon/k_B T = 6$) obtained for different sizes of the attractive patches on the $\{100\}$ facets. (d) State diagram for the truncated cubes with attractive $\{100\}$ facets as a function of the relative attractive patch size on a $\{100\}$ facet P_x/F_x , and the square-well interaction strength $\epsilon/k_B T$.

To test the postulated model, we investigated the formation of superlattices from PbSe NCs adsorbed at the liquid-gas interface using Monte Carlo simulations with periodic boundary conditions in the canonical ensemble, i.e. we fixed the number of particles N , the volume V , and the temperature T of the system. We model the NCs by truncated cubes as depicted in Fig. 4.6(a). The cubes are confined to a 2D plane and are oriented such that the $\{100\}$ facet points upwards. The nanocrystals are allowed to move freely in this plane. The ligand-free $\{100\}$ facets lead to an attractive driving force that attempts to position the nanocrystals with their vertical $\{100\}$ facets face-to-face. This directional driving force is mimicked in the simulations by introducing small patches on the center of the vertical $\{100\}$ facets. We assume the cantellated cubes to interact as hard particles, but with the attractive patchy interaction between the $\{100\}$ facets, as shown in Figure 4.6(a). The patchy interaction is modelled as a square patch that interacts with an attractive square-well potential^{35,36}. The patch size is defined by the ratio of the length of the patch P_x and the length of the $\{100\}$ facet F_x , i.e. P_x/F_x , and the attraction strength is given by $\epsilon/k_B T$ with k_B Boltzmann's constant. We simulate the self-assembled structures of the NCs as a function of the size of the attractive patch and the attraction strength in order to shed light on

the contraction and the symmetry change of the hexagonally packed layer towards the square superlattice, as shown in Fig. 4.2(g) to 4.2(k) and Fig. 4.5.

In Fig. 4.6(b) and 4.6(c), we show two typical configurations of the self-assembled structures for the cantellated cubes with different patch size. We clearly find that the self-assembled structure depends sensitively on the patch size, which determines the directionality of the attractive interaction. For a stronger directionality, i.e. smaller patch size, we observe a square symmetry for the superlattice (see Fig. 4.6(b)) whereas for a less directional interaction, i.e. a larger patch size, the superlattice shows hexagonal symmetry (see Fig. 4.6(c)). In Fig. 4.6(d) we present the state diagram of the nanocrystals as a function of the patch size P_x/F_x , and attraction strength $\epsilon/k_B T$. We observe that the particles self-assemble into a superlattice for attraction strengths $> 4 \epsilon/k_B T$, even with very small attractive patch sizes. The results corroborate our interpretation of the experimental data that the directional electrostatic and van der Waals interactions between the vertical $\{100\}$ facets drive the phase transition from hexagonal to square NC ordering and keep the $\{100\}$ facets face-to-face, finally enabling an atomic necking process and growth of attached nanocrystals that form single crystalline domains.

4.3 - Conclusion and outlook

In summary, we have shown that the formation of 2-D nanoperiodic superlattices with a square symmetry from colloidal nanocrystals can be described by a sequence of processes, rather than oriented attachment alone. Following the temporal evolution of the superlattice formation by ex-situ TEM and in-situ X-ray scattering shows that the nanocrystals attach to the liquid-gas interface and form a hexagonally packed layer, which then contracts and transforms through a pseudo-hexagonal structure into a structure with square symmetry. During this phase transition, the NCs align themselves atomically and finally form inter-particle bonds. Monte Carlo simulations show that a directed attractive electrostatic and van der Waals interactions between in-plane $\{100\}$ facets induce the (pseudo)-hexagonal to square phase transition.

The fact that it is possible to monitor in-situ the adsorption of colloidal particles at a liquid surface and to reveal the ensuing structural transformations of the particle monolayer will further our understanding of the mechanisms of interfacial self-assembly processes and the differences with self-assembly in three dimensions. This may result in bottom-up routes towards a diversity of 2-D electronic or photonic materials based on nanocrystals or (anisotropic) polymer-type colloids. We remark that improvements in the atomic coherency are desired for high quality 2-D optoelectronic materials. In such a way, colloid self-assembly can become a feasible alternative for top-down lithography based methods.

4.4 - Methods

Nanocrystal synthesis. The PbSe nanocrystals used for the oriented attachment experiments in this study were prepared using the method described by Steckel et al.³⁷. The synthesis was performed in a glovebox with a water and oxygen free environment. (a) 4.77g of lead acetate trihydrate (99.999% Aldrich), 10.35g of oleic acid (OA, 90% Aldrich) and 39.75g octadecene (ODE, 90% Aldrich) were heated to 130°C under low pressure (10^{-3} bar) for approximately 4 hours. (b) A second mixture containing 3.52g Se (99.999% Alfa Aesar), 46.59 mL trioctylphosphine (TOP, 90% Fluka) and 0.41mL diphenylphosphine (DPP, 98% Aldrich) was prepared by dissolving the Se. Subsequently solution (a) was heated in a three-necked round-bottom flasks to 180°C after which 15mL of solution (b) was rapidly injected. The particles were grown for approximately 60 seconds, after which the reaction was quenched with 20mL butanol. After the solution was cooled down to approximately 50°C, 10 mL methanol was added to induce precipitation of the nanocrystals. The resulting suspension was centrifuged at 2500 rpm for 10 minutes, the supernatant was removed and the washed particles were redispersed in toluene. This washing procedure was repeated two times.

Oriented attachment of truncated PbSe nanocubes. The ex-situ oriented attachment was performed at 20°C inside a glovebox with <1ppm O₂ and <1ppm H₂O. A glass petri dish (Ø 27mm) was filled with 6.5 mL ethylene glycol. The nanocrystal (NC) solution with an initial concentration of 3.0×10^{-5} mol/L was diluted by adding 4µL of the NC solution to 800µL of toluene. A total volume of 350µL of this dispersion was drop cast gently on top of the ethylene glycol. The ethylene glycol serves as an immiscible liquid substrate for the NC solution. After drying the NC solution on top of the EG for 60 minutes, a sample was scooped from the ethylene glycol interface on a copper TEM grid and dried in vacuum to remove any residual ethylene glycol.

In-situ GISAXS/GIWAXS. The in-situ X-ray scattering experiments under grazing incidence were performed at beamline ID10 of the European Synchrotron Radiation Facility (ESRF), Grenoble. The energy of the incident X-ray beam was set at 10.0 keV, below the Pb and Se absorption edges to minimize beam damage. We optimized the grazing angle to 0.3° for the best signal-to-noise ratio on both GISAXS and GIWAXS detectors. The scattering was recorded by two Pilatus detectors. The GIWAXS patterns were recorded on a Pilatus 300K detector with 619x487 pixels, each $172 \times 172 \mu\text{m}^2$ in size, positioned approximately 25 cm from the sample. The GISAXS patterns were recorded on a Pilatus 300K-W detector with 1475x195 pixels, each $172 \times 172 \mu\text{m}^2$ in size, positioned 0.578 m from the sample. Before drop casting the dispersion of NCs on top of the EG substrate, the X-ray beam was aligned to the surface. After drop casting and every three minutes the alignment was repeated in <10 sec to adjust for solvent evaporation. The oriented attachment was performed in a home-built liquid cell, which can be flushed with argon (or nitrogen) repeatedly to lower the oxygen and water levels (Fig. 4.13). A Teflon petri dish (Ø 64 mm) was filled with 28 mL of ethylene glycol. To the ethylene glycol we added 10 µL of an OA solution (1% (v/v) OA in ethylene glycol). The cell was then flushed five times with vacuum/argon cycles, and was filled with toluene saturated vapour (argon gas blown through hot toluene). Next, the PbSe NC solution (0.5 mL; 1.9×10^{-6} mol/L) was deposited on top of the liquid substrate. As the PbSe NCs proved to be sensitive to beam damage, we scanned the sample position in between the measurement, back and forth over a distance of 4 mm (in 21 steps) in the direction perpendicular to the incident X-ray beam. In this way, the dose of X-ray photons on each position of the sample was minimized. Each frame was recorded with a 10 s integration time, after which the position of the sample was changed. After each sequence of 21 positions, we returned to the starting position and repeated the procedure.

HAADF-STEM imaging and atom counting. HAADF-STEM imaging is performed using an aberration corrected FEI Titan microscope operated at 300 kV. By modelling images as a superposition of Gaussian functions located at the atomic columns, the volume under each peak can be estimated by fitting this model to the region of interest. These volumes are integrated intensities of electrons and thus correspond to scattering cross-sections. In a subsequent analysis, the distribution of scattering cross-sections of all atomic columns is decomposed into overlapping normal distributions, where the number of normal components is selected using an Integrated Classification Likelihood (ICL) approach^{25,26}. Based on the analysis of the image shown in Fig. 4.4, 10 components have been retrieved illustrating the presence of 1 up to a maximum of 10 atoms in a column. The number of atoms in each projected atomic column is then obtained by assigning the component which generates the experimental scattering cross-section with the highest probability. In this manner, a map reflecting the number of atoms in each column is retrieved as illustrated in Fig. 3b. Based on the counting results, a starting 3-D configuration is obtained by positioning all Pb atoms on a perfect crystal grid symmetrically arranged around a central plane. Next, the potential energy of this configuration is calculated using a Lennard-Jones potential and minimized using an iterative scheme. In each iteration step, one atomic column, selected by a monte-carlo based approach, is shifted over one unit cell and the total energy is again calculated. The previous 3D configuration is replaced by the new one if the total energy is decreased. This procedure is repeated until convergence is reached.

Calculation of the X-ray penetration depth. The incident X-ray energy of 10.0 keV corresponds to a wavelength $\lambda_0 = 0.124$ nm and a wavevector of magnitude $k_0 = 2\pi/\lambda_0 = 50.7$ nm⁻¹ in air. For our experiments we used a grazing angle of incidence of 0.3°, slightly larger than the critical angle for total external reflection of bulk PbSe. Since the refractive index of any material is negative at X-ray frequencies ($n = 1 - \delta + i\beta$), the wavevector inside the sample $k = nk_0$ is smaller than in air. Upon transmission of the beam into the sample, the wavevector component parallel to the air-sample interface $k_{||} = k_0 \cos^2(\alpha_i)$ is conserved. The wavevector component perpendicular to the sample is

$$k_z = \sqrt{k^2 - k_{||}^2} = k_0 \sqrt{n^2 - \cos^2(\alpha_i)} \quad 4.1$$

Since n is complex, k_z is complex. The imaginary part of k_z describes how quickly the X-ray intensity decays when going deeper into the sample. The penetration depth d , defined as the depth at which the X-ray intensity is lower by a factor e than at the interface, is given by

$$d = \frac{1}{2 \operatorname{Im}(k_z)} \quad 4.2$$

	δ	β
PbSe	1.292×10^{-5}	8.430×10^{-7}
Toluene	1.964×10^{-6}	1.750×10^{-9}
Ethylene glycol	2.539×10^{-6}	4.188×10^{-9}

Table 4.1: Values of the real (δ) and imaginary (β) part of the refractive-index decrement at 10 keV for the materials used in these experiments. δ and β define refraction and absorption in a material accordingly.

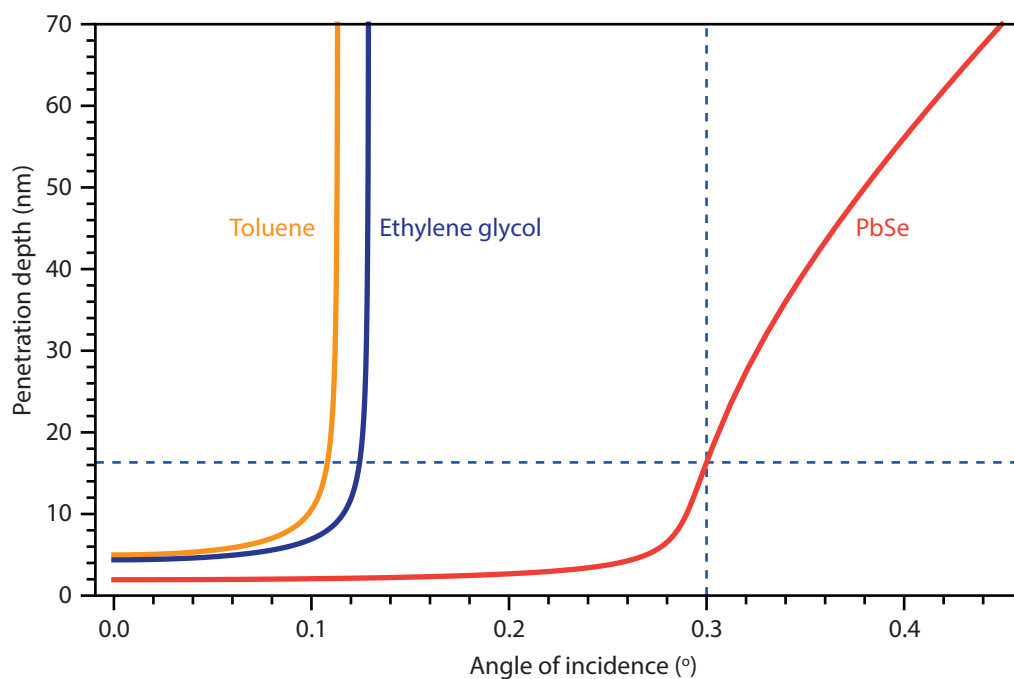


Figure 4.7: Calculation of the X-ray penetration depth as a function of incident angle. The red, blue and yellow lines depict the penetration depths as function of incident angle for PbSe, ethylene glycol and toluene respectively. The blue dashed lines show the incident angle of the experiments (0.3°) and the corresponding penetration depth for PbSe (16.3 nm). Working at the critical angle of either toluene or ethylene glycol would result in a minute penetration of the X-ray photons into the PbSe superstructure.

Peakwidth of atomically aligned, but not attached, nanocrystals. The diffraction signal is as a first order approximation equal to the squared Fourier Transform of the electron density profile. We approximate the NC superlattice here as a one-dimensional chain of connected crystal and we consider the horizontal [100] direction. The lattice vector in the [100] direction equals 6 Å. Each NC consists out of N (100) planes in the horizontal direction, for the NCs used in the experiments $N=8-10$. The length from the start of a nanocrystal to the next nanocrystal is L and the total chain consists out of M of these repeating units in the positive x direction.

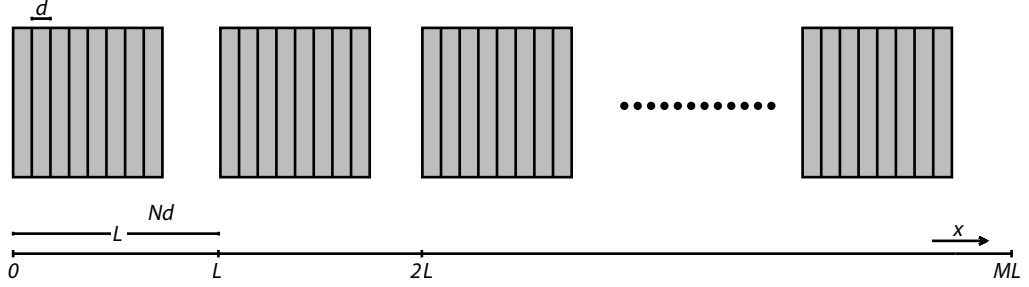


Figure 4.8: Nanocrystal model used to approximate the width of the diffraction peaks. Each nanocrystal has a N lattice planes with a lattice spacing d . The length from the start of the NC to its neighbour equals L .

The Fourier Transform of this chain of separated, but aligned, nanocrystals is given by

$$F(q) = \int_0^{ML} \rho(x) e^{-iqx} dx \quad 4.3$$

which can be split into a sum of repetitions of the first segment

$$F(q) = \sum_{j=0}^{M-1} \int_{0+jL}^{L+jL} \rho(x) e^{-iqx} dx \quad 4.4$$

This summation can be expanded as

$$\begin{aligned} F(q) &= \int_0^L \rho(x) e^{-iqx} dx + \int_L^{2L} \rho(x) e^{-iqx} dx + \int_{2L}^{3L} \rho(x) e^{-iqx} dx + \dots + \int_{(M-1)L}^{ML} \rho(x) e^{-iqx} dx \\ &= \int_0^L \rho(x) e^{-iqx} dx + \int_0^L \rho(x) e^{-iq(x+L)} dx + \int_0^L \rho(x) e^{-iq(x+2L)} dx \dots \\ &= \sum_{j=0}^{M-1} e^{-iqLj} \int_0^L \rho(x) e^{-iqx} dx \end{aligned} \quad 4.5$$

The summation above has a general solution, given by

$$S_N = \sum_{n=0}^N a_0 q^n = a_0 \frac{q^{N+1} - 1}{q - 1} \quad 4.6$$

Hence, the summation outside of the integral is given by

$$\sum_{j=0}^{M-1} e^{-iqLj} = \frac{e^{-iqML} - 1}{e^{-iqL} - 1} \quad 4.7$$

The integral itself, which runs over a single segment of length L can be evaluated in an equivalent manner.

$$\int_0^L \rho(x)e^{-iqx} dx = \int_0^{Nd} \rho(x)e^{-iqx} dx + \int_{Nd}^L \rho(x)e^{-iqx} dx \quad 4.8$$

The second integral is equal to zero as there is no electron density in between the nanocrystals. The second part of the integral in eq. 4.5 is evaluated equivalently and gives

$$\int_0^{Nd} \rho(x)e^{-iqx} dx = \frac{e^{-iqNd} - 1}{e^{-iqd} - 1} \int_0^d \rho(x)e^{-iqx} dx = \frac{e^{-iqNd} - 1}{e^{-iqd} - 1} S_n \quad 4.9$$

Where we treat the Fourier Transform of the electron density in between the lattice planes, S_n , as a constant. The intensity is measured as $|F(q)|^2$ and can now be approximated by:

$$I(q) \propto \frac{\sin^2\left(\frac{qML}{2}\right) \sin^2\left(\frac{qNd}{2}\right)}{\sin^2\left(\frac{qL}{2}\right) \sin^2\left(\frac{qd}{2}\right)} \quad 4.10$$

We assume a perfect positioning of the nanocrystals in the above derivation. This situation is not realistic, but can be improved by assuming a Gaussian distribution of the nanocrystal positions:

$$I(q) \propto \int_0^\infty e^{-\frac{1}{2}\left(\frac{L-L_0}{\sigma L}\right)^2} \frac{\sin^2\left(\frac{qML}{2}\right) \sin^2\left(\frac{qNd}{2}\right)}{\sin^2\left(\frac{qL}{2}\right) \sin^2\left(\frac{qd}{2}\right)} dL \quad 4.11$$

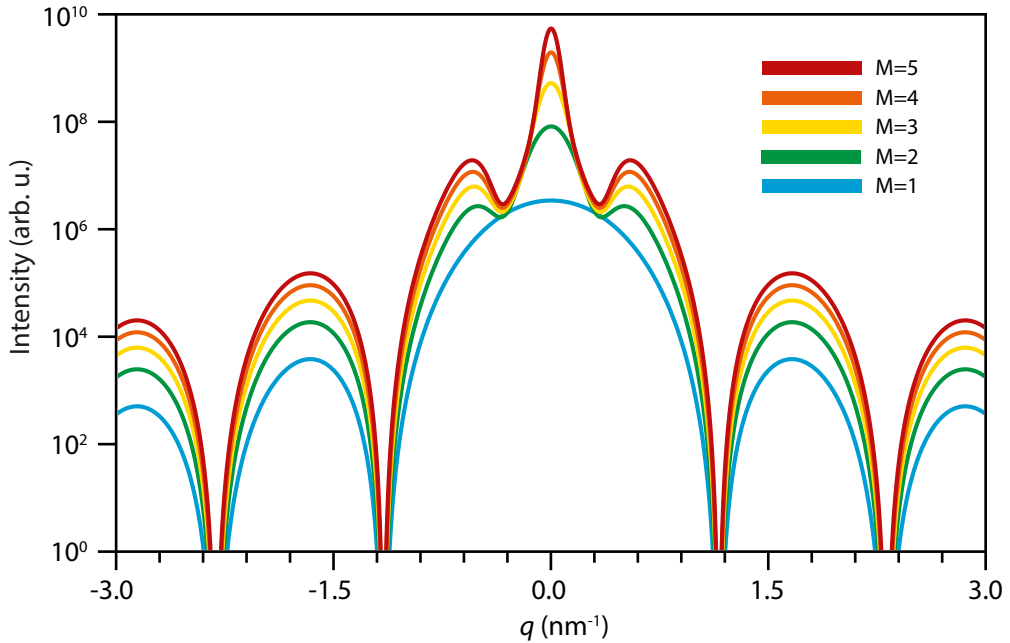


Figure 4.9: Peak width of aligned but not connected nanocrystal as a function of increasing number of attached nanocrystals. Plotted are the scattering curves using $d = 0.6$ nm, $N = 9$ (the product Nd gives a realistic nanocrystal size), $L_0 = 1.53Nd$. We used $\sigma L = 0.4L_0$.

It can be seen that the peak width decreases slightly upon increasing the number of aligned particles (~20%), due to the variations in the nanocrystal positions, assumed to mimic the in-situ experimental conditions.

Computer aided image analysis of the initial and final NC structures. To determine the bond-angles, average NC-NC distances and surface density, we employed computer aided image analysis. The code used was written in the Python scientific programming language, with the addition of the numpy, matplotlib, scipy and opencv libraries.

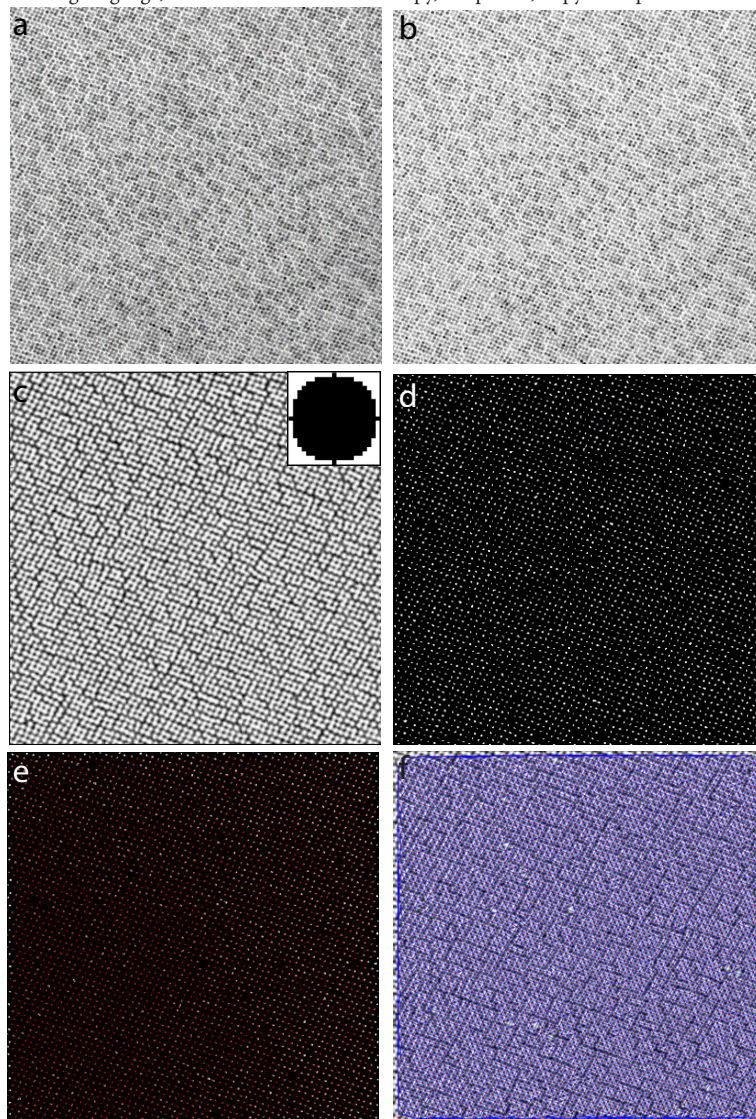


Figure 4.10: Schematic overview of the computer aided image analysis as performed in Python. (a) A TEM image is loaded into the program. (b) The TEM image is low-pass filtered with a 2D Gaussian ($\sigma < 0.6$ nm) to remove 'salt-and-pepper' noise. (c) A spherical template of a dark particle on a white background is created and the cross correlation (CC) of the template with each pixel on the filtered image is calculated and averaged over multiple sizes of the spherical template. (d) The CC image is binarized and the centers of mass (COM) of the segments are determined. (e) COMs within 15 pixels of the image edge (red spots) are discarded to avoid edge artefacts. (f) On the remaining COMs a Delaunay triangulation was performed (blue mesh over the image).

First, the centers-of-mass (COMs) of the PbSe NCs are automatically recognized using the procedure outlined in Figure S13. Next, from the COMs and the Delaunay triangulation the inter-particle distances and bond angles are determined. Furthermore from the surface area of the convex hull of the triangulation and the number of COMs, the number of particles per unit surface was determined.

From the histogram of the radial distances, the pair distribution function was extracted.

$$g(r) = \frac{\# \text{ particles at distance } r}{2\pi r \cdot dr \cdot \rho \cdot N} \quad 4.12$$

Where $g(r)$ is the pair distribution function, dr is the thickness of a circular shell at distance r , ρ is the average density of particles per unit surface and N the total number of detected particles.

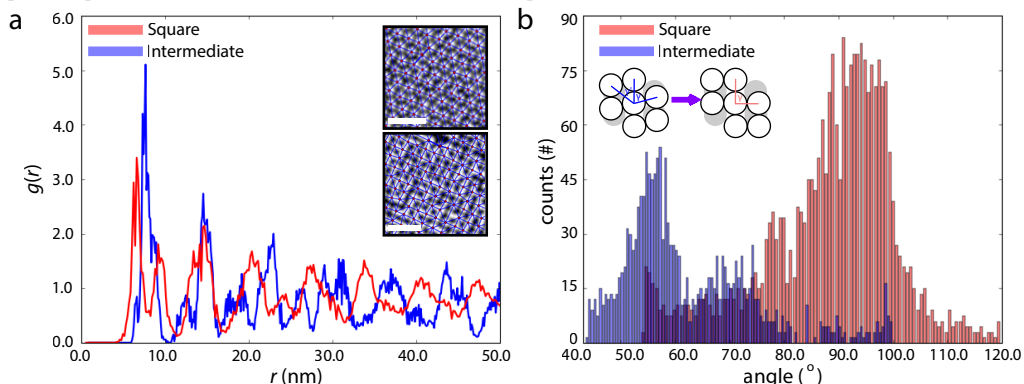


Figure 4.11: Image analysis on the initial and final phases of the self-assembly process. (a) Pair distribution function obtained from the detected centers of mass of the intermediate phase (blue) and square phase (red). The large number of oscillations is a signature of extended positional order in the superlattice. The insets show the detected particles with the Delaunay triangulation mesh for the intermediate (top) and square (bottom) phase. (b) Bond angles of the superlattice in the intermediate (blue) and square phases (red). The inset shows a schematic of the two phases displayed on top of a perfect hexagonal crystal (grey dots). Scale bars in the TEM inset are 25 nm.

To further analyze the intermediate phases occurring in the oriented-attachment process, we performed computer aided image analysis on the real-space TEM images of Fig. 4.2(g) and 4.2(k). Fig. 4.11(a) shows the pair distribution function of the NC-NC distances extracted for the intermediate phase (blue) and the square (red) phase. The nearest-neighbor distances decreases from 8.3 ± 0.3 nm for the intermediate phase to 7.4 ± 0.3 nm for the square phase. The contraction calculated from TEM images (11%) is smaller than that obtained from GISAXS (17%), as we could not isolate the pure hexagonal phase ex-situ. The bond angles of the superlattice are determined from the Delaunay triangulation, as shown in Fig. 4.11(b). The deviation of the bond-angles from 60° in the intermediate phase, i.e. 55° and 70° , shows that we isolated a pseudo-hexagonal phase (blue bars). The square phase (red bars) has bond angles close to 90° .

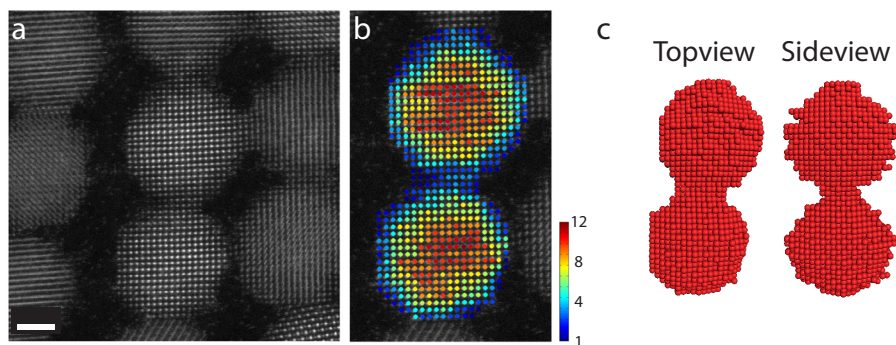


Figure 4.12: HAADF-STEM and atom counting reconstruction on attached NCs. (a) HAADF-STEM image of NCs attached in a square superlattice. The atomic periodicity is continued from a given NC to its neighbors. Slight misorientations can also be observed. (b) Results from the atom counting procedure, using (a) as an input image. The color bar represents the number of detected atoms in each vertical column. (c) Top-view and side-view of the reconstructed atomic model.

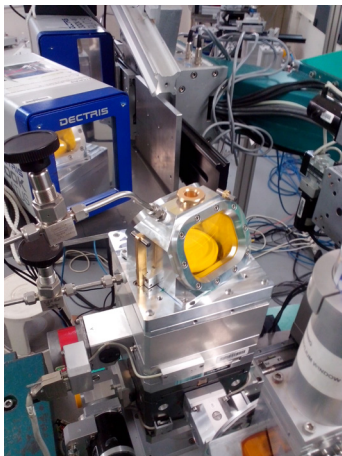


Figure 4.13: Photograph of the home-built liquid cell and setup used for the in-situ GISAXS/GIWAXS experiments at ID10 of the European Synchrotron Radiation Facility. The energy of the incident X-ray beam was set at 10.0 keV, below the Pb and Se absorption edges to minimize beam damage. We optimized the grazing angle to 0.3° for the best signal-to-noise ratio on both GIWAXS and GIWAXS detectors. As the PbSe NCs proved to be sensitive to beam damage, we scanned the sample position in between the measurement, back and forth over a distance of 4 mm (in 21 steps) in the direction perpendicular to the incident X-ray beam. In this way, the dose of X-ray photons on each position of the sample was minimized. Each frame was recorded with a 10 s integration time, after which the position of the sample was changed. After each sequence of 21 positions, we returned to the starting position and repeated the procedure.

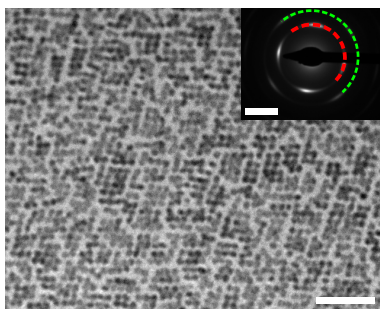


Figure 4.14: Characteristic TEM image of the sample scooped from the surface used in the in-situ experiments shown in Fig. 2 of the main text. Note the resemblance to Fig. 4.2(g). The micrograph shows that the NCs have assembled into a square superlattice. The NCs are atomically attached only in relatively small separate patches of 10-30 NCs, which could explain the peak broadening and absence of higher order diffraction rods in the GISAXS patterns. The electron diffraction pattern shows diffraction arcs, indicating atomic alignment of the particles. The coloured rings index the diffraction spots: red = {200} and green = {220}. Scalebars denote 50 nm in the TEM image and 20 nm^{-1} in the diffraction pattern. We should remark here that the formation of rather small domains that are atomically aligned has to do with the conditions under which in-situ measurements are done. Under better controlled conditions μm -large atomically coherent domains are observed.

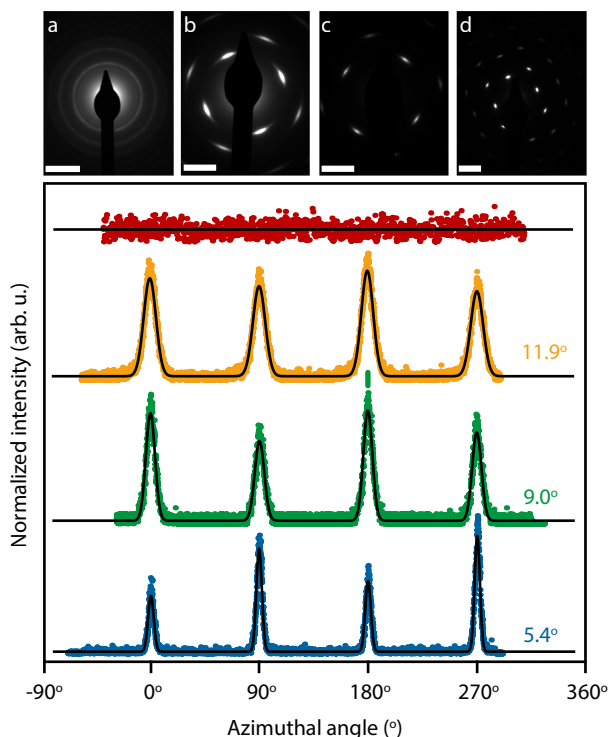


Figure 4.16: Azimuthal peak widths of the electron diffraction patterns during the self-assembly process. Azimuthal traces over the $\{400\}$ reflections from the electron diffraction patterns in Fig. 4.2 are presented in the Figure above. Each set of reflections in one trace is fitted with a Gaussian function, from which the average FWHM was determined. The red, orange, green and blue datapoints correspond to (a), (b), (c) and (d) respectively. Going from completely disordered NCs (a) to the square superlattice with attached nanocrystals (d) the peak widths of the $\{400\}$ reflections decrease, showing that the nanocrystals have less in-plane rotational freedom with respect to each other. We should remark here that the data should not be interpreted in a quantitative way, as instrumental broadening is not taken into account here.

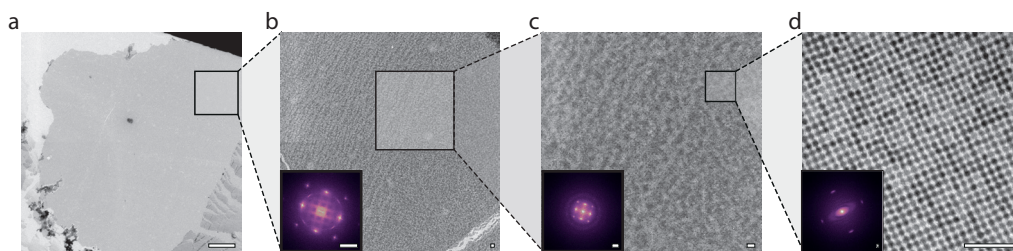


Figure 4.17: Conservation of nanocrystalline order on mesoscopic length scales. From (a) to (d) consecutive zoomed in TEM images are displayed, which show a very long-range periodicity. Even though the atomic coherency throughout the complete lattice is conserved over several nanocrystals, this does not perturb the long-range nano-crystalline order. From the widths of the $\{100\}$ -superlattice reflections in the Fourier transforms we obtain nanocrystal coherence lengths for the superlattice of 39.3 nm, 34.3 nm and 35.9 nm from left to right. Scale bars from left to right images are 2 μm for (a) and 40 nm for (b-d) and 1 nm^{-1} for all Fourier transform insets.

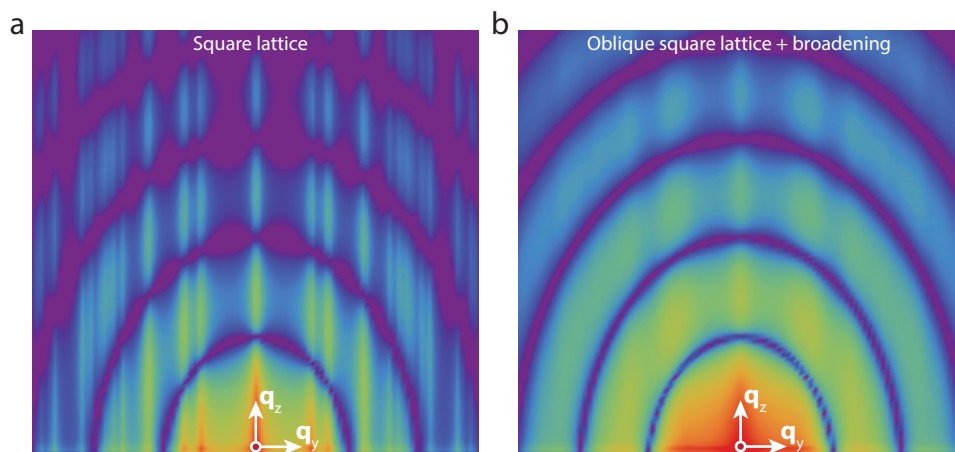


Figure 4.18: Simulation of GISAXS patterns for superlattices with a perfect square and slightly oblique square nanogeometry. (a) Calculated GISAXS pattern of a superlattice with a perfect square nanogeometry (i.e. bond angles of 90°) and a domain size of roughly 30 NC diameters. (b) Calculated GISAXS pattern of a superlattice with an oblique square nanogeometry (bond angles of $83^\circ/97^\circ$) and a domain size of 5 NC diameters. The latter is in good agreement with the experimental GISAXS data presented in Figure 4.2(d).

Acknowledgements

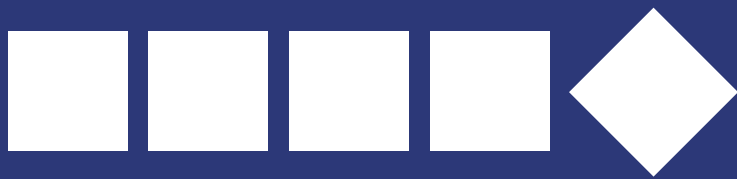
We are very grateful to for the excellent experimental support of Federico Zontone and Giovanni Li Destri of the ID10 beamline of the ESRF, who acted as local contacts during our experiments. We gratefully acknowledge dr. Ingmar Swart and dr. Marijn van Huis for fruitful discussions.

References

1. Evers, W. H. et al. “Low-dimensional semiconductor superlattices formed by geometric control over nanocrystal attachment”. *Nano Lett.* **13**, 2317–2323 (2013).
2. Boneschanscher, M. P. et al. “Long-range orientation and atomic attachment of nanocrystals in 2D honeycomb superlattices”. *Science* **344**, 1377–1380 (2014). doi:10.1126/science.1252642
3. Pound, G. M. & Mer, V. K. La. “Kinetics of Crystalline Nucleus Formation in Supercooled Liquid Tin 1,2”. *J. Am. Chem. Soc.* **74**, 2323–2332 (1952).
4. LaMer, V. K. & Dinegar, R. H. “Theory, Production and Mechanism of Formation of Monodispersed Hydrosols”. *J. Am. Chem. Soc.* **72**, 4847–4854 (1950).
5. Banfield, J. F. “Aggregation-Based Crystal Growth and Microstructure Development in Natural Iron Oxyhydroxide Biomineralization Products”. *Science* **289**, 751–754 (2000).
6. Pacholski, C., Kornowski, A. & Weller, H. “Self-assembly of ZnO: from nanodots to nanorods”. *Angew. Chem. Int. Ed. Engl.* **41**, 1188–1191 (2002).
7. Li, D. et al. “Direction-specific interactions control crystal growth by oriented attachment”. *Science* **336**, 1014–1018 (2012).
8. Schliehe, C. et al. “Ultrathin PbS sheets by two-dimensional oriented attachment”. *Science* **329**, 550–553 (2010).
9. Cho, K.-S., Talapin, D. V, Gaschler, W. & Murray, C. B. “Designing PbSe nanowires and nanorings through oriented attachment of nanoparticles”. *J. Am. Chem. Soc.* **127**, 7140–7147 (2005).
10. Kalesaki, E., Evers, W. H., Allan, G., Vanmaekelbergh, D. & Delerue, C. “Electronic structure of atomically coherent square semiconductor superlattices with dimensionality below two”. *Phys. Rev. B* **88**, 115431 (2013).

11. Kalesaki, E. et al. “Dirac Cones, Topological Edge States, and Nontrivial Flat Bands in Two-Dimensional Semiconductors with a Honeycomb Nanogeometry”. *Phys. Rev. X* **4**, 011010 (2014).
12. Beugeling, W. et al. “Topological states in multi-orbital HgTe honeycomb lattices”. *Nat. Commun.* **6**, 6316 (2015).
13. Evers, W. H. et al. “High charge mobility in two-dimensional percolative networks of PbSe quantum dots connected by atomic bonds”. *Nat. Commun.* **6**, 8195 (2015).
14. Whitham, K. et al. “Charge transport and localization in atomically coherent quantum dot solids”. *Nat. Mater.* **15**, 557–563 (2016).
15. Pietra, F. et al. “Semiconductor nanorod self-assembly at the liquid/air interface studied by in situ GISAXS and ex situ TEM”. *Nano Lett.* **12**, 5515–5523 (2012).
16. Bian, K. et al. “Shape-anisotropy driven symmetry transformations in nanocrystal superlattice polymorphs”. *ACS Nano* **5**, 2815–2823 (2011).
17. Li, R., Bian, K., Hanrath, T., Bassett, W. A. & Wang, Z. “Decoding the superlattice and interface structure of truncate PbS nanocrystal-assembled supercrystal and associated interaction forces”. *J. Am. Chem. Soc.* **136**, 12047–12055 (2014).
18. Choi, J. J. et al. “Controlling nanocrystal superlattice symmetry and shape-anisotropic interactions through variable ligand surface coverage”. *J. Am. Chem. Soc.* **133**, 3131–3138 (2011).
19. Choi, J. J., Bian, K., Baumgardner, W. J., Smilgies, D.-M. & Hanrath, T. “Interface-induced nucleation, orientational alignment and symmetry transformations in nanocube superlattices”. *Nano Lett.* **12**, 4791–8 (2012).
20. Weidman, M. C., Smilgies, D.-M. & Tisdale, W. A. “Kinetics of the self-assembly of nanocrystal superlattices measured by real-time in situ X-ray scattering”. *Nat. Mater.* **15**, 775–781 (2016).
21. Evers, W. H. et al. “Entropy-driven formation of binary semiconductor-nanocrystal superlattices”. *Nano Lett.* **10**, 4235–4241 (2010).
22. Bodnarchuk, M. I., Kovalenko, M. V., Heiss, W. & Talapin, D. V. “Energetic and entropic contributions to self-assembly of binary nanocrystal superlattices: temperature as the structure-directing factor”. *J. Am. Chem. Soc.* **132**, 11967–11977 (2010).
23. Hanrath, T., Choi, J. J. & Smilgies, D.-M. “Structure/processing relationships of highly ordered lead salt nanocrystal superlattices”. *ACS Nano* **3**, 2975–88 (2009).
24. Narayanan, S., Wang, J. & Lin, X.-M. “Dynamical self-assembly of nanocrystal superlattices during colloidal droplet evaporation by in situ small angle x-ray scattering”. *Phys. Rev. Lett.* **93**, 135503 (2004).
25. Simon, P. et al. “Interconnection of nanoparticles within 2D superlattices of PbS/oleic acid thin films”. *Adv. Mater.* **26**, 3042–3049 (2014).
26. Van Aert, S., Batenburg, K. J., Rossell, M. D., Erni, R. & Van Tendeloo, G. “Three-dimensional atomic imaging of crystalline nanoparticles”. *Nature* **470**, 374–347 (2011).
27. Van Aert, S. et al. “Procedure to count atoms with trustworthy single-atom sensitivity”. *Phys. Rev. B* **87**, 064107 (2013).
28. Jones, L., MacArthur, K. E., Fauske, V. T., van Helvoort, A. T. J. & Nellist, P. D. “Rapid estimation of catalyst nanoparticle morphology and atomic-coordination by high-resolution Z-contrast electron microscopy”. *Nano Lett.* **14**, 6336–6341 (2014).
29. Bals, S. et al. “Atomic scale dynamics of ultrasmall germanium clusters”. *Nat. Commun.* **3**, 897 (2012).
30. Woo, J. Y. et al. “Ultrastable PbSe Nanocrystal Quantum Dots via in Situ Formation of Atomically Thin Halide Adlayers on PbSe(100)”. *J. Am. Chem. Soc.* **136**, 8883–8886 (2014).
31. Peters, J. L. et al. “Ligand-induced shape transformation of PbSe nanocrystals”. *Chem. Mater.* [acs.chemmater.7b01103](https://doi.org/10.1021/acs.chemmater.7b01103) (2017).
32. Thapar, V. et al. “Entropic self-assembly of freely rotating polyhedral particles confined to a flat interface”. *Soft Matter* **11**, 1481–1491 (2015).
33. Sandeep, C. S. S. et al. “Epitaxially connected PbSe quantum-dot films: controlled neck formation and optoelectronic properties”. *ACS Nano* **8**, 11499–11511 (2014).

35. Baumgardner, W. J., Whitham, K. & Hanrath, T. "Confined-but-connected quantum solids via controlled ligand displacement". *Nano Lett.* **13**, 3225–3231 (2013).
36. Zhang, H., De Yoreo, J. J. & Banfield, J. F. "A Unified Description of Attachment-Based Crystal Growth". *ACS Nano* **8**, 6526,6530 (2014).
37. Zhang, H. & Banfield, J. F. "Energy Calculations Predict Nanoparticle Attachment Orientations and Asymmetric Crystal Formation". *J. Phys. Chem. Lett.* **3**, 2882–2886 (2012).
Steckel, J. S., Yen, B. K. H., Oertel, D. C. & Bawendi, M. G. "On the mechanism of lead chalcogenide nanocrystal formation". *J. Am. Chem. Soc.* **128**, 13032–13033 (2006).



Chapter 5

Entering the third dimension

• *Abstract* •

The adsorption and self-assembly of PbSe nanocrystals (NCs) at liquid-air interfaces has led to remarkable nanocrystal superlattices, which show atomic order and a superimposed nanoscale geometry. The experiments in Chapter 4 have unraveled the mechanism of formation of the superlattice with a square nanogeometry, which is governed by remarkable phase transitions. Following these results, we now focus on the adsorption geometry of PbSe NC monolayers at the liquid-air interface. We combine in-situ grazing-incidence small/wide angle X-ray scattering (GISAXS/GIWAXS) combined with X-ray reflectivity (XRR) to obtain the 3-D adsorption geometry of the nanocrystal monolayer. We extract the electron density profile in the direction perpendicular to the liquid-air interface from the XRR measurements, and show that nanocrystals larger than 5.5 nm align with a $\langle 100 \rangle$ direction perpendicular to the interface. We combine the information from the three techniques in order to build a full three-dimensional in-situ picture of PbSe nanocrystals adsorbed at the ethylene glycol-air interface. The adsorption geometry of the NCs before oriented attachment are expected to have great impact on the atomically connected 2-D superlattices.

Based on: The Adsorption Geometry of PbSe Nanocrystals at Liquid-Air Interfaces.

Jaco J. Geuchies, Ellenor Geraffy, Carlo van Overbeek, Federico Montanarella, Marlou R. Slot, Oleg Konovalov, Andrei V. Petukhov and Daniel Vanmaekelbergh.

In preparation

5.1 - Introduction

The self-assembly of semiconductor NCs on a liquid substrate has been pioneered by Murray et al.¹, who confined the synthesis of so called superlattices at a liquid-air interface. By dropcasting a suspension of NCs in an apolar, volatile solvent on top of diethylene glycol, the NCs are forced to adsorb at the liquid-air interface and self-organize into large-area binary superlattices upon solvent evaporation. Recently this method has been extended to form atomically connected quantum dot solids; through a process called oriented attachment, PbSe NCs are shown to align their atomic lattices and fuse epitaxially into a single-crystal of one NC in thickness². By tuning the synthesis conditions, various superlattice geometries could be obtained, such as a square superlattice geometry, where the NCs have a {100} facet pointing upwards and a honeycomb superlattice geometry, where the NCs have a {111} facet pointing upwards³. In both superlattice allotropes, the NCs attach via their {100} facets, which contain none or only loosely bound oleate ligands⁴.

Recently we have studied the formation mechanism of the square NC superlattice in-situ, and showed that the NCs undergo a remarkable sequence of phase transitions⁵. Upon solvent evaporation, the NCs adsorb at the liquid-air interface and form a monolayer with hexagonally packed particles. Upon ligand detachment from the NC surface, the NCs align crystallographically with a {100} facet pointing upwards. During this process, the hexagonal geometry of the superlattice is changed to a square geometry before the particles attach epitaxially via a necking process, where the surface atoms move to form the connection between the NCs. There are still a large number of open questions regarding the described self-assembly process: how is the honeycomb superlattice formed? What are the factors driving the final superlattice geometry towards a square or a honeycomb geometry? Which factors determine the amount of disorder on both atomic and nanocrystal length scales and can we try to reduce this⁶⁻¹⁰?

The adsorption geometry of the NCs at a liquid-air interface is expected to have a large impact on the final geometry of the NC superlattices. Ultimately, the balance of the shape and surface energies of the NC and the surrounding liquids will determine the way the NCs adsorb at the interface¹¹. Moreover, the interfacial adsorption of the NCs will also create a capillary distortion of the liquid. Soligno et al. showed that cubes can create a hexapolar distortion of a liquid-liquid interface which can induce directional interactions between the NCs¹². Recently, the relation between the surface chemistry and the shape of PbSe nanocrystals has been studied by Peters et al.⁴. They showed that chemisorption and surface reconfiguration results in a transformation of the NC shape from a truncated nanocube with rough surface facets to a truncated octahedron with larger and smooth {111} facets.

In this chapter, we focus on the nearly last stage of the process of superlattice formation, i.e. when the NC monolayer rests on the ethylene glycol substrate but in principle before atomic attachment has taken place. We adsorb PbSe NCs with different sizes at the ethylene glycol-air interface and study the in-plane NC geometry using grazing-incidence small-angle X-ray scattering (GISAXS) and the crystallographic orientation of the NCs at the liquid-air interface using grazing-incidence wide-angle X-ray scattering (GIWAXS). Furthermore, we extend these two techniques with specular X-ray reflectivity (XRR) measurements^{13,14}, which allowed us to obtain the density profile of the NC monolayer in the direction perpendicular to the interface.

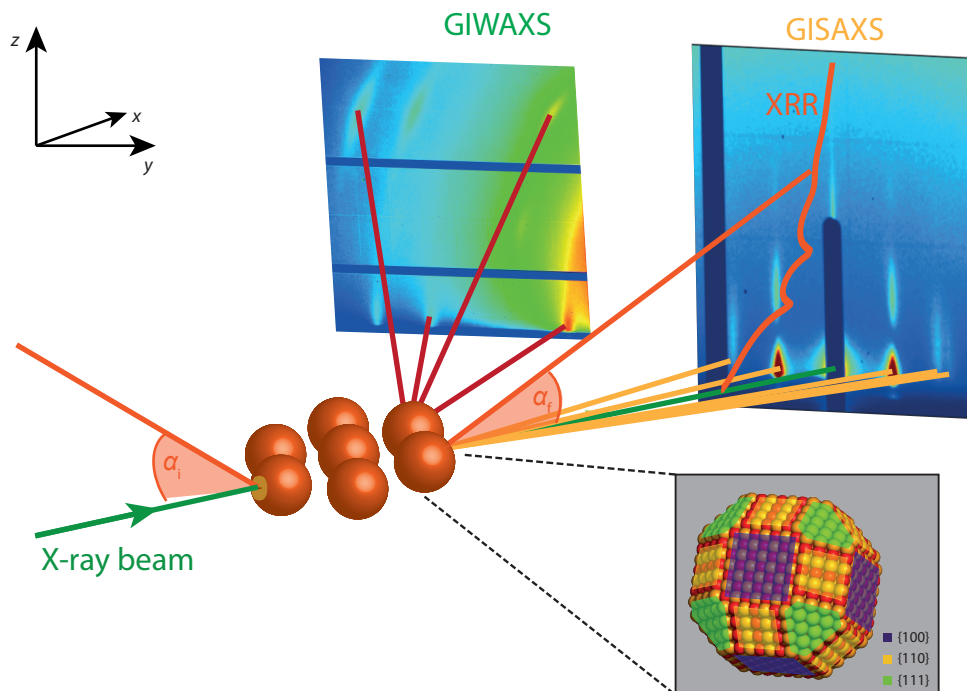


Figure 5.1: Schematic of the performed GISAXS, GIWAXS and XRR experiments performed at ID10 of the ESRF. The GISAXS/GIWAXS experiments, which reveal the order of the NCs in the plane of the monolayer, are done using an angle of incidence of 0.14° . A detector is placed in the forward scattering direction to collect the GISAXS data, which reveals information on the inter-nanocrystal order. A second detector is placed at a higher angle and closer to the sample to collect the GIWAXS signal, which reveals information on the crystallographic orientation of the NCs with respect to the NC monolayer. Upon completion of solvent evaporation, the specular XRR is collected using a dual crystal deflection scheme; the angle of incidence is varied and the intensity of the specular reflection is recorded. The inset shows a schematic of a PbSe truncated nanocrystal.

We show that larger PbSe NCs (≥ 6 nm) align crystallographically at the interface with a [001] axis perpendicular to the interface. Smaller NCs (≤ 5.5 nm) do not have a preferred atomic orientation. For the first time, we reveal the full 3-D structure of NC monolayers adsorbed at the liquid-air interface on the atomic and nanocrystal length scales.

5.2 - Results and discussion

Figure 5.1 shows a schematic of the performed X-ray scattering experiments. The incoming X-ray beam glances the liquid-air interface at an incident angle, α_i , of 0.14° , i.e. the critical angle for total external reflection at 22 keV for PbSe. The GISAXS pattern is recorded in the forward direction and reveals information on the periodicity and order in the NC monolayer. The atomic diffraction is recorded at a detector placed closer to the sample under a higher angle. The collected GIWAXS signal allows us to obtain the crystallographic orientation of the NCs at the liquid-air interface. The beforementioned techniques are complemented with specular XRR measurements. Using the dual crystal deflection diffractometer at the ID10 beamline of the ESRF, the angle of incidence is varied and the intensity of the specular beam is recorded on a 1D

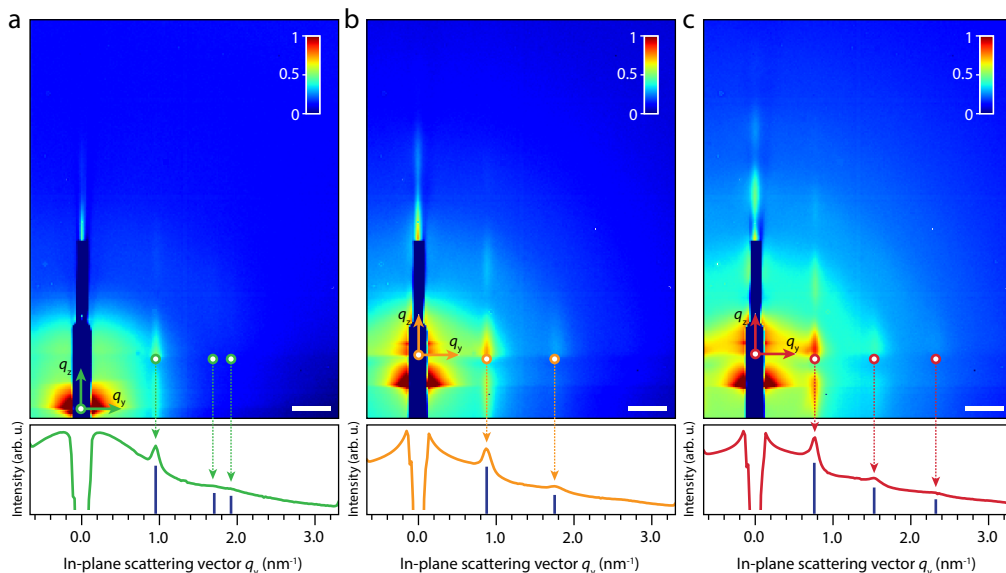


Figure 5.2: GISAXS analysis of monolayers of small, medium and large PbSe NCs at the ethylene glycol - air interface. Intensity traces in the horizontal scattering direction q_y are depicted below the GISAXS patterns. The obtained Bragg rod positions are indicated with blue vertical lines below the intensity traces. **(a)** GISAXS pattern of the small NCs. The relative positions of the Bragg rods in the horizontal scattering direction (depicted with green arrows) indicate the formation of an hexagonally close packed monolayer of NCs. **(b)** GISAXS pattern of the medium sized NCs. The position of the Bragg rods (depicted with yellow arrows) seem to indicate that there is a preference for NCs ordering in one dimension. **(c)** GISAXS pattern of the large NCs. The relative positions of the Bragg rods again indicate that there is a preference for NC ordering in one dimension. Comparing the small, medium and large NCs, the Bragg rods move inward, indicating an increased center-to-center distance of the particles in the NC monolayer. Scalebars in the GISAXS patterns equal 0.5 nm^{-1} .

detector on the diffractometer arm. The scattering vector for this specular reflection only has a component in the vertical direction, i.e. q_z , which allows us to obtain information on the density profile of the NC monolayer in the direction perpendicular to the liquid-air interface. When a monolayer of NCs is present at the liquid-air interface, the signal is modulated due to constructive and destructive interference upon scattering and so-called Keesig fringes can be observed. These fringes modulate with a period $2\pi/\Delta$ in reciprocal space, where Δ is the thickness of the NC monolayer¹⁵.

We synthesized NCs with varying sizes in the range of 4-10 nm, as outlined in the Methods section. From the literature it is already known that the truncation of the NCs is decreased when increasing the NC size¹⁶. The size of the {100} facets increases at the expense of the {110} and {111} facets giving more cubic shaped NCs. We will now focus the discussion of NCs with a size of $5.1 \pm 0.5 \text{ nm}$ (from now referred to as small NCs), $7.1 \pm 0.5 \text{ nm}$ (referred to as medium sized NCs) and $8.2 \pm 0.7 \text{ nm}$ (referred to as large NCs). The characterization of these NC building blocks is presented further in the Methods section.

The NC dispersion in toluene is dropcasted on ethylene glycol inside the liquid cell, which acts as an immiscible liquid substrate. To the ethylene glycol substrate we add $100 \mu\text{L}$ of a $31.7 \mu\text{M}$ oleic acid in ethylene glycol solution for two reasons. The first is to increase the wettability of the

toluene droplet with NCs on the ethylene glycol. The second reason is that addition of oleic acid to the ethylene glycol subphase has proven to stop oriented attachment of the NCs².

We start the discussion of the obtained results based on the GISAXS data presented in figure 5.2. The data is acquired upon complete solvent evaporation. The GISAXS signal for the small NCs, shown in figure 5.2(a) shows Bragg rods at positions of 0.94 nm^{-1} , 1.62 nm^{-1} and 1.88 nm^{-1} in the horizontal scattering direction q_y with a FWHM of 0.06 nm^{-1} . The peak positions of 1: $\sqrt{3}$:2 indicate that the NCs are ordered in a 2-D hexagonal lattice with a NC center-to-center distance of $7.7 \pm 0.4 \text{ nm}$, roughly the NC diameter plus interdigitated oleic acid ligands.

The GISAXS pattern of the medium sized NCs, depicted in figure 5.1(b), shows Bragg rods at 0.86 nm^{-1} and 1.71 nm^{-1} in the q_y direction with a FWHM of 0.08 nm^{-1} . The 1:2 relative peak positions indicate that there is a preference for NC ordering in one dimension, e.g. the formation of linear structures. The NC center-to-center distance is calculated to be $7.3 \pm 0.7 \text{ nm}$. The relatively small center-to-center distance of the NCs compared to the NC diameter is not fully understood. Hanrath and coworkers showed through Molecular Dynamics simulations that interparticle distances as small as 0.5 nm can be achieved when the ligand density of oleic acid on PbSe is low enough¹⁷. This is a hard parameter to quantify during these experiments, as the ligand density likely changes throughout the self-assembly process. For the large NCs, the GISAXS signal depicted in figure 5.1(c) shows Bragg rods at 0.75 nm^{-1} , 1.52 nm^{-1} and 2.18 nm^{-1} in the q_y direction with a FWHM of 0.05 nm^{-1} . Again the 1:2:3 relative peak positions indicate that there is a preference for NC ordering in one dimension. The center-to-center distance is calculated to be $8.4 \pm 0.5 \text{ nm}$. Even though the occurrence of oriented attachment cannot be fully excluded, which would explain the decreased center-to-center distances of the NCs, we think it is highly unlikely to occur due to the presence of additional ligands in the ethylene glycol subphase.

The crystallographic orientation of the NCs is obtained by measuring the diffraction from their atomic lattices, which is presented in figure 5.3. We calculated the expected GIWAXS pattern for NCs having a $\{001\}$ axis pointing perpendicular to the liquid-air interface in figure 5.3(a). Figures 5.3(b-d) show the GIWAXS patterns corresponding to the small, medium sized and large NCs respectively, which were recorded simultaneously with the GISAXS patterns in figure 5.2. For the small NCs we observe powder rings in the GIWAXS pattern, which means that the NCs do not have a preferential orientation at the liquid-air interface. Either the NCs are still freely rotatable, or the ensemble of NCs have random, static orientations which will average out in a ring in the GIWAXS pattern.

The GIWAXS pattern of the medium sized NCs, shown in figure 5.3(c), shows a series of well defined diffraction spots. An azimuthal intensity trace over the reflection originating from the $\{222\}$ planes shows that it has an orientation of 36.0° with respect to the liquid-air interface, corresponding to NCs having a $\{001\}$ facet pointing upwards. The FWHM of the reflection, which is an indication of the degree of rotational freedom the NCs still have at the liquid-air interface, is 6.5° . The GIWAXS pattern of the large NCs, shown in figure 5.3(d), matches the calculated GIWAXS pattern very well. It shows that the NCs have the same orientation as the medium-sized NCs, i.e. a $\{001\}$ facet pointing upwards. The distribution in orientations is slightly smaller, as the FWHM of the 222 reflection is 6.1° . This means that the large NCs have less rotational freedom at the liquid-air interface.

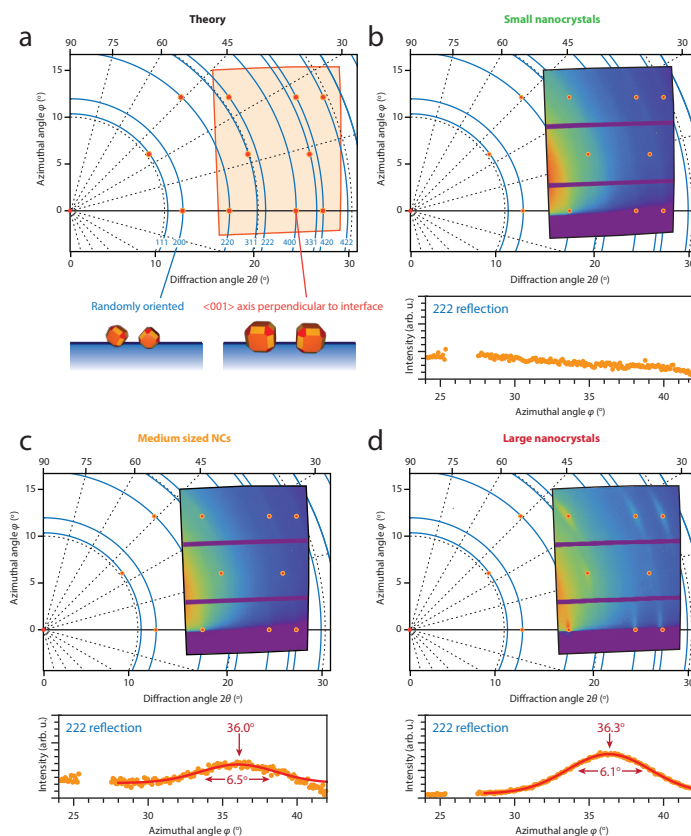


Figure 5.3: Analysis of the corresponding GIWAXS patterns reveal crystallographic alignment of larger PbSe NCs with respect to the liquid-air interface. Intensity traces are taken over the 222 diffraction ring vs. their azimuthal angle ϕ , and are shown below the image. **(a)** Calculated GIWAXS pattern for rocksalt PbSe NCs having a [001] axis perpendicular to the liquid-air interface (red dots) and when allowed full rotational freedom (blue rings). The orange area shows the position of the GIWAXS detector in this coordinate space. **(b)** GIWAXS pattern of the small NCs, showing no preferential crystallographic alignment. **(c)** GIWAXS pattern of the medium-sized NCs, which can be fitted well to NCs pointing a [001] axis upwards, perpendicular to the liquid-air interface. The width of the 222 reflection is an indication of how well the NCs are atomically aligned with respect to the liquid-air interface. The medium-sized nanocrystals have a 6.5° variation in orientation (FWHM). **(d)** GIWAXS pattern of the large NCs, which can also be fitted well to NCs pointing a [001] axis upwards. The width of the 222 reflection is smaller compared to the same reflection of the medium sized NCs; the large nanocrystals have a 6.1° variation in orientation (FWHM).

The orientation of the NCs is also verified by looking at intensity traces in the 2θ direction along the scattering horizon (azimuthal angle equals $\sim 1^\circ$), which are presented in Figure 5.9. For the medium-sized and the large NCs, only reflections originating from $\{hk0\}$ PbSe lattice planes are observed along the scattering horizon. These particular atomic planes are oriented perpendicular to the liquid-air interface when the NCs have a [001] axis pointing upwards, and hence scatter horizontally. Previously observed superlattices from PbSe NCs have been shown to show attachment of their $\{100\}$ facets^{2,3}. We are able to verify whether or not the NCs are attached, by looking at the FWHM of the 400 reflection in the horizontal scattering direction and estimating the crystalline size of the NCs. The results are presented in Table 5.1. Since the

diameters obtained using the Scherrer equation are not significantly larger than the NC diameters determined by TEM, we conclude that the NCs are not connected and no oriented attachment has occurred. NC alignment was also observed by Van der Stam et al., who recently showed that upon addition of oleic acid, 11 nm polyhedral ZnS bipyramid NCs align atomically with their {002} facet pointing upwards at the ethylene glycol-air interface¹⁷. They show that two crystallographic orientations of the NCs are possible at the liquid-air interface. The one which is observed experimentally is determined by the relative size of the specific NC facet; the orientation is such that the facet with the largest surface area is planar with the liquid-air interface¹⁹.

A similar explanation could be applied to the experiments shown here. As the NCs grow in size, the truncation is decreased and the NCs attain a more cubic shape. This means that the relative size of the {100} facets increases at the expense of the {110} and {111} facets. Especially for the large NCs, which have relatively large {100} facets, this would mean that the minima in the adsorption free energy are deeper compared to those for the other adsorption geometries. However, this does not explain why we do not observe any NCs which align crystallographically with a [111] axis perpendicular to the ethylene glycol-air interface, the alignment of the NCs for the honeycomb superlattice. Hanrath et al. showed that large cubic PbSe NCs with an edge length of 25 nm do align a [111] axis perpendicular to the toluene-air interface, but there the NCs formed 3-D BCC superlattices¹¹.

To obtain quantitative information in the direction perpendicular to the liquid-air interface we performed specular X-ray reflectivity (XRR) measurements. As explained in Chapter 2, the scattering vector \mathbf{q} only has a component in the direction perpendicular to the interface z , when one measures the specular reflection. The interference of the X-ray photons reflected from a stratified surface will give rise to periodic intensity oscillations, called Kiessig fringes. The periodicity of the oscillations contains information on the layer thickness, whereas the scattered intensity depends on the averaged scattering density profile across the interface. This means that one can fit the acquired reflectivity curve to get detailed information on a materials density gradient in the z -direction., e.g. how NCs adsorb at liquid-air or liquid-liquid interfaces.

The adsorption behaviour of nanoparticles at interfaces has already been studied using a combination of X-ray techniques. Vorobiev et al. studied self-assembly of ironoxide nanoparticles of different sizes at the water-air interface under different surface pressures to show the optimal conditions for making monolayer films of the particles²⁰. XRR has been used recently in a combination with GISAXS to study various types of Au nanoparticles on different substrates^{21,22}. Kosif et al. were able to produce rigid NC films at the water-air interface by connecting gold nanoparticles together with thiol-group containing linker molecules²³. They studied the film under different surface pressures structure using grazing-incidence X-ray diffraction and XRR to see how much force was necessary to buckle the NC film.

We continue the discussion here with a comparison of the XRR data from the small and large PbSe NCs, which is presented in Figure 5.4. For the fitting of the data, we apply a recursive fitting procedure based on a Parratt formalism²⁴. In this fitting procedure, the nanoparticles are approximated to be spherical and are placed on an ethylene-glycol air interface. The density profile in the z direction is divided into N strata, or layers, for which the average value of the

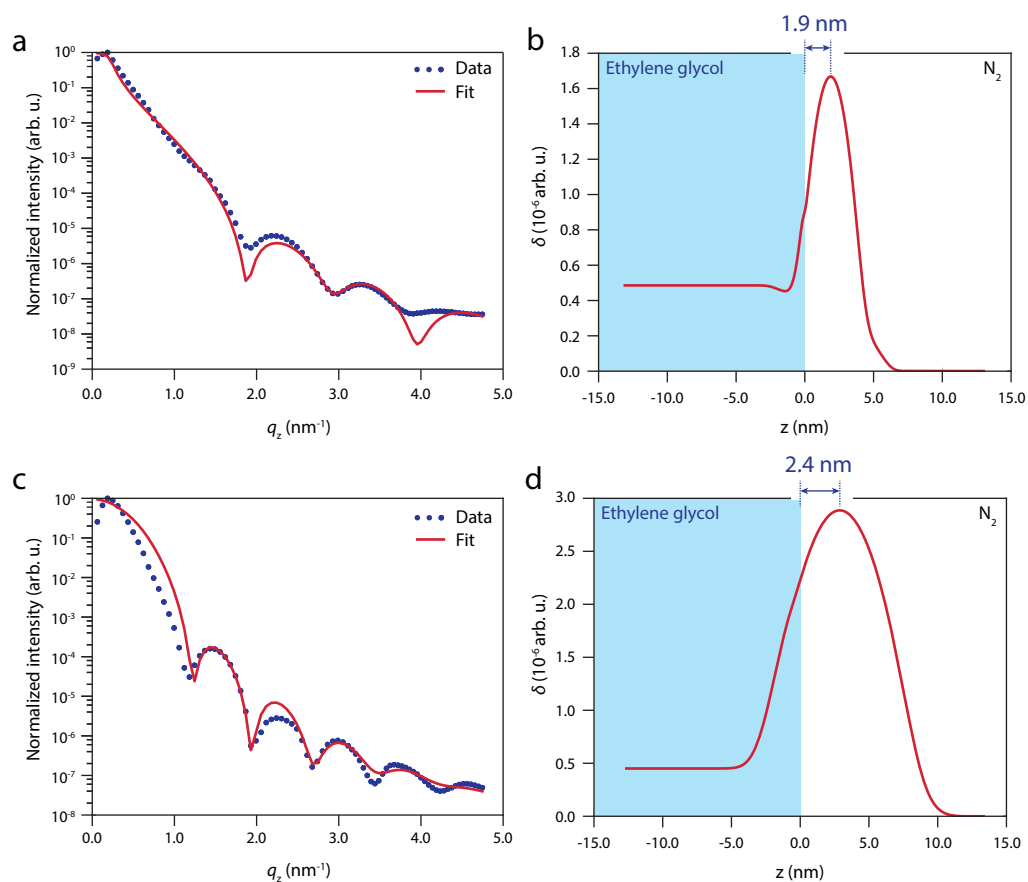


Figure 5.4: Analysis of the specular X-ray reflectivity of the small and large PbSe NCs. (a) Measured XRR curve from a monolayer of small PbSe NCs. The red line is the best fit of the data, in which we approximate the NCs as spherical. (b) Scattering length density (SLD) plot, obtained using the fitted data. The SLD is proportional to the electron density and hence gives a quantitative picture of how the nanocrystals adsorb at the liquid-air interface. The center of mass of the NCs is sticking out 1.9 nm above the ethylene glycol-air interface. (c) Measured XRR curve from a monolayer of large PbSe NCs. The red line is the best fit of the data. (d) SLD plot of the large PbSe nanocrystals, obtained using the fitted data. The center of mass of the NCs is sticking out 2.4 nm above the ethylene glycol-air interface.

refractive index, $n_j = 1 - \delta_j + i\beta_j$, is calculated. The fit takes into account the position of the particle with respect to the liquid-air interface, the thickness of the ligand corona around the NC and several density and roughness parameters (see Methods section).

Figure 5.4 (a) shows the measured XRR curve from the small NCs as blue dots, with the corresponding fit as a red solid line. The clear oscillations of the signal only show one period, proving that we truly are looking at a monolayer of NCs. The value of the real part of the refractive index of each layer j , δ_j , is proportional to the electron density of that layer. This is plotted in Figure 5.4(b). The maximum of the SLD profile corresponds to a mean value for the center of mass of the NCs above the liquid-air interface level. The center of mass of the small NCs is sticking out 1.9 nm above the ethylene glycol-air interface. This can be rationalized considering

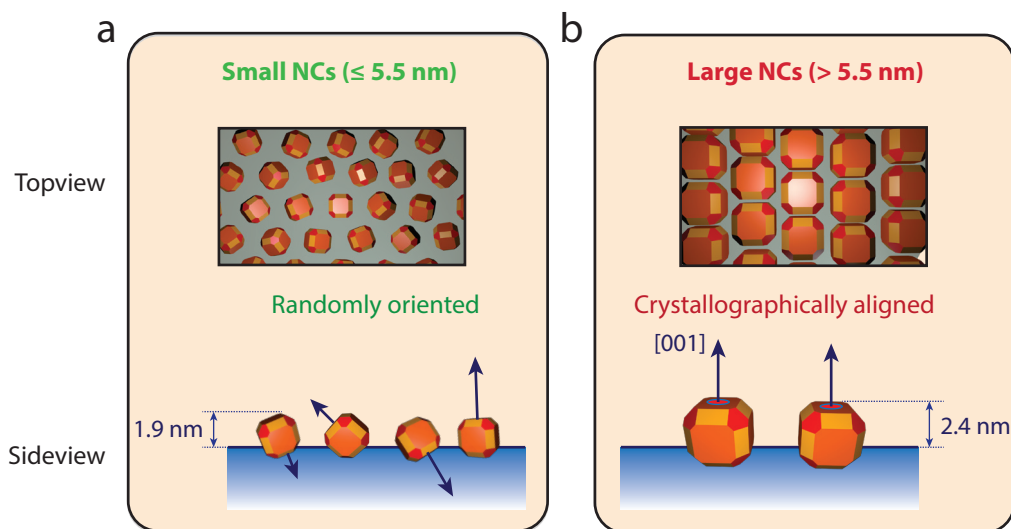


Figure 5.5: Schematic representation of the NCs adsorbed at the ethylene glycol-air interface. Combining the information from the GISAXS data (NC-NC distance), the GIWAXS data (crystallographic orientation) and the XRR measurements (height of the NCs with respect to the interface), we can create a 3-D model of how the NCs adsorb at the ethylene glycol-air interface. **(a)** The small NCs are randomly oriented at the liquid-air interface, presumably due to the limited faceting of the particles. **(b)** The larger NCs attain a more cubic shape, with larger {100} facets compared to the smaller NCs, making it favorable to align crystallographically at the liquid-air interface with a {100} facet pointing upwards.

the oleate ligands on the surface of the NCs. The apolar tails do not want to stick into the polar ethylene glycol and hence the particles prefer to be on top of the liquid. The acquired PbSe film thickness of 5.0 nm is in good agreement with the obtained size of the NCs using TEM.

Figure 5.4 (c) presents the measured XRR curve from the large NCs as blue dots, with the corresponding fit as a red solid line. Again only one periodicity of the XRR signal is observed, confirming that we are measuring a NC monolayer again. The corresponding SLD plot, shown in Figure 5.4(d) shows that the center of mass of the large NCs is sticking out 2.4 nm above the ethylene glycol-air interface. This also explains the easy transfer to solid substrates using a Langmuir-Schaefer type stamping technique. We do note that the models of the NCs can be improved significantly, e.g. by using a truncated cubic shape of the NCs with varying truncation parameters for the different NC sizes. This will ultimately result in better fits of the XRR data and a more detailed description of the adsorption behaviour of the NCs at the ethylene glycol-air interface. We note that the observed NC adsorption geometry could differ strongly from the initial adsorption geometry at the toluene-air interface. Future experiments will be focussed on obtaining a stable (i.e. non evaporating) toluene-air interface to see how the NCs adsorb and align during the early stages of the self-assembly process.

Combining the data from the GISAXS, GIWAXS and XRR experiments, we can create a size dependent 3-D model of how PbSe NCs adsorb at the ethylene glycol-air interface. A schematic representation is shown in Figure 5.5. The smaller NCs (with sizes ≤ 5.5 nm) are oriented randomly, which is likely the result of a reduced size of the NC facets compared to larger NCs. As the NCs grow in size, the truncation of the particles is reduced and they get a more cubic

shape with larger {100} facets. The increased facet size makes it energetically more favorable to align with a [001] axis perpendicular to the ethylene glycol-air interface. Furthermore, the NCs adsorb on top of this interface, as determined with XRR measurements.

5.3 - Conclusion and outlook

We studied the adsorption behaviour of PbSe NCs at the ethylene glycol-air interface, using a combination of X-ray scattering techniques. We show that larger PbSe NCs align crystallographically with a [001] axis perpendicular to the liquid-air interface, most likely due to the increased facetting of the NCs with increasing size. Furthermore, we combine GISAXS and GIWAXS with specular XRR measurements to obtain a 3-D picture on how these NCs adsorb at the ethylene glycol-air interface and show that the NCs are nearly on top of the ethylene glycol liquid. The adsorption geometry of the NCs in the early stages of oriented attachment are expected to have great impact on the atomically connected 2-D superlattices. Further research has to be performed to increase our understanding of the differences in NC orientation and adsorption that occur between the formation these superlattices with square and honeycomb nanogeometries.

Future X-ray scattering experiments will be focussed on unravelling the adsorption geometry of the PbSe NCs at the toluene-air interface. These experiments are more difficult, as the evaporation of toluene has to be stopped to perform the reflectivity measurements. A solution could lie in using specially developed liquid-cells, which controllably saturate the atmosphere inside the cell with solvent vapor²⁵.

5.4 - Methods

Nanocrystal synthesis. The PbSe nanocrystals used for the oriented attachment experiments in this study were prepared using adapted method of the synthesis described by Steckel et al.²⁶. The synthesis was performed in a glovebox with a water and oxygen free environment. (a) 4.77g of lead acetate trihydrate (99.999% Aldrich), 10.35g of oleic acid (OA, 90% Aldrich) and 39.75g octadecene (ODE, 90% Aldrich) were heated to 130°C under low pressure (10^{-3} bar) for approximately 4 hours. (b) A second mixture containing 3.52g Se (99.999% Alfa Aesar), 46.59 mL trioctylphosphine (TOP, 90% Fluka) and 0.41mL diphenylphosphine (DPP, 98% Aldrich) was prepared by dissolving the Se. Subsequently solution (a) was heated in a three-necked round-bottom flasks to 180°C after which 15mL of solution (b) was rapidly injected. The particles were grown for approximately 60 seconds, after which the reaction was quenched with 20mL butanol. After the solution was cooled down to approximately 50°C, 10 mL methanol was added to induce precipitation of the nanocrystals. The resulting suspension was centrifuged at 2500 rpm for 10 minutes, the supernatant was removed and the washed particles were redispersed in toluene. This washing procedure was repeated two times. For the medium-sized NCs, an additional 300 μ L of oleic acid was added to the Pb-oleate precursor before injection, and the NCs were grown for 180 seconds. For the large NCs, an additional 1000 μ L of oleic acid was added to the Pb-oleate precursor before injection, and the NCs were grown for 20 minutes. Additional oleic acid is known to reduce the activity of the Pb-oleate precursor during the NC formation and hence leads to larger NCs.

In-situ GISAXS/GIWAXS/XRR. The in-situ X-ray scattering experiments under grazing incidence were performed at beamline ID10 of the European Synchrotron Radiation Facility (ESRF), Grenoble. The energy of the incident X-ray beam was set at 22.0 keV, since we noticed that there was a lot less beam-induced sample damage at higher photon energies. We optimized the grazing angle to 0.14° for the best signal-to-noise ratio on both GISAXS and GIWAXS detectors. The scattering was recorded by two Pilatus detectors. The GIWAXS patterns were recorded on a Pilatus 300K detector with 619x487 pixels, each 172x172 μ m² in size, positioned approximately 36 cm from the sample. The GISAXS patterns were recorded on a Pilatus 300K-W detector with 1475x195 pixels, each 172x172 μ m² in size, positioned 0.988 m from the sample. The specular XRR experiments were recorded on a 1-D Mythen detector, which has a pixel size of 50 μ m. The angle of incidence of the X-ray beam was bent down by a dual crystal deflector setup as equipped on the ID10 beamline.

Before drop casting the dispersion of NCs on top of the EG substrate, the X-ray beam was aligned to the surface. The self-assembly was performed in a home-built liquid cell, which can be flushed with argon (or nitrogen) repeatedly to lower the oxygen and water levels (Fig. 4.13 & 5.6). A Teflon petri dish (\varnothing 64 mm) was filled with 28 mL of ethylene glycol. To the ethylene glycol we added 100 μ L of an OA solution (1% (v/v) OA in ethylene glycol) for all experiments. The cell was then flushed five times with vacuum/ N_2 cycles, and was left under a mild N_2 flow.

Next, the PbSe NC solution (1.0 mL; $\sim 3.0 \times 10^{-6}$ mol/L for all experiments) was deposited on top of the liquid substrate. Each frame was recorded with a 10 s integration time.

XRR data fitting. The XRR data was fitted using a least-square fitting procedure employing a Parratt formalism^{15,24}. Here, we simulate a NC at the ethylene glycol-air interface, and stratify the density profile into N layers (by definition, the N 'th layer is the bottom ethylene glycol layer). Each layer has a refractive index of the j 'th layer, $n_j = 1 - \delta_j + i\beta_j$, and thickness Δ_j . The wavevector in each layer q_j is then calculated as

$$q_j = \sqrt{q^2 - 8k^2\delta_j + i8k^2\beta_j} \quad 5.1$$

where k equals $2\pi/\lambda$. The reflectivity of the j 'th layer can be calculated using the Fresnel relation

$$r_{j,j+1} = \frac{q_j - q_{j+1}}{q_j + q_{j+1}} \quad 5.2$$

The first step is to calculate the reflectivity from the bottom N 'th interface. As the substrate is infinitely thick, there are no multiple reflections to consider. From there, it can be iterated upwards through the layers until the top is reached, where the reflectivity amplitude of each layer is calculated as

$$r_{j,j+1} = \frac{r_{j-2,j-1} + r_{j-1,j} p_{j-1}^2}{1 + r_{j-2,j-1} r_{j-1,j} p_{j-1}^2} \quad 5.3$$

Here, $p_j^2 = \text{Exp}(i\Delta_j q_j)$ is the phase factor, accounting for the difference in phase between photons scattered between the j 'th and $j+1$ 'th layer. From the bottom, the reflectivity amplitude is iterated recursively until the total reflectivity amplitude, $r_{0,1}$, at the interface between vacuum and the first layer is obtained.

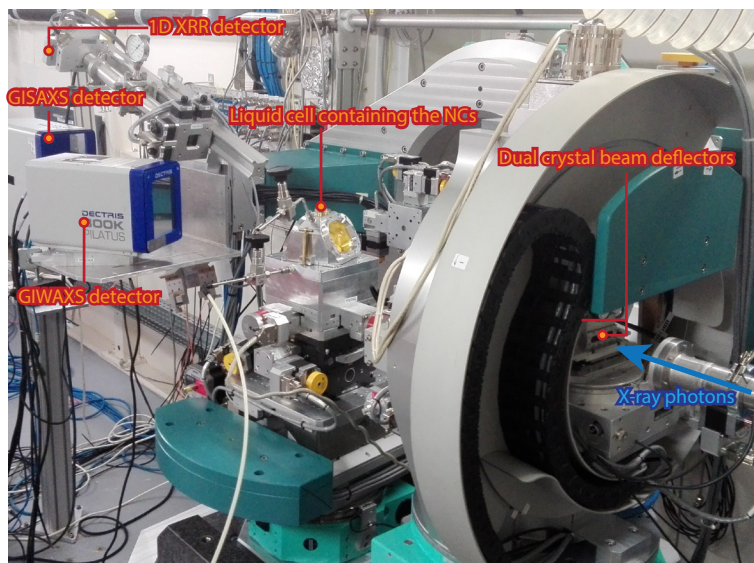


Figure 5.6: Photograph of the experimental geometry at ID10 beamline, ESRF. The X-ray beam is set to have an energy of 22 keV. The GISAXS signal is collected in the forward scattering direction at a sample-to-detector distance of 988 mm. The GIWAXS detector is placed closer to the liquid cell and at a higher angle to capture the atomic diffraction. After complete solvent evaporation, the arm of the diffractometer is lowered to perform XRR experiments. To vary the angle of incidence, we use the new diffractometer of ID10 with a dual crystal deflector to bend the beam down. The intensity of the specular reflection is collected on the 1D XRR detector.

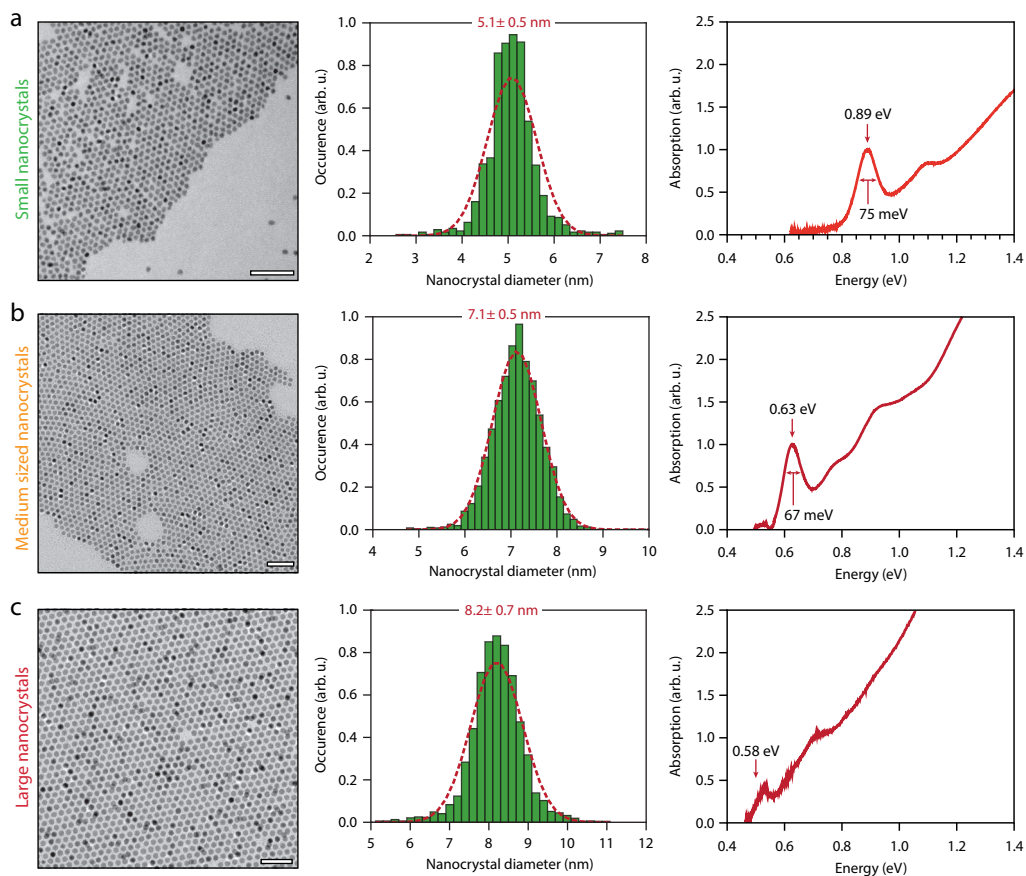


Figure 5.7: Characterization of the PbSe NCs as starting blocks for the self-assembly. The left, middle and right column show a characteristic TEM image, size distribution of the NCs and optical absorption spectrum respectively. The size distribution was obtained with a standard imageJ application. For each NC size, over 1000 NCs were detected to acquire the distribution. **(a)** The small NCs have a diameter of 5.1 ± 0.5 nm. **(b)** The medium sized nanocrystals have a diameter of 7.1 ± 0.5 nm. **(c)** The large NCs have a diameter of 8.2 ± 0.7 nm. The absorption spectrum for these large NCs below 0.6 eV is very noisy, due to the contribution of ligand (and possibly residual solvent) absorption.

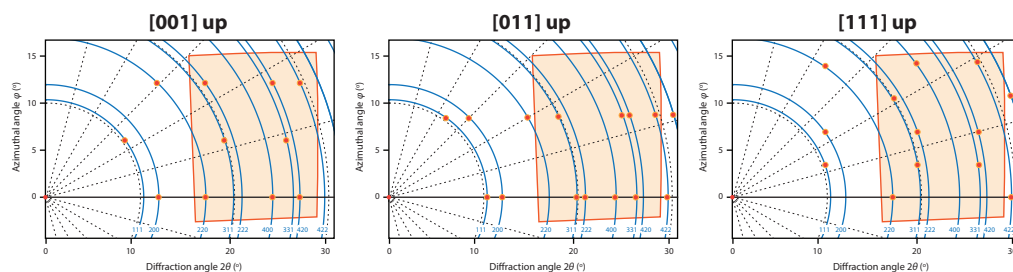


Figure 5.8: Theoretical GIWAXS patterns for different crystallographic orientation of the PbSe NCs. There are three main observed orientations of the PbSe NCs: [001] perpendicular to the plane of the NC monolayer, [011] perpendicular to the plane of the NC monolayer and [111] perpendicular to the plane of the NC monolayer. The acquired GIWAXS patterns match the first orientation, i.e. NCs with a [001] axis pointing upwards, the best.

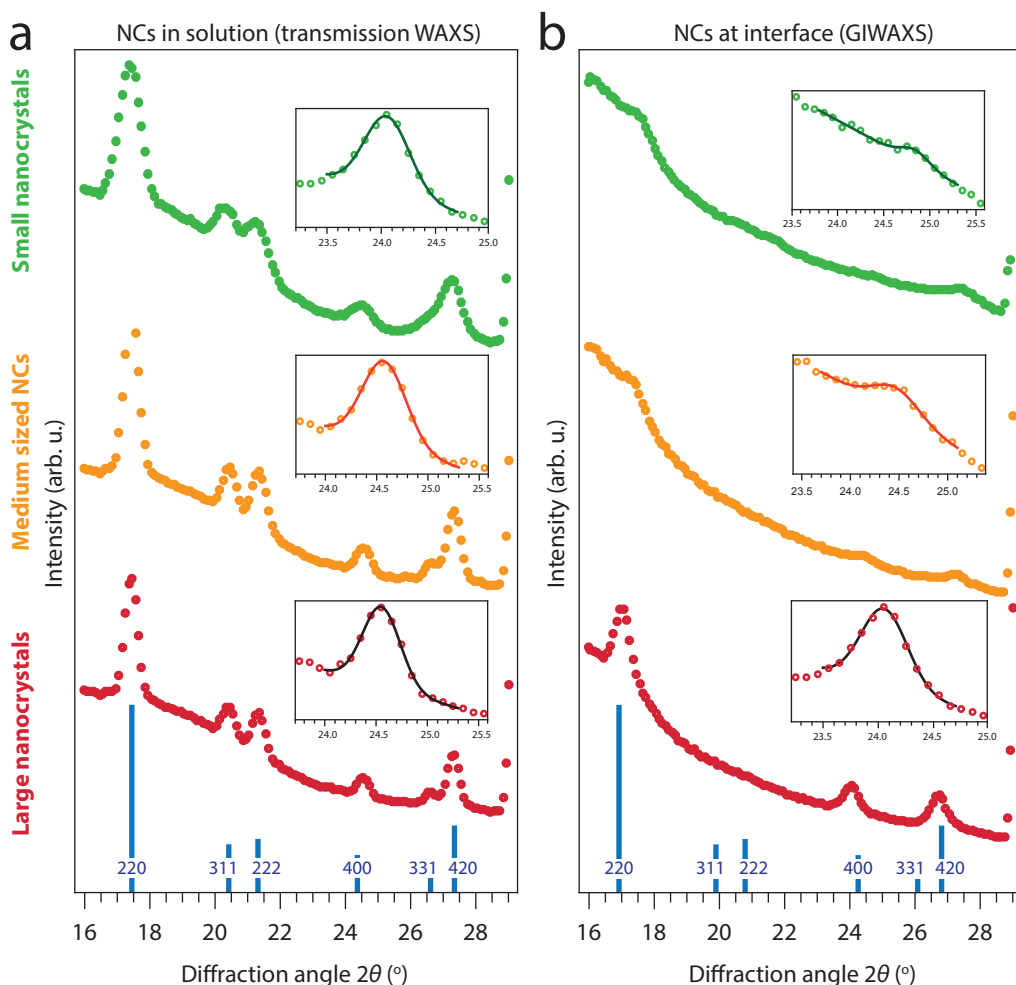


Figure 5.9: Intensity traces in along the 2θ direction of the WAXS signal. The traces were obtained by integrating the signal in the direction of the azimuthal angle from $1-3^\circ$ to increase the signal-to-noise ratio. (a) Transmission WAXS signal of the small (green), medium-sized (yellow) and large (red) NC solutions. The insets show the WAXS signal around the reflection originating from the $\{400\}$ lattice planes and a Gaussian fit to obtain the FWHM. (b) GIWAXS signal of the NC monolayer, obtained by integrating the signal displayed in Figure 5.3 in the azimuthal angle direction from $1-3^\circ$. Note how for the medium-sized NCs only reflections originating from $\{hk0\}$ lattice planes are visible, which indicates that the NCs have a $\{001\}$ facet pointing upwards.

	Solution FWHM (deg)	Solution diameter (nm)	Interface FWHM (deg)	Interface diameter (nm)
Small NCs	0.57	5.8	0.59	5.6
Medium sized NCs	0.47	7.0	0.45	7.4
Large NCs	0.40	8.3	0.38	8.8

Table 5.1: Acquired FWHM of the 400 reflection and the corresponding crystalline NC size. The acquired crystalline sizes of the NCs match the NC diameters obtained with TEM quite well. No significant increase of crystalline size is observed compared to the NC diameter, indicating that the NCs did not fuse together atomically in the performed experiments.

	δ	β
PbSe	2.799×10^{-6}	2.092×10^{-7}
Toluene	4.051×10^{-7}	1.224×10^{-10}
Ethylene glycol	5.218×10^{-7}	2.282×10^{-10}

Table 5.2: Values of the real (δ) and imaginary (β) part of the refractive-index decrement at 10 keV for the materials used in these experiments. δ and β define refraction and absorption in a material accordingly.

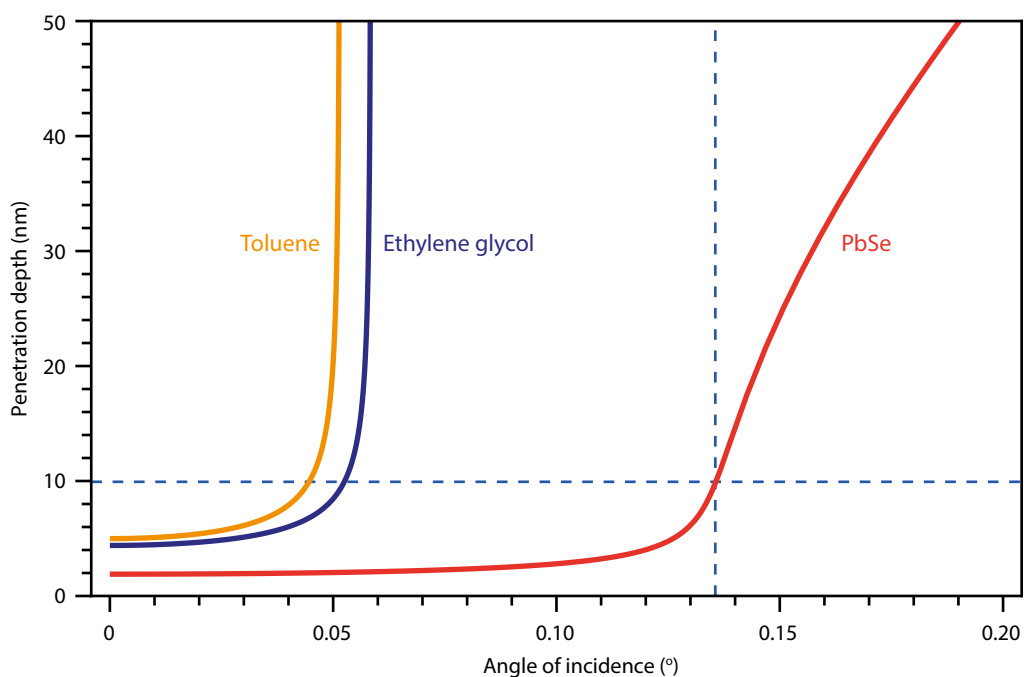


Figure 5.10: Calculation of the X-ray penetration depth as a function of incident angle. The red, blue and yellow lines depict the penetration depths as function of incident angle for PbSe, ethylene glycol and toluene respectively. The blue dashed lines show the incident angle of the experiments (0.14°) and the corresponding penetration depth for PbSe (10 nm). Working at the critical angle of either toluene or ethylene glycol would result in a minute penetration of the X-ray photons into the PbSe superstructure. The above graph is calculated similarly as described in Chapter 4, but with different values of the real and imaginary part of the refractive index, since a different photon energy (22 keV instead of 10 keV) was used here.

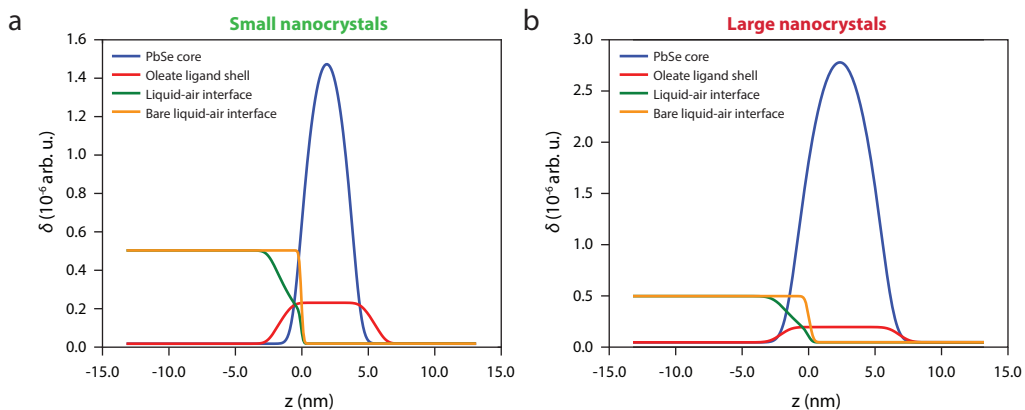


Figure 5.11: Separated scattering length density plots of the contributing components. (a) Scattering length density profile of the small NCs with separated contributing components: the PbSe NC core (blue), oleate ligand shell (red), the liquid-air interface with applied Gaussian broadening (green) and bare liquid-air interface without Gaussian broadening (yellow). (b) Scattering length density profile of the large NCs sample with separated contributing components: the PbSe NC core (blue), oleate ligand shell (red), the liquid-air interface with applied Gaussian broadening (green) and bare liquid-air interface without Gaussian broadening (yellow).

	Small NCs	Large NCs
δN_2 (density = $0.1251 \cdot 10^{-2}$ g/cm ³)	$5.36 \cdot 10^{-10}$	$5.36 \cdot 10^{-10}$
βN_2 (density = $0.1251 \cdot 10^{-2}$ g/cm ³)	$2.34 \cdot 10^{-13}$	$2.34 \cdot 10^{-13}$
δ Ethylene glycol (density = 1.1132 g/cm ³)	$5.86 \cdot 10^{-7}$	$4.54 \cdot 10^{-7}$
β Ethylene glycol (density = 1.1132 g/cm ³)	$1.61 \cdot 10^{-7}$	$1.05 \cdot 10^{-7}$
δ PbSe core (density = 8.1 g/cm ³)	$5.49 \cdot 10^{-6}$	$4.15 \cdot 10^{-6}$
β PbSe core (density = 8.1 g/cm ³)	$4.99 \cdot 10^{-7}$	$6.04 \cdot 10^{-7}$
PbSe core diameter (Å)	50	80
δ Oleate ligand shell (density = 0.895 g/cm ³)	$3.79 \cdot 10^{-7}$	$4.41 \cdot 10^{-7}$
β Oleate ligand shell (density = 0.895 g/cm ³)	$1.39 \cdot 10^{-10}$	$1.39 \cdot 10^{-10}$
Oleate ligand shell thickness (Å)	18.8	9.0
Area per nanocrystal (Å ²)	7272	7406
Particle wetting angle (degrees)	138	126
Roughness between two liquids (Å)	1.3	2.4
Distribution of particle centers (Å)	4.2	6.1

Table 5.2: Parameters used to model the XRR data presented in Figure 5.4 and Figure 5.11. The parameters were optimized with a least-squares fit to the experimental XRR data.

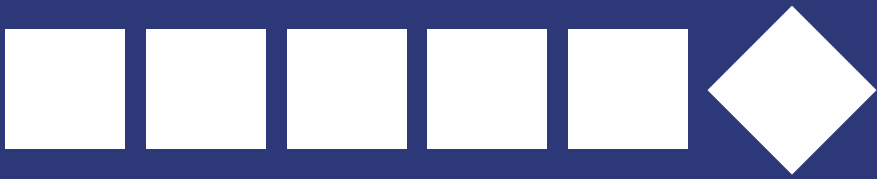
Acknowledgements

We are very grateful to for the excellent experimental support of Andrey Chumakov, who, besides Oleg Kononov, helped out as local contact during the X-ray scattering experiments at ID10, ESRF.

References

1. Dong, A., Chen, J., Vora, P. M., Kikkawa, J. M. & Murray, C. B. “Binary nanocrystal superlattice membranes self-assembled at the liquid-air interface”. *Nature* **466**, 474 (2010).
2. Evers, W. H. et al. “Low-Dimensional Semiconductor Superlattices Formed by Geometric Control over Nanocrystal Attachment”. *Nano Lett.* **13**, 2317–2323 (2013).
3. Boneschanscher, M. P. et al. “Long-range orientation and atomic attachment of nanocrystals in 2D honeycomb superlattices”. *Science* (80-.). science.1252642- (2014).
4. Peters, J. L. et al. “Ligand-Induced Shape Transformation of PbSe Nanocrystals”. *Chem. Mater.* **29**, 4122–4128 (2017).
5. Geuchies, J. J. et al. “In situ study of the formation mechanism of two-dimensional superlattices from PbSe nanocrystals”. *Nat. Mater.* **15**, 1248–1254 (2016).
6. Savitzky, B. H. et al. “Propagation of Structural Disorder in Epitaxially Connected Quantum Dot Solids from Atomic to Micron Scale”. *Nano Lett.* **16**, 5714–5718 (2016).
7. Treml, B. E. et al. “Successive Ionic Layer Absorption and Reaction for Postassembly Control over Inorganic Interdot Bonds in Long-Range Ordered Nanocrystal Films”. *ACS Appl. Mater. Interfaces* **9**, 13500–13507 (2017).
8. Zaluzhnyy, I. et al. “Quantifying Angular Correlations between the Atomic Lattice and Superlattice of Nanocrystals Assembled with Directional Linking”. *Nano Lett.* acs.nanolett.7b00584 (2017).
9. Evers, W. H. et al. “High charge mobility in two-dimensional percolative networks of PbSe quantum dots connected by atomic bonds”. *Nat. Commun.* **6**, 8195 (2015).
10. Whitham, K. et al. “Charge transport and localization in atomically coherent quantum dot solids”. *Nat. Mater.* **15**, 557–563 (2016).
11. Choi, J. J., Bian, K., Baumgardner, W. J., Smilgies, D.-M. & Hanrath, T. “Interface-Induced Nucleation, Orientational Alignment and Symmetry Transformations in Nanocube Superlattices”. *Nano Lett.* **12**, 4791–4798 (2012).
12. Soligno, G., Dijkstra, M. & van Roij, R. “Self-Assembly of Cubes into 2D Hexagonal and Honeycomb Lattices by Hexapolar Capillary Interactions”. *Phys. Rev. Lett.* **116**, 258001 (2016).
13. Chason, E. & Mayer, T. M. “Thin film and surface characterization by specular X-ray reflectivity”. *Crit. Rev. Solid State Mater. Sci.* **22**, 1–67 (1997).
14. Kohli, S., Rithner, C. D., Dorhout, P. K., Dummer, A. M. & Menoni, C. S. “Comparison of nanometer-thick films by x-ray reflectivity and spectroscopic ellipsometry”. *Rev. Sci. Instrum.* **76**, 23906 (2005).
15. Als-Nielsen, J. & McMorrow, D. “Elements of Modern X-ray Physics”. (John Wiley & Sons, Inc., 2011). doi:10.1002/9781119998365
16. Li, H. et al. “Size- and shape-controlled synthesis of PbSe and PbS nanocrystals via a facile method”. *CrystEngComm* **12**, 1127–1133 (2010).
17. Treml, B. E., Lukose, B., Clancy, P., Smilgies, D.-M. & Hanrath, T. “Connecting the Particles in the Box - Controlled Fusion of Hexamer Nanocrystal Clusters within an AB₆ Binary Nanocrystal Superlattice”. *Sci. Rep.* **4**, 6731 (2015).
18. Van der Stam, W. et al. “Oleic Acid-Induced Atomic Alignment of ZnS Polyhedral Nanocrystals”. *Nano Lett.* **16**, 2608–14 (2016).
19. Van der Stam, W. et al. “Self-assembly of colloidal hexagonal bipyramid- and bipyramid-shaped ZnS nanocrystals into two-dimensional superstructures”. *Nano Lett.* **14**, 1032–7 (2014).
20. Vorobiev, A., Khassanov, A., Ukleev, V., Snigireva, I. & Konovalov, O. “Substantial Difference in Ordering of 10, 15, and 20 nm Iron Oxide Nanoparticles on a Water Surface: In Situ Characterization by the Grazing Incidence X-ray Scattering”. *Langmuir* **31**, 11639–11648 (2015).
21. Wang, W., Zhang, H., Kuzmenko, I., Mallapragada, S. & Vaknin, D. “Assembling Bare Au Nanoparticles at Positively Charged Templates”. *Sci. Rep.* **6**, 26462 (2016).
22. Paczesny, J., Sozański, K., Dzieścielewski, I., Żywociński, A. & Hołyst, R. “Formation of net-like patterns of gold nanoparticles in liquid crystal matrix at the air–water interface”. *J. Nanoparticle Res.* **14**, 826 (2012).

23. Kosif, I. et al. "Robust Gold Nanoparticle Sheets by Ligand Cross-Linking at the Air-Water Interface". *ACS Nano* **11**, 1292–1300 (2017).
24. Parratt, L. G. "Surface Studies of Solids by Total Reflection of X-Rays". *Phys. Rev.* **95**, 359–369 (1954).
25. Calzolari, D. C. E., Pontoni, D., Daillant, J. & Reichert, H. "An X-ray chamber for in situ structural studies of solvent-mediated nanoparticle self-assembly". *J. Synchrotron Radiat.* **20**, 306–315 (2013).
26. Jonathan S. Steckel, Brian K. H. Yen, David C. Oertel, A. & Bawendi*, M. G. "On the Mechanism of Lead Chalcogenide Nanocrystal Formation". *J. Am. Chem. Soc.* **128**, 13032–13033 (2006).



Chapter 6

“I’m blue, dabadidabadaaa”

• Abstract •

Colloidal CsPbX₃ (X = Br, Cl, I) perovskite nanocrystals (NCs) have emerged as promising phosphors and solar cell materials due to their remarkable optoelectronic properties. These properties can be tailored not only by controlling the size and shape of the NCs, but also by post-synthetic composition tuning through topotactic anion exchange. In contrast, property control by cation exchange is still underdeveloped for colloidal CsPbX₃ NCs. Here, we present a method that allows partial cation exchange in colloidal CsPbBr₃ NCs, whereby Pb²⁺ is exchanged for several isovalent cations, resulting in doped CsPb_{1-x}M_xBr₃ NCs (M = Sn²⁺, Cd²⁺, Zn²⁺, 0 < x ≤ 0.1), with preservation of the original NC shape. The partial Pb²⁺ for M²⁺ exchange leads to a blue-shift of the optical spectra, while maintaining the high photoluminescence quantum yields (>50%), sharp absorption features and narrow emission of the parent CsPbBr₃ NCs. The blue-shift in the optical spectra is attributed to the lattice contraction that accompanies the Pb²⁺ for M²⁺ cation exchange, and is observed to scale linearly with the lattice contraction. This work opens up new possibilities to engineer the properties of halide perovskite NCs, which are demonstrated to be the only known system up to date where cation and anion exchange reactions can be sequentially combined, resulting in compositionally diverse perovskite NCs.

Based on: Highly-Emissive Divalent Ion Doped Colloidal CsPb_{1-x}M_xBr₃ Perovskite Nanocrystals through Cation Exchange.

Ward van der Stam^{||}, Jaco J. Geuchies^{||}, Thomas Altantzis, Karel H.W. van den Bos, Johannes D. Meeldijk, Sandra van Aert, Sara Bals, Daniel Vanmaekelbergh and Celso de Mello Donega.
JACS **344**, 6190, 1377-1380 (2017)

^{||} These authors contributed equally to this work

6.1 - Introduction

The recent development of colloidal CsPbX₃ (X = Cl, Br, I) perovskite nanocrystals (NCs) has resulted in a burst of scientific interest, owing to their outstanding optical properties¹⁻³. Due to their high photoluminescence quantum yields (PLQY's up to 90%) without any additional surface passivation, and tunable optical properties throughout the entire visible spectrum, CsPbX₃ NCs are promising new materials for various optoelectronic applications, such as low threshold one- and two-photon pumped^{4,5} gain materials for lasing and highly efficient LEDs⁶. Moreover, recently, colloidal CsPbI₃ NCs were used in solution processed photovoltaic cells with device efficiencies exceeding 10%⁷.

Currently, synthetic protocols for colloidal CsPbX₃ NCs with a variety of shapes are available, such as cubes^{1,8}, nanowires^{9,10} and nanoplatelets^{2,11,12}. Besides all-inorganic CsPbX₃ perovskite NCs, colloidal organic-inorganic perovskite NCs have also been recently prepared^{2,13}. Furthermore, the composition of colloidal halide perovskite NCs can easily be post-synthetically tailored through topotactic halide-exchange reactions with preservation of the size and shape of the parent NCs (despite a small lattice expansion or contraction, depending on the size of the guest halide)^{14,15}. This is in striking contrast to what has been commonly observed for anion exchange reactions in colloidal II-VI semiconductor NCs, which typically result in severe size and shape transformations, often leading to hollow NCs^{16,17}.

Topotactic cation exchange reactions, i.e. reactions where the symmetry within the final product is determined by the symmetry of the initial crystal, are commonplace in colloidal semiconductor II-VI and III-V NCs, allowing access to a variety of compositions and shapes that are not attainable through direct synthesis protocols¹⁸⁻²². In contrast, post-synthetic cation exchange in colloidal CsPbX₃ perovskite NCs remains elusive, and has only been addressed in two recent works, which reported conflicting observations^{14,15}. While Akkerman et al. report the observation of CH₃NH₃⁺ (MA⁺) for Cs⁺ exchange in CsPbBr₃ NCs as an undesired complication in anion exchange protocols using MA-X salts¹⁵, Nedelcu et al. state that attempts to exchange either Cs⁺ or Pb²⁺ for other cations (Rb⁺, Ag⁺, Cu⁺, Ba²⁺, Sn²⁺, Ge²⁺, or Bi³⁺) in CsPbBr₃ NCs were invariably unsuccessful and lead only to the decomposition of the parent NCs¹⁴. The resistance of CsPbBr₃ NCs to cation exchange was rationalized by Nedelcu et al. as a consequence of the fact that the perovskite crystal structure is stabilized primarily by the rigid cationic sublattice¹⁴.

The introduction of impurity ions in colloidal II-VI and III-V semiconductor NCs provides another synthetic tool to control the optoelectronic properties and to bestow the parent NCs with novel functionalities, such as magnetism due to unpaired electrons in the dopant²³, or increased effective Stokes shift due to exciton recombination on the impurity ions^{24,25}. Furthermore, impurity doping of perovskite thin films has been shown to improve their performance in solar cells²⁶⁻²⁸. Recently, Mn²⁺ doping in colloidal CsPbCl₃ perovskite NCs has been achieved by a direct synthesis method, in which PbCl₂ and MnCl₂ precursors were mixed in the desired ratio, leading to NCs with the characteristic Mn²⁺ emission²⁹. However, post-synthetic control over the perovskite composition by introducing different impurity ions has yet to be achieved.

In this work, we present a novel method to perform post-synthetic cation exchange reactions in CsPbBr₃ NCs, through which Pb²⁺ cations are partially replaced by divalent cations (M = Sn²⁺, Cd²⁺ and Zn²⁺), yielding doped CsPb_{1-x}M_xBr₃ NCs. The Pb²⁺ for M²⁺ cation exchange results in a blue-shift of the absorption and emission spectra, while preserving the high PLQY's (>50%) and narrow PL linewidth (80 meV) of the parent NCs. We attribute the blue-shift in the optical spectra to the contraction of the perovskite cubic unit cell, which results in shorter Pb-Br bonds and hence, a stronger ligand field within the Pb-halide octahedra. Interestingly, the blue-shift scales linearly with the lattice contraction. A blue-shift of the PL maximum is also observed upon anion exchange reactions from iodide to chloride^{14,15}. However, blue-emitting CsPbCl₃ NCs obtained by anion exchange methods or direct synthesis protocols have low PLQY's (<15%) and broad PL linewidths (>120 meV)^{1,2,14,15}, in contrast to the blue-emitting NCs synthesized with our approach (PLQY >50%, PL linewidth ~80 meV).

Our work opens up many new possibilities to engineer the properties of halide perovskite NCs, which are demonstrated to be the only known system where topotactic cation and anion exchange can be sequentially combined, resulting in compositionally diverse colloidal CsPb_{1-x}M_xBr₃ perovskite NCs (M = Sn²⁺, Zn²⁺, Cd²⁺ and x ≤ 0.1) with size and shape preservation and high PL quantum yields.

6.2 - Results and discussion

6.2.1 - Optical properties

Colloidal CsPbBr₃ NCs (PL maximum at 512 nm) were reacted inside a nitrogen purged glovebox at room temperature with metal bromide salts (SnBr₂, CdBr₂, ZnBr₂) and oleylamine dissolved in toluene, which lead to a blue-shift of the absorption and PL spectra (Figure 6.1). The use of metal bromide salts as precursors for the guest cation ensures that solely the cation can be exchanged, since both the parent NCs and the precursor contain the same halide. The spectral position of the PL band blue-shifted over a wide range, depending on the divalent metal cation used and the precursor concentration (Figure 6.1(a-c)). Interestingly, although the blue-shift of the absorption and PL spectra is observed in all cases (i.e., for all divalent cations and precursor concentrations), it is more pronounced for specific concentrations and cations. For example, the blue-shift is small (i.e., 30 meV) for both low and high concentrations of SnBr₂ (0.25 mM SnBr₂, PL maximum at 506 nm; 1.7 mM SnBr₂, PL maximum at 504 nm; Figure 1d), but is much larger (170 meV) for a SnBr₂ concentration of 0.5 mM, resulting in efficient PL in the blue region of the visible spectrum (PL maximum at 479 nm, PLQY 62%, Figure 6.9). By varying the concentration of SnBr₂ in toluene, while keeping all other reaction parameters constant, the position of the PL maximum can be tuned between 479 nm and 512 nm. The increase in the SnBr₂ concentration also results in the appearance of a weak and broad absorption feature at ~580 nm. The possible nature of this transition and of the observed spectral blue-shift will be discussed later in this chapter.

Reaction of the CsPbBr₃ NCs with other divalent ions (i.e. Cd²⁺ and Zn²⁺) leads to more pronounced blue-shifts than reaction with SnBr₂, resulting in efficient PL between 452 nm and 512 nm for CsPbBr₃ NCs reacted with CdBr₂ and between 462 nm and 512 nm for CsPbBr₃ NCs reacted with ZnBr₂ (Figure 6.1(e)). The key spectral features of the parent CsPbBr₃ NCs, such as the sharp optical absorption edge, well-defined absorption peaks, and the narrow PL linewidth

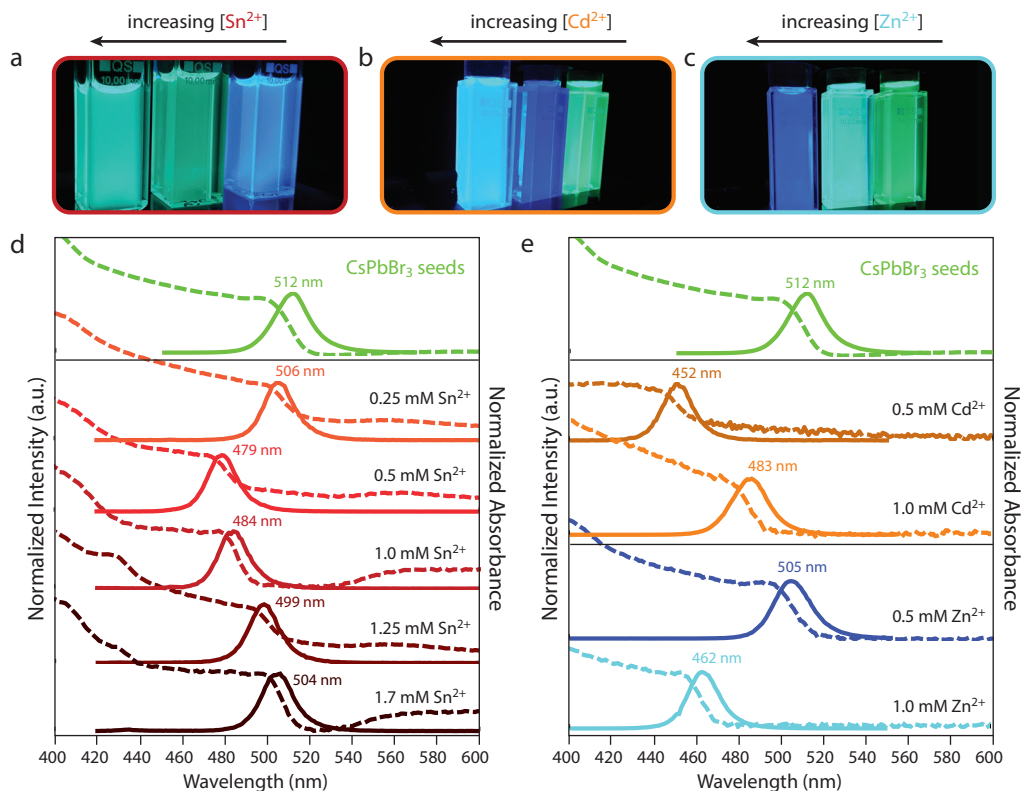


Figure 6.1: Tunable photoluminescence of CsPbBr₃ nanocrystals upon reaction with divalent cation bromide salts. Photographs of colloidal suspensions under UV illumination of (a) perovskite NCs after reaction of CsPbBr₃ NCs with different concentrations of SnBr₂ (0.5 mM, 1.25 mM, 1.7 mM) (b) parent CsPbBr₃ NCs (right vial) and product NCs after reaction of CsPbBr₃ NCs with different concentrations of CdBr₂ (0.5 mM, 1.0 mM) and (c) parent CsPbBr₃ NCs (right vial) and product NCs after reaction of CsPbBr₃ NCs with different concentrations of ZnBr₂ (0.5 mM, 1.0 mM). Photoluminescence (full lines) and absorption (dashed lines) spectra of (d) parent CsPbBr₃ NCs (green lines) and product NCs obtained after reaction with different concentrations of SnBr₂ (red and brown lines); and (e) parent CsPbBr₃ NCs (green lines) and product NCs obtained after reaction with different concentrations of CdBr₂ (orange lines) and ZnBr₂ (blue lines). In all cases, a blue-shift of both the absorption and the photoluminescence spectra is observed after reacting CsPbBr₃ NCs with divalent cation bromides, while the well-defined absorption features and the narrow PL FWHM (~80 meV) are preserved.

(FWHM ~80 meV), are maintained after reaction with metal bromide salts. High PLQY's over 60% are observed after reaction with divalent cations for all samples (see figure 6.9). We note that the PL peak shifts further over time (100-200 meV over 4 weeks), due to the presence of metal bromide precursor in the stored colloidal dispersions, since the samples could not be purified due to difficulties with precipitation of the NCs. However, the NCs do not deteriorate, and maintain their size, shape, high PLQY's and colloidal stability in toluene over the course of (at least) several months. Furthermore, we find that the absorption increases with 2% over the first 90 min of reaction. The increase in absorption on longer time scales is hard to quantify, since the absorption spectrum also shifts to higher energies. It has also been observed in other reports that colloidal perovskite NCs require very high centrifugation speeds to be destabilized from colloidal suspension and precipitated³⁰. In the present case, such high centrifugation speeds also

lead to precipitation of the unreacted metal-bromide precursor, while using stronger anti-solvents (e.g., methanol) deteriorates the NCs.

A recent study by Luther and co-workers reported a novel purification procedure for perovskite NCs, involving methyl acetate as anti-solvent, which does not lead to degradation of the NCs, although still requiring high centrifugation speeds⁷. We also used this purification method, but were able to recover only a very small amount of NCs from the reaction mixtures (see the methods section below for details).

The PL lifetimes of the parent CsPbBr₃ NCs and the product perovskite NCs after reaction with metal bromide salts were measured, displaying multi-exponential decay for all samples, both before and after the cation exchange reactions (Figure 6.10). Therefore, the average lifetime (τ_{avg}) was calculated³¹, which reveals that τ_{avg} is of the same order of magnitude (~10 ns) in all cases. Furthermore, we note that the higher the PL energy, the shorter τ_{avg} is, as expected based on Fermi's golden rule³². For the CsPbBr₃ NCs reacted with SnBr₂, the average exciton lifetime decreases from 16.8 ns for the parent CsPbBr₃ NCs to 6.8 ns for the product NCs obtained upon reaction with 1.7 mM SnBr₂. A decrease in τ_{avg} is also observed for the product NCs obtained upon reaction with CdBr₂ and ZnBr₂, to 6.4 ns and 7.2 ns, respectively.

6.2.2 - Lattice contraction after reaction with MBr₂ salts

Transmission Electron Microscopy (TEM) measurements reveal that the shape and size of the NCs are preserved after reaction with metal-bromide salts (see Figure 6.2), since cubes of ~9 nm are observed in all cases. Electron Diffraction (ED) analysis shows that the atomic reflections are shifted to larger scattering vectors after the reaction with divalent ions. This indicates that the atomic CsPbBr₃ lattice contracts due to the incorporation of the smaller Sn²⁺/Cd²⁺/Zn²⁺ guest cations. The 1D Powder ED (PED) patterns in Figure 2(d,h) were obtained by azimuthally integrating the 2D ED patterns, displayed as insets in the TEM images (Figure 6.2(a-c,e-g))³³. As displayed in Figure 6.2, the lattice contraction after reaction with Cd²⁺- and Zn²⁺-bromide salts is larger than after reaction with SnBr₂. This is expected based on the ionic radii of the divalent cations, in the case that Pb²⁺ ($r(\text{Pb}^{2+}) = 119$ pm, coordination number (CN) = 6) is replaced by the guest divalent cation ($r(\text{Cd}^{2+}) = 95$ pm, $r(\text{Zn}^{2+}) = 74$ pm, $r(\text{Sn}^{2+}) = 118$ pm, CN = 6 in all cases)³⁴. Quantification of the {100} d-spacing is displayed in Figure 2, panels d and h. The diffraction patterns were calibrated with both TlCl and Au reference samples.

The lattice contraction of CsPbBr₃ NCs after reaction with MBr₂ salts is also observed in the high-angle annular dark-field scanning transmission electron microscopy (HAADF-STEM) images (Figure 6.3). Here, statistical parameter estimation theory is used to extract structure parameters from the images^{35,36}. One of the structure parameters corresponds to the atomic column positions, which have been used to estimate the absolute distance between neighboring Pb/halide columns in order to quantify the lattice parameter (Figure 6.3). By fitting a normal distribution to these distance estimates, the mean lattice parameter has been determined. The lattice parameter of the parent CsPbBr₃ NCs was calibrated to the value reported in the literature for the cubic perovskite structure of CsPbBr₃. A lattice contraction from $|a| = 5.849 \pm 0.003$ Å to $|a| = 5.839 \pm 0.005$ Å is observed upon reaction of CsPbBr₃ NCs with 0.5 mM SnBr₂. The obtained CsPbBr₃ unit vector corresponds well to recent X-ray diffraction experiments for the

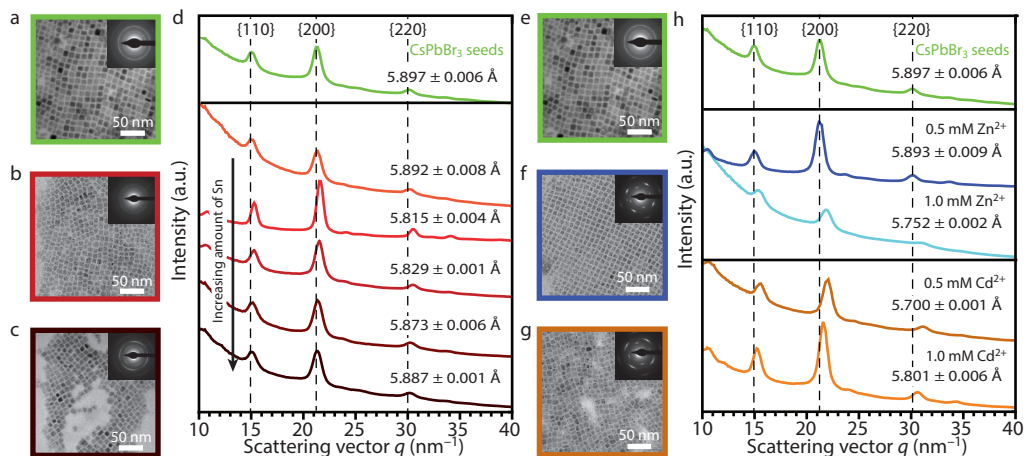


Figure 6.2: Size and shape preservation and lattice contraction of CsPbBr₃ nanocrystals (NCs) after reaction with MBr₂ (reaction time: ~16 h). Transmission Electron Microscopy (TEM) images of (a) parent CsPbBr₃ NCs and (b,c) product NCs obtained after reaction of CsPbBr₃ NCs with different concentrations of SnBr₂ precursor (0.5 and 1.7 mM, respectively). The insets in (a-c) display the 2D Electron Diffraction (ED) patterns, which result in (d) 1D Powder ED (PED) patterns after azimuthal integration (concentration of SnBr₂: 0.25, 0.50, 1.0, 1.25, and 1.7 mM, from top to bottom, respectively). The colors of panels a-c correspond to the colors of the 1D PED patterns in panel d. TEM images of (e) parent CsPbBr₃ NCs and (f) product NCs obtained after reaction of CsPbBr₃ NCs with ZnBr₂ and (g) with CdBr₂. The insets in (e-g) display the 2D ED patterns, which result in (h) 1D PED patterns after azimuthal integration. The colors of panels e-g correspond to the colors of the 1D PED patterns in panel h. A large lattice contraction is observed upon reaction of CsPbBr₃ NCs with Cd²⁺ and Zn²⁺ (h), whereas a minor lattice contraction is observed upon reaction with Sn²⁺ (d). Quantification of the {100} d-spacing is given in panel d and h.

cubic perovskite crystal structure, but does not exclude the presence of a small portion of orthorhombic distortions of the octahedra in the atomic lattice³⁷. Similar analysis on CsPbBr₃ NCs reacted with 0.5 mM CdBr₂ and 1.0 mM ZnBr₂ shows a lattice contraction from $|a| = 5.849 \pm 0.003 \text{ \AA}$ to $|a| = 5.819 \pm 0.008 \text{ \AA}$ (Cd²⁺) and $|a| = 5.808 \pm 0.014 \text{ \AA}$ (Zn²⁺), respectively. We do not observe clustered areas with larger/smaller lattice vectors in the images showing the deviations from the mean lattice vector (Figure 6.3, middle row, red: larger than mean distances, blue: smaller than mean distances). From this we deduce that the incorporated guest cations are homogeneously distributed throughout the NCs. Thickness profiles obtained from the total scattered intensities of the atomic columns confirm this observation (see figure 6.11).

As can be seen, the lattice contraction for Cd- and Zn-dopants (0.5 % and 0.7 %, respectively) is larger than for the Sn-doped NCs (0.2%), which is in full agreement with the electron diffraction data presented in Figure 6.2. The statistical student's t-test with unequal variances has been used to verify that the found differences are significant³⁸. Here, the distribution of the measured lattice parameters of the parent CsPbBr₃ NCs have been compared to a distribution of the measurements on the doped CsPb_{1-x}M_xBr₃ NCs at a significance level of 10%, indicating that the distributions have different means. Based on these results, we conclude that guest divalent cations are indeed present in the perovskite NCs and are distributed homogeneously across the perovskite lattice.

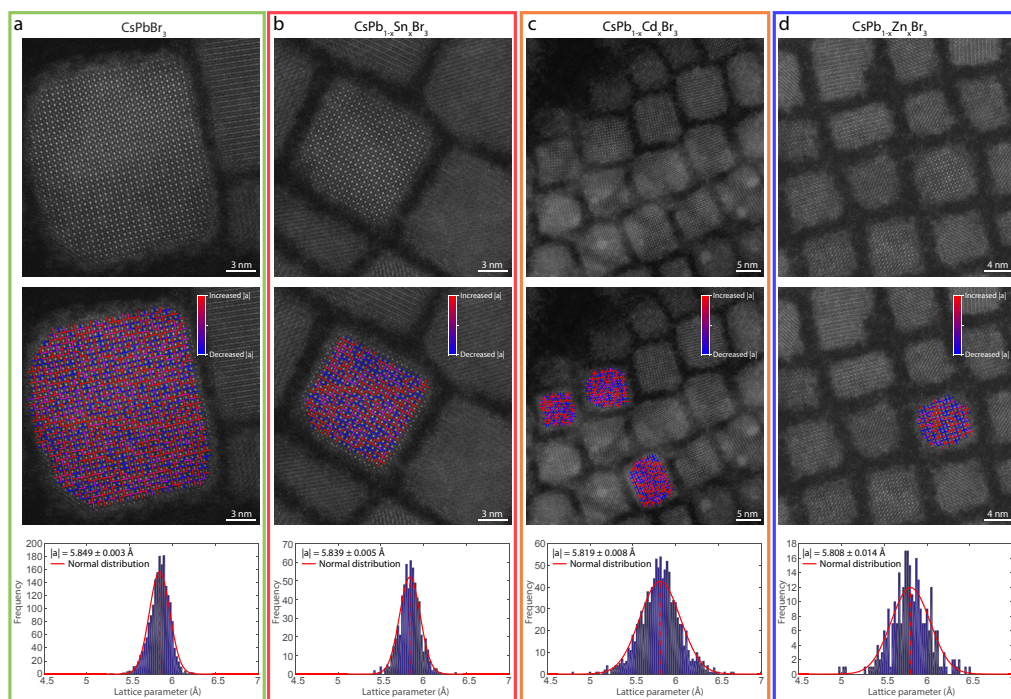


Figure 6.3: Quantitative High-Angle Annular Dark-Field STEM. HAADF-STEM measurements reveal a lattice contraction of (a) parent CsPbBr₃ NCs ($|a| = 5.849 \pm 0.003 \text{ \AA}$) upon reaction with (b) 0.5 mM SnBr₂ ($|a| = 5.839 \pm 0.005 \text{ \AA}$), (c) 0.5 mM CdBr₂ ($|a| = 5.819 \pm 0.008 \text{ \AA}$) and (d) 1.0 mM ZnBr₂ ($|a| = 5.808 \pm 0.014 \text{ \AA}$) (reaction time: 16 h). In the HAADF-STEM images, the mixed Pb/halide (bright contrast), Cs (intermediate contrast) and halide (low contrast) atomic columns can be easily assigned (top panels). After detecting the positions of the Pb/halide columns from the HAADF-STEM images, we calculate the interatomic distances (i.e. the lattice spacing, middle panels). Red bars indicate a larger distance than the mean $|a|$ and blue bars a smaller distance than the mean $|a|$. The histogram of distances together with the estimated normal distribution reveal a contraction of the cubic perovskite CsPbBr₃ atomic lattice upon reaction with SnBr₂, CdBr₂ and ZnBr₂ NCs (bottom panels).

Interestingly, the PL energy of doped CsPb_{1-x}M_xBr₃ perovskite NCs scales linearly with the lattice vector (Figure 6.4) independently of the type of cation that has been incorporated. This is most evident for the Sn-doped NCs, for which more data points are available (Figure 6.4(a)), but is also clear when the other two cations are taken into account (Figure 6.4(b)).

The bandgaps of ABX₃ perovskites are known to increase with the increase of the electronegativity of both B and X atoms and with the decrease of the unit cell volume⁴¹. It is thus quite remarkable that the trends for the three cations are very similar despite their different radii, electronic configurations and properties (Pb²⁺ [5d¹⁰6s²6p⁰]: $r = 119 \text{ pm}$, electronegativity $\chi = 1.6$; Sn²⁺ [4d¹⁰5s²5p⁰]: $r = 118 \text{ pm}$, $\chi = 1.7$; Cd²⁺ [4d¹⁰5s⁰]: $r = 95 \text{ pm}$, $\chi = 1.5$; Zn²⁺ [3d¹⁰4s⁰]: $r = 74 \text{ pm}$, $\chi = 1.7$; polarizability and Lewis hardness decrease from Pb²⁺ to Zn²⁺). This implies that the observed blue-shift of the optical transitions is primarily due to the lattice contraction, and that the MBr₆ guest octahedra are electronically decoupled from the PbBr₆ framework. This is particularly clear for the Sn-doped NCs, since it is reported in literature that the band gap of CsSnBr₃ and CsPb_{1-x}Sn_xBr₃ are red-shifted with respect to that of CsPbBr₃^{42,43}. This shows that the band-edge absorption and the PL transition of the CsPb_{1-x}Sn_xBr₃ NCs prepared in this work

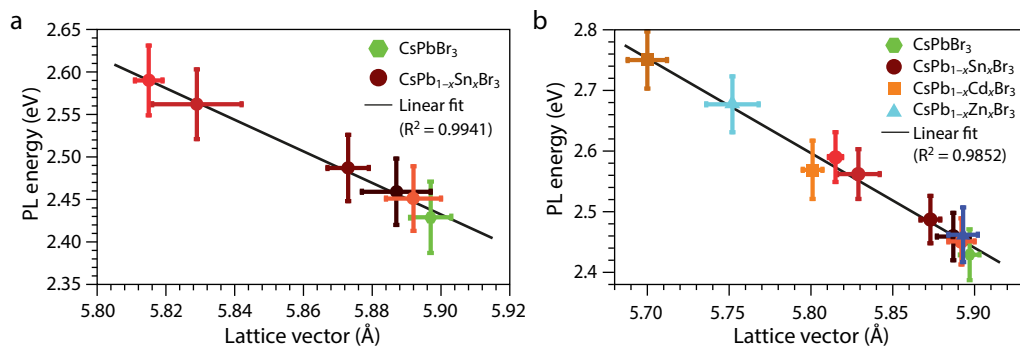


Figure 6.4: Photoluminescence (PL) energy and lattice vector correlation in $\text{CsPb}_{1-x}\text{M}_x\text{Br}_3$ perovskite NCs. (a) PL energy as a function of the lattice vector in doped $\text{CsPb}_{1-x}\text{Sn}_x\text{Br}_3$ NCs obtained by post-synthetic Pb^{2+} for Sn^{2+} cation exchange in parent CsPbBr_3 NCs. **(b)** PL energy as a function of the lattice vector in doped $\text{CsPb}_{1-x}\text{M}_x\text{Br}_3$ ($\text{M} = \text{Sn}, \text{Cd}, \text{Zn}$) NCs obtained by post-synthetic Pb^{2+} for M^{2+} cation exchange in parent CsPbBr_3 NCs. The different colors of the symbols in panels **(a)** and **(b)** correspond to the colors used to identify the different samples in Figures 6.1 and 6.2.

are solely determined by the PbBr_6 octahedra, despite the presence of SnBr_6 groups in the NC. The additional feature observed at lower energies (540-600 nm) in the absorption spectra of the $\text{CsPb}_{1-x}\text{Sn}_x\text{Br}_3$ NCs (Figure 1d) can thus be ascribed to these electronically isolated SnBr_6 octahedra.

The PL transition of ABX_3 halide perovskites has also been reported to blue-shift upon proceeding along the I, Br, Cl series, as clearly illustrated by the PL tunability achieved by synthetic and post-synthetic compositional control in both bulk and nanocrystalline ABX_3 ^{14,15,44,45}. Although this is accompanied by a contraction of the unit cell, the PL shift does not depend linearly on the lattice contraction, since the widening of the band gap is largely due to the increase in electronegativity along the halide series, which effectively increases the ionic character of the B-X bond^{41,44,45}.

In fact, our work provides the first clear observation of a linear relationship between lattice vector and PL energy in perovskites. A recent work reported a blue-shift of the PL peak of bulk CsSnBr_3 upon warming (lattice expansion)⁴⁶, in striking contrast with our results. Similar observations (i.e., PL blue-shift with increasing temperature) have also been reported for CsPbBr_3 NCs⁴⁷ and bulk CsSnI_3 ⁴⁸. However, it should be noted that this behavior (linear increase of the bandgap with increasing temperature) is anomalous, since most semiconductors show the opposite temperature-dependence (i.e. a linear increase of the bandgap with decreasing temperature)⁴⁸⁻⁵¹. This anomalous temperature-dependence is also observed for copper halides (CuBr , CuCl), lead chalcogenides, and black phosphorus, and has been attributed to a dominance of the lattice thermal expansion contribution over the electron-phonon interaction contribution^{48,50}. In the specific case of CsSnBr_3 and CsPbBr_3 the widening of the bandgap upon lattice expansion is ascribed to simultaneous narrowing and stabilization of both the valence and conduction bands, as a result of the antibonding character of their maximum and minimum, respectively⁴⁶.

PL shifts have also been recently reported for MAPbX_3 bulk films and single crystals subjected to high-pressures^{52,53}. Interestingly, small red-shifts (≤ 50 meV) were observed in the low-pressure regime (below 0.35-1 GPa), while strongly non-linear blue-shifts (up to 200 meV) were observed

in the high-pressure regime (above 1-2.5 GPa), and were ascribed to amorphization of the MAPbX₃ lattice^{52,53}. This explanation is however inadequate for the PL blue-shifts reported in our work, since we do not observe any signs of loss of crystallinity, disorder or phase transitions in the doped CsPb_{1-x}M_xBr₃ NCs obtained by post-synthetic Pb²⁺ for M²⁺ cation exchange, despite very clear lattice contractions. It should be pointed out that also from this perspective the behavior of bulk ABX₃ halide perovskites seems to be anomalous, since the PL of most common semiconductors (e.g. GaN, CdTe) blue-shifts linearly with increasing pressure^{54,55}.

The behavior observed for the CsPb_{1-x}M_xBr₃ NCs prepared in the present work by post-synthetic Pb²⁺ for M²⁺ cation exchange in 9 nm CsPbBr₃ NCs is thus in line with the normal pressure-dependence of the bandgap energies of bulk semiconductors, but is opposite to what is observed for bulk ABX₃ halide perovskites^{52,53}. This is striking, and is likely due to nanoscale effects. The contribution of quantum confinement effects to the blue-shift observed in the optical spectra of the CsPbBr₃ NCs after the cation exchange reaction is however negligible, since the NCs under study here are larger than the estimated exciton Bohr diameter for CsPbBr₃ (7 nm), and are therefore in the weak confinement regime¹. Although the reduction in the NC size should result in an increase in quantum confinement, the effect would be too small to account for the magnitude of the spectral shifts observed after the cation exchange reactions (up to 300 meV, which would require a size reduction from 9 nm to ~5 nm, according to the theoretical size dependence of the band gap reported in ref. 1). Furthermore, Protesescu et al. have shown that blue-emitting CsPbBr₃ NCs are in the sub-4 nm size regime¹, whereas the CsPb_{1-x}M_xBr₃ NCs obtained in this work have a diameter of 9 nm and yet display efficient PL in the blue region of the electromagnetic spectrum.

We thus propose that the remarkable behavior observed here for doped CsPb_{1-x}M_xBr₃ NCs indicates that they can accommodate larger isotropic compressive strains than bulk ABX₃ halide perovskites, and, as a result, all PbBr₆ octahedra within a NC contract without significant (additional) distortion, so that the compressive strain is homogeneously distributed throughout the NC (as indicated by Figure 6.3 above). Distortion and tilting of the BX₆ octahedra is known to induce bandgap reduction⁴¹. These distortions are however always accompanied by lattice constant changes that act in the opposite direction, thereby decreasing the extent of the red-shift⁴⁰. Recent X-Ray diffraction analysis of CsPbBr₃ NCs suggests that orthorhombic distortions are an important feature of these materials³⁷. Although the linear relationship observed in the present work between the degree of lattice contraction and the blue-shift of the PL of CsPb_{1-x}M_xBr₃ NCs (Figure 6.4) does not rule out the possibility of orthorhombic distortions in the NCs, it implies that their contribution does not significantly change with the nature of M or the extent of the replacement, and therefore that the contraction is the dominant effect. The contraction of the PbBr₆ octahedra leads to shorter Pb-Br bonds and therefore stronger interactions between the Pb and Br orbitals. This widens the bandgap because the conduction band minimum (CBM) is composed of the antibonding combinations between Pb(6p) and Br(4p) orbitals⁴⁸, and therefore should shift to higher energies with stronger interactions. Although the valence band maximum is also antibonding⁴⁴, we expect it to shift less than the CBM because it emerges from the relatively weaker interaction between the Br(4p⁶) orbitals and the Pb(6s²) orbitals, which are stabilized by lone pair and relativistic effects⁵⁴. In contrast, the Pb(6p)-Br(4p) interaction is largely responsible for the chemical bonding in APbX₃ perovskites as it leads to charge transfer from the Pb(6p) to the X(np) orbitals⁴³. The above process is schematically depicted in Fig. 6.5⁴⁸.

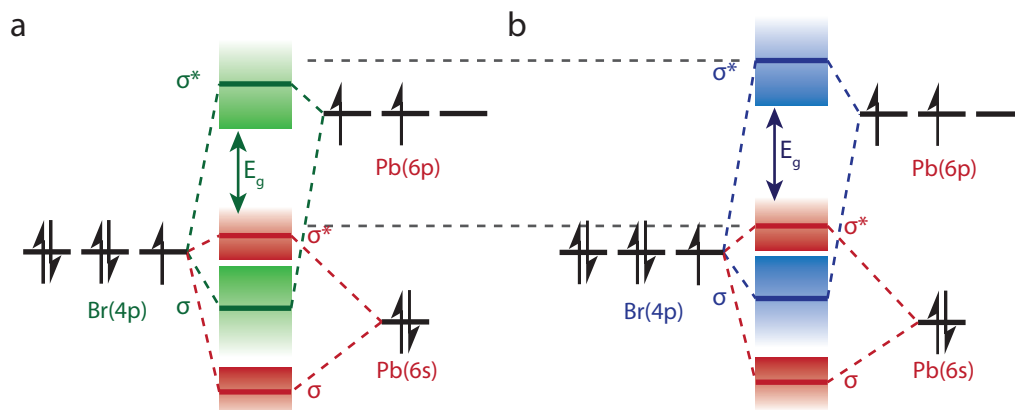


Figure 6.5: Orbital diagram of (a) CsPbBr₃ and (b) CsPb_{1-x}M_xBr₃ nanocrystals. (a) Both the upper valence states and lower conduction states are antibonding in nature. The valence states mainly consist out of Pb(6s) orbitals, while the conduction states mainly consist out of Br(4p) orbitals. **(b)** Due to the decrease Pb-Br bond length, the ligand field strength is increased, which pushes the orbitals to higher energy. As the overlap between the Pb(6p) and Br(4p) orbitals is more favorable than the overlap between the Pb(6s) and Br(4p) orbitals, the antibonding conduction band minimum is pushed to a higher energy than the antibonding valence band maximum. Combined with the arguments in the text, this mechanism is postulated for the observed blueshift in the photoluminescence.

6.2.2 - Elemental analysis

The results presented above suggest that Pb²⁺ cations in CsPbBr₃ NCs are replaced by other divalent cations, i.e. Sn²⁺/Cd²⁺/Zn²⁺, resulting in a lattice contraction due to the smaller ionic radius of the incorporated cations. To verify the incorporation and the distribution of the guest cations, Energy Dispersive X-ray Spectroscopy (EDS) chemical mapping was performed. We note that the EDS measurements were performed on areas containing a large amount of NCs, in order to obtain a statistically relevant result. The EDS measurements show that Cd (Figure 6.6(a-e)) and Zn (Figure 6.6(f-j)) are incorporated in the CsPbBr₃ NCs in low concentrations. Moreover, no indication for surface preference or phase segregation is observed, which leads us to conclude that the distribution of the guest cations within the CsPb_{1-x}M_xBr₃ NCs is homogeneous, consistent with the observations presented above. Quantification of the EDS measurements reveals a Cd:Pb ratio of 0.16 for the product CsPb_{1-x}Cd_xBr₃ NCs obtained after 16 h reaction with 0.5 mM CdBr₂ and a Zn:Pb ratio of 0.05 for the product CsPb_{1-x}Zn_xBr₃ NCs obtained after 16 h reaction with 1.0 mM ZnBr₂. The CsPbBr₃ NCs reacted with 0.5 mM SnBr₂ for 16 h were also analyzed with bulk EDS measurements, which reveal a Sn:Pb ratio of 0.1. We also performed an EDS quantification of the product CsPb_{1-x}Cd_xBr₃ perovskite NCs, and of portions of the TEM grid surrounding clusters of NCs (i.e. the background). This analysis clearly shows a Cd peak at 3.1 keV for the area containing NCs, whereas Cd-peaks are below the noise level in the background (see Fig. 6.13). The EDS analysis thus clearly demonstrates that divalent guest cations are successfully incorporated in CsPbBr₃ NCs upon reaction with MBr₂ salts. It should be noted that the elemental concentrations are upper limit estimates, since the samples were not washed prior to the EDS measurements. A few selected samples were thoroughly purified by precipitating with methyl acetate, which yielded only very small amounts of NCs (see methods section for details). The purified NCs showed reduced carbon contamination upon prolonged exposure to the e-beam. Furthermore, the Sn:Pb ratio for purified NCs was 0.085 and is similar to the Sn:Pb ratio for the unpurified samples (0.1).

This lead us to conclude that the above presented cation:Pb ratios are valid upper limit estimates for the incorporated divalent cations. A possible mechanism for the post-synthetic incorporation of divalent cations into CsPbBr_3 NCs will be discussed below.

It must be noted that we observe bright spots on the CsPbBr_3 NCs upon exposure to the electron beam (see e.g. Figure 6.3). High resolution HAADF-STEM analysis shows that these spots correspond to metallic Pb nanoparticles (See Fig. 6.14). This indicates that, upon imaging the NCs with an electron beam, part of the Pb^{2+} ions are reduced to metallic Pb. Furthermore, the measured atomic ratios indicate that the parent CsPbBr_3 NCs are halide deficient (Cs:Pb:Br = 1:1:2; ratio cation charge/anion charge= 1.5), and that the halide deficiency is preserved after reaction with MBr_2 salts (ratio cation charge/anion charge= 1.5). Cation/anion ratios significantly larger than unity are commonly observed for NCs of II-VI (e.g., CdSe) and IV-VI (e.g., PbSe) semiconductors synthesized in the presence of X-type ligands (e.g., oleate), and have been rationalized by considering that the stoichiometric NC is coated by a layer of M-X units³⁹. A similar explanation may apply in the present case, since the CsPbBr_3 NCs were synthesized from Cs-oleate and Pb-oleate. Nevertheless, halide deficiency is commonly

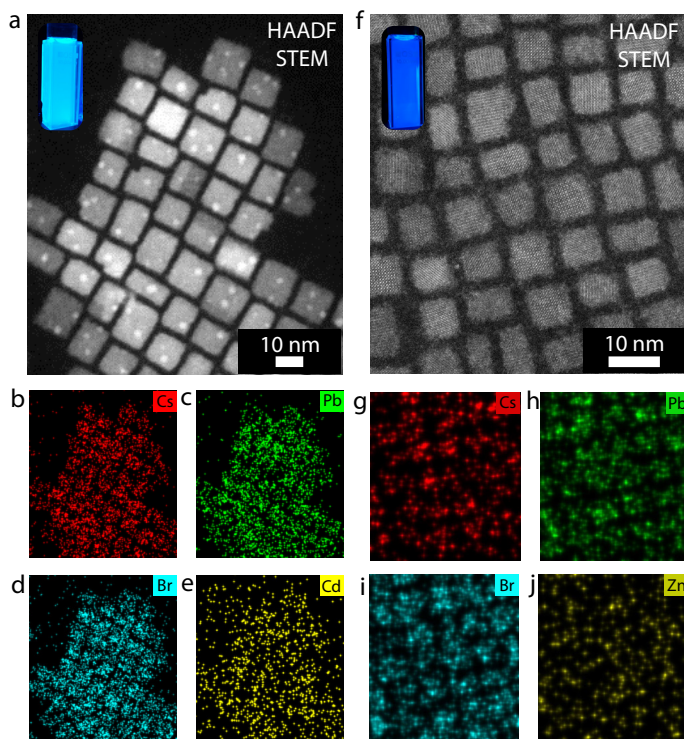


Figure 6.6: Energy Dispersive X-ray Spectroscopy mapping of $\text{CsPb}_{1-x}\text{Cd}_x\text{Br}_3$ and $\text{CsPb}_{1-x}\text{Zn}_x\text{Br}_3$ nanocrystals. (a) HAADF-STEM image of $\text{CsPb}_{1-x}\text{Cd}_x\text{Br}_3$ NCs and the corresponding (b) Cs map, (c) Pb map, (d) Br map and (e) Cd map, demonstrating the presence of Cd in the perovskite NCs. The inset in panel (a) shows a photograph of a colloidal suspension of the NCs under UV illumination. (f) HAADF-STEM image of $\text{CsPb}_{1-x}\text{Zn}_x\text{Br}_3$ NCs and the corresponding (g) Cs map, (h) Pb map, (i) Br map and (j) Zn map, indicating the presence of Zn in the perovskite NCs. The inset in panel (f) shows a photograph of a colloidal suspension of the NCs under UV illumination. The bright spots observed in the HAADF-STEM images are metallic Pb nanoparticles, formed upon prolonged exposure to the electron beam (see Figure SXX).

observed in bulk perovskites, due to the very low activation energies for the creation of anion vacancies in these materials⁴⁰⁻⁴², and is likely also present in perovskite NCs. Density Functional Theory calculations show that anion vacancies do not result in mid-gap trap states in halide perovskites, since their energy levels lie within the conduction band⁴⁸. Therefore, despite the presence of halide vacancies, the exciting optoelectronic properties of the parent CsPbBr₃ NCs, such as high PLQY and sharp excitonic features, are preserved in the product CsPb_{1-x}M_xBr₃ NCs.

6.2.3 - Cation exchange mechanism

The results presented above show that divalent guest cations (Sn²⁺, Cd²⁺, Zn²⁺) can be incorporated into CsPbBr₃ NCs by post-synthetic cation exchange reactions. Considering that aliovalent exchange of Cs⁺ (radius: 1.88 Å) for M²⁺ would strongly destabilize the perovskite structure, since it would result in smaller M²⁺ cations in sites with coordination number 12 and would require charge compensation, we will assume below that only isovalent exchange of Pb²⁺ for M²⁺ has taken place, leading to partial substitutional replacement of PbBr₆ octahedra by MBr₆ octahedra (Figure 6.7).

Cation exchange reactions have been extensively investigated in NCs of II-VI, IV-VI, III-V, and I-VI semiconductors^{18-22,59,60}, and shown to consist of several inherently linked elementary kinetic steps, which must proceed in a concerted way. The first step is the extraction of the native cation from the parent NCs, which may occur by a direct place exchange reaction (i.e., extraction of the native cation and incorporation of the guest cation occur in a direct reaction mediated by a ligand in solution, e.g. Zn²⁺ for Cd²⁺ exchange in ZnSe mediated by oleate ligands⁵⁹), or by an independent chemical pathway that is only kinetically coupled to the incorporation of the guest cation (e.g., cation exchange in Cu_{2-x}S NCs in the presence of excess phosphines)⁶¹. The rates of

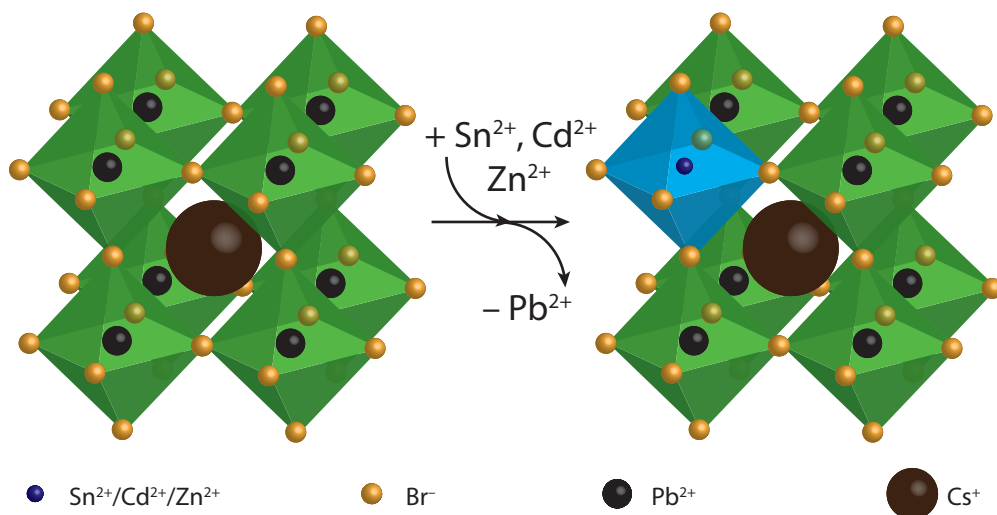


Figure 6.7: Schematic overview of the partial cation exchange in CsPbBr₃ nanocrystals. Pb²⁺ cations are partially replaced by other divalent cations (Sn²⁺, Cd²⁺, Zn²⁺) by post-synthetic cation exchange reactions, resulting in divalent cation doped CsPb_{1-x}M_xBr₃ NCs (the MBr₆ octahedra are schematically depicted by the blue metal-halide octahedra). Incorporation of smaller divalent cations results in contraction of the atomic lattice, which induces a blue shift of the optical transitions (absorption and PL). The halide anions are depicted smaller for clarity.

extraction of the native cation and incorporation of the guest cation must be balanced, otherwise the accumulation of cation vacancies eventually leads to the collapse of the NC^{20,21}. There are several factors involved in the cation extraction process, such as breaking of the cation-anion bonds within the NC and formation of cation-ligand bonds, while the incorporation of the guest cation requires breaking the cation-ligand bonds and formation of the cation-anion bonds in the NC^{18,20}. The thermodynamic driving force for the cation exchange is determined by the energy balance of the overall reaction. It should also be noted that the cation exchange process is essentially a surface reaction, which, in the absence of cation diffusion in the NC, would stop as soon as all surface cations had been exchanged by the guest cations⁵⁹. Therefore, the cation exchange rates are often limited by the diffusion rates of the outgoing and incoming cations^{18,20,59}. Cation diffusion in semiconductor NCs is often attributed to vacancy-mediated migration^{18,20,59,60}, and its rate is therefore limited by the activation energies for vacancy formation.

Cation exchange reactions have not yet been studied in detail in perovskite NCs, but topotactic anion exchange has been shown to be very efficient and fast in CsPbX₃ (X= Cl, Br, I) halide perovskite NCs, due to the low activation energy for the formation and diffusion of halide vacancies in these materials^{14,15}. In contrast, cation diffusion in perovskites is a very slow process, owing to the high activation energies for the formation of cation vacancies and the lack of interstitial sites for interstitial diffusion. A recent study on bulk CH₃NH₃PbI₃ has concluded that vacancy-assisted iodide diffusion in this perovskite material has an activation energy of only 0.58 eV, leading to fast diffusion even at room temperature (diffusion coefficient: 10⁻¹² cm²s⁻¹), while cation diffusion has much higher activation energies (0.84 eV and 2.31 eV for CH₃NH₃⁺ and Pb²⁺, respectively)⁶². As a result, CH₃NH₃⁺ diffusion is four orders of magnitude slower than Iodide diffusion, and the Pb²⁺ sublattice is essentially immobile⁶². This implies that cation exchange processes involving Pb²⁺ in CsPbX₃ perovskites would be limited by very slow diffusion fluxes for both the outgoing Pb²⁺ and the incoming M²⁺ guest cations. Our results show that this is indeed the case, since the Pb²⁺ for M²⁺ exchange reaction is very slow and only occurs partially, despite the large excess of M²⁺ cations with respect to the parent CsPbBr₃ NCs (from 8×10³ to 3×10⁵, see Methods section). The number of Pb²⁺ cations in a 9 nm CsPbBr₃ NC is ~3600 (unit cell volume: 0.2 nm³, NC volume: 729 nm³). This means that even in the low precursor concentration regime, there is a two-fold excess of guest M²⁺ cations with respect to Pb²⁺, implying that full exchange would be possible, if a sufficiently strong driving force would be present. As it will be discussed below, the fact that the cation exchange does not reach completion despite the large M/Pb ratios used, shows that the driving force is small and that the reaction may in fact be self-limited.

The use of metal bromide precursors has multiple benefits in our cation exchange protocol, leading to successful partial exchange of Pb²⁺ for M²⁺ cations in CsPbBr₃ NCs, resulting in doped CsPb_{1-x}M_xBr₃ NCs. The presence of Br in the guest cation precursor allows us to take advantage of the ease of formation of halide vacancies in CsPbX₃ NCs and to explore the fact that CsPbX₃ NCs quickly establish an equilibrium with solvated halides in the solution phase, especially in the presence of amines, allowing fast cross-exchange between NCs with different halides^{14,15}. Given that MBr₂ does not dissociate in toluene, it binds to the surface Br vacancies as a molecular unit, thereby incorporating MBr₂ in the NC. This releases energy due to the formation of bonds between the incoming Br and the NC, but does not consume energy because the M-Br bonds do not need to be broken. The energy released can then be used to break the

bonds between a PbBr_2 unit and the NC. Because the bonds formed and broken are similar, the energy balance is close to zero, and therefore the surface Pb^{2+} cations can be quickly exchanged into guest M^{2+} cations, despite the low temperatures (i.e. room temperature) used in our cation exchange protocol. To allow the cation exchange process to continue, two diffusion fluxes have to be established: inward diffusion of guest M^{2+} cations and outward diffusion of Pb^{2+} cations. As discussed above, these fluxes will be slow, since they have high activation energies, and will be primarily driven by the increase in entropy that results from the formation of $\text{CsPb}_{1-x}\text{M}_x\text{Br}_3$ solid solutions. However, the exchange of Pb^{2+} by smaller M^{2+} cations leads to a progressive contraction of the lattice, which leads to strain within the NC. This increasing strain field counteracts the entropic gain, eventually becoming sufficiently strong to halt the cation exchange process. This could be a reason for a self-limited cation exchange, as we have observed here for several isovalent ions. A schematic representation of the cation exchange mechanism proposed above is given in the figure below. We would like to point out that a more detailed mechanistic study has to be performed to confirm the postulated model for the cation exchange reaction.

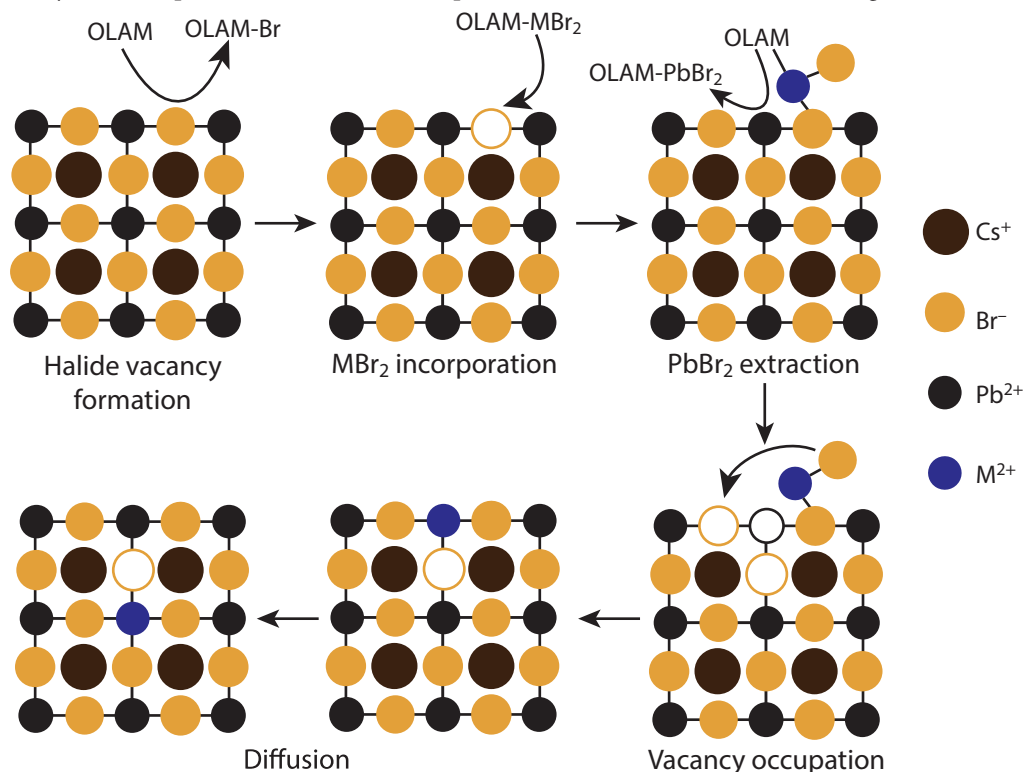


Figure 6.8: Schematic representation of the proposed cation exchange reaction mechanism. In the first step, surface halide vacancies are created by oleylamine (OLAM) molecules in solution. In the second step, a Br anion of an OLAM-MBr₂ unit occupies the halide vacancy. In a third step, the bound OLAM molecule extracts a PbBr₂ unit, leaving a cation and halide vacancy behind, which are occupied by the bound MBr₂ species. Finally, the incorporated divalent guest cation diffuses into the perovskite lattice, leaving behind a halide vacancy at the surface for a second cation exchange process to occur.

6.3 - Conclusion and outlook

We present a post-synthetic cation exchange method, which allows us to partially exchange Pb²⁺ ions in CsPbBr₃ NCs for several other divalent cations (Sn²⁺, Cd²⁺, Zn²⁺). This isovalent cation exchange results in a blue-shift of the PL bands, without loss of the high PLQYs (>60%), narrow emission bandwidth, and sharp excitonic absorption transitions. The blue-shift is attributed to contraction of the perovskite lattice due to the incorporation of smaller divalent guest cations (Sn²⁺/Cd²⁺/Zn²⁺), resulting in shorter Pb-halide bonds and hence an increased interaction between Pb and Br orbitals. We show that the blue-shifted PL energy scales linearly with the lattice vector of the doped CsPb_{1-x}M_xBr₃ NCs, in striking contrast to what has been reported for bulk perovskite materials. This is the first example of post-synthetic cation exchange in CsPbBr₃ perovskite NCs, demonstrating that halide perovskite NCs are the only known system in which the complete composition can be post-synthetically tailored with size and shape preservation, by sequentially combining topotactic anion and cation exchanges. This opens up a library of possible compositions attainable for colloidal CsPbX₃ NCs, which might possess unprecedented and unparalleled optoelectronic properties and may prove beneficial for a number of applications.

6.4 - Methods

CsPbBr₃ nanocrystal synthesis. The CsPbBr₃ NCs were prepared according to the method described by Protesescu et al.¹ First, Cs-oleate precursor stock solution was prepared. Cs₂CO₃ (0.814g, 99% Aldrich), 2.5 mL oleic acid (OA, 90% Aldrich) and 40 mL 1-octadecene (ODE, 90% Aldrich) were loaded into a 100 mL round-bottom flask. The mixture was dried under vacuum for approximately 1h at 120 °C, and then heated under N₂ to 150 °C until all Cs₂CO₃ had reacted with OA. ODE (5 mL) and PbBr₂ (0.069g, 99.999% Aldrich) were loaded into a separate 25 mL flask and dried under vacuum for 1h at 120 °C. Oleylamine (OLAM 0.5 mL, 70% Aldrich) and OA (0.5 mL) were injected at 120 °C under N₂ atmosphere. After PbBr₂ had dissolved, the temperature was raised to 180 °C and a 0.4 mL portion of the Cs-oleate stock solution was quickly injected. We note that the Cs-oleate stock solution had to be preheated to ~100 °C before injection. After five to ten seconds the reaction mixture was cooled by an ice-water bath in order to quench the reaction.

Purification of the nanocrystals. The CsPbBr₃ NCs were purified following the method described by De Roo et al.³⁰ (for a synthesis based on 69 mg of PbBr₂). The crude synthesis solution was centrifuged for 3 min at 10000 rpm and the colored supernatant was discarded. Then, 300 µL of hexane was added and the NCs were dispersed using a vortex mixer. Subsequently, the suspension was again centrifuged for 3 min at 10 000 rpm, after which the precipitate, containing larger NCs and agglomerates, was discarded. Another 300 µL of hexane was added to the supernatant, resulting in a colloidal dispersion of CsPbBr₃ NCs.

A second purification procedure was based on recent work by Luther and co-workers⁷. The additional purification of the colloidal perovskite NCs was performed by adding 1 mL of methyl acetate (99.5% Aldrich) to the crude NC solution, followed by centrifugation at 13000 rpm for 1 hour. The amount of precipitate was extremely small. After removing the supernatant, the precipitate was redispersed in 300 µL hexane. Subsequently, 300 µL methyl acetate was added and the NCs were again centrifuged at 13000 rpm. The supernatant was discarded and the even smaller amount of precipitate was redispersed in 50 µL of hexane before being dropcast on a Cu TEM grid for further analysis.

Cation exchange. Cation exchange precursor stock solutions were prepared by dissolving 1 mmol metalbromide salt (MBr₂, with M = Sn²⁺, Zn²⁺, Cd²⁺) in 10 mL toluene (0.1M MBr₂), in the presence of 100 µL OLAM. In a typical cation exchange experiment, 1.5 mL diluted NCs in toluene (concentration: ~0.01 µM, using an extinction coefficient of 37.9 cm⁻¹ µM⁻¹ at 335 nm, for cubes of roughly 9 nm)³⁰ and 0.5 mL cation-precursor (different concentrations, ranging between 0.125 mM and 1.67 mM, [M²⁺]/[NC] ratio varied between ~8000 and ~300 000) were mixed and stirred at room temperature for ~16 h. In the majority of the cases, the NCs were not purified after the cation exchange reactions, due to difficulties with precipitation of the NCs. The second purification procedure described above, in which methyl acetate is used as anti-solvent, was applied to a few selected samples after reaction with SnBr₂, but yielded only very small amounts of NCs, which were only enough to get sub-monolayer coverage on a TEM grid.

Transmission Electron Microscopy (TEM) and Energy Dispersive X-Ray Spectroscopy (EDS). TEM measurements were performed using a Tecnai20F (FEI) microscope equipped with a Field Emission Gun and a Gatan 694 CCD camera. The microscope was operated at 200 kV. EDS measurements were performed on FEI Talos F200X and an aberration corrected 'cubed' FEI Titan 60-300 electron microscope equipped with a ChemiSTEM system operated at 200 kV and 300 kV, respectively. Acquisition time for EDS measurements was ~ 300 s. Samples for TEM imaging were prepared by dripping a diluted nanocrystal solution in toluene on a carbon coated polymer film copper grid (300 mesh). The solvent was allowed to evaporate prior to imaging.

HAADF-STEM. High-resolution High-Angle Annular Dark-Field Scanning Transmission Electron Microscopy (HAADF-STEM) measurements were performed using an aberration corrected cubed FEI Titan 60-300 electron microscope operated at 300 kV.

1D Powder Electron Diffraction (PED). PED patterns were obtained by azimuthally integrating the 2D ED patterns (with the freely available software package CrysTBox)³³ acquired on a Tecnai-12 transmission electron microscope using a selected-area aperture. 2D ED patterns were acquired on areas containing a large number of nanocrystals to make the 1D PED patterns statistically valid.

Optical spectroscopy. Samples for optical measurements were prepared by diluting the colloidal dispersion of NCs with anhydrous toluene under nitrogen and stored in sealed quartz cuvettes. Absorption spectra were measured on a double beam Perkin-Elmer Lambda 16 UV/Vis spectrometer. Photoluminescence (PL) spectra were recorded on an Edinburgh Instruments FLS920 Spectrofluorimeter equipped with a 450 W Xenon lamp as excitation source and double grating monochromators. PL decay curves were obtained by time-correlated single-photon counting on a Hamamatsu H7422-02 photomultiplier tube with low dark count rate (< 10 cts/s). A pulsed diode laser (EPL-445 Edinburgh Instruments, 375 nm, 55 ps pulse width, 0.2 MHz repetition rate) was used as the excitation source.

Photoluminescence quantum yields (PLQY). The PLQYs of the perovskite NCs were determined with respect to the fluorophore Lumogen red 350 (PLQY = 95%)⁶⁴. Samples for PLQY measurements were prepared by diluting the colloidal dispersion of NCs with anhydrous toluene under nitrogen in sealed quartz cuvettes, keeping the optical density of both the Lumogen Red and the perovskite NCs below 0.1 at 442 nm in order to minimize reabsorption. The absorption and PL emission spectra were measured using the instruments mentioned above.

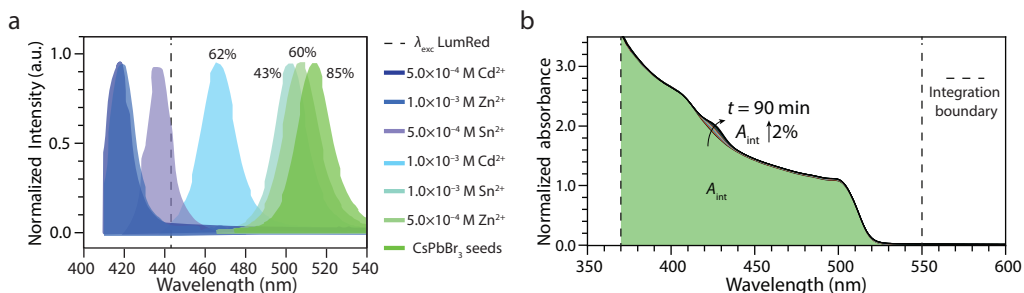


Figure 6.9: Photoluminescence quantum yields and time resolved absorption measurements. (a) PLQYs of parent CsPbBr_3 NCs (green spectrum) reacted with different concentrations of MBr_2 precursor. The blue emitting NCs could not be measured, because their PL maximum lies at shorter wavelengths than the excitation wavelength of the fluorophore used as PLQY standard (Lumogen Red, LumRed, $\lambda_{\text{exc}} = 442$ nm). (b) Integrated absorption of CsPbBr_3 NCs reacted with 0.5 mM SnBr_2 precursor for 90 min, showing an increase in absorption of 2%.

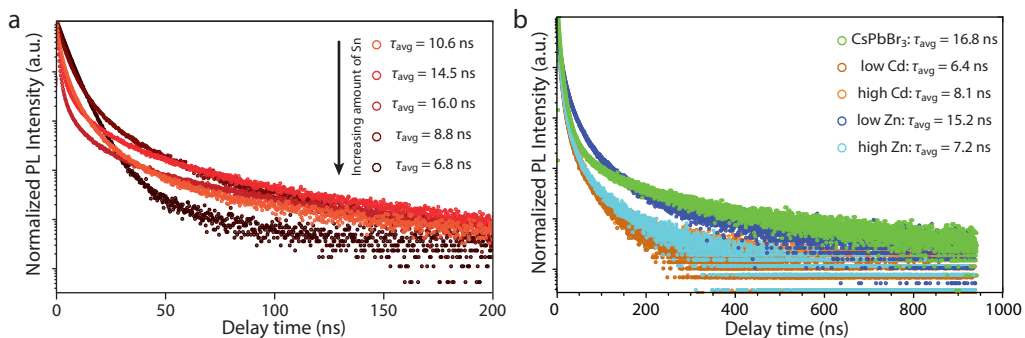


Figure 6.10: PL decay measurements on doped CsPb_{1-x}M_xBr₃ NCs (a) PL decay traces of the CsPb_{1-x}Sn_xBr₃ NCs with their calculated average exciton lifetimes. (b) PL decay traces of the CsPb_{1-x}Cd_xBr₃ and CsPb_{1-x}Zn_xBr₃ NCs with their calculated average exciton lifetimes.

The average exciton lifetime is calculated as:

$$\tau_{avg} = \frac{\sum_{t=0}^t I(t) * t}{\sum_{t=0}^t I(t)}$$

Where $I(t)$ is the intensity of the PL signal after a time t after laser excitation. Fitting the results with a bi-exponential, resulted in bad fits.

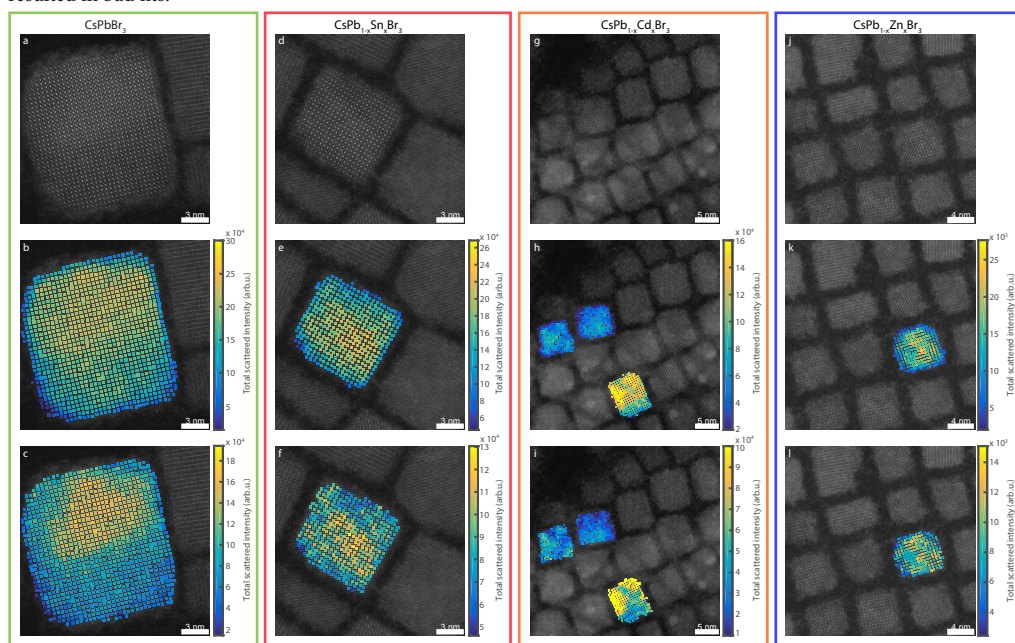


Figure 6.11: Intensity profile mapping in HAADF-STEM images of CsPb_{1-x}M_xBr₃ NCs. The total scattered intensity of each atomic column for (a-c) the parent CsPbBr₃ NCs and (d-l) the doped perovskite NCs obtained by statistical parameter estimation theory. The total scattered intensity is proportional to both the thickness and composition. Differences in thickness profiles between the Pb/halide and Cs columns may arise due to the presence of lighter elements like Sn, Cd and Zn in the Pb/halide columns. (b,e,h,k) The total scattered intensity of the Pb/halide columns. (c,f,i,l) The total scattered intensity of the Cs columns. The intensity profiles of the Pb/halide and Cs columns are similar, indicating that either the dopant level is below the detection limit or the dopants are homogeneously distributed among the different Pb/halide columns.

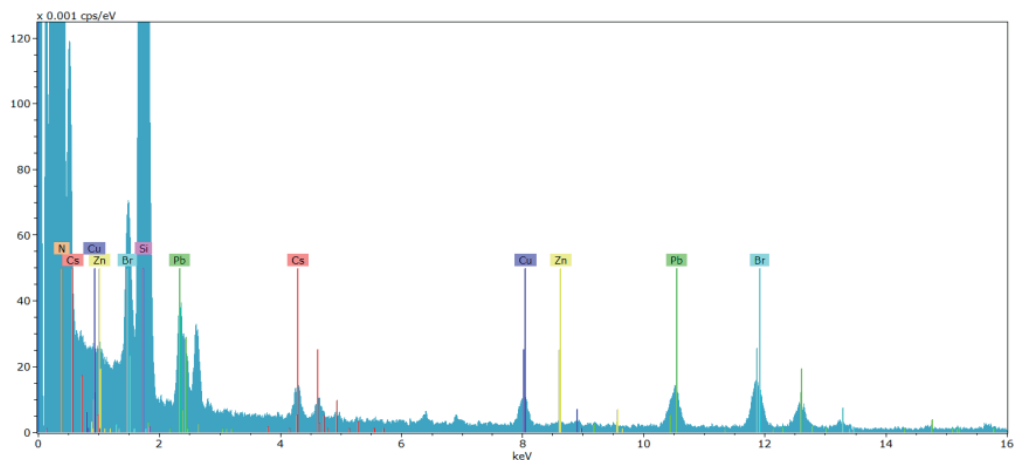


Figure 6.12: Energy Dispersive X-ray Spectroscopy of $\text{CsPb}_{1-x}\text{Zn}_x\text{Br}_3$ nanocrystals. Quantification of the EDS spectrum reveals a Cs:Pb:Zn:Br atomic ratio of 0.4:1.0:0.05:1.6. The Si and N signals emerge from the SiN grid we used to deposit the sample and the Cu signal from the sample holder, measured on a FEI Titan 60-300.

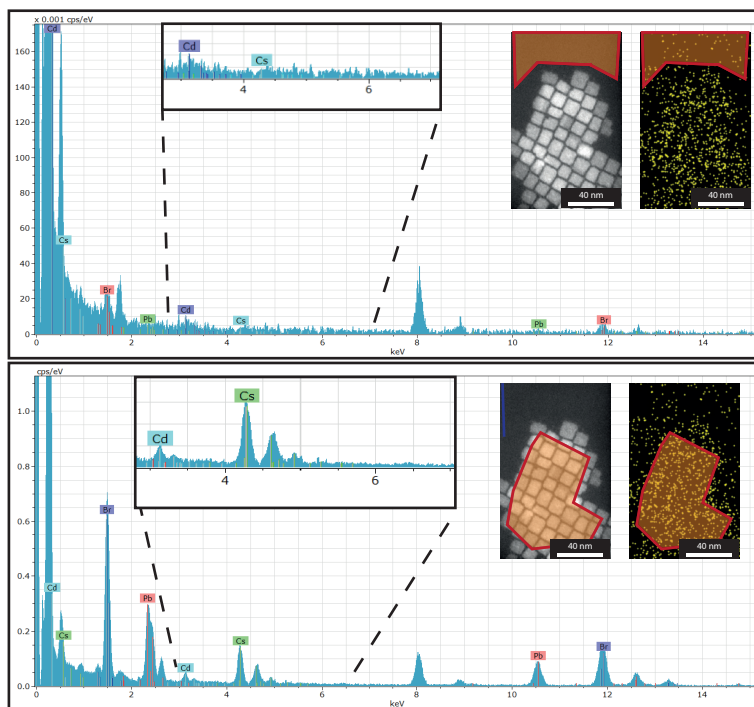


Figure 6.13: Comparison of EDS spectra on top of the $\text{CsPb}_{1-x}\text{Cd}_x\text{Br}_3$ NCs (bottom panel) and on the sample background (top panel). The right insets show the areas on which the EDS signal was integrated to obtain the spectra (orange region). The left insets show zooms around the Cs and Cd lines of the EDS spectrum. The Cd peak at 3.1 keV is barely observable in the background spectrum (top panel), but is quite evident in the spectrum acquired over the NCs, indicating that Cd^{2+} has been successfully incorporated into CsPbBr_3 NCs, resulting in doped $\text{CsPb}_{1-x}\text{Cd}_x\text{Br}_3$ perovskite NCs.

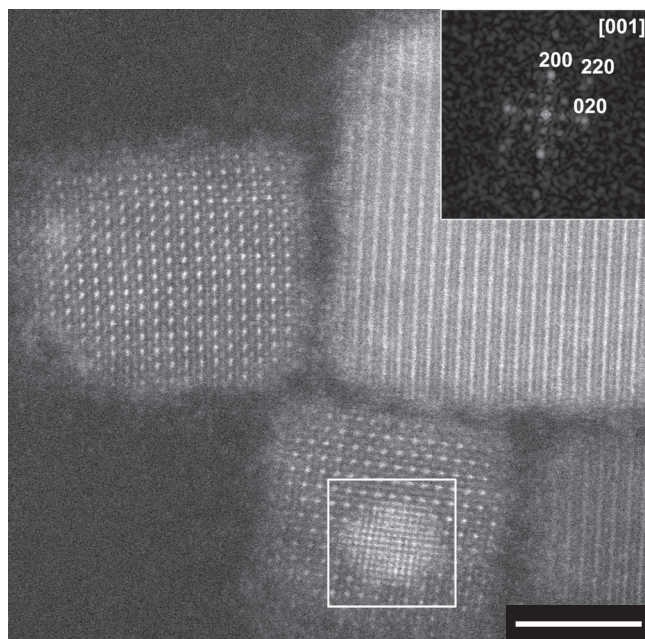


Figure 6.14: High resolution HAADF-STEM image of CsPbBr_3 nanocrystals, showing the formation of metallic Pb particles upon electron beam exposure. The area indicated with the white square displays crystalline material which does not have the cubic CsPbBr_3 crystal structure. From the FFT analysis of this region, displayed in the top right corner, it can be confirmed that the white particles correspond to metallic Pb particles (pdf card: 040686). Possibly, these metallic Pb particles form upon imaging of the CsPbBr_3 NCs with the electron beam for long exposure times, necessary for high resolution TEM measurements. The d-spacings for the {200}/{020} and {220} reflections are 2.475 Å and 1.75 Å, respectively. The scalebar in the HAADF-STEM image equals 5 nm.

References

1. Protesescu, L. et al. "Nanocrystals of Cesium Lead Halide Perovskites (CsPbX_3 , $X = \text{Cl, Br, and I}$): Novel Optoelectronic Materials Showing Bright Emission with Wide Color Gamut". *Nano Lett.* **15**, 3692–3696 (2015).
2. Weidman, M. C., Seitz, M., Stranks, S. D. & Tisdale, W. A. "Highly Tunable Colloidal Perovskite Nanoplatelets through Variable Cation, Metal, and Halide Composition". *ACS Nano* (2016). doi:10.1021/acsnano.6b03496
3. Sun, S., Yuan, D., Xu, Y., Wang, A. & Deng, Z. "Ligand-Mediated Synthesis of Shape-Controlled Cesium Lead Halide Perovskite Nanocrystals via Reprecipitation Process at Room Temperature." *ACS Nano* **10**, 3648–3657 (2016).
4. Yakunin, S. et al. "Low-threshold amplified spontaneous emission and lasing from colloidal nanocrystals of caesium lead halide perovskites". *Nat. Commun.* **6**, 8056 (2015).
5. Xu, Y. et al. "Two-Photon-Pumped Perovskite Semiconductor Nanocrystal Lasers". *J. Am. Chem. Soc.* **138**, 3761–3768 (2016).
6. Zhang, X. et al. "Enhancing the Brightness of Cesium Lead Halide Perovskite Nanocrystal Based Green Light-Emitting Devices through the Interface Engineering with Perfluorinated Ionomer". *Nano Lett.* **16**, 1415–1420 (2016).
7. Swarnkar, A. et al. "Quantum dot-induced phase stabilization of α - CsPbI_3 perovskite for high-efficiency photovoltaics". *Science* (80-.). **354**, (2016).
8. Lignos, I. et al. "Synthesis of Cesium Lead Halide Perovskite Nanocrystals in a Droplet-Based Microfluidic Platform: Fast Parametric Space Mapping". *Nano Lett.* **16**, 1869–1877 (2016).

9. Zhang, D., Eaton, S. W., Yu, Y., Dou, L. & Yang, P. "Solution-Phase Synthesis of Cesium Lead Halide Perovskite Nanowires". *J. Am. Chem. Soc.* **137**, 150716143900005 (2015).
10. Imran, M. et al. "Colloidal Synthesis of Strongly Fluorescent CsPbBr₃ Nanowires with Width Tunable down to the Quantum Confinement Regime". *Chem. Mater.* **28**, 6450–6454 (2016).
11. Akkerman, Q. A. et al. "Solution Synthesis Approach to Colloidal Cesium Lead Halide Perovskite Nanoplatelets with Monolayer-Level Thickness Control". *J. Am. Chem. Soc.* **138**, 1010–1016 (2016).
12. Sichert, J. A. et al. "Quantum Size Effect in Organometal Halide Perovskite Nanoplatelets". *Nano Lett.* **15**, 6521–6527 (2015).
13. Protesescu, L. et al. "Monodisperse Formamidinium Lead Bromide Nanocrystals with Bright and Stable Green Photoluminescence". *J. Am. Chem. Soc.* **138**, 14202–14205 (2016).
14. Nedelcu, G. et al. "Fast Anion-Exchange in Highly Luminescent Nanocrystals of Cesium Lead Halide Perovskites" (CsPbX₃, X = Cl, Br, I)". *Nano Lett.* **15**, 5635–5640 (2015).
15. Akkerman, Q. A. et al. "Tuning the Optical Properties of Cesium Lead Halide Perovskite Nanocrystals by Anion Exchange Reactions". *J. Am. Chem. Soc.* **137**, 10276–10281 (2015).
16. Hodges, J. M., Kletetschka, K., Fenton, J. L., Read, C. G. & Schaak, R. E. "Sequential Anion and Cation Exchange Reactions for Complete Material Transformations of Nanoparticles with Morphological Retention". *Angew. Chemie* **127**, 8793–8796 (2015).
17. Wu, H.-L. et al. "Formation of pseudomorphic nanocages from Cu₂O nanocrystals through anion exchange reactions". *Science* (80-.). **351**, (2016).
18. Beberwyck, B. J., Surendranath, Y. & Alivisatos, A. P. "Cation Exchange: A Versatile Tool for Nanomaterials Synthesis". *J. Phys. Chem. C* **117**, 19759–19770 (2013).
19. Gupta, S., Kershaw, S. V. & Rogach, A. L. "25th Anniversary Article: Ion Exchange in Colloidal Nanocrystals". *Adv. Mater.* **25**, 6923–6944 (2013).
20. De Trizio, L. & Manna, L. "Forging Colloidal Nanostructures via Cation Exchange Reactions". *Chem. Rev.* **116**, 10852–10887 (2016).
21. Van der Stam, W., Bladt, E., Rabouw, F. T., Bals, S. & de Mello Donega, C. "Near-Infrared Emitting CuInSe₂/CuInS₂ Dot Core/Rod Shell Heteronanorods by Sequential Cation Exchange". *ACS Nano* **9**, 11430–11438 (2015).
22. Li, H. et al. "Blue-UV-Emitting ZnSe(Dot)/ZnS(Rod) Core/Shell Nanocrystals Prepared from CdSe/CdS Nanocrystals by Sequential Cation Exchange". *ACS Nano* **6**, 1637–1647 (2012).
23. Dana A. Schwartz, Nick S. Norberg, Quyen P. Nguyen, Jason M. Parker, and Gamelin*, D. R. "Magnetic Quantum Dots: Synthesis, Spectroscopy, and Magnetism of Co²⁺- and Ni²⁺-Doped ZnO Nanocrystals". (2003). doi:10.1021/JA036811V
24. Knowles, K. E., Nelson, H. D., Kilburn, T. B. & Gamelin, D. R. "Singlet–Triplet Splittings in the Luminescent Excited States of Colloidal Cu⁺:CdSe, Cu⁺:InP, and CuInS₂ Nanocrystals: Charge-Transfer Configurations and Self-Trapped Excitons". *J. Am. Chem. Soc.* **137**, 13138–13147 (2015).
25. Meinardi, F. et al. "Large-area luminescent solar concentrators based on 'Stokes-shift-engineered' nanocrystals in a mass-polymerized PMMA matrix". *Nat. Photonics* **8**, 392–399 (2014).
26. Pérez-del-Rey, D. et al. "Strontium Insertion in Methylammonium Lead Iodide: Long Charge Carrier Lifetime and High Fill-Factor Solar Cells". *Adv. Mater.* **28**, 9839–9845 (2016).
27. Frolova, L. A., Anokhin, D. V., Gerasimov, K. L., Dremova, N. N. & Troshin, P. A. "Exploring the Effects of the Pb²⁺ Substitution in MAPbI₃ on the Photovoltaic Performance of the Hybrid Perovskite Solar Cells". *J. Phys. Chem. Lett.* **7**, 4353–4357 (2016).
28. Abdelhady, A. L. et al. "Heterovalent Dopant Incorporation for Bandgap and Type Engineering of Perovskite Crystals". *J. Phys. Chem. Lett.* **7**, 295–301 (2016).
29. Liu, W. et al. "Mn²⁺-Doped Lead Halide Perovskite Nanocrystals with Dual-Color Emission Controlled by Halide Content". *J. Am. Chem. Soc.* **138**, 14954–14961 (2016).
30. De Roo, J. et al. "Highly Dynamic Ligand Binding and Light Absorption Coefficient of Cesium Lead Bromide Perovskite Nanocrystals". *ACS Nano* **10**, 2071–2081 (2016).
31. Driel, A. F. Van et al. "Statistical analysis of time-resolved emission from ensembles of semiconductor quantum dots: Interpretation of exponential decay models". *Phys. Rev. B.* **75** 1–8 (2007).

32. Delerue, C. & Lannoo, M. "Nanostructures - Theory and Modelling". (Springer Berlin Heidelberg, 2004). doi:10.1007/978-3-662-08903-3
33. Klinger, M. & Jäger, A. "Crystallographic Tool Box (CrysTBox): automated tools for transmission electron microscopists and crystallographers". *J. Appl. Crystallogr.* **48**, 2012–2018 (2015).
34. Peter W. Shriver & Atkins, "Inorganic Chemistry - 5th edition". (Oxford University Press, 2010).
35. Van Aert, S. et al. "Quantitative atomic resolution mapping using high-angle annular dark field scanning transmission electron microscopy". *Ultramicroscopy* **109**, 1236–1244 (2009).
36. De Backer, A., van den Bos, K. H. W., Van den Broek, W., Sijbers, J. & Van Aert, S. "StatSTEM: An efficient approach for accurate and precise model-based quantification of atomic resolution electron microscopy images". *Ultramicroscopy* **171**, 104–116 (2016).
37. Cottingham, P. et al. "On the crystal structure of colloidally prepared CsPbBr₃ quantum dots". *Chem. Commun.* **52**, 5246–5249 (2016).
38. Student. "The Probable Error of a Mean". *Biometrika* **6**, 1 (1908).
39. Boles, M. A., Ling, D., Hyeon, T. & Talapin, D. V. "The surface science of nanocrystals". *Nat. Mater.* **15**, 141–153 (2016).
40. Castelli, I. E., García-Lastra, J. M., Thygesen, K. S. & Jacobsen, K. W. "Bandgap calculations and trends of organometal halide perovskites". *APL Mater.* **2**, 81514 (2014).
41. Jellicoe, T. C. et al. "Synthesis and Optical Properties of Lead-Free Cesium Tin Halide Perovskite Nanocrystals". *J. Am. Chem. Soc.* **138**, 2941–2944 (2016).
42. Hao, F., Stoumpos, C. C., Chang, R. P. H. & Kanatzidis, M. G. "Anomalous Band Gap Behavior in Mixed Sn and Pb Perovskites Enables Broadening of Absorption Spectrum in Solar Cells". *J. Am. Chem. Soc.* **136**, 8094–8099 (2014).
43. Chen, Q. et al. "Under the spotlight: The organic–inorganic hybrid halide perovskite for optoelectronic applications". *Nano Today* **10**, 355–396 (2015).
44. Li, C. et al. "Halide-Substituted Electronic Properties of Organometal Halide Perovskite Films: Direct and Inverse Photoemission Studies". *ACS Appl. Mater. Interfaces* **8**, 11526–11531 (2016).
45. Fabini, D. H. et al. "Dynamic Stereochemical Activity of the Sn 2+ Lone Pair in Perovskite CsSnBr₃". *J. Am. Chem. Soc.* **138**, 11820–11832 (2016).
46. Wei, K. et al. "Temperature-dependent excitonic photoluminescence excited by two-photon absorption in perovskite CsPbBr₃ quantum dots". *Opt. Lett.* **41**, 3821 (2016).
47. Yu, C. et al. "Temperature dependence of the band gap of perovskite semiconductor compound CsSnI₃". *J. Appl. Phys.* **110**, 63526 (2011).
48. Brandt, R. E. & Ginley, D. S. "Identifying defect-tolerant semiconductors with high minority-carrier lifetimes: beyond hybrid lead halide perovskites". doi:10.1557/mrc.2015.26
49. Cardona, M. & Thewalt, M. L. W. "Isotope effects on the optical spectra of semiconductors". *Rev. Mod. Phys.* **77**, 1173–1224 (2005).
50. Villegas, C. E. P., Rocha, A. R. & Marini, A. "Anomalous Temperature Dependence of the Band Gap in Black Phosphorus". *Nano Lett.* **16**, 5095–5101 (2016).
51. Oshero, A. et al. "The Impact of Phase Retention on the Structural and Optoelectronic Properties of Metal Halide Perovskites". *Adv. Mater.* **28**, 10757–10763 (2016).
52. Wang, Y. et al. "Pressure-Induced Phase Transformation, Reversible Amorphization, and Anomalous Visible Light Response in Organolead Bromide Perovskite". *J. Am. Chem. Soc.* **137**, 11144–11149 (2015).
53. Szafranski, M. & Katrusiak, A. "Mechanism of Pressure-Induced Phase Transitions, Amorphization, and Absorption-Edge Shift in Photovoltaic Methylammonium Lead Iodide". *J. Phys. Chem. Lett.* **7**, 3458–3466 (2016).
54. Teisseyre, H. et al. "Photoluminescence in doped GaN bulk crystal". *J. Phys. Chem. Solids* **56**, 353–355 (1995).
55. Gilliland, S. et al. "Pressure and temperature dependence of the band-gap in CdTe". *Phys. status solidi* **235**, 441–445 (2003).

56. Walsh, A., Scanlon, D. O., Chen, S., Gong, X. G. & Wei, S.-H. "Self-Regulation Mechanism for Charged Point Defects in Hybrid Halide Perovskites". *Angew. Chemie Int. Ed.* **54**, 1791–1794 (2015).
57. Yang, T.-Y., Gregori, G., Pellet, N., Grätzel, M. & Maier, J. "The Significance of Ion Conduction in a Hybrid Organic-Inorganic Lead-Iodide-Based Perovskite Photosensitizer". *Angew. Chemie Int. Ed.* **54**, 7905–7910 (2015).
58. Buin, A. et al. "Materials Processing Routes to Trap-Free Halide Perovskites". *Nano Lett.* **14**, 6281–6286 (2014).
59. Groeneveld, E. et al. "Tailoring ZnSe–CdSe Colloidal Quantum Dots via Cation Exchange: From Core/Shell to Alloy Nanocrystals". *ACS Nano* **7**, 7913–7930 (2013).
60. Lesnyak, V., Brescia, R., Messina, G. C. & Manna, L. "Cu Vacancies Boost Cation Exchange Reactions in Copper Selenide Nanocrystals". *J. Am. Chem. Soc.* **137**, 9315–9323 (2015).
61. van der Stam, W. et al. "Luminescent CuInS₂ Quantum Dots by Partial Cation Exchange in Cu_{2-x}S Nanocrystals". *Chem. Mater.* **27**, 621–628 (2015).
62. Eames, C. et al. "Ionic transport in hybrid lead iodide perovskite solar cells". *Nat. Commun.* **6**, 7497 (2015).



Chapter 7

“Playing with Legos”

• Abstract •

CsPbBr₃ perovskite nanocrystals have emerged as promising candidates for various optoelectronic applications, such as light emitting diodes^{1,2}, photodetectors³ and solar cells^{4,5}. Here we show how these nanocrystals can self-assemble into ordered cuboidal supraparticles and investigate the resulting structural and optical properties. The formation takes place in dispersion and can be induced by the addition of methylacetate, which we prove through in-situ X-ray scattering. The constituent nanocrystals inside the superlattice are crystallographically aligned, but not atomically connected into a single crystal. The 3-D structure of the supraparticles was resolved through electron tomography. Combined with secondary-electron STEM we observe both surface defects, and localized defects inside the bulk of the supraparticle in the form of missing nanocrystals. The optical properties of single supraparticles are studied with confocal microspectroscopy and compared to ensemble measurements in solution. The emission spectrum of the supraparticles is red-shifted compared to the individual nanocrystals, indicating an increase of electronic coupling between the constituent nanocrystals.

Based on: Structural and Optical Properties of Supraparticles formed by Self-Assembly of CsPbBr₃ Perovskite Nanocrystals.

Julia S. van der Burgt^{||}, Jaco J. Geuchies^{||}, Berend van der Meer, Hans Vanrompay, Daniele Zanaga, Yang Zhang, Wiebke Albrecht, Andrei V. Petukhov, Laura Fillion, Sara Bals, Ingmar Swart and Daniel Vanmaekelbergh.

In preparation

^{||} These authors contributed equally to this work

7.1 - Introduction

Over the past decade a large amount of research has been devoted to the properties and improvement of hybrid organic-inorganic perovskite materials (e.g. $\text{CH}_3\text{NH}_3\text{PbX}_3$, $\text{X} = \text{Cl}, \text{Br}, \text{I}$) for solar cell applications, which has led to an increase in efficiency from 3.8%⁵ to over 20%⁶. This success has motivated researchers all over the world to look at other types of perovskite materials and other optoelectronic applications, such as photodetectors⁷, light-emitting diodes⁸ and one-⁹ and two-photon pumped gain media for lasers¹⁰. A recently discovered class of these materials is the group of fully inorganic cesium lead halide (CsPbX_3) perovskite nanocrystals (NCs). These colloidal nanocrystals can be synthesized with a facile hot-injection method and possess readily tunable opto-electronic properties¹¹. An advantage of the inorganic CsPbBr_3 is that it possesses a higher temperature stability than the hybrid $\text{CH}_3\text{NH}_3\text{PbX}_3$ ³. Moreover, these NCs show narrow emission peaks with a FWHM of 50-80 meV and exhibit quantum yields of up to 90% without passivating the nanocrystal surface¹². The emission can be tuned over the full visible spectrum by varying the composition of the anionic sublattice, either through direct synthesis or anion exchange reactions¹³⁻¹⁵.

In this chapter, we show that we are able to induce self-assembly of colloidal CsPbBr_3 nanocubes into large cuboidal supraparticles, consisting out of several hundreds to thousands of nanocrystals. Although cubic particles can achieve high packing fractions up to 100% theoretically, they are not encountered often in nature. The observed CsPbBr_3 supraparticles have a cubic symmetry which propagates over three different lengthscales; the cubic symmetry of the atomic perovskite lattice (Ångstroms), combined with the appropriate surface energies of the nanocrystal facets, ensures the NCs to have a cubic shape (size ranging between 7-11 nm), which in turn allows them to self-assemble into a simple cubic packing of NCs inside supraparticles (several hundreds of nm). We have studied the structure of the superlattices in real space using a combination of electron microscopy, electron diffraction and electron tomography, and show that the NCs inside the simple cubic geometry of the supraparticle are atomically aligned, but not connected. Moreover we show that the supraparticles form in solution upon adding a non-solvent to the NC dispersion. The optical properties are studied on both the single-supraparticle level with confocal microspectroscopy, and on the ensemble level in solution with (time-resolved) photoluminescence (PL) spectroscopy. We show that the PL shifts to higher energies by 30 meV, which can either be due to an increase of quantum mechanical coupling in between the particles, or energy transfer through dipolar interactions.

7.2 - Results and discussion

7.2.1 - Structural characterization

The nanocrystal building blocks are synthesized by the method reported by Protesescu et al.¹² (see Methods section for more details). We characterized their optical absorption and emission spectrum in solution. Throughout this chapter we used several different batches of nanocrystals, all showing emission around 2.4 eV with narrow (<80 meV) FWHM. The quantum yield varies in between batches, in between 86-95% for all the used NC batches, as determined with an integrating sphere. Figure 7.1(a) shows the characteristic absorption spectrum and emission spectrum for the NCs with an edge length of roughly 8.5 nm. The NCs are in the weak confinement regime (Bohr exciton radius of 3.5 nm)^{11,16} and no clear bulk

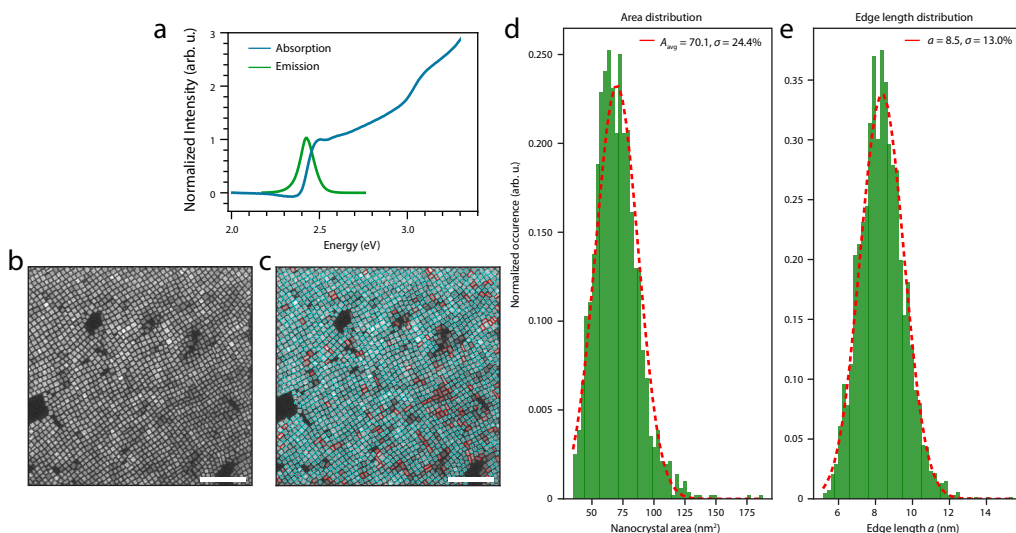


Figure 7.1: Characterization of the CsPbBr₃ nanocrystals as starting blocks for the self-assembly. (a) Normalized optical absorption and PL spectra of the CsPbBr₃ nanocubes. The PL energy for all batches is roughly 2.4 eV and the NCs have a quantum yield varying between 86-95%. (b) HAADF-STEM image of a sub-monolayer of nanocrystals. (c) Computer aided image analysis allows us to obtain statistics on the size and shape of the particles. Particles with an aspect ratio ≤ 1.5 are defined cubic and are outlined with a blue square. Particles with an aspect ratio > 1.5 are defined as platelet-like and are outlined with a red rectangle. (d) Distribution of the areas of the detected nanocrystals. (e) Distribution of the detected edge length of the nanocrystals. Several HAADF-STEM micrographs were used to gather statistics of over 5000 nanocrystals. Scalebars in the HAADF-STEM images equal 100 nm.

excitonic peak is visible in the absorption spectrum. We will compare the optical properties of freely dispersed NCs with those of the NCs assembled in supraparticles.

The geometry of the NCs was characterized by high-angle annular dark-field (HAADF) scanning transmission electron microscopy (STEM), as shown in figure 7.1(b). We employ a custom made Python code to gather information on the geometry of the synthesized nanocrystals. After filtering and binarizing the HAADF-STEM image, the particles are fitted with a rectangle (for more information, see Methods section). The results of the particle detection are shown in figure 7.1 (c). We define detected particles with an aspect ratio ≤ 1.5 as cubic and outline the detected shape with a blue square. Detected particles with an aspect ratio > 1.5 are defined as rectangular, and are outlined with a red rectangle. Over 95% of the particles in a single HAADF-STEM image are detected, and the resulting outlines seem to match the particle contours very well. Over 5000 particles were detected over several HAADF-STEM micrographs, which allows us to obtain decent statistics on the particle size and shape. The area of the detected particles is shown in figure 7.1 (d) and the detected edge length is shown in figure 7.1(e). The acquired data is binned into a histogram and fitted with a normal distribution. The nanocrystals have $\{100\}$ facets with an average surface area of $70 \pm 17 \text{ nm}^2$ and an edge length of $8.5 \pm 1.1 \text{ nm}$.

The self-assembly is induced via two methods; (1) concentrating the nanocrystal dispersion, or (2) through addition of methyl acetate as an anti-solvent. The reason for the use of methyl acetate is that it is shown that this is one of the few polar solvents that do not damage the rather ionic NCs¹⁷.

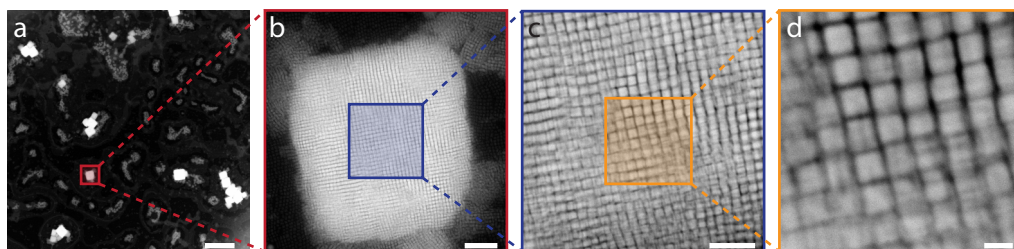


Figure 7.2: HAADF-STEM overview image and zoom-series on a single supraparticle. (a) Low-magnification overview image, showing a relatively low coverage of large, cubic-shaped supraparticles. (b) Zoom on the marked region in (a). (c) Zoom on the marked area in (b). The individual NCs in the supraparticle are clearly visible. (d) Zoom on the marked area in (c). The columns of NCs in the lattice of the supraparticle are clearly visible, hinting towards a simple-cubic packing of the constituent NCs in the supraparticle. Scalebars denote 2 μm , 100 nm, 50 nm and 10 nm from left to right respectively.

Equivalent supraparticles are formed and in the following we focus on the geometry of the formed aggregates. Figure 7.2 shows a series of HAADF-STEM images with increasing magnification. A low magnification image is presented in figure 7.2(a). The supraparticles appear as large white cubes on the dark background. From this low-magnification image, another remarkable observation is that besides some supraparticle clustering, the supraparticles have a more or less uniform size, which is discussed further in section 7.2.2.

Upon zooming-in on one supraparticle in figure 7.2(b-d), it becomes clear that the supraparticle consists out of several hundreds of nanocrystals. Moreover, the columns of nanocrystals are clearly distinguished in the highest magnification image. The degree of ordering inside the supraparticle is apparent through the observed contrast in the HAADF-STEM image, hinting towards a simple cubic stacking of the NCs inside the cuboidal supraparticle. The NCs are clearly not attached into a single-crystalline structure through some form of oriented attachment¹⁸, but are still separated by their oleic acid and oleylamine capping ligands. The contrast between the particles appears to be blurred out slightly, which is probably due to some positional and rotational disorder of the NCs. Further on, we will also show the presence of surface defects, and localized NC vacancies in the bulk of the supraparticle, which also contribute to the amount of disorder inside the supraparticle and hence, the blurring of the contrast in the HAADF-STEM images. More images of the formed supraparticles are depicted in 7.11 at the end of this chapter.

To have a more quantitative look at the rotational freedom of the NCs inside the supraparticles, we performed electron diffraction (ED) on the supraparticle presented in figure 7.2. In figure 7.3, the selected area (SA) diffraction pattern is shown in figure 7.3 (a). The presence of well defined diffraction spots instead of powder rings already indicates that the particles are atomically aligned, with a [100] zone axis (i.e. one of their {100} facets pointing upwards). The diffraction pattern can be indexed at least up to reflections from the {420} atomic planes. In figure 7.3(b), azimuthal traces at constant scattering vector \mathbf{q} are presented for the {100}, {110}, {200} and {220} planes (depicted in red, blue, green and yellow respectively). All 12 peaks were fitted with Gaussians to obtain an average FWHM of $9.6 \pm 1.4^\circ$, which reflects an upper limit of their in-plane rotational freedom. The degree of atomic alignment of the constituent NCs can be well rationalized, considering their well defined cubic shape. A schematic of the measured rotational disorder of the nanocubes is shown in Figure 7.3(c).

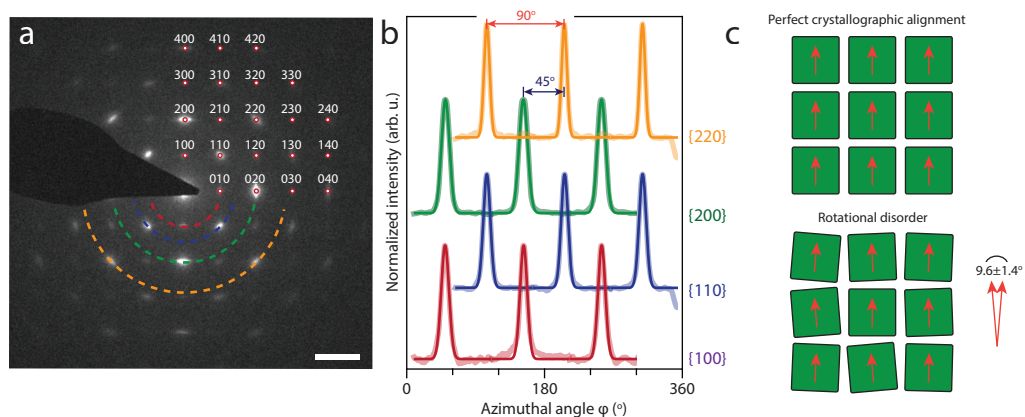


Figure 7.3: Electron diffraction on a single supraparticle. (a) Electron diffraction pattern on the supraparticle shown in figure 7.2, acquired along the [100] NC zone axis. The appearance of well defined diffraction spots over powder rings indicate that the NCs are crystallographically aligned. The diffraction spots can be indexed clearly up to reflections from the {420} atomic planes. (b) Azimuthal traces at constant scattering vectors q for different atomic reflections. Fitting the twelve peaks gives an average FWHM of $9.6 \pm 1.4^\circ$, which depicts an upper limit of the in-plane rotational freedom of the NCs inside the supraparticle. (c) Schematic comparison of a simple cubic lattice of nanocubes without (top) and with (bottom) the presence of rotational disorder. The orange arrows represent the orientation of the atomic lattice of the nanocubes. The scalebars in the diffraction patterns equal 10 nm^{-1} .

The surface of the supraparticles was studied using secondary electron-STEM (SE-STEM), where electrons are backscattered from the surface of the object of interest. The HAADF-STEM of a supraparticle is shown in figure 7.4(a). The backscattered electrons are collected simultaneously and result in the image displayed in figure 7.4(b). The slightly more grey areas are missing NCs at the surface of the supraparticles, or surface defects. Both individual NC surface defects, as well as groups of missing NCs can be seen. From all our SE-STEM images we estimate the total amount of defects to equal $5.5 \pm 1.5\%$ of the total supraparticle surface area. See also Figure 7.13.

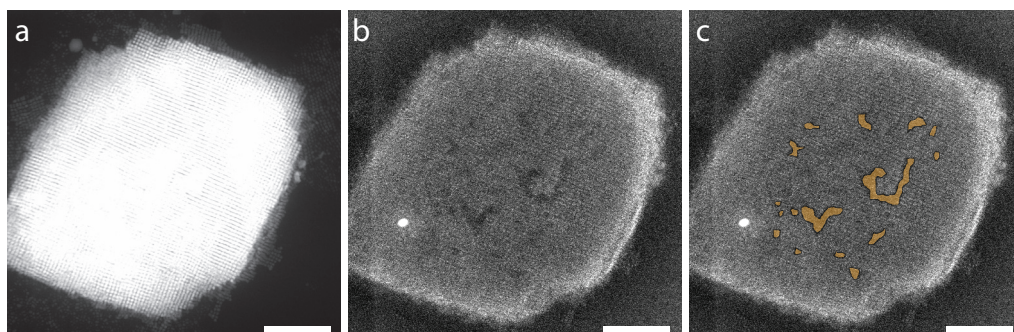


Figure 7.4: SE-STEM imaging of the surface of a supraparticle. (a) HAADF-STEM image of a supraparticle. (b) Corresponding SE-STEM image of the supraparticle. The missing nanoparticles appear as a darker grey area on the surface of the supraparticle. The white spot is a result of the carbon build up by the electron beam. (c) For clarity the regions are indicated in yellow. From all obtained SE-STEM images we estimate that the total amount of defects equals $5.5 \pm 1.5\%$ of the total surface area of the supraparticle. The scalebars equal 200 nm .

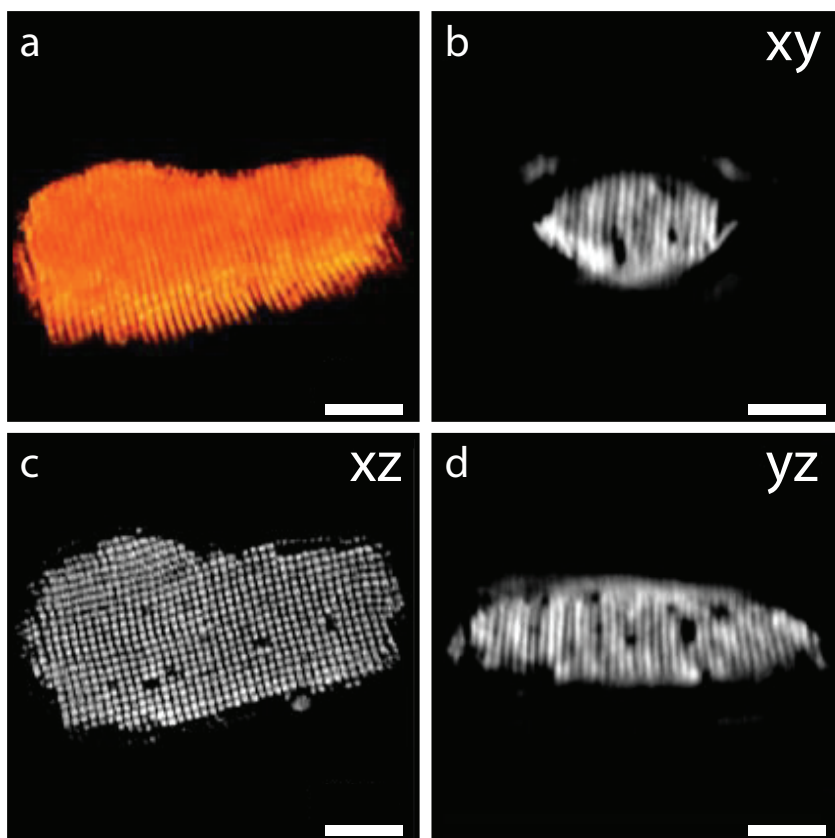


Figure 7.5: HAADF-STEM tomography, revealing defects in the bulk of the supraparticle. (a) Visualization of the 3-D reconstruction of a single SP, acquired by rotating the sample over two orthogonal tilt series and reconstructed using a TVM algorithm. Orthoslices through the xy (b), xz (c) and yz (d) directions of the tomogram reveal several vacancies in the bulk of the supraparticle. The scalebars equal 50 nm.

In order to get insight into the stacking of the NCs inside the supraparticles, a single supraparticle was studied using HAADF-STEM tomography. A series of projection images was acquired with an angular range of -70° to 78° and a tilt increment of 2° . Orthogonal to that a second tilt series was acquired from -76° to 76° to reduce the missing wedge of tilt angles to a missing pyramid. Using this dual tilt series as an input for several mathematical reconstruction algorithms, we found that the total variation minimization (TVM) based algorithm gave the clearest reconstruction. This algorithm promotes the sparsity of the gradient image of the reconstruction and therefore results in a smooth reconstructed tomogram.

A visualization of the acquired tomogram is presented in figure 7.5(a). We are not able to clearly resolve all individual NC positions inside the supraparticle using any of the reconstruction techniques. The orthoslices in figure 7.5(b-d) show interesting features nonetheless. In all three orthogonal directions, we clearly observe empty places on a crystal site. There appear to be localized single point vacancies and missing groups of NCs. From the tomogram we estimate a volume fraction of vacancies in the bulk of the supraparticle of 3.3%. This is in contrast with what

previous Monte Carlo and molecular dynamics simulations have predicted for hard cubes, i.e. non-interacting cubes. Dijkstra et al. showed that for hard cubes, defects manifest themselves as a finite-length chain of particles along one of the principal axes in the crystal¹⁹. Hence, the vacancy is now spread over many lattice positions. The free energy of the system is subsequently lowered, as one vacancy provides additional free volume for multiple nearby particles, decreasing the entropy of the crystal. Additionally the authors showed that the amount of positional order inside the simple cubic crystal is increased upon the addition of these delocalized defects. The volume fraction at which melting occurs is significantly decreased, indicating that the relative stability is increased by the defects. Localized vacancies are also observed by Rossi et al.²⁰, where colloidal cubes of roughly one micron are self-assembled into simple cubic lattices through addition of a depletant, which induces effective attractions between the cube facets. The localization and grouping of defects in our experiments point towards attractive interactions between the NCs. The NCs do not behave as hard particles anymore, and the energy decrease due to the NC-NC attraction overcomes the entropic penalty for defect localization.

7.2.2 - Formation mechanism

The growth of the supraparticles is monitored ex-situ using electron microscopy. Figure 7.6(a) shows a typical bright-field TEM overview image of a substrate containing many supraparticles. In general, two methods can be used to form the supraparticles: (1) solvent evaporation and (2) addition of anti-solvent. Both methods lead to an increase of the chemical potential of the NCs in solution;

$$\mu = \mu^* + k_B T \ln\left(\frac{c}{c^*}\right) \quad 5.1$$

Where μ is the total chemical potential of the NCs in solution and μ^* is the standard chemical potential of the NCs in solution, which accounts for the potential energy of the particles inside a certain solvent. Upon addition of methyl acetate, μ^* is increased and the system can lower its total chemical potential by crystallizing into a supraparticle. Upon solvent evaporation, the particle concentration is increasing over time and this also increases the total chemical potential of the NCs in solution. Both methods lead to identical supraparticles, however larger sizes are obtained by solvent evaporation, as shown in Figure 7.6 (b). The drawback here is that the time of formation is rather long (> 1 month). In principle this can be reduced by performing the evaporation under reduced pressures. Care has to be taken to operate the assembly under (nearly) reversible conditions, as fast kinetics can lead to disordered, non-equilibrium structures. In the present case this was, e.g. seen with supraparticles with a high amount of anti-solvent. In figure 7.6(c) a low magnification image of a sample where methyl acetate was added to the NC dispersion up to a volume fraction of 0.5. Large clusters with an irregular shape are obtained, which show no clear nanocrystalline order, as shown in figure 7.6(d).

One of the remaining open questions is whether the supraparticles form in solution, or if their formation is an effect of solvent evaporation when preparing a TEM grid. To this end we performed transmission small-angle X-ray scattering (SAXS), both on pure nanocrystal suspensions, and suspensions where we added methyl acetate as an anti-solvent. A schematic of the experiment is shown in figure 7.7(a). A solution of NCs was added to a quartz capillary with an outer diameter of 1.5 mm and placed inside a Linkam stage positioned at a distance of 1 m from the SAXS detector. A WAXS detector, collecting the atomic diffraction of the NCs, was positioned at the inlet of the vacuum tube holding the SAXS detector.

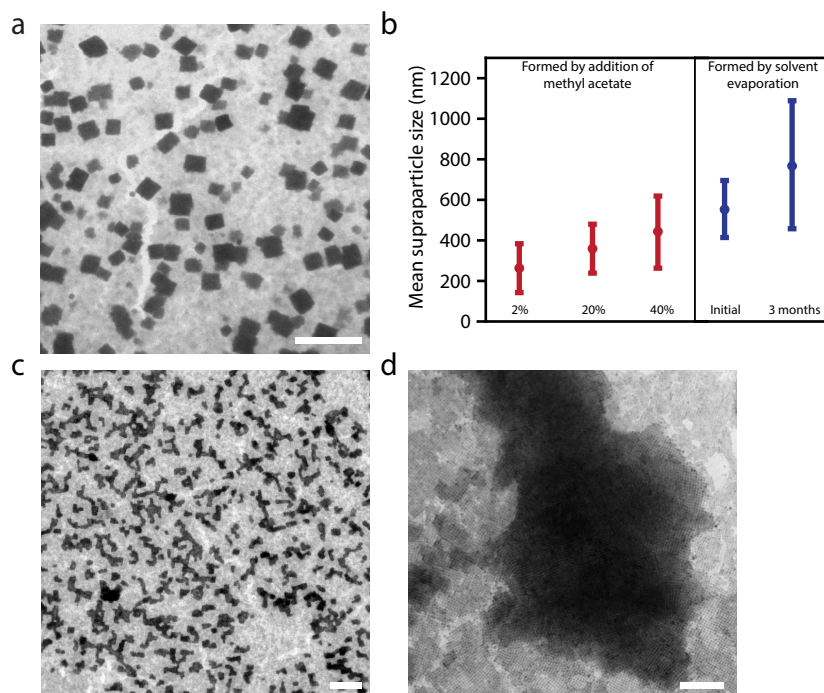


Figure 7.6: Supraparticle growth over time. (a) Bright-field TEM overview of supraparticles, grown by addition of methyl acetate up to a volume fraction of 0.2. The TEM image was taken one week after addition of methyl acetate. (b) Average supraparticle size after one week of growth (for anti-solvent addition), and by solvent evaporation after one month and three months. The error bars depict the standard deviation of the size dispersion (c) Upon increasing the volume fraction of methyl acetate above 0.40 (here 0.5), the supraparticles possess irregular shapes and (d) the nanocrystals appear randomly agglomerated. Scalebars equal 2 μm for (a) and (c) and 200 nm for (d).

The SAXS and WAXS pattern of a solution without anti-solvent is shown in figure 7.7(b). The SAXS region (light blue), where the NCs scatter, only shows form factor scattering from unclustered NCs in solution. The WAXS signal (dark blue) shows sharp diffraction peaks, originating from the atomic perovskite lattice of the NCs. The sample with a volume fraction of 0.2 was measured after three days of incubation and is presented in figure 7.7(c). The SAXS pattern shows clear Bragg peaks at positions of 0.55 nm^{-1} , 0.78 nm^{-1} , 1.11 nm^{-1} and 1.23 nm^{-1} . Their relative peak positions correspond to $1:\sqrt{2}:2:\sqrt{5}$, which corresponds to scattering from the $\{100\}$, $\{110\}$, $\{200\}$ and $\{210\}$ lattice planes of a simple-cubic lattice of NCs. The measured NC-NC distance inside the supraparticle equals 11.4 nm, corresponding to NCs still separated by their oleic acid and oleylamine ligands. The FWHM of the $\{100\}$ reflection is 0.0378 nm^{-1} , which corresponds to a crystalline domain size of roughly 166.3 nm.

Recent work by Bertolotti et al. also showed that the CsPbBr_3 NCs have the tendency to stack in solution²¹, similar to concentrated solutions of nanoplatelets²². The stacking direction occurs most likely in the $[100]$ direction. Such stacks could hence be a precursor phase in the formation of the supraparticles presented in this chapter. However, this remains to be verified by performing time-resolved in-situ SAXS and WAXS on the self-assembly process.

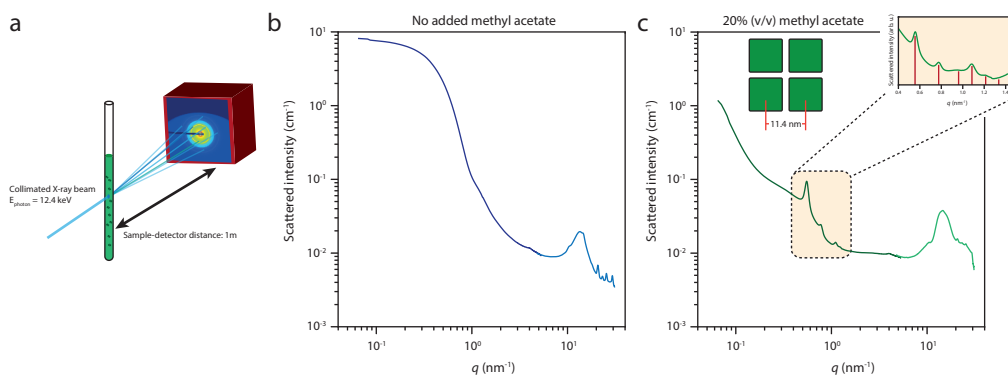


Figure 7.7: Transmission X-ray scattering on NC solutions with and without anti-solvent addition. (a) Schematic of the experimental set-up. A quartz capillary is loaded with a solution of nanocrystals (with or without anti-solvent addition), which has been left to incubate for three days. The capillary is placed in a linkam stage, which is located at a 1 m distance from the detector to collect the small-angle scattering. Also wide-angle scattering is recorded by a detector placed at the inlet of the vacuum tube with the SAXS detector. **(b)** The NC dispersion without addition of anti-solvent only shows the form factor scattering of the individual NCs in solution. **(c)** Diluted NC solution with 20% (vol%) methyl acetate shows clear Bragg peaks, indicating the formation of a crystalline supraparticle. The inset shows a zoom on the region with the Bragg peaks, which is scaled by the form factor scattering from **(b)**. The red lines indicating the expected peak positions for a simple-cubic packing of the NCs.

The supraparticles all seem to have a cuboidal shape, rather than a completely cubic one, i.e. the supraparticles have less NCs in the direction perpendicular to the substrate than that they have in the two directions parallel to the substrate. We cannot fully exclude that this happens during the drying of the dispersion on the TEM grids. When the supraparticles form in solution and attain their final shape, the symmetry of the self-assembly process has to be broken. Since the NCs have a well defined cubic shape, and they only have their six {100} facets exposed in solution, there is no clear chemical reason for the apparent breaking of the symmetry. Recent work from Riedinger et al. has shown that there is an intrinsic instability in growth kinetics of isotropic materials that leads to the two-dimensional growth of nanoplatelets²³. During CdSe nuclei formation, the addition of monomers is isotropic, but monomers rapidly diffuse to the sides of the nanoplatelet. This is unexpected, since the CdSe NCs (can) have a zinc blende cubic crystal structure. The proposed growth mechanism took a lot of inspiration from the theory for epitaxial growth of crystals, where newly added monomers also rapidly diffuse to the edge of the not completely finished atomic layer, i.e. a step-edge. Finally, the symmetry of the self-assembly process could be broken around an interface, similar to the oriented attachment presented in previous chapters, that is the liquid-air interface or the solid-liquid interface. At this point, we cannot exclude or confirm that either of these two mechanisms is at play during the formation of the supraparticles presented in this chapter.

We observed the formation of single crystalline sheets of CsPbBr₃ after incubation times longer than 1.5 weeks from dispersions which had shown supraparticles of NCs after incubation of one week (see figure 7.12). Possibly the capping ligands of the NCs are gently removed upon prolonged exposure to the anti-solvent-containing dispersion. The ligand-free {100} facets are then free to attach epitaxially. This hypothesis remains to be proven experimentally and goes beyond the scope of the work presented in this chapter.

7.2.3 - Optical characterization

In order to study the optical properties of single supraparticles and compare them to the optical properties of the individual NCs, we performed confocal microspectroscopy. A dispersion containing the supraparticles was dropcast on a microscope slide and the solvent of the dispersion was allowed to evaporate. A droplet of immersion oil was placed on the sample and a second cover slide was placed on top of the sample. The results are presented in figure 7.8 below.

Figure 7.8(a) shows a digital photograph of a solution of NCs under daylight illumination, and under UV excitation. All the acquired data is shown in a light solid line, while the fitted Gaussian profile is shown as a dark solid line. The data from the confocal microspectroscopy is shown in figure 7.8(b-f). We compare the background region, which we assume to be a layer of NCs, to regions which resemble the supraparticle shapes as observed with electron microscopy. The fitted PL maxima of the supraparticles are all redshifted compared to the monolayer of

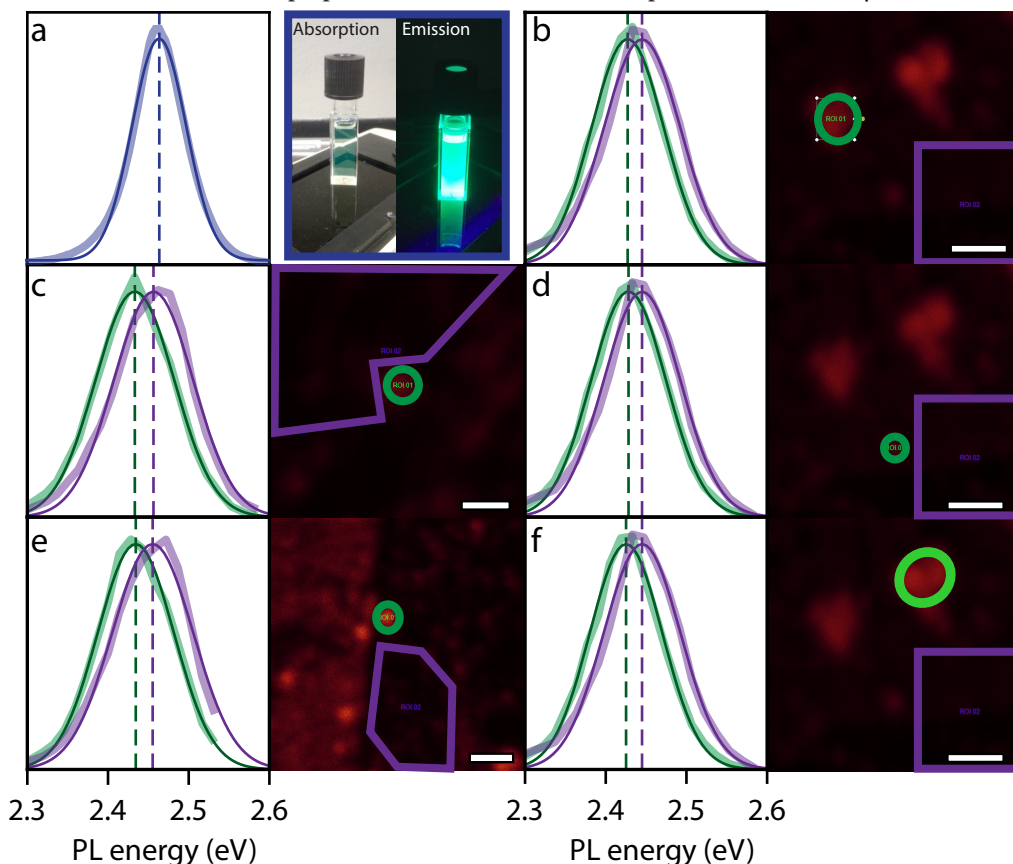


Figure 7.8: Confocal microspectroscopy on single supraparticles. The lighter lines are the data, the darker solid lines are the Gaussian fits. **(a)** Emission from a diluted solution of NCs. The photograph shows the NC dispersion under daylight and UV illumination. **(b-f)** Selection of confocal microscopy images of supraparticles and their corresponding PL spectrum. The spectrum of the supraparticle, depicted in green, is averaged over the area indicated in a green circle and is plotted as a green line and fit. It is compared to the background PL spectrum, averaged over the area depicted in purple (a NC monolayer) and is plotted as a purple line and fit. Scalebars in the confocal micrographs equal 1 μm.

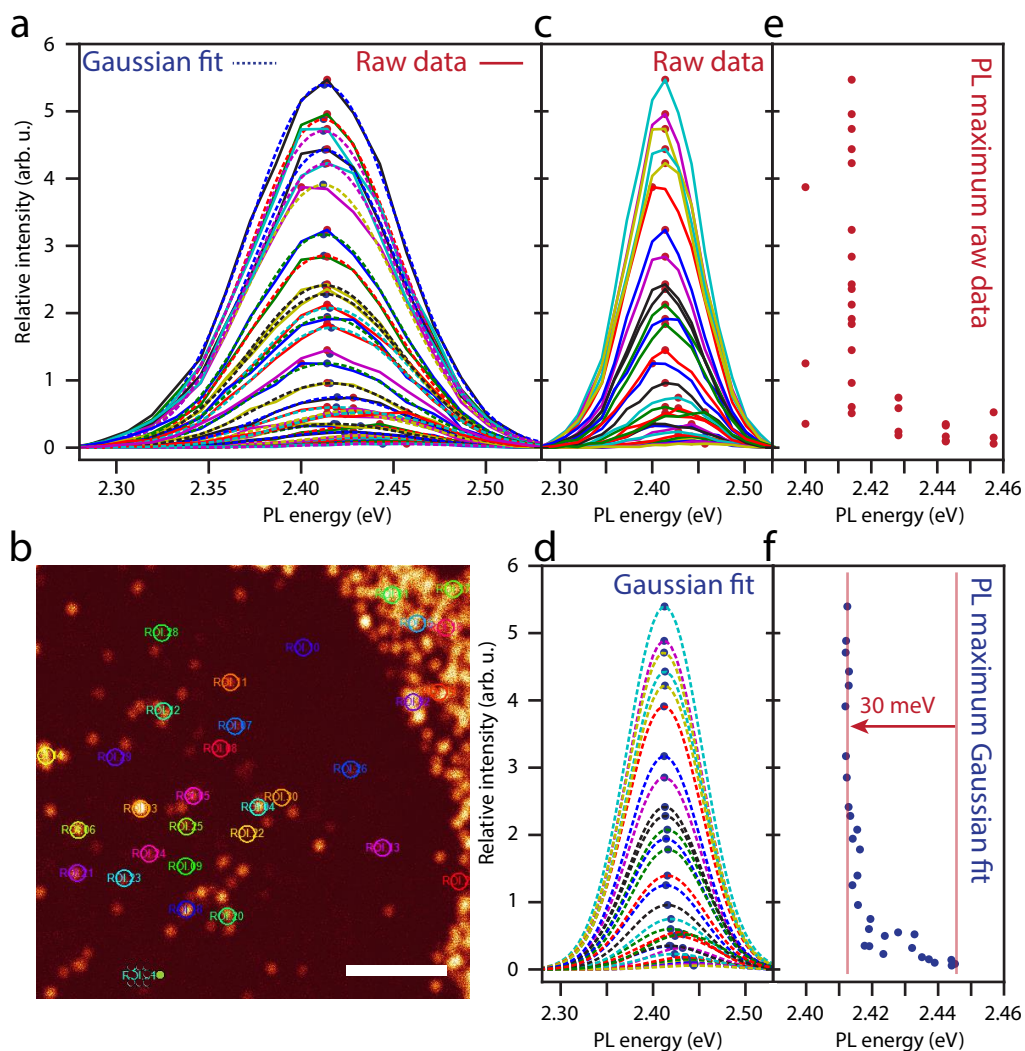


Figure 7.9: Intensity vs. PL energy on a large number of supraparticles. The emission spectrum of a large number of areas is depicted in (a). The area on which the PL signal was integrated is depicted in the confocal micrograph in (b). The solid lines shown the data, the dashed lines show the Gaussian fit to the PL signal. The data and the fit are displayed separately in (c) and (d) respectively for clarity. The obtained maxima from the raw data and the fits are displayed in (e) and (f) respectively. A clear trend is observed in both cases; the higher the PL intensity (i.e. the denser NC regions or supraparticles) emit 30 meV redshifted compared to the NC monolayer background.

nanocrystals in the background, hinting towards some degree of electronic coupling or energy transfer between the NCs when brought in close proximity to each other. As there are in the weak exciton confinement regime, we suspect that electronic coupling is not the main cause of the PL redshift. To check if the shift in energy of the PL maximum is an effect occurring inside supraparticles, we measured the PL spectrum of 30 different regions in the confocal micrograph of varying intensity. The reasoning behind this is that the high intensity regions, often identified as larger objects on the confocal image, are assumed to correspond to supraparticles, while the

lower intensity regions are identified as sub-monolayers of NCs. The data is presented in figure 7.9(a), where the solid lines show the recorded PL signal and the dashed lines are the Gaussian fits to the intensity profile. Figure 7.9(b) shows the low magnification confocal micrograph, with the regions where the PL signal was averaged indicated in a colored circle. We obtained a statistically valid dataset by keeping the area over which the PL signal was integrated constant. The detected maximum together with the recorded data and the fitted Gaussian profiles and the fitted maximum are displayed in Figure 7.9(c) and (d) respectively. Both the maximum of the data (figure 7.9(e)) and the fitted maximum (figure 7.9(f)) show that the PL maximum continuously redshifts for higher intensity regions with a maximum of 30 meV. A similar redshift is observed when comparing NCs in solution to supraparticles in solution using time-resolved emission spectroscopy (TRES), which is shown in figure 7.16.

There are several mechanisms for energy transfer that could be effective inside our system, both non-radiative and radiative. As the exciton Bohr diameter is relatively small (7 nm^{12,16}) compared to the NC diameter, we are in the weak confinement regime and we believe that the contribution of quantum coupling to the observed redshift of the PL maximum is rather small. There is also the possibility of coupling between the NCs through Förster resonance energy transfer (FRET)²⁴. It is mediated by resonant dipole-dipole coupling between a donor and an acceptor, has an r^{-6} distance dependency and is believed to be the most dominant form of energy transfer between NCs²⁴⁻²⁶. FRET also depends on the overlap between the emission and absorption spectra of the donor and acceptor respectively, which is relatively large as shown in figure 7.1. Even if we accept FRET as a mechanism for exciton diffusion, we need a second element, which is places in the supraparticle with lower exciton energy, i.e. fluctuations in the bandgap. Also there is the possibility of radiative energy transfer, i.e. reabsorption, which again depends on the amount of spectral overlap. Other mechanism include emission from a phonon-relaxed state²⁷, or an increase of the local dielectric constant in the supraparticle, which leads to a lower exciton binding energy. Currently, we cannot pinpoint the exact mechanism responsible for the PL redshift.

7.3 - Conclusion and outlook

To summarize, we study the self-assembly of CsPbBr₃ NCs into 3-D cuboidal supraparticles. Inside the supraparticles, the NCs are crystallographically aligned, but not atomically connected, and stack into a simple cubic lattice. The structural characterization pinpoints to a lot of localized NC vacancies, both on the surface and in the bulk of the supraparticles, which hints to attractive interactions between the nanocrystals. This is currently being investigated using Monte Carlo and Molecular Dynamics simulations. In addition, cryo-TEM or FIB-SEM could exclude the presence of artefacts due to solvent evaporation even further, by directly measuring the samples in their solute state. The emission spectrum of the supraparticles is red shifted by 30 meV compared to a diluted solution of NCs, which indicates that there is a energy transfer, most likely through FRET, between the NCs inside the supraparticles. The complete origin of the spatially varying exciton energy in the supraparticles is not precisely known. The fact that the obtained supraparticles are still highly emissive makes them promising candidates for opto-electronic applications. Moreover they could be used as microcavities, to study the confinement of the PL and lasing inside supraparticles.

7.4 - Methods

CsPbBr₃ nanocrystal synthesis. The CsPbBr₃ NCs were prepared according to the method described by Protesescu et al¹². First, Cs-oleate precursor stock solution was prepared. Cs₂CO₃ (0.814g, 99% Aldrich), 2.5 mL oleic acid (OA, 90% Aldrich) and 40 mL 1-octadecene (ODE, 90% Aldrich) were loaded into a 100 mL round-bottom flask. The mixture was dried under vacuum for approximately 1h at 120 °C, and then heated under N₂ to 150 °C until all Cs₂CO₃ had reacted with OA. ODE (5 mL) and PbBr₂ (0.069g, 99.999% Aldrich) were loaded into a separate 25 mL flask and dried under vacuum for 1h at 120 °C. Oleylamine (OLAM 0.5 mL, 70% Aldrich) and OA (0.5 mL) were injected at 120 °C under N₂ atmosphere. After PbBr₂ had dissolved, the temperature was raised to 180 °C and a 0.4 mL portion of the Cs-oleate stock solution was quickly injected. We note that the Cs-oleate stock solution had to be preheated to ~100 °C before injection. After five to ten seconds the reaction mixture was cooled by an ice-water bath in order to quench the reaction.

Purification of the nanocrystals. The CsPbBr₃ NCs were purified following the method described by De Roo et al²⁸. (for a synthesis based on 69 mg of PbBr₂). The crude synthesis solution was centrifuged for 3 min at 10000 rpm and the colored supernatant was discarded. Then, 300 µL of hexane was added and the NCs were dispersed using a vortex mixer. Subsequently, the suspension was again centrifuged for 3 min at 10 000 rpm, after which the precipitate, containing larger NCs and agglomerates, was discarded. Another 300 µL of hexane was added to the supernatant, resulting in a colloidal dispersion of CsPbBr₃ NCs.

Self assembly into supraparticles. The CsPbBr₃ NCs were self-assembled into supraparticles by adding a varying amount of methyl acetate into a solution containing 0.1 µM of NCs (as determined from absorption spectroscopy²⁸). The solutions were incubated at room temperature in a dark place for five days, unless mentioned otherwise. Self-assembly through solvent-evaporation occurred in nanocrystal solutions with a concentration higher than 1 µM NCs. Note that the latter number is a rough estimate, since the exact determination of the concentration was hampered due to the saturation of the absorption signal.

Electron microscopy and electron diffraction. Electron micrographs were recorded on a FEI Technai 12 operated at 120 kV (bright-field images). HAADF-STEM and selected-area electron diffraction was performed on a FEI Talos F200X operated at 120 kV. The HAADF-STEM tomography was performed on a FEI Osiris microscope operated at 120 kV. A tilt series was acquired with an angular range of -70° to 78° and a tilt increment of 2°. To reduce the effects of the missing wedge, a second, orthogonal tilt series was combined with the former one in order to reduce the missing wedge to a missing pyramid. The orthogonal series of projection images was recorded with an angular range of -76° to 76° and a tilt increment of 2°. We used a TVM algorithm to reconstruct the images presented in figure 7.5. Also a SIRT and PDART²⁹ algorithms were attempted, but gave a less clear reconstruction.

Transmission SAXS and WAXS experiments. Small and wide-angle X-ray scattering (SAXS and WAXS) experiments were performed at the ID02 beamline, European Synchrotron Radiation Facility, Grenoble, France. The SAXS detector was a Rayonix MX-170HS mounted at a distance of 1m from the sample, which allowed us to probe the entire q range from 6.5×10^{-2} to 4.8 nm^{-1} . The wavelength of the collimated X-ray beam was 0.1 nm (12.4 keV). The WAXS detector was a Rayonix LX-170HS mounted on the beginning of the SAXS vacuum tube (calibrated with $\alpha\text{-Al}_2\text{O}_3$). A capillary with a nanocrystal solution in toluene (or a diluted NC solution in toluene with additional methyl acetate) was placed inside a Linkam stage.

Optical spectroscopy. Samples for optical measurements were prepared by diluting the colloidal dispersion of NCs with anhydrous toluene under nitrogen and stored in sealed quartz cuvettes. Absorption spectra were measured on a double beam Perkin-Elmer Lambda 16 UV/Vis spectrometer. Photoluminescence (PL) spectra were recorded on an Edinburgh Instruments FLS920 Spectrofluorimeter equipped with a 450 W Xenon lamp as excitation source and double grating monochromators. PL decay curves were obtained by time-correlated single-photon counting on a Hamamatsu H7422-02 photomultiplier tube with low dark count rate (< 10 cts/s). A pulsed diode laser (EPL-445 Edinburgh Instruments, 375 nm, 55 ps pulse width, 0.2 MHz repetition rate) was used as the excitation source.

Confocal microspectroscopy. Individual supraparticles were studied using a Leica TCS SP8 confocal spectromicroscope. We used a 63x/1.4 oil-immersion confocal Leica objective. The sample was excited with a fiber-based white light laser at 470 nm. A droplet of the dispersion containing supraparticles was placed on a microscope slide and the solvent (toluene) was allowed to evaporate. A droplet of immersion oil was placed on top of the sample to index-match the oil objective, followed by another cover microscope slide (with a thickness of 160-190 µm). Another droplet of immersion oil was placed on top of the cover slide and the sample was loaded into the microscope.

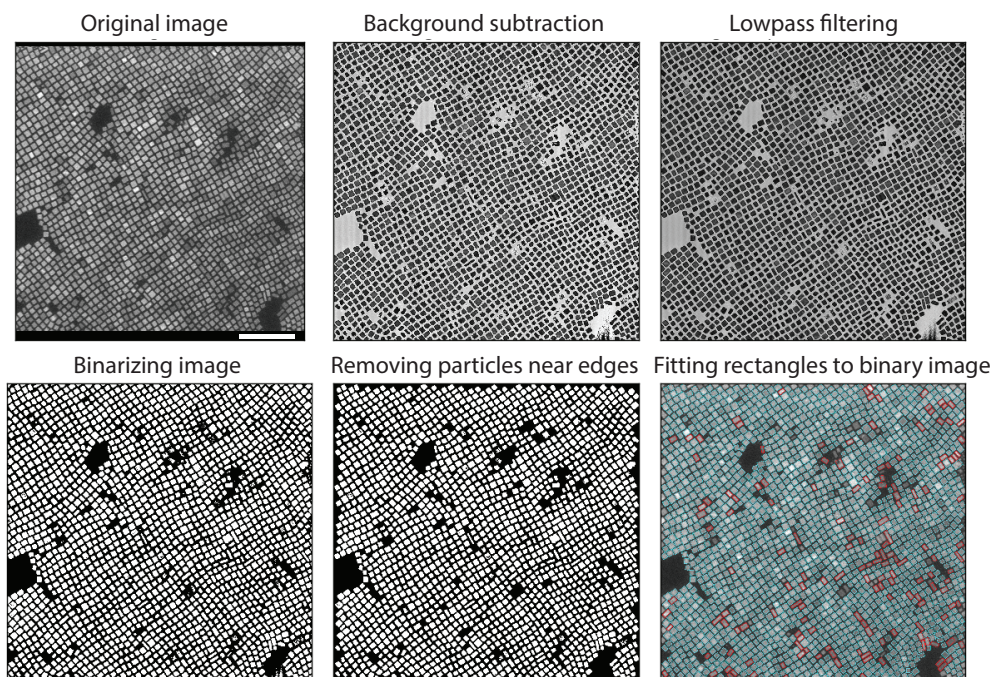


Figure 7.10: Outline of the used particle detection scheme. An electron micrograph is loaded into the program. The background is detected by fitting each column of the image matrix with a third-order polynomial and is subtracted from the original image, after which the image is low-pass filtered through an FFT. The resulting filtered image is binarized and particles near the edges and too small particles are filtered out before fitting the binary areas with rectangles. The scalebar equals 100 nm.

A schematic outline of the particle detection tool programmed in Python is shown in figure 7.10. The TEM image is loaded and the scalebar is automatically detected to determine the size of one pixel. The background is subtracted by fitting a third order polynomial to each column in the image matrix. These polynomials are then subtracted from the image, after which a Fourier Transform is taken of the image, from which the high-frequency noise is filtered out. The image is hence low-pass filtered via a back Fourier Transformation. For the particle detection afterwards, we binarize the low-pass filtered image and label the centers of mass of each white object. The Mahotas package in Python is used for the labelling of each particle and each particle too close to the edge, or below a certain size, are discarded from further analysis to avoid artefacts. The fitting is done by detecting the contour of each detected particle and fitting this with a rectangle, from which the length and width are determined. Particles with an aspect ratio larger than 1.5 are labeled as a rectangular particle and their contours are shown with a red rectangle. Particles with an aspect ratio between 1 and 1.5 are labeled as a cubic particle and their contours are shown with a blue rectangle. The data is binned in a histogram, of which an example is shown in figure 7.1.

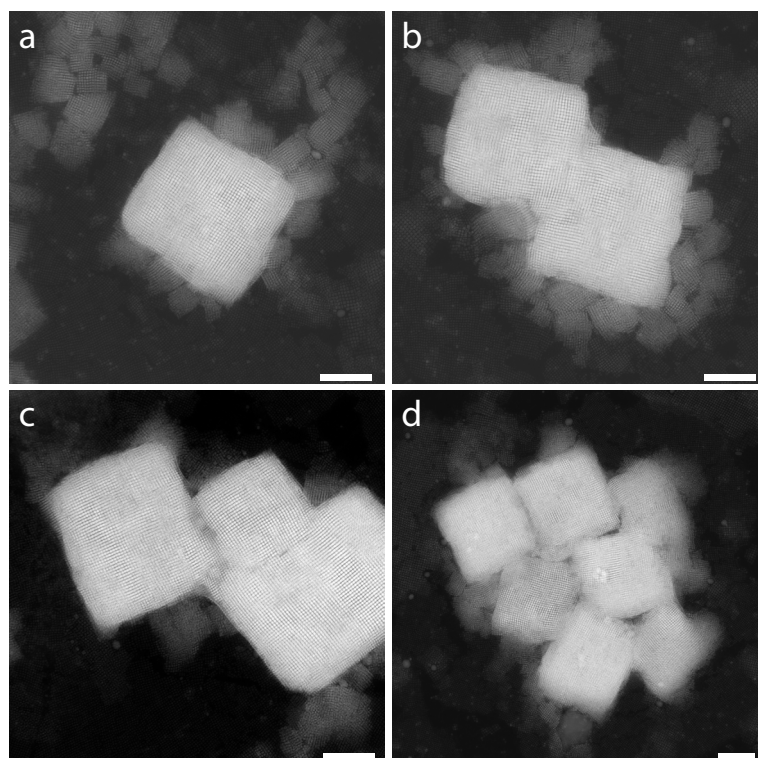


Figure 7.11: HAADF-STEM overview images of typical supraparticles. (a) Single supraparticles are most commonly observed. (b) Micrograph of two aggregated supraparticles. (c) Micrograph of three aggregated supraparticles. (d) Micrograph of multiple aggregated supraparticles. Note how (b) and (c) appear to show the same orientation of the NC lattice, while in (d) the rotational disorder is larger. Scalebars equal 200 nm for all images.

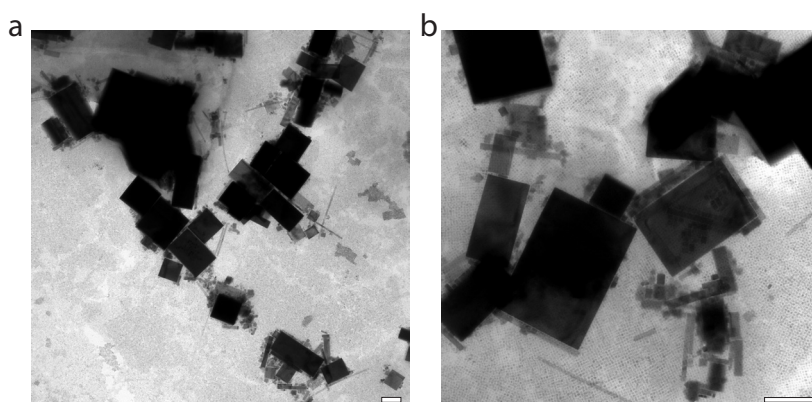


Figure 7.12: Formation of single crystalline particles. (a) and (b) both show bright-field TEM images of a supraparticle sample which was left a week longer to incubate in a solution with 20% (vol%) methyl acetate. The supraparticles which were observed a week before seem to have transformed into single crystalline sheets of CsPbBr₃. Possibly the ligands are slowly removed inside the dispersion, allowing the nanocrystals to fuse epitaxially, however this mains to be confirmed experimentally. Scalebars equal 200 nm.

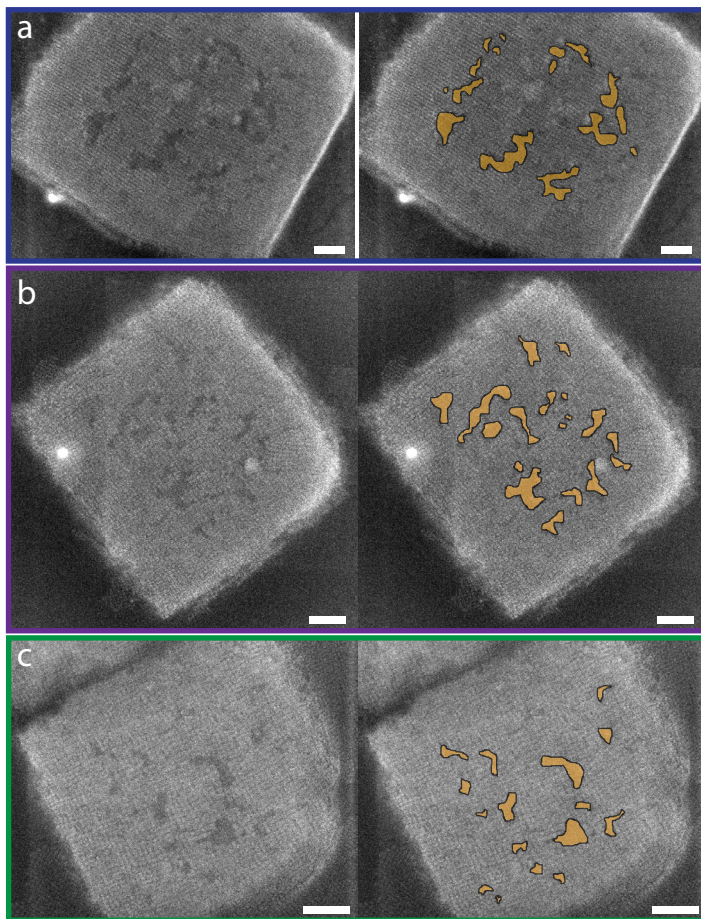


Figure 7.13: SE-STEM micrographs of more supraparticles, showing the occurrence of surface defects. (a-c) Images of several supraparticles, all of which seem to contain surface defects in the form of missing (groups of) NCs. The areas containing the missing NCs appear as slightly darker gray and are highlighted in yellow in the column of images of the right. We manually estimated the area of the surface defects. All scalebars equal 100 nm.

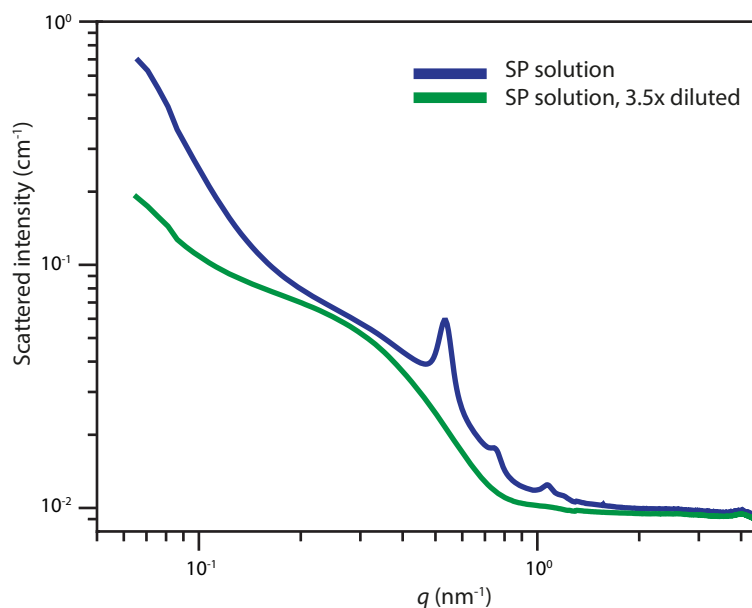


Figure 7.14: Transmission SAXS showing the dissolution of the supraparticles. The solution of supraparticles (blue curve) is diluted with additional toluene (green curve). As can be observed, the structure factor peaks of the SP disappear and only form factor scattering of the nanocrystals in solution is observed, i.e. the supraparticles redissolve upon dilution.

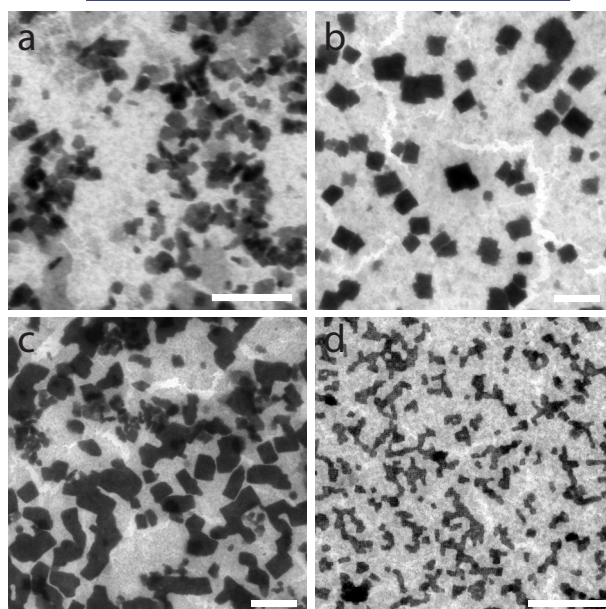


Figure 7.15: Effect of the amount of added anti-solvent on the supraparticle formation. From (a) to (d) we have added 8%, 20%, 40% and 80% (vol%) of methyl acetate to the solution containing NCs. There is still nanocrystalline order visible in the sample displayed in (c), but the supraparticle outline shows less sharp edges. In (d) there is no order of the NCs inside the supraparticle. Scalebars equal 1 μm .

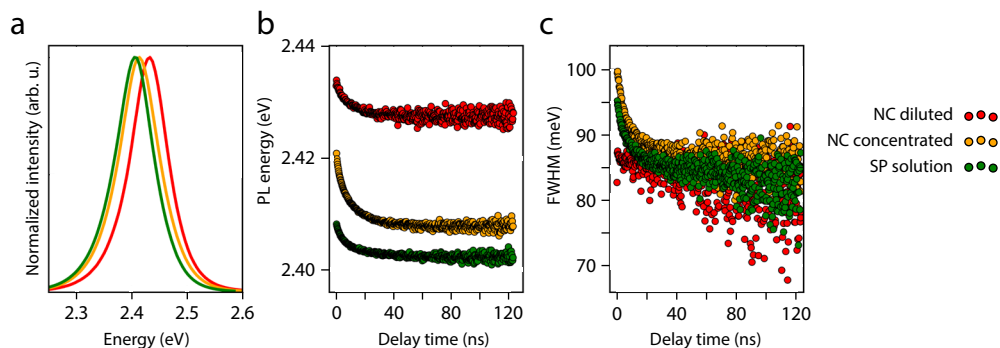


Figure 7.16: Time-resolved emission spectroscopy on supraparticle solutions - spectral evolution. Since we cannot fully separate NCs from supraparticles in solution, care has to be taken that we always measure a signal which is a convolutions of both species. **(a)** Time averaged emission spectrum of a diluted NC solution, a concentrated NC solution and a solution containing supraparticles. It can be seen that both the concentrated solution and the solution containing supraparticles are redshifted by 20-30 meV. **(b)** Evolution of the maximum of the PL signal over time over the first 120 ns. The redshift over the first 30-40 ns is attributed to two factors: Fermi's Golden Rule, stating that the higher the PL energy of a NC, the faster it will emit and to the possibility of energy transfer within the supraparticle. Also note the 30 meV redshift of the PL of the supraparticle solution compared to the diluted NCs, corresponding well to the data from the confocal microspectroscopy experiments in figure 7.9. **(c)** Evolution of the FWHM of the PL signal over the first 120 ns.

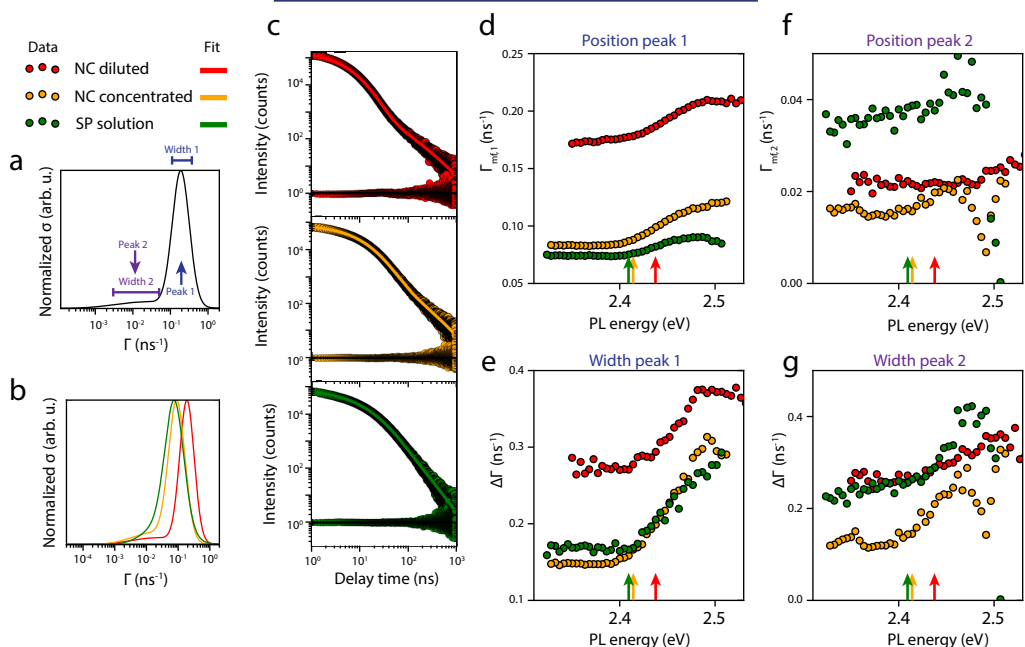


Figure 7.17: Time-resolved emission spectroscopy on supraparticle solutions - time evolution. We obtain a best fit using the sum of two log-normal distribution of decay rates³⁰. **(a)** Example of a log-normal distribution of decay-rates, with the four fitting parameters (two times peak average decay rate and width of the distribution) indicated. **(b)** Fitted distribution of decay rates for the diluted NC solution, concentrated NC solution and SP solution. **(c)** Fits through the acquired decay curves at the maximum of the PL intensity (indicated with green, yellow and red arrows in figure (d-g)). The fit residuals are shown below the decay curve. **(d-g)** Acquired decay rate and width of the decay rate distribution for different PL energies as acquired with the TRES experiments.

Acknowledgements

We are very grateful to for the excellent experimental support at the ID02 beamline. We thank Rajeev Dattani as local contact and Jacques Gorini for technical assistance. We would like to thank Federico Montanarella, P. Tim Prins and Carlo van Overbeek for their contribution to the SAXS experiments.

References

1. Wang, P. et al. "Multicolor fluorescent light-emitting diodes based on cesium lead halide perovskite quantum dots". *Appl. Phys. Lett.* **109**, 63106 (2016).
2. Zhang, X. et al. "Enhancing the Brightness of Cesium Lead Halide Perovskite Nanocrystal Based Green Light-Emitting Devices through the Interface Engineering with Perfluorinated Ionomer". *Nano Lett.* **16**, 1415–1420 (2016).
3. Ramasamy, P. et al. "All-inorganic cesium lead halide perovskite nanocrystals for photodetector applications". *Chem. Commun.* **52**, 2067–2070 (2016).
4. Kulbak, M., Cahen, D. & Hodes, G. "How Important Is the Organic Part of Lead Halide Perovskite Photovoltaic Cells? Efficient CsPbBr₃ Cells". *J. Phys. Chem. Lett.* **6**, 2452–2456 (2015).
5. Kojima, A., Teshima, K., Shirai, Y. & Miyasaka, T. "Organometal Halide Perovskites as Visible-Light Sensitizers for Photovoltaic Cells". *J. Am. Chem. Soc.* **131**, 6050–6051 (2009).
6. Eperon, G. E. et al. "Perovskite-perovskite tandem photovoltaics with optimized bandgaps". *Science* (80-.). (2016).
7. Dou, L. et al. "Solution-processed hybrid perovskite photodetectors with high detectivity". *Nat. Commun.* **5**, 5404 (2014).
8. Wang, N. et al. "Perovskite light-emitting diodes based on solution-processed self-organized multiple quantum wells". *Nat. Photonics* **10**, 699–704 (2016).
9. Yakunin, S. et al. "Low-threshold amplified spontaneous emission and lasing from colloidal nanocrystals of caesium lead halide perovskites". *Nat. Commun.* **6**, 8056 (2015).
10. Xu, Y. et al. "Two-Photon-Pumped Perovskite Semiconductor Nanocrystal Lasers". *J. Am. Chem. Soc.* **138**, 3761–3768 (2016).
11. Lignos, I. et al. "Synthesis of Cesium Lead Halide Perovskite Nanocrystals in a Droplet-Based Microfluidic Platform: Fast Parametric Space Mapping". *Nano Lett.* **16**, 1869–77 (2016).
12. Protesescu, L. et al. "Nanocrystals of Cesium Lead Halide Perovskites (CsPbX₃, X = Cl, Br, and I): Novel Optoelectronic Materials Showing Bright Emission with Wide Color Gamut". *Nano Lett.* **15**, 3692–3696 (2015).
13. Nedelcu, G. et al. "Fast Anion-Exchange in Highly Luminescent Nanocrystals of Cesium Lead Halide Perovskites (CsPbX₃, X = Cl, Br, I)". *Nano Lett.* **15**, 5635–5640 (2015).
14. Akkerman, Q. A. et al. "Tuning the Optical Properties of Cesium Lead Halide Perovskite Nanocrystals by Anion Exchange Reactions". *J. Am. Chem. Soc.* **137**, 10276–10281 (2015).
15. Koscher, B. A., Bronstein, N. D., Olshansky, J. H., Bekenstein, Y. & Alivisatos, A. P. "Surface- vs Diffusion-Limited Mechanisms of Anion Exchange in CsPbBr₃ Nanocrystal Cubes Revealed through Kinetic Studies". *J. Am. Chem. Soc.* jacs.6b08178 (2016).
16. Butkus, J. et al. "The Evolution of Quantum Confinement in CsPbBr₃ Perovskite Nanocrystals". *Chem. Mater.* acs.chemmater.7b00478 (2017).
17. Swarnkar, A. et al. "Quantum dot-induced phase stabilization of α -CsPbI₃ perovskite for high-efficiency photovoltaics". *Science* (80-.). 354, (2016).
18. Evers, W. H. et al. "Low-Dimensional Semiconductor Superlattices Formed by Geometric Control over Nanocrystal Attachment". *Nano Lett.* **13**, 2317–2323 (2013).
19. Smallenburg, F., Filion, L., Marechal, M. & Dijkstra, M. "Vacancy-stabilized crystalline order in hard cubes". *Proc. Natl. Acad. Sci. U. S. A.* **109**, 17886–90 (2012).
20. Rossi, L. et al. "Cubic crystals from cubic colloids". *Soft Matter* **7**, 4139–4142 (2011).

21. Bertolotti, F. et al. “Coherent Nanotwins and Dynamic Disorder in Cesium Lead Halide Perovskite Nanocrystals”. *ACS Nano* acsnano.7b00017 (2017).
22. Bekenstein, Y., Koscher, B. A., Eaton, S. W., Yang, P. & Alivisatos, A. P. “Highly Luminescent Colloidal Nanoplates of Perovskite Cesium Lead Halide and Their Oriented Assemblies”. *J. Am. Chem. Soc.* **137**, 16008–16011 (2015).
23. Riedinger, A. et al. “An intrinsic growth instability in isotropic materials leads to quasi-two-dimensional nanoplatelets”. *Nat. Mater.* (2017).
24. Allan, G. & Delerue, C. “Energy transfer between semiconductor nanocrystals: Validity of Förster’s theory”. *Phys. Rev. B* **75**, 195311 (2007).
25. De Weerd, C. et al. “Energy Transfer between Inorganic Perovskite Nanocrystals”. *J. Phys. Chem. C* **120**, 13310–13315 (2016).
26. Kholmicheva, N., Moroz, P., Eckard, H., Jensen, G. & Zamkov, M. “Energy Transfer in Quantum Dot Solids”. *ACS Energy Lett.* **2**, 154–160 (2017).
27. Hutter, E. M. et al. “Direct–indirect character of the bandgap in methylammonium lead iodide perovskite”. *Nat. Mater.* **16**, 115–120 (2016).
28. De Roo, J. et al. “Highly Dynamic Ligand Binding and Light Absorption Coefficient of Cesium Lead Bromide Perovskite Nanocrystals”. *ACS Nano* **10**, 2071–2081 (2016).
29. Chen, D. et al. “The properties of SIRT, TVM, and DART for 3D imaging of tubular domains in nanocomposite thin-films and sections”. *Ultramicroscopy* **147**, 137–148 (2014).
30. Van Driel, A. F. et al. “Statistical analysis of time-resolved emission from ensembles of semiconductor quantum dots: Interpretation of exponential decay models”. *Phys. Rev. B* **75**, 35329 (2007).





Chapter 8

Summary and outlook

• *Abstract* •

The experiments presented in this thesis have provided new insights regarding the self-organization of colloidal semiconductor nanocrystals in two- and three dimensions. We have studied the self-assembly of PbSe nanocrystals into two-dimensional superlattices with different nanogeometries: (1) a honeycomb nanogeometry and (2) a square nanogeometry. We extensively characterized the formed superlattices using different types of electron microscopy and electron tomography, and followed their mechanism of formation using synchrotron X-ray scattering techniques at the ethylene glycol-air interface. Furthermore we have studied the adsorption geometries of these NCs with different sizes. Also, we have demonstrated cation-exchange reactions in perovskite CsPbBr₃ nanocrystals and shown that we are able to induce the self-assembly of these nanocrystals into three-dimensional cuboidal supraparticles.

In this chapter, we will summarize the main results and discuss potential ideas for future research.

8.1 - Introduction

Semiconductor nanocrystals (NCs) have gained a lot of attention due to their opto-electronic properties that are tunable by size, shape and composition. The ability to emit and absorb light of different wavelengths make them very interesting as phosphors for use in lighting applications, or vice versa, as absorbers in solar cells. In the experiments presented in this thesis we studied the self-organization of these NCs into two- and three dimensional ordered structures, called superlattices or superstructures. These structures do not only show periodic order on the length scale of the nanocrystals, but also align their atomic lattices with respect to each other.

8.2 - Formation of 2-D PbSe superlattices

Semiconductor NCs made out of PbSe have a rocksalt atomic crystal lattice and a truncated cubic NC shape. Chapters 3, 4 and 5 deal with the formation and characterization of two-dimensional superlattices from these NCs. The self-assembly takes place on top of a liquid-substrate, in our case ethylene glycol, which enables us to synthesize superlattices with a thickness of one NC. The process is outlined in Figure 8.1. We are able to synthesize two different superlattices nanogeometries: (1) a honeycomb nanogeometry and (2) a square nanogeometry.

In **Chapter 3** we show that the honeycomb nanogeometry is actually buckled, and neighbouring NCs are occupying a different plane of height. The NCs have a $[111]$ axis pointing perpendicular to the plane of the superlattice. Furthermore, they are atomically aligned and epitaxially connected via three out of six $\{100\}$ facets. We also show that we are able to convert the rocksalt PbSe atomic lattice into zinc blende CdSe through a cation-exchange reaction. The CdSe honeycomb superlattice is expected to have Dirac-type valence and conduction bands, which should result in charge carriers behaving as massless particles.

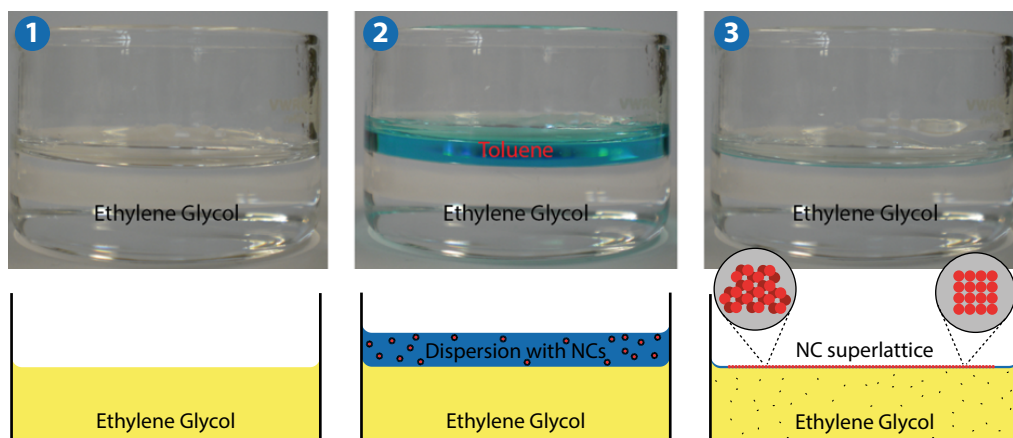


Figure 8.1: Self-organization of PbSe nanocrystals on top of an ethylene glycol liquid substrate. The top row shows digital photographs, the bottom row shows schematic representations. Step 1: Ethylene glycol, which acts as a liquid substrate, is placed inside a petri-dish. Step 2: A dispersion of NCs in toluene (or another volatile apolar solvent) is carefully dropcast on top of the liquid substrate. The toluene is allowed to evaporate over the course of one hour. Step 3: After solvent evaporation, a layer with the thickness of roughly one NC is left on top of the ethylene glycol substrate, and can be scooped or stamped off with a range of different solid substrates for characterization.

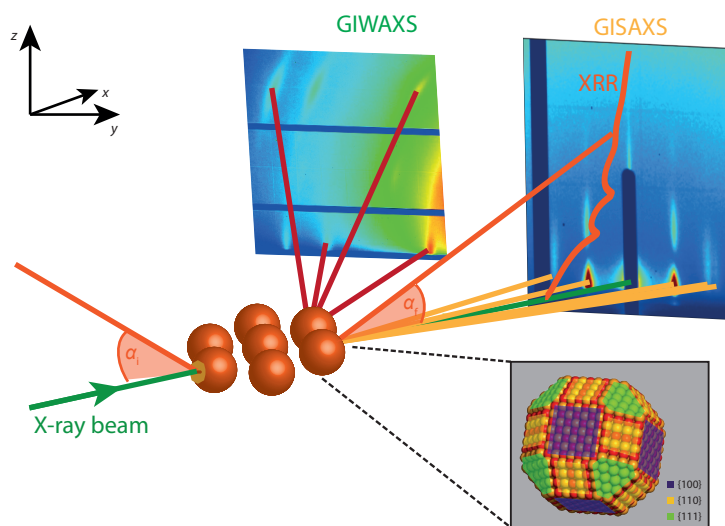


Figure 8.2: The plethora of X-ray scattering techniques used during the experiments presented in this thesis. In the forward scattering direction, the GISAXS signal is collected which gives information on for example the NC-NC distance. Closer to the sample, and under a wider angle, the atomic diffraction is collected on a GIWAXS detector. This can be used to determine the crystallographic orientation of the NCs with respect to the liquid-air interface. Finally, we performed specular X-ray reflectivity measurements, which gives the density profile of the NC monolayer in the direction perpendicular to the liquid-air interface.

In **Chapter 4** we study in-situ and time-resolved the formation mechanism of superlattices with a square nanogeometry. To this end, we use synchrotron based small-angle (and wide-angle) X-ray scattering (GISAXS/GIWAXS). Photons which are scattered under small angles will provide geometric information on the NC length scale (e.g. the interparticle distance), whereas photons which are scattered under wider angles will provide information on the crystallographic orientation and atomic attachment of the NCs. The X-ray beam is aligned such that the photons glance the substrate at a grazing-angle around the critical angle for total external reflection for PbSe. This means the photons have a very low penetration depth (<20 nm) into the liquid and we are able to probe the NC crystallization at the liquid-air interface.

We show that the NCs adsorb at the liquid-air interface and form a hexagonal monolayer. As the capping ligands are gradually desorbed from the $\{100\}$ facets into the ethylene glycol subphase, the interparticle distance is reduced and the lattice is transformed via a pseudo-hexagonal phase into a square superlattice. During this process the NCs align atomically and connect via the in-plane $\{100\}$ facets. The resulting structures are analyzed with high-angle annular dark-field (HAADF) scanning transmission electron microscopy (STEM) to show the residual disorder on the atomic length scale. Furthermore the experiments are corroborated with Monte Carlo simulations, which give further insight into the inter-NC interactions during the self-assembly.

Chapter 5 presents a study of the adsorption geometry of PbSe NCs with different sizes. We add specular X-ray reflectivity (XRR) measurements to GISAXS and GIWAXS measurements. Fitting of the XRR data allows us to obtain a density profile in the direction perpendicular to the ethylene glycol-air interface and, combined with GISAXS and GIWAXS, gives us a full three-dimensional description of the NC monolayer at the interface. We show that the larger PbSe NCs

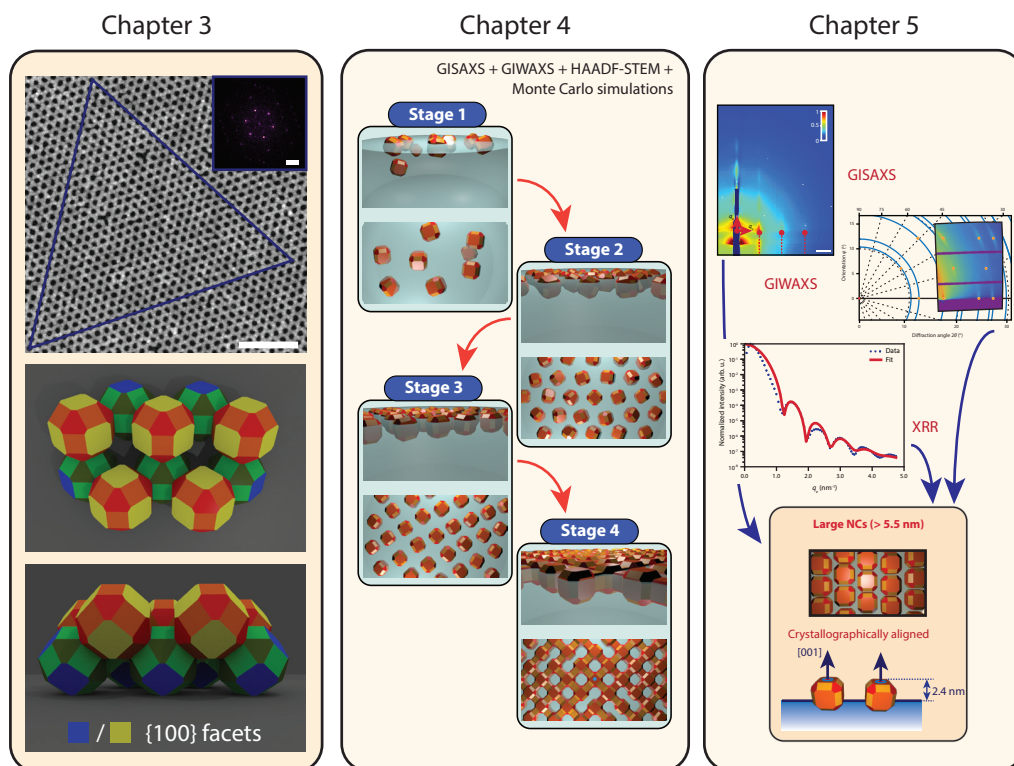


Figure 8.3: Schematic summary of Chapters 3, 4 and 5. In Chapter 3 we studied the formation and structure of a PbSe honeycomb nanocrystal superlattice. The superlattice turned out to be buckled, with the constituent NCs occupying a different plane of height. The NC connect atomically via three out of six {100} facets. In Chapter 4 we studied the mechanism of formation of PbSe superlattices with a square nanogeometry. We resolved the process using a combination of X-ray scattering techniques, advanced electron microscopy and Monte Carlo simulations. In Chapter 5 we studied adsorption geometry of PbSe NCs with different sizes at the ethylene glycol-air interface. We showed that large NCs (> 5.5 nm) align crystallographically with a [001] axis perpendicular to the ethylene-glycol air interface. We combine GISAXS and GIWAXS with XRR measurements to obtain a full three-dimensional description of the adsorption geometry of these PbSe NCs.

align crystallographically with a [001] direction pointing upwards and prove that the NCs all float on top of the ethylene glycol-air interface.

Future research should be divided into two directions: (1) structural investigations regarding the self-assembly process and (2) studies regarding the electronic structure of the superlattices. Regarding the first direction, there are still a lot of unanswered questions.

First of all, we do not fully understand the formation mechanism of the honeycombs superlattice, and how it is different from the formation of the square superlattice. Initial GISAXS and GIWAXS experiments have been performed, but the data is inconclusive. Furthermore the adsorption behaviour of PbSe NCs at the toluene-air interface should be studied. This is significantly more challenging than the experiments presented in Chapter 5, as the toluene evaporation has to be halted. It requires the design of a new liquid cell which is dedicated to these experiments, for which inspiration can be drawn from work done by Calzolari and coworkers¹.

Naturally, different NC systems which self-organize at liquid-air interfaces should also be considered in future experiments, e.g. iron oxide NCs under the influence of a magnetic field.

The electronic structure characterization should be focussed on measuring whether or not the charge carriers behave relativistically. For the moment, this is on-going: scanning tunneling microscopy and spectroscopy (STM/STS) data has been collected, but is also not conclusive yet. The difficulty here lies in the fact that the samples are relatively 'dirty' and measurements are hindered by ligand molecules desorbing from the samples and adsorbing to the STM tip, which hampers stable measurements. Different types of surface passivation techniques can be attempted, either replacing the oleate ligands with smaller carboxylic chains or passivating the superlattice with inorganic shells. Angle-resolved photo-emission (ARPES) can be used to directly measure a materials band structure (i.e. the E, \mathbf{k} relationship). For now, the angular resolution with this technique is the limiting factor for characterizing the superlattices obtained in this thesis. Other experimental techniques that can be considered and are being utilized are transport measurements (either by electrochemical gating or in transistor geometries²) and ultrafast optical spectroscopy (transient-absorption and THz-spectroscopy³).

8.3 - Perovskite CsPbBr_3 nanocrystals

Perovskite NCs made of CsPbX_3 ($X = \text{Cl, Br, I}$) have received a tremendous amount of attention since their first discovery in 2015 by the group of Kovalenko at the ETH, Zürich. Their emission spectrum can be tuned over the complete visible spectrum by changing the constituent halides of the anion sublattice. Since they have a simple cubic atomic lattice, the NCs themselves attain a well defined cubic shape. Chapters 5 and 6 deal with *cation*-exchange reactions and the self-assembly of these NCs respectively.

In **Chapter 6** we present a novel method to perform cation-exchange on CsPbBr_3 NCs. As the NCs are stabilized by the cation sublattice instead of the anion sublattice (in contrast with many II-VI and VI-VI semiconductor NCs), this is not straightforward. We exchange Pb^{2+} for other divalent metal ions such as Cd^{2+} , Zn^{2+} and Sn^{2+} and show that upon doping the NCs a blueshift of the photoluminescence (PL) spectrum is observed, while retaining the narrow PL linewidth and high PL quantum yield. We argue that due to the smaller size of the incorporated ions, the atomic lattice contracts, which leads to an increase in ligand field strength and hence a blueshift of the PL. This is shown through a combination of electron diffraction and high-resolution HAADF-STEM measurements. Up to date, this is the only known system in which sequential cation- and anion-exchange reactions can be combined.

The results presented in **Chapter 7** show that we can induce the self-assembly of CsPbBr_3 NCs into cuboidal supraparticles. Inside the supraparticles the NCs are aligned crystallographically, but are not epitaxially connected, and stack into a simple cubic lattice. We observe the formation of localized NC vacancies in the bulk and on the surface of the supraparticles, which hints towards attractive interactions between the NCs during the self-assembly process. The clustering of the NCs into a supraparticle is induced by addition of an anti-solvent and, using X-ray scattering techniques, is proven to happen in solution. Furthermore we study the optical properties of the supraparticles and show that the PL is redshifted by 30 meV, which is most likely due to energy transfer inside the supraparticle.

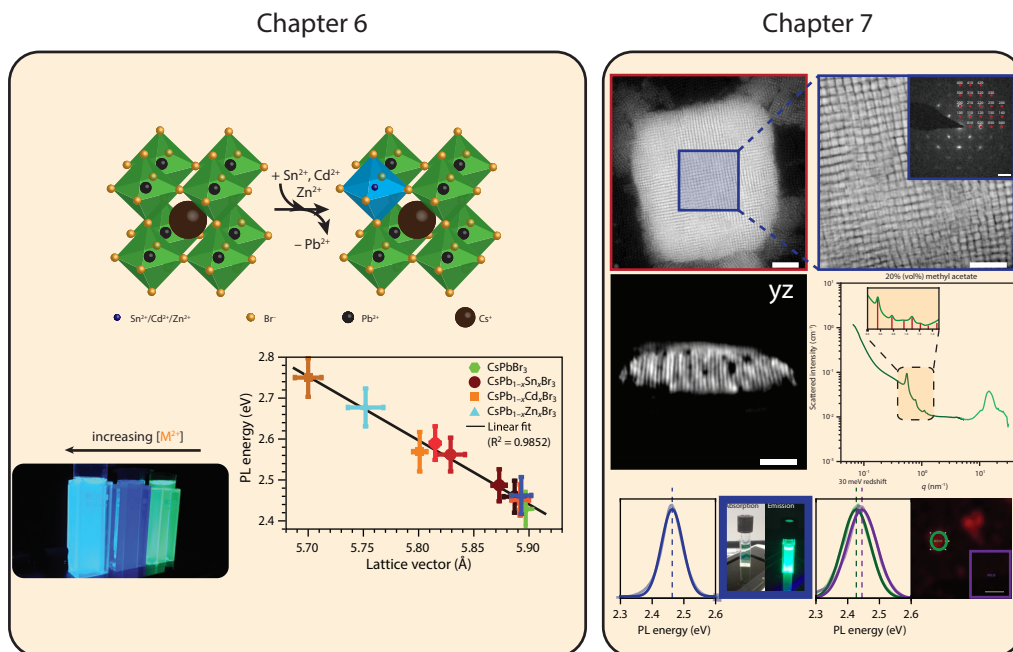


Figure 8.4: Schematic summary of Chapters 6 and 7. In Chapter 6 we demonstrated that we can perform cation exchange on the CsPbBr_3 NCs, removing Pb ions and incorporating Sn, Cd or Zn ions. The PL is blueshifted with respect to the undoped NCs, which is caused by an atomic lattice contraction which leads to an increase in ligand field in the emitting PbBr_6 octahedra inside the NCs. In Chapter 7 we show that we can self-assemble the CsPbBr_3 nanocubes into cuboidal supraparticles consisting out of hundreds of NCs. The NCs inside such a supraparticle are crystallographically aligned, but not connected into a single crystal. We observed localized NC vacancies on both the surface and in the bulk of the supraparticles, which hint towards attractive interactions between the NCs. The PL spectrum of the supraparticles is slightly redshifted compared to the individual NCs in solution.

Several different directions can be explored in future experiments. Based on Chapter 6, there are a number of relevant follow-up experiments possible. First of all it would be interesting to see the extend of the observed blueshift of the PL spectrum with decreasing lattice constants, by performing diffraction experiments at elevated pressures. Not only will this, after full Rietveld refinement of the data, give the full unit cell structure, it can be combined with simultaneous optical spectroscopy. This will ultimately link the unit cell structure (and deviations of the ideal unit cell structure) to the observed changes in optical properties⁴. Also, a variety of spectroelectrochemical experiments can be performed. Recently, it has been shown that the main non-radiative channel in pure CsPbBr_3 NCs is the capture of photogenerated holes in structural defects⁵. Similar experiments on the doped NCs can shed light on the reduction in quantum yield that is observed during the cation-exchange experiments.

The experiments presented in Chapter 7 provide a pathway towards more optical experiments. Due to the high refractive index contrast between the CsPbBr_3 supraparticle and its surrounding, the PL can be confined inside and give rise to whispering gallery modes⁶. These supraparticles would be, owing to the high PL quantum yields of the constituent NCs, ideal candidates for lasing cavities. Not only optical experiments can be explored, also more structural characterization would be interesting. One could try to create monolayers of the CsPbBr_3 NCs and fuse them into

single crystalline materials. It has already been shown that it is possible to directly pattern lead structures into these perovskite materials through electron- or X-ray lithographic techniques⁷⁻⁹. This leaves behind a metallic Pb structure in the sample and opens up a route to ‘write’ a Pb lattice with any type of geometry into the perovskite thin film. Of particular interest here is again the honeycomb lattice, which, combined with the Pb lattice, could give rise to superconductivity in a material with large spin-orbit coupling and a nanoscale honeycomb geometry.

References

1. Calzolari, D. C. E., Pontoni, D., Daillant, J. & Reichert, H. “An X-ray chamber for in situ structural studies of solvent-mediated nanoparticle self-assembly”. *J. Synchrotron Radiat.* **20**, 306–315 (2013).
2. Whitham, K. et al. “Charge transport and localization in atomically coherent quantum dot solids”. *Nat. Mater.* **15**, 557–563 (2016).
3. Evers, W. H. et al. “High charge mobility in two-dimensional percolative networks of PbSe quantum dots connected by atomic bonds”. *Nat. Commun.* **6**, 8195 (2015).
4. Bian, K. et al. “Optical properties of PbS nanocrystal quantum dots at ambient and elevated pressure”. *Phys. Chem. Chem. Phys.* **16**, 8515–8520 (2014).
5. Lorenzon, M. et al. “Role of nonradiative defects and environmental oxygen on exciton recombination processes in CsPbBr₃ perovskite nanocrystals”. *Nano Lett.* (2017).
6. Vanmaekelbergh, D. et al. “Shape-Dependent Multiexciton Emission and Whispering Gallery Modes in Supraparticles of CdSe/Multishell Quantum Dots”. *ACS Nano* **9**, 3942–3950 (2015).
7. Palazon, F. et al. “Changing the Dimensionality of Cesium Lead Bromide Nanocrystals by Reversible Postsynthesis Transformations with Amines”. *Chem. Mater.* (2017).
8. Palazon, F., Akkerman, Q. A., Prato, M. & Manna, L. “X-ray Lithography on Perovskite Nanocrystals Films: From Patterning with Anion-Exchange Reactions to Enhanced Stability in Air and Water”. *ACS Nano* **10**, 1224–1230 (2016).
9. Dang, Z. et al. “In Situ Transmission Electron Microscopy Study of Electron Beam-Induced Transformations in Colloidal Cesium Lead Halide Perovskite Nanocrystals”. *ACS Nano* **11**, 2124–2132 (2017).





Samenvatting in het Nederlands

• Samenvatting •

Voor je ligt een proefschrift waarin experimenten staan beschreven die onderzoek doen naar de zelforganisatie van halfgeleider nanokristallen. Deze nanokristallen gedragen zich elektronisch en optisch niet zoals hun bulk variant doordat ze ontzettend klein zijn: ongeveer 0.000000001 meter. Zonder dat de chemische samenstelling van de nanokristallen verandert, kunnen de eigenschappen aangepast worden door de grootte en de vorm van de deeltjes te veranderen.

De niet ingewijde lezer zal door de hoeveelheid vakjargon, wat waarschijnlijk wordt omgezet in 'bla bla bla', al snel willen stoppen met lezen. Om ervoor te zorgen dat u als lezer meer overhoudt aan het lezen van dit hoofdstuk, wordt er voor een breder publiek en in begrijpelijk taal een beeld geschetst van het gedane onderzoek. Voor de lezer die meer diepgang zoekt verwijs ik graag naar de voorgaande hoofdstukken in dit proefschrift.

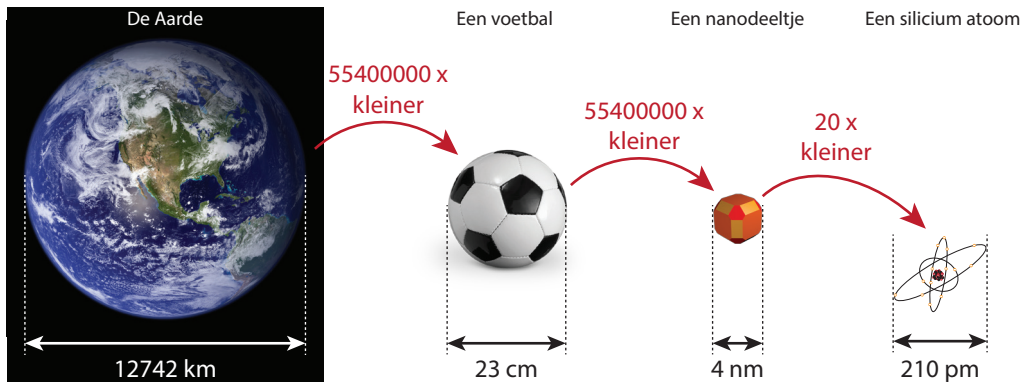
9.1 - Introductie

Nanotechnologie is niet meer weg te denken uit het alledaagse leven. Of je nu kijkt naar je smartphone, computer of televisie, er zitten een hoop optische en elektrische onderdelen in deze systemen die ontzettend klein zijn en gemaakt worden met geavanceerde technieken. Wanneer je in een online woordenboek de term ‘nanotechnologie’ opzoekt, kom je al snel een aardige uitleg tegen: “*Nanotechnologie is de technologie die zich bezighoudt met de ontwikkeling van materialen en componenten die iets groter zijn dan individuele atomen en moleculen. (minder dan 100 nanometer)*”¹.

Het woord ‘nano’ in nanotechnologie en nanodeeltjes stamt af van het Griekse woord ‘nánnos’, wat dwerg betekend. Het wordt gebruikt om de grootte aan te duiden van de deeltjes waarmee in dit proefschrift gewerkt wordt, namelijk een miljardste van een meter: 1 nanometer is gelijk aan 0.000000001 meter (10^{-9} m). In alledaagse bulk materialen, die uit ontelbaar veel atomen bestaan, maakt de grootte van dat materiaal niet uit voor de fysisch-chemische eigenschappen hiervan. Een goudklompje heeft bijvoorbeeld dezelfde kleur als goud poeder. Wanneer de goud deeltjes in grootte gereduceerd worden tot een aantal honderd tot duizend atomen, verandert dit volledig. Een oplossing met goud nanodeeltjes heeft een roze- tot roodachtige kleur afhankelijk van de grootte van de deeltjes. Om de eigenschappen van nanodeeltjes te verklaren moeten we eerst een stap terug doen en kijken naar de bouwstenen van deze materialen.

9.2 - Bouwstenen

Alle materiaal om je heen zijn opgebouwd uit atomen. De atomen zijn weer opgebouwd uit een kern van positief geladen protonen en ongeladen neutronen. Om deze kern heen zwermen negatief geladen elektronen. De grootte en eigenschappen van een atoom hangen af van het element waar we naar kijken, de ladingstoestand van dit element (geen lading vs. geladen elementen ofwel ionen) en in sommige gevallen ook de hoeveelheid neutronen in de kern (waterstof heeft



I: Van de aarde, naar een voetbal, naar een nanodeeltje, naar een atoom. Vergeleken met de diameter van een voetbal (23 cm) is de aarde meer dan 55 miljoen keer groter (met een diameter van 12742 km). Als nu de voetbal met dezelfde factor verkleind wordt, dan komt je op een diameter van 4 nanometer uit, ruwweg de diameter van de nanokristallen die gebruikt zijn in dit proefschrift. De nanokristallen zelf bestaan weer uit honderd tot een paar duizend atomen.

¹Geciteerd van: <http://www.woorden.org/woord/nanotechnologie>.

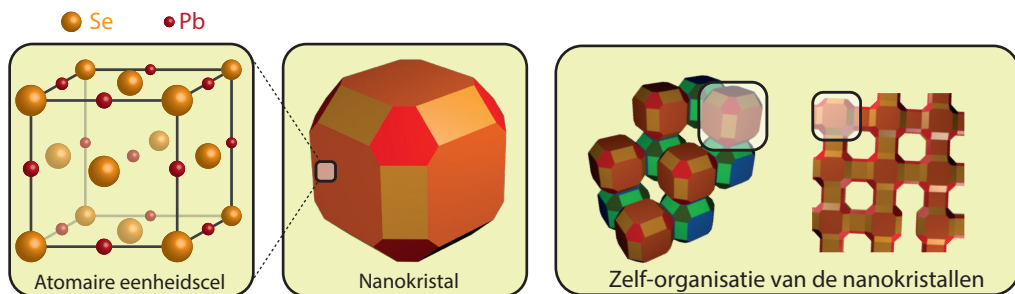
1 proton in de atoomkern, deuterium heeft een proton en een neutron in de atoomkern). De optische en elektrische eigenschappen van veel materialen hangen af van de buitenste elektronen van de atomen en hoe deze binden met hun naaste burens. Het juiste beeld van een elektron is overigens niet dat het als een deeltje in een bepaalde baan om de kern zoeft (zoals de planeten om de zon). Het correcte beeld is dat er een bepaalde kansdichtheid is om het elektron in een soort wolk om de atoomkern heen te vinden. Deze 'wolk' wordt ook wel orbitaal genoemd.

9.3 - Structuur 1: van klein naar groot

In dit proefschrift hebben we voornamelijk gekeken naar vaste stoffen. Atomen kunnen zich in vaste stoffen op twee manieren rangschikken: niet-geordend, ook wel amorf genoemd, of geordend. Wanneer atomen zich ordenen in een vaste stof zijn er een aantal manieren om de atomen te rangschikken. Er is hier een bepaald groepje atomen wat zich steeds herhaalt door de gehele ruimte van de vaste stof. Deze herhalende eenheid wordt een eenheidscel genoemd.

Als voorbeeld nemen we loodselenide, ofwel PbSe. De atomen zitten hier in een zogenaamd vlakgecentreerd-kubisch rooster, exact hetzelfde zoals bijvoorbeeld keukenzout (NaCl). Ieder lood ion wordt hier omgeven door zes selenium ionen en vice versa. De manier waarop de atomen zich hebben geordend wordt ook wel het kristalrooster van een materiaal genoemd. Vaak kunnen materialen ook meerdere kristalrooster aannemen. Cadmium selenide kan bijvoorbeeld zowel een zink blende (kubisch symmetrisch) of een wurtziet (hexagonaal symmetrisch) kristalrooster aannemen. Welke kristalfase er wordt aangenomen wordt bepaald door de relatieve energie van dat rooster en het gevormde oppervlakte van de deeltjes; hoe lager de totale vrije energie onder een gegeven set van omstandigheden, hoe gunstiger dit is voor de vorming van die fase.

De uiteindelijke elektronische eigenschappen, en de daaruit volgende optische eigenschappen, van een vaste stof worden bepaald door de stapeling van de atomen in het rooster. Door deze stapeling kunnen de atomen met elkaar binden door elektronen te delen. Het type binding en de sterkte hiervan is bepalend of elektronen zich wel of niet vrij kunnen bewegen door het materiaal.



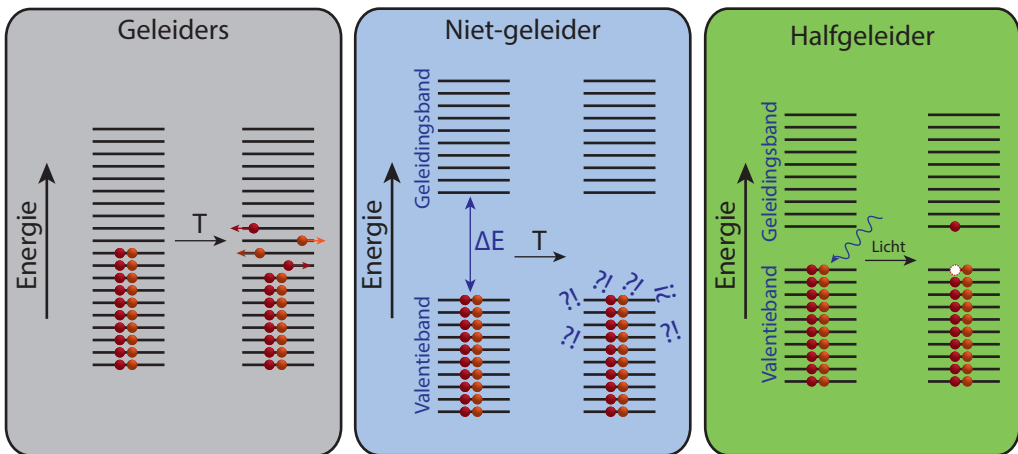
II: Structuur van kristallijne vaste stoffen over verschillende ordes van grootte. De atomen worden als bouwstenen gebruikt om een grotere, geordende structuur te maken. De herhalende bouwsteen wordt de eenheidscel genoemd. In het geval van PbSe is dit een steenzout atomair rooster. Oppervlaktenspanning en de symmetrie van de eenheidscel bepalen vervolgens de vorm van een nanokristal. Deze nanokristallen kunnen gebruikt worden om een groter kristal te bouwen; een kristal van nanokristallen. Hierin zijn de bouwstenen niet de atomen, maar de nanodeeltjes zelf. Met de PbSe nanokristallen kunnen de zelf-georganiseerde roosters zowel een honingraat als een vierkante symmetrie aannemen.

9.4 - Vreemde natuurkunde en elektronische eigenschappen

Om de elektronische eigenschappen van materialen te beschrijven, en tevens de interactie met licht, moet er een rare gedachtesprong gemaakt worden. Tegen het eind van de 19^e eeuw konden wetenschappers een behoorlijk hoeveelheid experimenten niet meer met klassieke natuurkunde verklaren. Er werden een aantal stellingen voorgelegd die tot op de dag van vandaag niet weerlegd zijn. Een van de stellingen houdt in dat bepaalde eigenschappen gekwantiseerd zijn; ze nemen in stapjes toe en af en niet in een continue vorm. Vandaar de naam kwantummechanica (ook soms golfmechanica genoemd).

Een experiment dat veel invloed heeft gehad is het twee-spleten experiment van Young. In dit experiment is bepaald dat licht zich zowel als deeltje en als golf kan gedragen. Uiteindelijk is vastgesteld dat dit ook voor elektronen geldt. Deze vreemde gedachtesprong is waarschijnlijk moeilijk te begrijpen als lezer, maar begrip hiervoor is niet wat ik wil bereiken door deze samenvatting. Accepteer het voor nu, want we hebben het later nodig om eigenschappen van materialen en licht te begrijpen. De eerder genoemde 'wolk' van het elektron, of het orbitaal, is hier een voorbeeld van.

De eigenschappen van vaste stoffen kunnen nu bepaald worden door de bewegingsvergelijkingen (of golfvergelijkingen) van de elektronen in deze stof op te lossen. Geen nood, dat gaan we hier niet doen, maar het is wel goed om de belangrijkste resultaten die hieruit volgen te bespreken. Uit deze uitwerking krijgen we de energieën van de orbitalen van de elektronen en hoe ze ruimtelijk over het materiaal verdeeld zitten. In de kristallijne vaste stoffen worden zogenaamde banden gevormd; de orbitalen zijn uitgesmeerd over het gehele kristalrooster en zitten energetisch



III: De elektronische structuur van vaste stoffen ingedeeld in verschillende groepen. In de meeste vaste stoffen liggen de energie niveaus dicht op elkaar. In geleiders kunnen dus elektronen van de hoogst bezette gebonden orbitaal door thermische energie alleen in een onbezet vrij orbitaal terecht komen. Omdat deze orbitalen over het hele materiaal aan elkaar vastgeknoopt zitten, kunnen deze elektronen simpel van punt A naar punt B reizen: er kan een stroom door het materiaal lopen. In een niet-geleider of isolator, zit er een energiegat tussen het hoogst energie niveau met elektronen en het laagste energie niveau zonder elektronen: de zogenaamde bandkloof. De elektronen kunnen hier dus niet vrij door het materiaal heen bewegen. In een halfgeleider is de bandkloof voldoende klein dat een elektron door absorptie van een foton van de valentieband in de conductieband kan worden gebracht.

gezien erg dicht op elkaar. We kunnen nu twee hoofdgroepen van kristallijne vaste stoffen maken; geleiders en niet-geleiders. Het onderscheid tussen deze twee materialen volgt direct uit de naam.

In geleiders zitten de gevulde orbitalen energetisch gezien erg dicht tegen de lege orbitalen aan. Hierdoor kan door toevoeging van een kleine hoeveelheid energie (in de vorm van warmte) een elektron van een gebonden toestand naar een aangeslagen toestand gaan. Simpel gezegd kun je dit zien als een elektron die van een gevuld naar een leeg orbitaal wordt verplaatst. Hierin kan het elektron vrij door het materiaal heen reizen; er kan dus gemakkelijk een stroom door dit materiaal heen lopen. Metalen zoals koper en goud zijn voorbeelden van geleiders.

In niet-geleiders, ook isolators genoemd, zit er een gat tussen de gevulde en lege orbitalen, ookwel bandkloof genoemd. In de bandkloof zitten geen orbitalen waar een elektron zich kan bevinden. Dit betekent dat warmte alleen niet genoeg is om een elektron aan te slaan van de gevulde orbitalen (of valentieband) naar lege orbitalen (of conductieband). Er is een extra 'zetje' nodig om deze energiekloof te overbruggen. Indien de bandkloof klein genoeg is kan er gebruik gemaakt worden van licht om het electron aan te slaan en van een gevulde toestand naar een lege toestand te brengen. Het lichtdeeltje, of foton, moet dan een energie met zich meedragen die tenminste even groot is als de bandkloof energie. Vaak worden materialen halfgeleiders genoemd wanneer dit mogelijk is, maar het verschil met een isolator is meer een kwestie van stijl dan een hard getal. In dit proefschrift wordt onderzoek gedaan naar halfgeleiders.

Wanneer een elektron in de aangeslagen toestand zit laat hij een leegte achter in het orbitaal waar het vandaan kwam, ook wel een 'gat' genoemd. Wanneer het electron met dit gat gebonden is (door simpele aantrekking van de negatieve lading van het electron en de 'positieve lading' van het gat) wordt dit een exciton genoemd. Er kunnen vervolgens twee dingen gebeuren; of het electron valt terug naar de grondtoestand en zend energie uit (in de vorm van licht, of in de vorm van trillingen of warmte) of het exciton wordt uit elkaar getrokken en er gaat een stroompje lopen. Dit laatste is bijvoorbeeld hoe uit zonlicht energie wordt opgewekt.

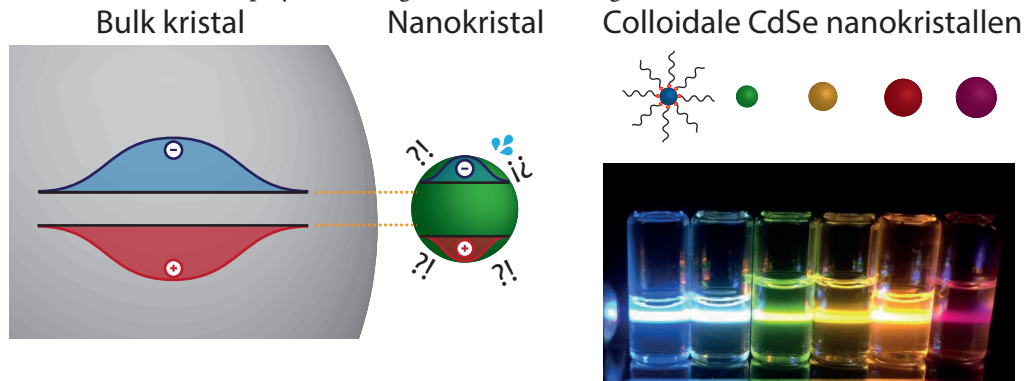
9.5 - Structuur 2: van groot naar weer iets kleins

We gaan nu weer van de grote kristallen kleine deeltjes maken. Hierbij spelen een aantal factoren een belangrijke rol. Neem bijvoorbeeld een baksteen en hak deze doormidden. Je krijgt nu twee extra oppervlakken die blootgesteld worden, maar het materiaal heeft in totaal nog steeds hetzelfde volume; er is hogere oppervlakte tot volume verhouding. Het maken van oppervlak in de natuur is energetisch ongunstig. Je kan je dus wel voorstellen dat nanodeeltjes, die een enorme oppervlakte tot volume verhouding hebben, erg reactief zijn. Dit kan nuttig zijn in de wereld van de katalyse, maar is voor de halfgeleider nanodeeltjes die we in dit proefschrift bekijken niet erg handig: Er zitten aan het oppervlak vaak een hoop atomen die niet zoveel naaste burens hebben als dat ze zouden willen. De bindingen die deze oppervlak atomen niet hebben zorgen voor plaatsen waar het exciton zijn energie kan dumpen zonder licht uit te zenden. Bovendien willen de nanodeeltjes zelf vaak niet oplossen in de olie-achtige oplosmiddelen waarin we ze maken. Om bovengenoemde problemen te omzeilen gebruiken we liganden die we chemisch aan het oppervlak vastzetten. Dit zijn zeep-achtige moleculen die met een lange olie-achtige staart wel in het oplosmiddelen willen zitten en met een bindende groep aan de andere kant

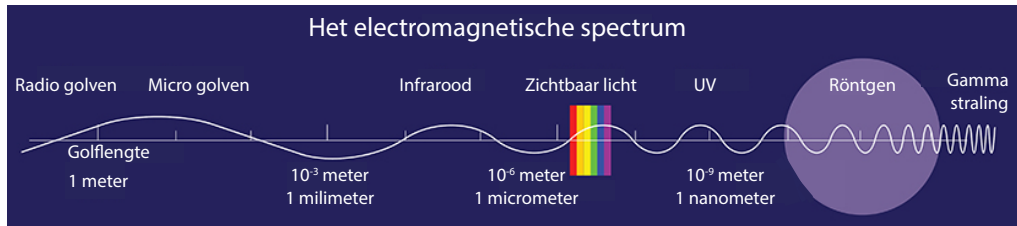
aan een atoom van het oppervlak van het nanodeeltje binden. In dit proefschrift kijken we naar nanodeeltjes met bijzondere elektronische eigenschappen die we kunnen veranderen door alleen de grootte van het deeltje aan te passen. Dit komt doordat de elektronen in een nanodeeltje zich anders gedragen dan in de bulk variant van hetzelfde materiaal.

Zoals eerder uitgelegd bewegen elektronen zich voort als golven en in een halfgeleider kan een elektron aangeslagen worden naar een lege toestand. Er kan dan een gebonden paar van een elektron en een gat vormen; het exciton. Dit exciton wil ruimtelijk gezien een bepaalde grootte aannemen: de exciton Bohr diameter. Wanneer we een deeltje kleiner maken dan deze diameter dan wordt dit exciton als het ware ongelukkig. Hij kan immers niet zoveel ruimte innemen als het zou willen. Het exciton wordt samengeknepen in het deeltje en krijgt hierdoor meer kinetische energie. Vergelijk het bijvoorbeeld met wat er gebeurt als je een van nature druk persoon met claustrofobie in een lift opsluit; hij of zij begint te stuiteren in paniek. Deze toename in kinetische energie duwt de gevulde elektron toestanden naar een lagere energie en de lege elektron toestanden naar een hogere energie: de bandkloof wordt groter. Halfgeleider nanodeeltjes waar dit in voorkomt worden kwantum-stippen genoemd.

Een typisch voorbeeld is cadmium selenide, het meest onderzochte materiaal in halfgeleider nanodeeltjes. Dit materiaal heeft een Bohr exciton diameter van 10 nanometer. Tegenwoordig kunnen we hier nanodeeltjes van maken die kleiner zijn dan deze exciton diameter. Hoe kleiner het deeltje, des te meer het exciton samengeknepen wordt en des te groter de bandkloof wordt. De fotonen die door het deeltje worden uitgezonden wanneer het exciton recombineert zullen dan ook meer energie hebben (en dus 'blauwer' licht uitzenden). Dit wordt gedemonstreerd in de foto die hieronder staat. De colloïdale CdSe nanodeeltjes zitten in een oplossing van hexaan en worden beschenen met een UV laserpointer. Dit UV licht wordt door de deeltjes opgenomen en omgezet in een exciton, dat uiteindelijk weer licht uitzendt van verschillende kleuren (afhankelijk van de grootte van het deeltje). Tegenwoordig zijn de eerste televisies met dit type nanodeeltjes beschikbaar. Deze display technologie heeft een veel groter kleurbereik dan normale LED



IV: Halfgeleider nanokristallen. In een bulk kristal kan het exciton, het gebonden elektron-gat paar, zich ruimtelijk uitspreiden door het kristal tot zijn natuurlijke grootte. In een nanokristal kan dit niet, en wordt het exciton opgesloten in het deeltje. Hierdoor neemt de kinetische energie van het exciton toe en worden de gevulde en lege elektron toestanden uit elkaar gedrukt. Dit effect is goed te zien in colloïdale CdSe nanokristallen, die zichtbaar licht uitzenden. In de kleine CdSe nanokristallen (links op de foto) wordt het exciton hard samengeknepen, wordt de bandkloof groot en zenden de deeltjes blauw licht uit. Hoe groter de deeltjes worden (meer naar rechts op de foto), des te minder hard wordt het exciton samengeknepen en des te meer de deeltjes licht uit gaan zenden die terug naar de 'bulk' waarde evolueert.



V: Licht en het elektromagnetische spectrum². Licht bestaat uit een trillend elektrisch veld met loodrecht daarop een trillend magnetisch veld. Één enkel lichtdeeltje wordt ook wel een foton genoemd. Een foton heeft een karakteristieke golflengte die beschrijft hoe lang een periode van een oscillatie is. De golflengte kan omgerekend worden in een frequentie van het licht (hoeveel oscillaties per seconde heeft het licht).

beeldschermen. Je moet er helaas ook een veel grotere portomonnee voor hebben.

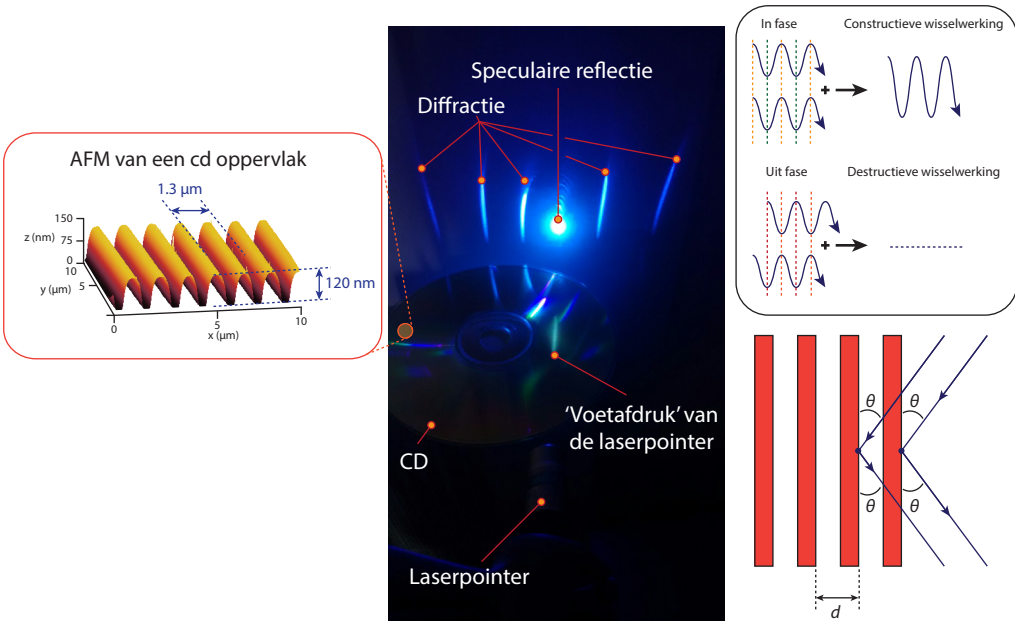
9.6 - Licht, verstrooiing en diffractie

Tot zover hebben we het voornamelijk over de nanokristallen gehad die we hebben gebruikt in dit proefschrift. Deze deeltjes zijn te klein om te zien met normale lichtmicroscopen, dus we hebben andere manieren nodig om naar deze deeltjes te kijken. Dit komt doordat er een fundamenteel limiet is aan wat we met licht van een bepaalde golflengte kunnen zien. Ruwweg moet de golflengte van het licht wat je gebruikt om naar een object te kijken kleiner of gelijk zijn aan de grootte van het object zelf. Zichtbaar licht heeft een kleinste golflengte van ongeveer 390 nanometer. De deeltjes die we bestuderen in dit proefschrift zijn kleiner dan 10 nanometer, dus dit gaan we bij lange na niet redden. Één oplossing ligt in het gebruik van Röntgenverstrooiings- of diffractie technieken, wat hieronder verder toegelicht wordt.

Diffractie is een fenomeen wat plaatsvindt wanneer een periodieke structuur, dus een structuur met een herhalend patroon, wordt beschenen met monochromatisch licht (licht met maar één golflengte component). Dit licht wordt alleen in specifieke richtingen verstrooid door de aanwezigheid van deze periodieke structuur. De fotonen die verstrooid worden moeten precies in-fase zijn; dat wil zeggen dat de top van een oscillatie van foton 1 gelijk moet vallen met de top van van een oscillatie van foton 2. Dit is alleen het geval als foton 2 een geheel aantal golflengtes door het materiaal heeft afgelegd ten opzichte van foton 1. Er treedt dan constructieve wisselwerking op; de intensiteit van de golf neemt toe. Wanneer dit niet het geval is treedt er zogenaamde destructieve wisselwerking op en dooft het gereflecteerde licht zichzelf uit. In het reflectiepatroon zul je dus afwisselend regio's met hoge intensiteit en lage intensiteit zien, die corresponderen met constructieve wisselwerking en destructieve wisselwerking van de fotonen. De richting waarin je je reflectie verwacht is vrij gemakkelijk uit te rekenen met de wet van Bragg: $2d \sin(\theta) = \lambda$. Hier is d de lengte van de herhalende periodiciteit is, λ de gebruikte golflengte en θ de hoek waaronder het licht constructief gereflecteerd wordt.

Uit de richtingen van het gereflecteerde licht kan je dus terug rekenen wat voor herhalende eenheid er aanwezig is in je structuur. In het geval van kristallen zijn dit dus herhalende eenheidscellen van atomen, in het geval van een kristal van nanokristallen krijg je hieruit dus een eenheidscel van nanokristallen. Omdat we zulke kleine afstanden tussen atomen willen

²Aangepast van: <http://www.esrf.eu/about/synchrotron-science/synchrotron-light>. Dit is overigens een erg leuke website over de principes achter en het gebruik van synchrotrons in verschillende wetenschapsdisciplines.



Constructieve wisselwerking alleen als: $2d \sin(\theta) = \lambda$

VI: Doe-het-zelf diffractie. Voor een diffractie experiment heb je een aantal dingen nodig. (1) Een object met een daarop periodieke structuur (zoals een CD of DVD). (2) Een laserpointer met een golflengte die kleiner is dan de lengte van de herhalende eenheid op je structuur (hierboven een blauwe laserpointer met een golflengte van 405 nm). Door periodieke structuur op de CD, hier zichtbaar gemaakt met een AFM, kan het laserlicht alleen in hele specifieke richtingen gereflecteerd worden: we zien hierboven diffractie. In ietwat technische taal: de gereflecteerde fotonen zijn alleen in fase, wat leidt tot constructieve wisselwerking, in bepaalde richtingen. Deze richtingen kan je uitrekenen met de wet van Bragg.

bekijken, moeten we ook erg kortgolvig licht gebruiken. Röntgenlicht, ook wel bekend als *X-rays*, hebben een golflengte van ongeveer één-tiende nanometer en dit is klein genoeg om de orde in onze structuren zichtbaar te maken. De resultaten zijn vaak niet eenvoudig te begrijpen, omdat je een indirect beeld krijgt van je materiaal. Er is een gezonde hoeveelheid data analyse nodig om je verstrooiings patronen om te zetten in begrijpelijke taal, zoals afstanden tussen nanodeeltjes en de orientatie van deze deeltjes aan vloeistof oppervlaktes. Daarover later meer.

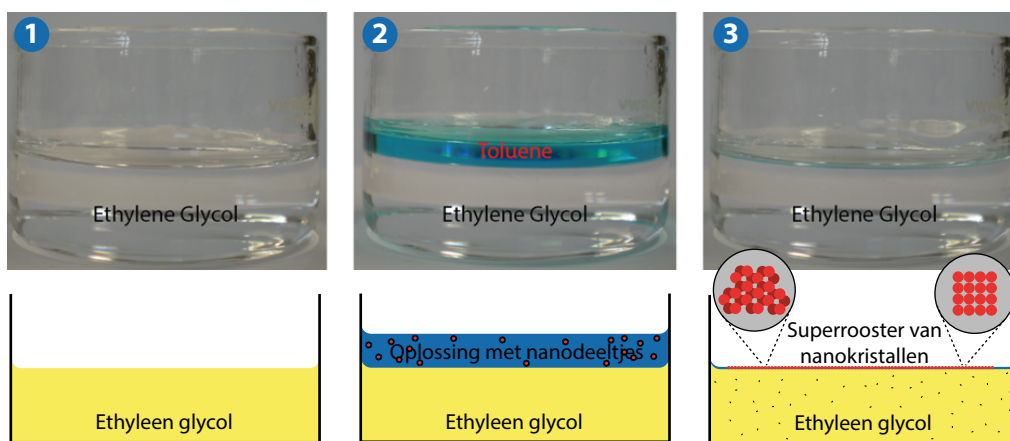
Een eenvoudig experiment wat je zelf kan doen staat hierboven uitgelegd. Een eenvoudig object met een herhalende structuur is een CD of een DVD. De herhalende structuur is zichtbaar gemaakt met een atoom-kracht microscoop (engels *atomic force microscope*, AFM), die een beetje werkt zoals een oude platenspeler. De CD heeft ingeëtste groefjes die zich elke 1.3 micrometer herhalen en 120 nanometer hoog zijn. Je kan dus voor een dergelijk experiment ook een laserpointer gebruiken. Als je je laserpointer onder een kleine hoek van inval op de CD richt, zal het licht allereerst rechtdoor gereflecteerd worden. De reflectie die je ziet heeft eenzelfde hoek van inval als hoek van uitval en wordt de speculaire reflectie genoemd. Je ziet overigens ook dat deze heel erg fel is (een reden waarom je deze bij Röntgendiffractie experimenten vaak moet blokkeren). Daarnaast zie je ook links en rechts van de speculaire reflectie een diffractiepatroon ontstaan, waarbij de afstand tussen de diffractiestaven gelijk is. Uit de hoek van de reflecties kun je vervolgens terugrekenen wat de afstand is tussen de groeven op de CD.

9.7 - Het onderzoek in dit proefschrift

Nu je zover bent gekomen in deze samenvatting kan je verder begrijpen wat voor onderzoek er in dit proefschrift staat beschreven. Hier is vooral onderzoek gedaan naar structuren met een bepaalde hiërarchie; kristallen van nanokristallen. We gebruiken nanokristallen als een soort legostenen om een nog groter kristal te bouwen. Theoretische modellen voorspellen dat deze zogenaamde superkristallen of superroosters spectaculaire eigenschappen hebben die afhankelijk zijn van de geometrie waarop de nanokristallen zich ordenen.

Hoofdstuk 3 t/m 5 richten zich op twee-dimensionale (platte) kristallen van lood selenide (PbSe) nanokristallen. Deze deeltjes ordenen zich niet alleen, maar klikken ook aan elkaar vast (zoals lego) om vellen te vormen met de dikte van één enkel nanokristal. Tijdens dit proces, wat georiënteerde aaneenhechting heet, draaien de nanokristallen op een dusdanige manier dat hun atomaire roosters precies uitgelijnd zijn. Ieder nanokristal in zulke PbSe superroosters heeft dus dezelfde oriëntatie als al zijn burens. De deeltjes hebben de vorm van een afgeknotte kubus; een kubus waarvan de hoeken en zijkanten ietwat zijn afgesneden. We zijn in staat om twee verschillende 2-D superroosters te maken van PbSe; een rooster met vierkante symmetrie en een rooster met honingraat symmetrie. Deze zullen verderop meer toegelicht worden.

Normaal gesproken zijn de deeltjes opgelost in een vluchtig, olie-achtig oplosmiddel: een colloïdale oplossing. Enkele voorbeelden van andere colloïdale oplossingen zijn bijvoorbeeld melk (vettige oliedruppels in water) of mayonaise. De oplossing met nanodeeltjes wordt bovenop een andere oplossing geplaatst, waar de nanodeeltjes niet in oplossen. Vervolgens kan het oplosmiddel van de nanodeeltjes verdampen en wat er overblijft is een dunne laag nanodeeltjes die op het vloeistof oppervlak kan drijven. Deze kan er vervolgens vrij gemakkelijk vanaf geschept worden met ieder gewenst substraat om verdere metingen te verrichten.



VII: Georiënteerde aaneenhechting van PbSe nanokristallen. Een petrischaaltje wordt gevuld met ethyleen glycol. Deze vloeistof mengt niet met de nanodeeltjes en het oplosmiddel hiervan. De nanodeeltjes zitten opgelost in een vluchtig, olie-achtig oplosmiddel. Deze wordt voorzigt aangebracht bovenop de ethyleen glycol. Het oplosmiddel van de nanodeeltjes (blauw) kan rustig verdampen. Wat er na de verdamping overblijft is een film met de dikte van één nanodeeltje met een vierkant of honingraat superrooster. Deze kan vervolgens van het vloeistof oppervlak afgeschept worden.

In **Hoofdstuk 3** bespreken we de geometrische structuur van een PbSe superrooster, waarbij de nanokristallen in een honingraat patroon ordenen. Dit superrooster van nanokristallen is bijzonder, omdat hij een zelfde soort periodiciteit vertoont als grafeen. Theoretici voorspellen dan ook dat de spectaculaire elektronische eigenschappen van grafeen, zoals elektronen die zich als lichtdeeltjes gedragen, ook in deze roosters te vinden zouden moeten zijn.

Met behulp van elektron-tomografie hebben we een drie-dimensionaal beeld opgebouwd van de nanokristallen in het superrooster. Hiermee hebben we aangetoond dat naburige nanokristallen een andere hoogte hebben in het rooster en dat ze via drie van de zes {100} facetten (de zijanten van de kubussen) aan elkaar vast groeien. De deeltjes klikken niet aan elkaar vast tot legodeeltjes; ze lijnen de roosters atomair uit, en groeien dan aan elkaar vast door een brug, of nek, van materiaal tussen de deeltjes te vormen.

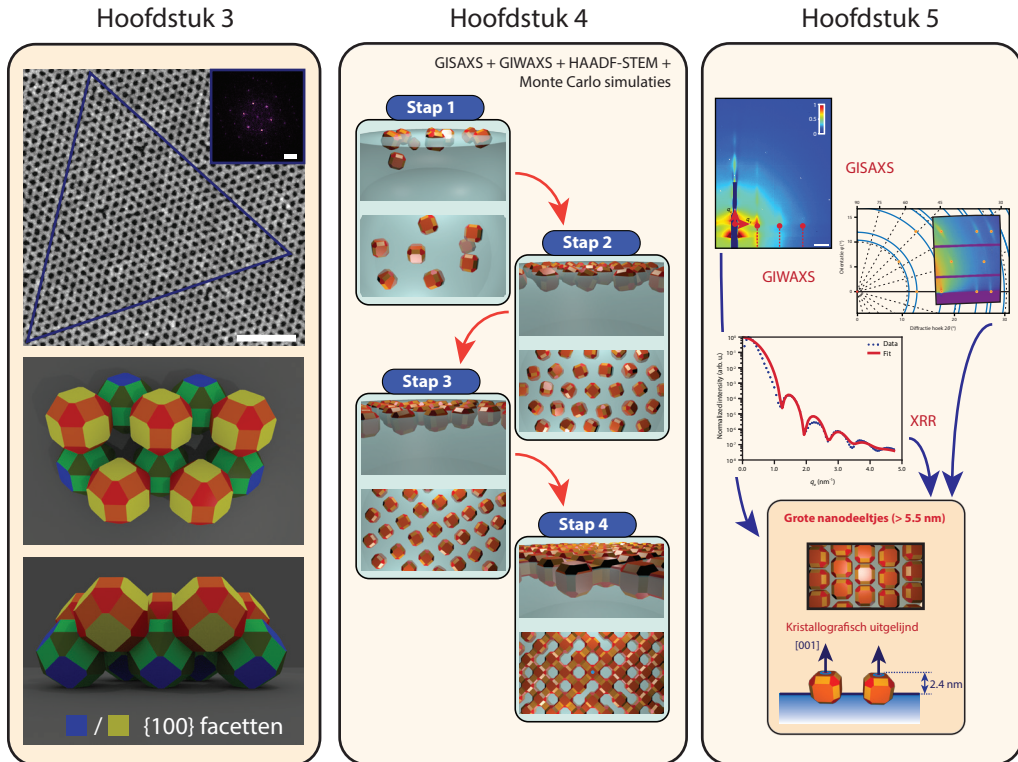
In **Hoofdstuk 4** hebben we de vorming van PbSe superroosters met een vierkante geometrie bestudeerd met behulp van Röntgenverstrooiings technieken (zoals eerder uitgelegd in de samenvatting). We maken hier gebruik van kleine-hoeks verstrooiing en grote-hoeks verstrooiing, waardoor we zowel de ordening van de nanodeeltjes en het samengroeien van de atomaire roosters van de nanodeeltjes tegelijkertijd kunnen volgen. De röntgenbundel raakt bovendien het vloeistofoppervlak met een hele kleine hoek van inval, waardoor we specifiek de zelf-organisatie aan het vloeistof-lucht grensvlak kunnen volgen.

We bewijzen dat de deeltjes zich eerst ordenen in een 2-D rooster met hexagonale symmetrie, waarbij de deeltjes zelf nog vrij kunnen roteren aan het vloeistof-lucht grensvlak. Vervolgens worden de liganden van het oppervlak van de nanodeeltjes gestript. Dit zorgt ervoor dat er een verchuiving plaats vindt in het 2-D kristal van nanodeeltjes, namelijk van een hexagonale naar een vierkante symmetrie. Hierdoor gaan de reagerende {100} oppervlakken recht tegenover elkaar zitten. Pas in de laatste fase van de zelf-organisatie groeien de deeltjes aan elkaar vast. We hebben ook gekeken naar hoe de deeltjes precies aan elkaar vast zitten met hoge-resolutie elektronen microscopie. Hier laten we zien dat er nog vrij veel defecte bindingen zijn, die transport van elektriciteit door deze materialen kan hinderen. Verder zijn er simulaties gedaan, die meer inzicht te geven in de interacties tussen de deeltjes.

In **Hoofdstuk 5** kijken we naar de volledige 3-D adsorptie geometrie van de PbSe nanodeeltjes aan het ethyleen glycol - lucht oppervlak vlak voor ze aan elkaar vast gaan zitten. We hebben hiervoor een reeks nanodeeltjes met verschillende groottes gemaakt, deze op een laag van ethyleen glycol geplaatst en gekeken met behulp van röntgenverstrooiing en röntgen reflectie metingen hoe ze precies adsorberen aan het grensvlak. Behalve dat we de structuur in het vlak van het vloeistof-lucht grensvlak krijgen, kunnen we door de reflectie metingen te analyseren ook de structuur loodrecht op dit grensvlak gedetailleerd in kaart brengen. Dit is de eerste keer dat er een volledig driedimensionaal beeld van nanodeeltjes aan een vloeistof-lucht grensvlak is gemaakt, zowel op de nanodeeltjes als op de atomaire lengte schaal.

e maken in dit hoofdstuk de vergelijking tussen kleine (5 nm), middelgrote (7.1 nm) en grote (8.5 nm) PbSe nanodeeltjes. We hebben geprobeerd de zelf-organisatie te stoppen in de fase waar de deeltjes nog niet aan elkaar vast zijn gegroeid. We laten zien dat de kleine nanodeeltjes vrij kunnen roteren aan het vloeistof oppervlak, en dat de middelgrote- en grote nanodeeltjes

atomair uitlijnen en dus niet vrij kunnen roteren. Deze laatstgenoemde deeltjes hebben dan een {100} vlak (de bovenkant van het kubusvormige deeltje) omhoog staan ten opzichte van het vloeistof-lucht grensvlak. Nu de structuur in het vlak van het grensvlak bekend is, wordt er gekeken naar de reflectie data, waaruit wordt afgeleid dat alle deeltjes bovenop de vloeistof drijven (en niet eronder). Uit deze data kan een dichtheidsprofiel van de nanodeeltjes bovenop het grensvlak verkregen worden. Er is nu voor het eerst een nauwkeurig 3-D beeld gemaakt van hoe de deeltjes adsorberen aan het ethyleen glycol-lucht grensvlak.



VIII: Uitgebeelde samenvatting van Hoofdstuk 3 t/m 5. In deze hoofdstukken wordt gekeken naar de zelforganisatie van PbSe nanokristallen. **Hoofdstuk 3** beschrijft de vorming van een honingraat superrooster via georiënteerde aaneenhechting van deze nanokristallen. Het blijkt dat de nanodeeltjes via de {100} vlakken aan elkaar vast gaan zitten in een octaëdrisch rooster, waardoor het rooster golfte; ieder nanokristal heeft zijn buren op een andere hoogte zitten. In **Hoofdstuk 4** is de vorming van een superrooster met vierkante symmetrie bestudeerd met behulp van geavanceerde Röntgenverstrooiingstechnieken. Door te kijken naar het reflectiepatroon onder kleine hoeken en onder grote hoeken kan indirect een filmpje worden gemaakt van hoe de nanokristallen bewegen aan het vloeistof-lucht grensvlak. Ten eerste adsorberen de deeltjes aan het grensvlak, waarna ze samen worden gedrukt in een hexagonaal rooster waarbij de deeltjes nog vrij kunnen roteren. Langzamerhand worden de liganden van de deeltjes afgestript en wordt het rooster vervormt richting een vierkante symmetrie. Pas aan het eind wordt een brug van PbSe tussen de deeltjes gevormd (de deeltjes 'klikken' niet echt aan elkaar vast). In **Hoofdstuk 5** wordt voor het eerst een volledig 3-D beeld geschetst van hoe de PbSe nanodeeltjes, met verschillende groottes, aan het vloeistof-lucht grensvlak adsorberen. Dit wordt gedaan door diffractie experimenten te combineren met reflectie metingen. Analyse van de reflectie metingen laat zien dat de deeltjes boven op de ethyleen glycol vloeistof drijven. Bovendien kunnen we aantonen dat grote nanodeeltjes atomair uitgelijnd zijn, terwijl kleine nanodeeltjes nog rotationele vrijheid hebben aan het vloeistof-lucht grensvlak.

In **Hoofdstuk 6** wordt gekeken naar de uitwisseling van kationen in CsPbBr_3 perovskiet nanokristallen. Deze nanokristallen zijn bijzonder, omdat ze extreem hoge licht opbrengst hebben. Normaal worden de optische eigenschappen van deze deeltjes aangepast door de anionen in de kristallen uit te wisselen (CsPbCl_3 zendt blauw licht uit, CsPbBr_3 groen licht en CsPbI_3 rood licht). We tonen aan dat we de Pb ionen in de kristallen kunnen uitwisselen voor Sn, Cd en Zn ionen. Hierbij gaan de nanodeeltjes blauw licht in plaats van groen licht uitzenden, waarbij het nauwe emissieprofiel en de hoge licht opbrengst behouden blijven. Door middel van electron-diffractie en speciale hoge-resolutie electron microscopie hebben we aangetoond dat deze blauwverschuiving van het uitgezonden licht wordt veroorzaakt door een contractie van het atomaire rooster. Door deze contractie worden de orbitalen van broom en lood iets verder op elkaar gedrukt, waardoor de bandkloof groter wordt gemaakt. De gepresenteerde methode van kationen uitwisseling vergroot de mogelijkheden om de optische eigenschappen van perovskiet nanokristallen te variëren op een chemische manier.

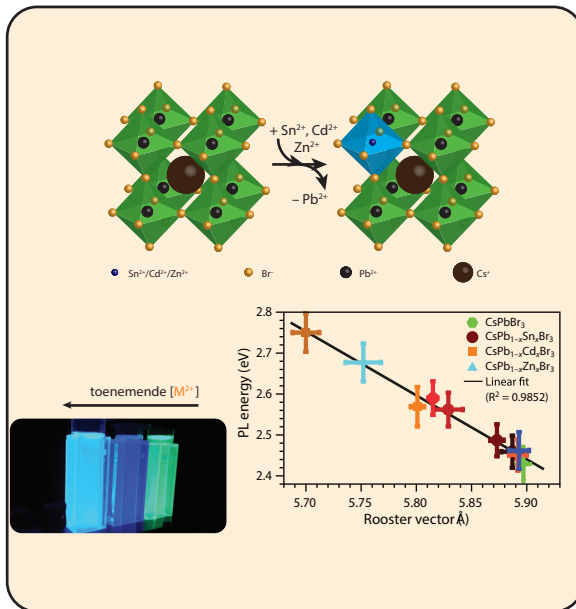
In **Hoofdstuk 7** wordt gekeken naar de zelf-organisatie van de CsPbBr_3 nanodeeltjes. De oplossing van nanodeeltjes wordt gedestabiliseerd door toevoeging van een slecht oplosmiddel. Dit zorgt ervoor dat de nanodeeltjes gaan klusteren in kuboïdale supradeeltjes: een soort van platgedrukte kubus. De nanodeeltjes in dit supradeeltje zijn wel atomair uitgelijnd, maar zitten niet aan elkaar vastgegroeid zoals de PbSe nanodeeltjes in de superkristallen. We hebben aangetoond dat de supradeeltjes in oplossing vormen, met behulp van Röntgenverstrooiingstechnieken. Verder hebben we laten zien dat er veel kristallografisch gedefiniëerde defecten (zoals gelocaliseerde vacatures) aan het oppervlak en in de bulk van het supradeeltje te vinden zijn. Dit is een aanwijzing dat er attractieve interacties zijn tussen de nanokubusjes gedurende het zelf-organisatie proces. Ook laten we zien dat de optische eigenschappen een klein beetje veranderen (de emissie laat een kleine roodverschuiving zien), die we kunnen verklaren aan de hand van energie-overdracht. Deze supradeeltjes zouden interessant kunnen zijn als miniatuur lasers.

9.8 - Hoe nu verder?

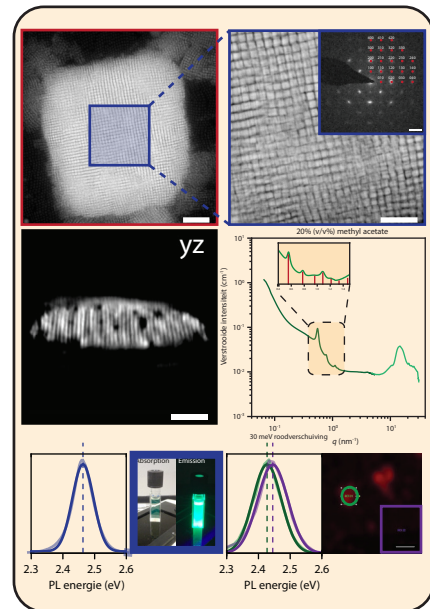
Na al het gedane onderzoek is meest logische vraag: wat kan er in de toekomst onderzocht worden? Er zijn een hoop verschillende mogelijkheden die hieronder wat verder toegelicht worden.

Voor de PbSe superroosters moet de elektronische structuur uitgebreid gekarakteriseerd worden. Er zijn al veel resultaten op dit gebied gemeten met raster tunnel microscopie en spectroscopie, maar er moet meer data verkregen worden. De transport eigenschappen van de ladingen in deze materialen, oftewel hoe (snel) loopt de stroom door deze materialen, wordt op dit moment onderzocht met behulp van ultra-snelle spectoscopische technieken, elektrochemische gating en transistor metingen. Qua structuur begrijpen we nog niet hoe het honingraat superrooster vormt. Er is al Röntgenverstrooiingsdata gemeten, maar deze data is niet duidelijk genoeg. Verder is het waarschijnlijk belangrijk hoe de deeltjes aan het toluen-lucht oppervlak adsorberen (vergeleken met het ethylene glycol-lucht oppervlak). Dit is veel moeilijker dan de experimenten beschreven in hoofdstuk 5, omdat de toluen verdampt. Er kan wel een speciale vloeistofcel gebouwd worden, waarbij de damp verzadigd wordt met toluen, wat ervoor zorgt dat de toluen verdamping vertraagd wordt.

Hoofdstuk 6



Hoofdstuk 7



IX: Uitgebeelde samenvatting van Hoofdstuk 6 en 7. In deze hoofdstukken wordt gekeken naar de chemische aanpassing en zelf-organisatie van CsPbBr_3 perovskiet nanodeeltjes. In **Hoofdstuk 6** wordt onderzoek gedaan naar het aanpassen van de chemische samenstelling van deze nanodeeltjes. We hebben door middel van kationen uitwisselings reacties de Pb ionen in de deeltjes voor een klein deel vervangen door Sn, Zn en Cd ionen. Deze ionen zijn kleiner dan de Pb ionen, wat ervoor zorgt dat het atomaire rooster in de nanodeeltjes zelf krimpt. Door dit krimpen gaan de nanodeeltjes blauw licht uitzenden in plaats van groen licht. In **Hoofdstuk 7** is de vorming van supradeeltjes van CsPbBr_3 nanokristallen bestudeerd. In dit superrooster zijn de nanodeeltjes gepakt in een simpel kubisch rooster, zijn ze atomaair uitgelijnd, maar zitten ze niet aan elkaar vast gebonden. Hierbij is de vorming in de vloeistof geïnduceerd door een slecht oplosmiddel toe te voegen, waarna de nanodeeltjes klusteren in oplossing (wat is bevestigd met Röntgenverstrooiing). We hebben gekeken naar de defecten, die zowel in het oppervlak als in de bulk van het materiaal zitten. Kristallografische nanokristal vacatures vormen een hint dat er attractieve interacties zijn tussen de nanodeeltjes gedurende het zelf-organisatie proces. De optische eigenschappen van een supradeeltje zijn iets veranderd ten opzichte van die van de nanodeeltjes, wat waarschijnlijk komt door een vorm energie overdracht tussen de nanodeeltjes.

Voor de perovskiet nanodeeltjes is het grootste probleem water: omdat het eigenlijk kleine zoutkristallen zijn worden de deeltjes opgelost bij contact met vocht. Het groeien van een schil om deze deeltjes heen zou een grote stap zijn in de richting van verlichtingstoepassingen. De blauwverschuiving van het emissie spectrum zou verder onderzocht kunnen worden door een combinatie van diffractie en optische technieken. Verder zou er uitgezocht kunnen worden hoe de kationen uitwisseling precies verloopt, door tijdens de reactie de absorptie en emissie spectra van de nanodeeltjes te meten. Het mechanisme van de groei van deze deeltjes zou gevolgd kunnen worden met Röntgenverstrooiing, waarbij er dan ook van dit proces indirect een filmpje gemaakt kan worden. Ook zou de vorming van éénkristallijne materialen van deze nanodeeltjes verder bestudeerd kunnen worden. Hierbij moet ook gedacht worden aan het schrijven van patronen met een licht- of elektronenbundel in deze materialen. Er is al aangetoond dat er op deze manier roosters van lood in dit materiaal gemaakt kunnen worden. Dit is interessant, omdat er op deze manier structuren kunnen worden gemaakt die niet in de natuur voorkomen.

9.9 - Waarom is het nuttig?

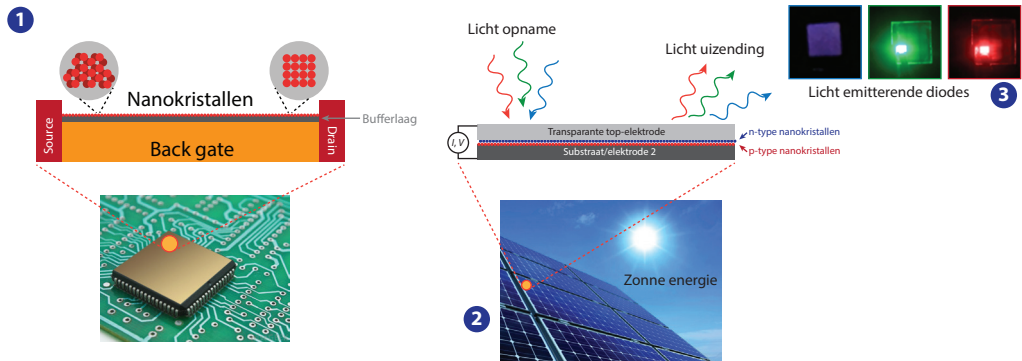
De vragen ‘waarom is het nuttig?’ en ‘wat hebben we er aan?’ worden vaak gesteld. Het ‘hoezo’ en ‘waarom’ van het onderzoek wat tijdens promoties wordt gedaan is soms wat lastig te begrijpen. Het onderzoek in dit proefschrift is voornamelijk fundamenteel: we doen het om te begrijpen hoe processen tijdens de zelf-organisatie van nanokristallen (de vorming van superroosters) werken. Vervolgens zit er wel een bepaald nut achter, want door het proces van vorming van superroosters te begrijpen, kunnen we aanpassingen en verbeteringen voorstellen.

Maar waar kunnen de nanokristallen en superrooster in dit proefschrift dan precies voor gebruikt worden? Er zijn wel toepassingen mogelijk, maar voordat het zover is, is er nog een hoop vervolgonderzoek nodig. De PbSe superroosters geleiden bijvoorbeeld best goed elektriciteit. Bovendien is het een halfgeleider, dus er is de mogelijkheid om deze structuren elektrisch ook ‘aan’ en ‘uit’ te zetten. Dit is de basis van een transistor, het kleine onderdeel achter de rekenkracht van de computerchips. Het voordeel van deze superroosters is, is dat we ze van nature vrij klein kunnen maken, wat ertoe leidt dat we ook kleine transistors zouden kunnen produceren. Nogmaals, voordat er geconcentreerd kan worden met de hedendaagse generatie van transistors is er nog een hoop onderzoek nodig.

Zoals eerder uitgelegd, wordt er in een halfgeleider materiaal een exciton (een gebonden paar van een elektron met een gat) gevormd wanneer er licht geabsorbeerd wordt. Hier is PbSe erg goed in; het heeft van nature een hoge extinctie coëfficiënt, wat wil zeggen dat het erg goed is in het absorberen van licht. Dit exciton kan recombineren en het opgenomen licht uitzenden, maar er is ook een tweede proces mogelijk. Het gebonden elektron - gat paar kan ook opgebroken worden in een vrij elektron en een vrij gat. Deze vrij elektronen en vrije gaten kunnen naar elektrodes gezonden worden om stroom op te wekken. Dit is het principe achter een zonnecel. Nu zouden de elektronen en gaten in de PbSe superroosters een erg hoge mobiliteit moeten hebben, aangezien de nanokristallen aan elkaar vast gegroeid zitten. Dit verhoogt de kans dat de elektronen en gaten gescheiden kunnen worden, wat van groot belang is in zonnecellen. Ook hier is nog een hoop vervolgonderzoek nodig. Bovendien is Pb vrij giftig, en zou men liever andere materialen in consumenten producten willen gebruiken. Vooralsnog zijn de PbSe superroosters ook vooral interessant als platform om complexe natuurkundige fenomenen te bestuderen.

De perovskiet nanodeeltjes zijn ook interessant als absorberend materiaal in zonnecellen. De laatste jaren is er in deze materialen veel winst behaald wat betreft energie rendement. De opbrengst van een gelaagde perovskiet zonnecel gaat richting de 20%, wat erg hoog is voor een materiaal dat nog niet lang onderzocht wordt. De hoge mobiliteit van de elektronen en gaten in deze materialen speelt daar zeker een rol in. Ook hier is de aanwezigheid van Pb niet erg wenselijk, maar er wordt een hoop onderzoek gedaan naar ‘gezondere’ materialen.

Verder is het duidelijk dat de CsPb-halide nanokristallen, zoals onderzocht in dit proefschrift, ook erg goed zijn in het uitzenden van zichtbaar licht. Door het halide ion te veranderen van Cl, naar Br, naar I verandert het uitgezonden licht van blauw naar groen naar rood. Door de hoge licht opbrengst en het nauwe emissie profiel kunnen hier waarschijnlijk erg goede licht emitterende diodes (LEDs) van gemaakt worden. Leuk is ook dat de blauw-licht-uitzende nanokristallen uit Hoofdstuk 6 een veel hogere lichtopbrengst hebben dan de chloride-variant



X: Uitgelichte voorbeelden van het gebruik van nanokristallen. (1) Het gebruik van de PbSe superroosters als transistor. Transistors zitten bijvoorbeeld in computerchips, en zijn in staat om berekeningen te doen wanneer ze in een logisch circuit worden geplaatst. (2) Het gebruik van nanokristallen in een zonnecel en (3) als licht emitterende diodes, of LEDs. Dit zijn maar drie uitgelichte voorbeelden; er zijn nog meer verschillende ideeën en mogelijkheden omtrend het gebruik van nanodeeltjes in commerciële toepassingen.

van de nanokristallen. Het grote probleem bij het commercialiseren van deze perovskiet materialen is voornamelijk dat ze niet zo goed tegen water kunnen, maar er wordt veel onderzoek gedaan naar verschillende manieren om deze nanodeeltjes te coaten met een bescherm laag.

Verder moet er ook vermeld worden dat het onderzoek ook vooral uit nieuwsgierigheid gedaan wordt. We begrijpen niet hoe iets werkt, en gaan op een logische manier op zoek naar een antwoord. Uit dit onderzoek komen niet alleen nieuwe materialen, nieuwe meettechnieken en analyse methodes voort, maar ook veel kennis die uiteindelijk toegepast kan worden op weer een nieuw probleem of onderzoeksvraag. Onderzoek is wat dat betreft nooit echt klaar en er komen altijd wel nieuwe vragen naar boven borrelen. Kort gezegd: het is vooral erg leuk!

(1) De afbeelding van de computerchip komt van: <http://www.wisegEEK.com/what-is-a-computer-chip.htm#didyouknowout>.

(2) De afbeelding van het zonnepaneel komt van: <https://www.slashgear.com/solar-cell-project-creates-hydrogen-fuel-and-bypasses-batteries-14313242/>.

(3) De afbeelding van de LEDs is met toestemming van de American Chemical Society gekopieerd van: Zhang, X.; Sun, C.; Zhang, Y.; Wu, H.; Ji, C.; Chuai, Y.; Wang, P.; Wen, S.; Zhang, C.; Yu, W. W. "Bright Perovskite Nanocrystal Films for Efficient Light-Emitting Devices". *J. Phys. Chem. Lett.* **2016**, 7, 4602–4610.

List of publications

This thesis is based on the following publications:

Mark. P. Boneschanscher, Wiel. H. Evers, [Jaco. J. Geuchies](#), Thomas Altantzis, Bart Goris, Freddy T. Rabouw, Laurens D.A. Siebbeles, Gustaaf Van Tendeloo, Ingmar Swart, Jan Hilhorst, Andrei V. Petukhov, Sara Bals and Daniel Vanmaekelbergh, “Long-range orientation and atomic attachment of nanocrystals in 2D honeycomb superlattices”. *Science* **344** (6190), 1377-1380 (2014). (Chapter 3)

[Jaco J. Geuchies](#), Carlo van Overbeek, Wiel H. Evers, Bart Goris, Annick de Backer, Anjan P. Gantapara, Freddy T. Rabouw, Jan Hilhorst, Joep L. Peters, Oleg Konovalov, Andrei V. Petukhov, Marjolein Dijkstra, Laurens D.A. Siebbeles, Sandra van Aert, Sara Bals and Daniel Vanmaekelbergh, “In-situ study of the formation mechanism of two-dimensional superlattices from PbSe nanocrystals”, *Nature Materials* **15** (12), 1248-1254 (2016). (Chapter 4)

[Jaco J. Geuchies](#), Ellenor Geraffy, Carlo van Overbeek, Federico Montanarella, Marlou L. Slot, Oleg Konovalov, Andrei V. Petukhov and Daniel Vanmaekelbergh, “The adsorption geometry of PbSe nanocrystals at liquid-air interfaces”, *in preparation*. (Chapter 5)

Ward van der Stam, [Jaco J. Geuchies](#), Thomas Altantzis, Karel H.W. van den Bos, Johannes D. Meeldijk, Sandra van Aert, Sara Bals, Daniel Vanmaekelbergh and Celso de Mello Donega, “Highly emissive divalent-ion-doped colloidal $\text{CsPb}_{1-x}\text{M}_x\text{Br}_3$ perovskite nanocrystals through cation exchange” *J. Am. Chem. Soc.* **139** (11), 4087-4097 (2017). (Chapter 6)

Julia S. van der Burgt, [Jaco J. Geuchies](#), Berend van der Meer, Hans Vanrompay, Daniele Zanaga, Yang Zhang, Wiebke Albrecht, Andrei V. Petukhov, Laura Filion, Sara Bals, Ingmar Swart and Daniel Vanmaekelbergh, “Structural and optical properties of supraparticles formed by self-assembly of CsPbBr_3 nanocrystals”, *in preparation*. (Chapter 7)

Other publications:

Ward van der Stam, Freddy T. Rabouw, Sander J.W. Vonk, [Jaco J. Geuchies](#), Hans Ligthart, Andrei V. Petukhov and Celso de Mello Donega, “Oleic acid-induced atomic alignment of ZnS polyhedral nanocrystals”. *Nano Lett.* **16** (4), 2608-2614 (2016).

Ward van der Stam, Freddy T. Rabouw, [Jaco J. Geuchies](#), Anne C. Berends, Stijn O.M. Hinterding, Robin G. Geitenbeek, Joost van der Lit, Sylvain Prévost, Andrei V. Petukhov and Celso de Mello Donega, “In-situ probing of stack-templated growth of ultrathin Cu_{2-x}S nanosheets”. *Chem. Mater.* **28** (17), 6381-6389 (2016).

Claudiu M. Iaru, [Jaco J. Geuchies](#), Paul M. Koenraad, Daniel Vanmaekelbergh and Andrei Y. Silov, "Strong carrier-phonon coupling in lead halide perovskite nanocrystals". *Submitted to ACS Nano*.

Conference contributions and lectures

Atomically connected nanocrystal superlattices via oriented attachment of PbSe nanocrystals (poster).

NvvM materials science meeting, Utrecht, the Netherlands, November 2013. Prize for best poster.

Connecting the dots: Long-range orientation and atomic attachment of nanocrystals into 2D honeycomb superlattices (oral presentation).

Physics@FOM, Veldhoven, the Netherlands, January 2014.

Connecting the dots: Long-range orientation and atomic attachment of nanocrystals into 2D honeycomb superlattices (oral presentation).

MRS spring meeting, San Francisco, USA, April 2014.

Long-range orientation and atomic attachment of nanocrystals into 2D honeycomb superlattices (poster).

Science and Student Days - ESRF, Grenoble, France, December 2014. Prize for best poster.

Reactive self-assembly of PbSe nanocrystals into two-dimensional superlattices probed in-situ with GISAXS/GIWAXS (poster).

Synchrotron and neutron workshop (SYNEW), Utrecht, the Netherlands, June 2015. Prize for best poster.

Nanocrystals in motion: in-situ study of consecutive phase transitions in the formation of atomically coherent two-dimensional superlattices from PbSe nanocrystals (oral).

GISAS conference, Nice, France, September 2015.

Nanocrystals in motion: in-situ study of consecutive phase transitions in the formation of atomically coherent two-dimensional superlattices from PbSe nanocrystals (oral).

Physics@FOM, Veldhoven, the Netherlands, January 2016.

Charge carrier storage leading to delayed luminescence in ultra-thin colloidal CsPbBr₃ perovskite nanoplatelets (poster).

Functional quantum dots, Berlin, Germany, September 2016.

Nanocrystals in motion: in-situ study of consecutive phase transitions in the formation of atomically coherent two-dimensional superlattices from PbSe nanocrystals (oral).

Functional quantum dots - SOL2D, Berlin, Germany, September 2016.

A closer look at nanocrystals at an interface - using X-ray scattering techniques to study interfacial self-assembly (invited speaker).

PHONSI spring meeting, Utrecht, the Netherlands, September 2016.

Watching the birth of a superlattice: in-situ study of the formation mechanism of two-dimensional superlattices from PbSe nanocrystals (oral presentation).

Debye lunch lecture, Utrecht, the Netherlands, November 2016.

Watching the birth of a nanocrystal superlattice (invited speaker).

CHAINS conference, Veldhoven, the Netherlands, December 2016.

Using X-ray scattering techniques to the self-organization of nanocrystals at liquid-air interfaces (invited speaker).

CUI Winterschool (DESY synchrotron), Rügen, Germany, February 2017.

Determining the full 3-D adsorption geometry in-situ of PbSe NC monolayers at the liquid-air interface (oral presentation).

NaNAX8 conference, Braga, Portugal, July 2017.

Acknowledgements - Dankwoord

Dankjewel, thanks, danke schön, merci, grazie, arigatou... Ik kan niet genoeg benadrukken hoeveel ik iedereen dankbaar ben voor de afgelopen vier fantastische jaren van mijn promotie onderzoek. Vier jaar lang onderzoek, het was een avontuur. Nu ik rustig kan terugkijken is het tijd voor het belangrijkste gedeelte van dit proefschrift. Door de vele onderwerpen die ik interessant vind, mocht ik met een hoop mensen samenwerken, zonder wie dit proefschrift niet was geworden wat het nu is. Bedankt!

De eerste ontmoeting met mijn promotor, [Daniel Vanmaekelbergh](#), was tijdens mijn prémaster bij het vak kwantum-chemie. Toendertijd vond ik het vak al reuze interessant en ik stond dan ook te springen om mijn masterthesis onder jouw supervisie te mogen doen. Je hebt me de afgelopen vier jaar enorm veel vrijheid gegeven tijdens het onderzoek, waarvoor ik je erg dankbaar ben. Je kritische blik en vele ideeën hebben het onderzoek (en het opschrijven hiervan) altijd geholpen net dat ene stapje verder te gaan. Daarnaast was het erg leuk om een gedeelte van je lezing te verzorgen op de DESY winterschool in Rügen. Bedankt voor alles van de afgelopen vier jaar!

Naast Daniel ben ik al vanaf mijn masteronderzoek ook begeleid door [Ingmar Swart](#). Als er één ding is waarover ik niet tevreden ben, is het dat we er niet in zijn geslaagd om fatsoenlijke STM metingen op de superroosters te doen. Desalniettemin stond je altijd klaar met raad en daad binnen (het artikel met Julia is bijna af!) en buiten (een zeker akkefietje bij de practica) mijn onderzoek. Bovendien ben je volgens mij de hoofdschuldige voor mijn promotie onderzoek, omdat je me tijdens mijn master hebt gemotiveerd om een onderzoeksvoorstel hiervoor te schrijven. Bedankt voor alles, en ik zie je op het water tijdens het kitesurfen :).

A lot of the research done in this thesis revolves in and around reciprocal space. An easy place to get lost without the proper navigation systems. I was extremely lucky to have two tremendously good supervisors; [Andrei Petukhov](#) and [Oleg Kononov](#). Andrei, your enthusiasm is very contagious, and I'm very happy that you always succeeded to explain the difficult concepts around X-ray scattering with ease to me. Furthermore, you were one of the first people who pushed me to go to the ESRF in Grenoble, which turned out to be a great move! Thanks for everything the last four years (including the huge amount of candy which is always present in your office). Oleg, your knowledge - both theoretically and experimentally - never ceases to amaze me. The work I performed under your supervision has led to some great results and I'm sure that many more will follow. You always were very patient with me, and took your time to explain difficult concepts around reciprocal space. My time in Grenoble would not have been as good without you as a supervisor! I also always liked your 'let's try to do it like this' mentality (90° beam deflection, going through the liquid instead of doing grazing incidence for example). It is my hope that the very fruitful Utrecht-Grenoble collaboration will continue with a new generation of PhD and postdoc students! Большое спасибо!

Naast goede begeleiding heb ik ook altijd met erg slimme mensen mogen samenwerken. Te beginnen met mijn eerste-generatie kantoor genoten in OL110. De eerste periode heb ik samen met [Elleke](#), [Tim S.](#) en [Carlo](#) de spits af mogen bijten van een periode met een vrachtlading aan

nieuwe promovendi. Carlo, we hebben een fantastische run experimenten achter de rug! De ups en downs van het eerste jaar (in een niet werkende glovebox de (over)gevoelige oriented attachment aan de praat proberen te krijgen) werden later ruimschoots goedge maakt door al onze experimenten bij het ESRF :). Ik heb je nuchtere kijk op het onderzoek (en eigenlijk alles wel) enorm gewaardeerd de afgelopen 4 jaar en ben ervan overtuigd dat je over een paar maanden ook een supermooi boekje aflevert. Tim S. (niet te verwarren met Paul Thimoteüs) zat op een compleet ander onderzoek. Je was een stille kracht in het kantoor en ik geloof ook de eerste die toevlucht nam in een andere kamer. Desalniettemin was je een fijne kantoorgenoot, die vaak ook op toffe dansfeestjes (in o.a. de Tivoli) te vinden was. Ik kijk erg uit naar je boekje! Elleke, de InP synthese koningin van onze groep, je maakt altijd de mooiste oplossingen met kale en gecoat quantum dotjes. Naast mooie nanodeeltjes was je ook altijd een bron van updates rond de laatste CMI gossip; voor updates over BN'ers en B-CMI'ers kon je bij jou terecht. Veel succes met het afronden van je promotie!

Toen ik terug kwam uit Grenoble ben ik verhuisd naar OL158 (wegens drukte), beter bekend als de kamer met Herman (de plant). Ik mocht de supperpromising plek van Professor Rabouw overnemen (het schijnt dat dit al eerder is voorgekomen). Al sinds ik een bachelor student was, heb ik erg veel van je geleerd. Ik bewonder de manier waarop je altijd iedereen kan en wil helpen met hun onderzoek en de enorme hoeveelheid kennis die je in huis hebt. Het verbaast me ook helemaal niks dat je inmiddels al een 'echte' professor bent geworden en eigenlijk is het jammer dat ik zelf geen colleges meer van je kan volgen. Het was fijn samen een aantal papertjes te schrijven, want je feedback en tips waren altijd erg goed! Jammer genoeg hebben we nooit de licht absorptie van perovskiet nanodeeltjes goed kunnen meten, maar hopelijk gaat Paul Thimoteüs daar nog mee verder. Bedankt voor alles, Freddy! Ik kijk erg uit naar de uitreikingsceremonie in Zweden. Ook Joost was present in OL158, wat vaak te horen was aan de eindeloze herhaling van 'Sultans of Swing', nummers van de 'Bloodhound Gang' of 'Catch and Release' die op de achtergrond draaiden. Ik heb veel van je geleerd over AFM en STM. Bovendien was je 'recht-door-zee-maniër' van problemen aanpakken vaak erg nuttig (gewoon doen, ducttape fixed alles). Ik ben nog steeds jaloers op je grote verzameling t-shirts met puns ('4-uur borreltijd')! Bedankt voor alle hulp de afgelopen jaren. Last but not least is er Ward, die ik graag aanspreek als 'chef'. We kennen elkaar van de tijd als bachelor/master student, al is het wat meer bonding geworden toen we allebei eenmaal aan het promoveren waren. De trip naar Amerika was zowel supertof als beangstigend (tussen de Mexicaanse bendes in Santa Maria) en ik kijk er nog steeds met veel plezier op terug. Bovendien hebben we een fantastische run experimenten achter de rug, zowel in Grenoble op al je gezonde en superstabele deeltjes, maar ook met de kationen-uitwisseling op de perovskiet deeltjes uit Hoofdstuk 6 (vandaar je titel 'King of Cation Exchange'). Ook was het tof om goede (Kensington) en erg goede (concert van Golden Earring) muziekervaringen te delen. I'll keep you on the height voor als de eerstgenoemde band nog een tof concert geeft :)!

The second generation of PhD students I shared the office with in OL158 has been as great as the first! First of all the princess of Persia, Maryam, always managed to ask me 'just one question'. Afterwards, this turned out to be not just one question, but nonetheless it was always interesting to see an electrical engineer's point of view on our research. You are slowly evolving into a chemist (even making your own 'black gold' PbSe nanoparticles!), and are managing to do nice electrochemistry and optical measurements on the elusive superlattices. You even came to the ESRF for some experiments, which was I think the first time we met. The dinners at your place were always very nice and I'm looking forward to more of your Persian delicacies. Federico,

a.k.a. Monty, a.k.a. Giovanni (or Gio), it is great to have you as an office-mate, a great friend, swimming-buddy, game-buddy, to keep it short I should just keep it at buddy. We often discuss science (your supraparticles, the mysteries around energy transfer between nanocrystals) and non-science (politics, tv-series, certain websites which induce procrastination, etc.) related topics, which both led to new ideas for experiments. The most promising is that we measured the crystallization of your supraparticles in Grenoble! We have yet to 'measure' the crystallization of Bismuth into nice crystals though. You even came a couple days early to Grenoble to join in on my own experiments and we went on a very bonding surfing trip together with Paul Timotheüs! It will be a pleasure to come back for some more experiments in the future :). I'm happy to have you as a good friend, and honored that you will be one of my paranimsf. I do fear for the audio-visual health of people when you show them a certain video, but I will strike back in 1.5 years.

De synthese van superroosters is een hot-topic geworden de afgelopen jaren, en Daniel heeft vele promovendi op dit onderwerp aangenomen. Als eerste was er volgens mij [Marlou](#). We hebben samen hard gewerkt om weer spectroscopische metingen in de kelder te doen, maar helaas is het nog niet gelukt. Het was mooi om te zien het dat je je eigen draai hebt kunnen geven aan het onderzoek. Je enthousiasme als het op wetenschap aankomt is aanstekelijk, wat goed te merken was in Grenoble, waar je iedereen nog net niet achter de computer vandaan trok om de diffractie experimenten aan te sturen. Veel succes met het afronden van je promotie, ik kijk uit naar de STS experimenten op de honingraat roosters! De grootste syntheticus van het project is nog steeds [Joep](#) (tevens de social boy van CMI). Je had vaak een frisse kijk op de experimenten (en de huidige politiek-economische stand van zaken). Ook was je erg vaak actief betrokken bij alle experimenten in Grenoble, waarvoor dank. We verschillen nog steeds van mening over hoe het honingraat rooster nou precies vormt, maar ik ben ervan overtuigd dat je in de komende twee jaar het definitieve antwoord vindt.

De basis van het gedane onderzoek op de PbSe superroosters ligt bij de oud-CMI promovendus [Wiel](#). Ik denk dat iedereen die met je samenwerkt wel onder de indruk is van je 'gouden handen'. Bedankt voor al je hulp voor en tijdens mijn promotie. Je was altijd bereid om meer TEM plaatjes aan te leveren en nog belangrijker, om advies te geven als we hier in Utrecht vastliepen. Heel erg bedankt! Ik ben tijdens mijn masteronderzoek samen met [Mark \(Boon\)](#) begonnen aan de superroosters. We zijn gedurende mijn eerste jaar als promovendus verder gegaan waar we waren gebleven, waaruit het mooie honingraat artikel uit Hoofdstuk 3 is gekomen. Ik ben je erg dankbaar voor alle dingen die je me hebt geleerd, van het kritische denken tot en met de beeld-analyse technieken uit Matlab (nu in Python).

De CMI groep is enorm uitgebreid de afgelopen jaren (van 7 promovendi naar inmiddels 26!!!), wat het onderzoek wel ten goede is gekomen. Twee weken voordat ik ben begonnen aan mijn promotieonderzoek is ook [Nadine](#) gestart. Je hebt de mooiste AFM plaatjes geschoten die ik tot dusver heb gezien. Het was erg fijn dat ik je schema's mocht gebruiken met de tijdsplanning aan het eind van mijn promotie. Bovendien heb ik nog een belangrijke skill van je geleerd: het vouwen van origami kraanvogeltjes uit theezakjes, die nog lang op het ESRF zullen blijven rondslingeren :) Heel veel succes in het nieuwe Zeeland samen met Jelmer! Samen met [Robin](#) mocht ik officieel pleisters plakken als EHBO'er als er iemand gewond was op de vakgroep. Veel succes met het afronden van je promotie! Met [Anne](#) heb ik de analyse practica overleefd. Helaas moest je het nog een keer doen een jaar later, maar je leeft nog, dus dat is een goed teken! Veel succes met je gezonde deeltjes en je promotie! [Peter J.](#), ik ben jaloers op je dichte bindings technieken. Het lijkt je allemaal makkelijk af te gaan. Bovendien heb je een gezonde dosis droge humor die ik wel kon waarderen. Succes met het afronden van je promotie, kerel! [Chenghui](#) is a

bit of a silent force in the group. Nonetheless he sometimes sneaks up on me and we talk about research. Thanks a lot for letting us borrow your nice dyes! The rest of team Italy: [Serena](#) and [Annalisa](#). It was very nice to hang out with you two during the Phonsi summerschool in the South of France. Thanks for picking us up for lunch every day, Annalisa (even though it's getting less by now). Serena, you're the newest PhD student in the group, but you're finding your way around very well already (the karaoke was very bonding)! Good luck with the next four years :). Paul Thimoteüs, beter bekend als [Tim Prins](#), is een van de jongste promovendi in de groep. De surftrip in Portugal was supergaaf. Hopelijk pomp je er nog 1 of 2 artikelen over de perovskietjes uit (vooral mooie single-dot metingen)! Veel succes de komende jaren. Also present on the trip to Portugal was [Kelly](#), our American prodigy from Buffalo. You always managed to cheer me up when I started to stress out about my thesis. Unfortunately, your perseverance to visit a Fado concert in Porto did not work out completely, but you managed to go there later on. I'm sure you will enjoy the rest of your stay here in our flat country and in the group. [Saoirsé](#), we share a mutual passion for the Zelda videogames. I'm still tempted to snatch your Switch after I'm done writing. Good luck with your research!

I had the pleasure to supervise an entire load of talented students. It is incredibly cool to see everyone growing as a scientist. Het begon met [Annelies](#), die maar liefst 3 papers (!!!) uit haar masteronderzoek heeft gescoord (zonder mij). Het was een verademing om je te begeleiden, vooral omdat je bijna geen begeleiding nodig had. Heel veel succes met je eigen promotie, collega! [Paolo](#), you had a bit less success with your research, but managed to pull off your thesis in the end. Good luck with your PhD in Nijmegen! De meeste resultaten uit Hoofdstuk 7 zijn bij elkaar geraapt door [Julia](#). Het is verbazingwekkend hoe snel je analyses jezelf eigen maakt. Wanneer ik dacht je werk voor 2 maanden te geven, stond je na 2 weken alweer te springen om je analyse te laten zien. Ik hoop stiekem dat je nog wel gaat promoveren, maar wens je wat je ook gaat doen het allerbeste toe! [Ellenor](#) has joined me in the last year of my PhD. You got a very challenging, but cool, project to work on and even came to the synchrotron for experiments. I very much appreciated your independence during my stressful last months while writing my own thesis. We will write a supernice article on the adsorption geometry of PbSe nanocrystals at interfaces together. Mijn enige bachelorstudent was [Jesper](#), die aan de optische eigenschappen van perovskiet platelets heeft gewerkt. Jammer genoeg heb ik nooit tijd gehad om jouw onderzoek helemaal af te maken, maar hopelijk gebeurt dit verder in de groep nog. Ik wens je heel veel succes toe, waar je ook ter wereld gaat werken of studeren! Mister Sparkles, oftewel [Sander](#); officieel was je niet mijn student, maar ik heb je toch met erg veel plezier begeleid. Je mocht een maand of twee wonen en werken bij het ESRF. Samen met Ward en Freddy hebben we erg mooi werk gedaan op de organisatie van ZnS deeltjes. Zodra je klaar bent met zowel scheikunde als natuurkunde studeren (en weer voor professor Rabouw werken) denk ik dat je een mooie toekomst te wachten staat. Veel succes met alles! Ook mocht ik interim supervisor zijn van [Maaike](#), die naast Annelies de mooiste nanoplatelets kan maken. Hopelijk ga je ook nog PhD'en! Verder wil ik ook alle eerste- en tweedejaars studenten bedanken voor de leuke projecten die we samen hebben gedaan.

Furthermore, I would like to thank all current groupmembers that I haven't mentioned yet for the great atmosphere: Sophia, Pedro, Christa, Jacobine, Christiaan, Winston, Weiwei, Allan, Wenjin, Ting and everyone I forgot to mention. Thanks for everything the last couple of years!

From the previous generation of CMI PhD's I would also like to acknowledge some people for the good times at the CMI group. [Francesca](#), our rivalry already started when I was a bachelor student. Luckily we never truly clashed, but managed to work together quite well. You were able

to drag out the entire group to come party in the Tivoli every time there was a possibility for a Spice-Girls song. Which, ofcourse, was very much appreciated. I wish you and Ben the very best in England, even after you decolonize from the rest of Europe again. [Rosa](#), I think you had the same obsession with the Spice-Girls as Francesca. The parties at FOM Veldhoven were legendary together. I hope we will manage to actually meet up in Santander in the future :). [Esther](#), ik denk dat je proefschrift een voorbeeld is voor veel mensen in de groep. Het is tof dat we elkaar nog bij feestjes in de Tivoli tegenkomen. [Joren](#), de trip samen met Ward naar de USA was legendarisch, net zoals je ietwat beruchte rijstijl. Ik zal de sprint naar de auto in Yosemite park onder het geluid van grommende beren nooit meer vergeten. I would also like to thank [Zhixiang](#), [Dominika](#) and [Relinde](#) for the great atmosphere and collaborations.

I had the opportunity to work together with [Celso](#) on the cation-exchange-in-perovskite-nanocrystals-project. Your knowledge on the synthesis of nanoparticles is incredible, and you had a lot of insights on how to improve our work. You even started plotting data yourself in ways we didn't come up with, discovering linear trends everywhere :)! Thanks for all the great collaborations and I hope we can still work together in the future. Ik ken [Andries](#) al vanaf het begin van mijn bachelor thesis bij CMI. Toentertijd heb je me met veel sympathie en steun begeleid, waarvoor ik je nog steeds erg dankbaar ben. Als professor in de lichtkunde heb je ook altijd veel advies over spectroscopie gegeven (ik heb helaas je colleges nooit gevolgd), waar niet alleen ik, maar ook mijn studenten (de term λ^2) veel aan hebben gehad. Wat veel mensen ook niet weten is dat Andries een geduchte tegenstander is bij het basketballen bij de Debye sportdagen! Bovendien kan ik je droge gevoel voor humor wel waarderen (microfoons met echo opties bij het kerstdiner) en is je boerenkool bij het jaarlijkse kerstdiner echt fantastisch! Bedankt ook voor je deelname aan mijn leescommissie. Ook [Harold](#) wil ik bedanken voor zijn leerzame colleges over natuurkunde voor chemici en het sporadisch binnenwandelen om over diffractie te praten.

Een promotie onderzoek is niet zonder technische problemen. Gelukkig is er zeer sterke technische hulp vanuit de vakgroep. Als eerste was er [Hans](#). Iedere groep zou een 'Hans' moeten hebben. Nieuwe cel nodig voor experimenten? Hans denkt mee en regelt het. Iets kapot? Morgen werkt het weer! Ik heb je hulp altijd erg op prijs gesteld. Bovendien was er altijd tijd voor een praatje over de meest verschillende onderwerpen. Geniet van je pensioen, hopelijk kun je snel samen met Bea even goed op vakantie! Toen Hans wegging werd er naar een goede vervanging gezocht. Niet gemakkelijk, maar in [Peter](#) is er zeker een sterke technicus gevonden. Ik vind het knap dat je je draai in de vakgroep zo snel hebt gevonden. Veel succes en plezier in de groep de komende jaren! Ook de computerhulp van [Stephan](#) was vaak erg nuttig. Bedankt voor de hulp met Python gerelateerde problemen de afgelopen jaren. Tevens wil ik [Thea](#) en [Marion](#) bedanken voor de hulp met papierwerk en het verzenden van pakketjes voor experimenten. Daarnaast is sinds kort [Linda](#) begonnen op CMI. Ik wil je erg bedanken voor al je hulp bij het boeken van reizen, invullen van formulieren en verzenden van pakketjes. De andere Hans, [Hans Meeldijk](#), is de TEM expert hier in Utrecht. Bedankt voor de vele gezellige uren achter de verschillende microscopen. Samen met [Chris](#) was je nooit te beroerd om even te helpen als de uitlijning van de microscoop weer niet goed wilde, of om de wat duurdere microscopen zelf aan te sturen onder begeleiding van je verhalen over wilde fietsavonturen en vakanties. Allebei heel erg bedankt!

The year I spend in Grenoble has been truly amazing, which would not have been such a great experience without some great colleagues and friends. I started together with [Simon](#) from day one. My friend, it was an absolute pleasure to go hike together, visit French movies (which we pretended to understand fully) and joining the weekly pubquiz in the Subway (finishing up at Batman's place). Partially our mutual interest for 'pumping iron' made us work together

well. I have to admit it was a bummer you had to go after four months, but your visit with Anke in our flat country made up for that. [Giovanni](#), as an Italian you wore your Antarctica outfit in summer as well. In fact everything below 25°C was cold. Thanks a lot for helping me out with experiments, especially spending time together with [Luca](#) behind the AFM as well. I really hope you quickly find a great position in science. Also thanks for introducing us around in the beginning of our stay. Your perseverance at the pubquiz was very much appreciated, even after you were offended multiple times by the French women.

Tijdens het verblijf bij het ESRF had ik een Nederlands baken in de duisternis; [Jan Hilhorst](#). Je was altijd bereikbaar voor vragen en wilde graag meedoen met experimenten. Ik heb enorm veel van je geleerd over diffractie. Je kritische blik op alle resultaten waren vaak erg nuttig en zorgde ervoor dat onze tunnelvisie soms werd doorbroken. De hikes waren een groot succes, de Via Ferrata iets minder. Bedankt voor alle hulp en de supertoffe tijd in Grenoble! Veel succes en geluk samen met Lisa in Heidelberg!

My stay at the ESRF could not have been at a nicer beamline. [Yuri](#), your Python skills still make me jealous. Even though I just started learning this at the ESRF, you always had simple and creative tricks to improve some codes of mine. I hope that we manage to do some coherent experiments together in the future! [Bea](#)(trice), thanks for everything! You were always interested and excited about our research. I have to admit that I still think crystals are cooler than glasses, but your research on the metallic glasses is pretty awesome as well. Your continuous effort to invite me (and Simon and Jens) to social events helped getting into the city life of Grenoble. I hope your future efforts in Lyon and wherever abroad together with [Roberto](#) will bring you all the best. [Federico](#) (Zontone), your polenta is one of the best I have ever tasted, thanks a lot for being our local contact numerous times! [Jens](#), hopefully we didn't make you sick every time we invited you for the hikes. [Steven](#), my French amigo, thanks for all the great French classes we had from Nely. It was nice seeing you even after I left the ESRF officially. Your dry sense of humor was always appreciated and I hope you, your detective-wife and your daughters will fare well in Grenoble over the next years. [Martin](#), our time together at ID10 was short, but it was very nice to have drinks at la Bobine together every once in a while. I would also like to thank the many other people I interacted with, however short it was sometimes. Honorable mentions go to: [Michael Wulff](#) (my across-the-hall-neighbor, thanks for all the friendly discussions and your continued interest in my research), [Yannick](#), [Enrico](#), [Jeeves](#) (thanks for being our local contact during your last days), [Theyencheri Narayanan](#), [Peter Boesecke](#), [Tobias Schulli](#), [Luca](#) (thanks for all the endless AFM sessions), [Thomas](#), [Julian](#), [Anja](#), [Chris](#), [Britta](#), and everyone I forgot to mention personally!

Mijn scheikunde avontuur begon op de HU. Helaas scheiden sommige wegen zich, maar ik wil [Léon](#), [Dide](#), [Kevin](#) en [Danny](#) voor alles bedanken en ik wens jullie niks minder dan het allerbeste. [Maarten](#), je bent te vroeg gegaan, ik mis je vrolijke insteek op alles. Het lukt vaak niet om te meeten met [Dayinta](#), omdat we allebei ziek worden wanneer we een ontmoeting plannen (zelfs op gezamenlijke conferenties). Hopelijk gaat dit meer gebeuren als ik in Delft kom werken, want ik word altijd erg blij als we elkaar zien! Succes met de laatste loodjes van je promotie! Van mijn tijd bij Akzo plan ik met [Bob](#)-taisama nog steeds de maximaal (twee-)jaarlijkse meet-up! Het is altijd tof om je te zien, chef. Hopelijk kunnen we de frequentie wat omhoog gooien :)!

Mister-mister [Joris](#) Dee, tevens mijn tweede paranimf. We komen uit dezelfde regio en hebben heel erg lang samen gestudeerd. Ik denk nog steeds dat je onderzoek moet gaan doen naar carbon nanotubes in zwaarden gemaakt van damascus staal. Mijn gaarste herinnering samen is nog steeds dat je me zover hebt gekregen om mee te larpen voor de trailer van 'In den

Gulden Draek, verkleed als orc. Ik vind het tof dat we, ondanks dat we elkaar niet heel vaak zien, nog steeds contact hebben, af en toe films pakken en nog belangrijker: dat je nog steeds je dansmoves niet verleerd bent (ik ben jaloers). Hopelijk komen er in de toekomst nog heel veel (foute) feestjes!

Ik ben mijn hele leven al geïnspireerd door uitstekende docenten. Het begon met [Harry Mons](#) op het Griftland college (door wie ik scheikunde ben gaan studeren). Hierna heb ik op de HU veel goede zetjes in juiste richting gekregen. De docenten die me het meest zijn bijgebleven zijn [Rob Nickel](#), [Richard van der Laan](#), [Cees Schneiders](#) en [Robert Stolk](#). Ook op de UU waren er een hoop inspirerende professoren. In het bijzonder wil ik graag [Willem Kegel](#) bedanken voor de fantastische Fysische Chemie colleges (en de deelname aan mijn leescie). Tevens wil ik [Annik van Keer](#) en [Jos Koeckhoven](#) bedanken voor de goede begeleiding tijdens mijn prémaster.

During my research I had the extreme pleasure (and perhaps luck) to work closely together with the people from the EMAT institute in Antwerp. The team of professor [Sara Bals](#) always manages to help us with the best electron microscopy analyses I could wish for. In particular my thanks go out to [Bart Goris](#), [Thomas Altantzis](#), [Daniele Zanaga](#), [Yang Zhang](#), [Hans Vanrompay](#) and [Karel van der Bos](#) for their patience, dedication and the awesome collaboration. I hope the great and fruitful collaboration with the CMI group will continue in the future! Thanks again for always being willing to analyze even our most difficult samples and bringing our research to the next level! Besides that, I would like to thank Sara for joining my reading committee.

We hebben ook veel samengewerkt met het simulatie team uit de groep van [Marjolein Dijkstra](#). Ik wil naast Marjolein ook graag [Anjan Gantapara](#), [Laura Filion](#) en [Berend van der Meer](#) bedanken voor de discussies en samenwerking op het gebied van de zelf organisatie van nanokristallen.

Het geexplodeerde zijproject over de perovskiet nanodeeltjes heeft ook voor een nauwe samenwerking met de TU Eindhoven gezorgd. I had the pleasure to supply [Claudiu](#) with an endless stream of CsPbBr_3 nanocrystals. We still need to do something with this awesome movie we made together! Hopefully your manuscript will get accepted soon! I would also like to thank [Paul Koenraad](#) and [Andrei Silov](#) for the very pleasant collaboration. I learned a lot about coupling of excitons to vibrations in nanocrystals from the both of you.

I know [Wiebke](#) already from my time as masterstudent at CMI. It's nice to have you as a good friend, especially when a van needs to be driven to help moving houses! We even managed to get a paper together (it's almost done!). The dinners with [Roland](#) were also always great, you two are very good chefs (except for the no-champignon-criterium)! I wish you nothing but the best in Antwerp, hopefully also your proposal for a combined position in Leiden will get through. I would also like to thank the rest of the SCM group. Even minor interactions or simple chats at the coffee machine, both on scientific and weather related topics, were sometimes a welcome distraction. Special thanks to [Jessi](#), [Wessel](#), [Ernest](#), [Navid](#), [Gerhard](#) and the rest of the SCM group for the nice time in the Ornstein lab.

Mijn eerste huisvesting in Utrecht heb ik te danken aan [Jeroen](#) (van Olffen). AL16 was een erg toffe plek om te wonen als student. Volgens mij is het ook jouw schuld dat ik begonnen ben met salsa, dus dankjewel daarvoor :)! Ik wil ook graag alle huisgenoten bedanken met wie ik met veel plezier heb samengewoond. In het bijzonder [Iris](#), [Sven](#) en [Holson](#) (team Marvel!), [Lilian](#) en [Maurits](#); bedankt voor de fijne tijd!

Mijn poging om professioneel salsa danser te worden is uiteindelijk niet helemaal geslaagd. Samen met [Wout](#) en [Jeffrey](#) heb ik jarenlang café Maria en de Stairway in Utrecht onveilig gemaakt. De dansverslaving is vooral bij Jeffrey volgens mij doorgeslagen, maar ik vind het ook

nog steeds tof om af en toe dansjes te wagen in de stad. Het was ook erg leuk om je paranimf te mogen zijn Jeffrey, en bovendien erg nuttig om alvast een insider-look te hebben van hoe het er aan toegaat. Veel succes en plezier in Slovenië met al je moeilijke topologische problemen, maar dat komt volgens mij wel goed. We moeten vaker gaan bowlen Wout! Dat, of eindelijk officieel mee gaan doen aan Rocket League kampioenschappen. Hopelijk komen er nog veel bezoeken aan meneer Smakers in de toekomst!

Ik heb bij (I just wanna feel...) Udance altijd een hele toffe tijd gehad. Na de eerste danslessen (van mr. Percy, thanks a lot!) was ik hooked on salsa. Naast Percy wil ik ook graag Rogier, Ceasar (thanks for the awesome pachanga classes), Brian en Vivaldo & Belinha bedanken voor alle toffe danslessen de afgelopen jaren. De vele mensen die ik over de jaren tijdens de danslessen en op feesten heb leren kennen, zal ik niet snel vergeten. Ik ben vooral blij dat ik nog veel contact heb met Karin, Wieke en Jasper. De afgelopen tijd heeft mijn sociale leventje op een laag pitje gestaan en ik zie jullie te weinig. Gelukkig gaat Jasper inmiddels mee baantjes trekken op zondag en komt Wieke ook af en toe mee :). Met Karin moet vooral meer gedanst gaan worden. De komende periode is daar gelukkig wat meer tijd voor dan de afgelopen maanden. Bedankt voor alle lieve berichtjes en de steun de afgelopen tijd! Special thanks go to Gabriel & Floor en Chris & Zahira tijdens het wekelijkse kizomba uurtje het afgelopen jaar :). Het is onmogelijk om alle mensen uit de danswereld persoonlijk te bedanken, maar ik heb dankzij jullie allemaal een supertoffe tijd achter de rug! 's Zomers ben ik meestal een paar weken te vinden op de stranden van Texel. Ik wil iedereen van de Texelse Reddingsbrigade bedanken voor de hele toffe tijden, hopelijk kan ik volgend jaar gewoon weer meedraaien :).

Familie is belangrijk en ik zie ze te weinig. Zowel de gehele familie Lummen (de volgende familiedag komen we weer) als de familie Geuchies wil ik bedanken voor de interesse en steun de afgelopen jaren. Marieke, Pascal en de kids, het is altijd leuk om langs te komen, ook al is het maar voor kort. Ik kom wat dichterbij in de buurt van Zeeland werken, dus hopelijk gaat het lukken wat meer te komen buurten. Naomi, nog een geval van we zien elkaar ook te weinig. Je begrijpt naar eigen zeggen 'helemaal niks' van wat ik doe. Je moet eindelijk een keertje komen kijken, dan kan ik het je allemaal live uitleggen. Ook bedankt voor updates over Utrecht uit de *Cosmopolitan* :), dat was erg nuttig! Hopelijk vind je snel je eigen stekje.

My dearest Ronja, you've been with me from almost the start of my PhD adventure. It's been quite the dance together. Your endless support, even when I moved a year abroad, has meant the world to me. We've made quite the number of awesome trips together and discovered the addicting new hobby of wavesurfing :). I hope I can be as good of a support to you during your own PhD as you were for me. I love you!

Het laatste stuk in mijn dankwoord gaat uit naar mijn ouders. Ik ben jullie allebei ontzettend dankbaar voor alle vrijheid en steun die jullie me al mijn gehele leven geven. Al hebben jullie op een gegeven moment niet meer volledig begrepen waar ik mee bezig was, jullie toonden altijd veel belangstelling, interesse en bewondering voor wat ik doe. Pa, je bent van jongs af aan al een voorbeeld voor me. Je houdt je in moeilijke tijden staande en bent er altijd voor ons. Lieve mam, je bent er fysiek helaas niet meer bij, maar ik draag je nog iedere dag bij me. Deze is ook voor jullie!

- Jaco, juli 2017.

About the author

Jacob Jan Geuchies (Jaco) was born in Amersfoort, the Netherlands, on the 27th of January 1990. He obtained his highschool diploma ('Havo') from the Griffland College in Soest in 2007. In the same year he started his bachelor studies in Chemistry at the Utrecht University for Applied Science (Hogeschool Utrecht). During his bachelor studies, he did a six-month internship at Akzo Nobel in Arnhem under supervision of Drs. Hettie Verlaan, Dr. Auke Talma and Dr. Richard van der Laan on the synthesis of a disulfide monomer compound. After this, he followed a premaster track at Utrecht University to qualify for the 'Nanomaterials: Chemistry and Physics' master programme. He finished his bachelorthesis in 2011 under supervision of Dr. Robert Stolk and Prof. dr. Andries Meierink on 'Downconversion with lanthanide ion couples' and graduated *cum laude*.

In 2011, Jaco started the masterprogramme 'Nanomaterials: Chemistry and Physics' at Utrecht University, following courses on the physical chemistry and chemical physics of nanostructured materials. For his masterthesis, he did research under supervision of Dr. Mark Boneschanscher, Dr. Ingmar Swart and Prof. dr. Daniel Vanmaekelbergh on the geometric structure and electronic properties of PbSe honeycomb semiconductor superlattices. During his master's, Jaco wrote a proposal to obtain a Ph.D. position which would allow him to continue with the research of his masterthesis, for which he was awarded the first place in the Debye Graduate Programme under supervision of Dr. Andrei Petukhov, Dr. Ingmar Swart and Prof. dr. Daniel Vanmaekelbergh. He received his master's degree *cum laude* in 2013.

In the same year, Jaco started his Ph.D. under supervision of Prof. Dr. Daniel Vanmaekelbergh, Dr. Andrei Petukhov, Dr. Oleg Konovalov and Dr. Ingmar Swart. The main topic of his research was to study the formation of self-assembled nanocrystal superlattices using X-ray scattering techniques. To this end, he spend one year working at the ID10 beamline of the European Synchrotron Radiation Facility (ESRF) in Grenoble, France, under supervision of Dr. Oleg Konovalov. The main results of his worked are described in this thesis, published in peer-reviewed journals and presented at (inter) national conferences. During his Ph.D. project, Jaco supervised four master students and one bachelor student. Furthermore he supervised several second-year research projects, he was an assistant during the first-year analytical practicals for chemistry students and he was a teaching assistant for 'Mathematics for chemists', 'Quantum chemistry 1' and the 'Solids and surfaces' courses.

